Abstract

Title of Dissertation: The Fossils of the First Galaxies in the Local Universe

Mia Sauda Bovill, Doctor of Philosophy, 2011

Dissertation directed by: Professor Massimo Ricotti
Department of Astronomy

We argue that, at least a fraction of the newly discovered population of ultra-faint dwarfs in the Local Group constitute the fossil relics of a once ubiquitous population of dwarf galaxies formed before reionization with maximum circular velocities, $v_{max} < 20$ km s^{-1}, where $v_{max} \sim M^{1/3}$. To follow the evolution and distribution of the fossils of the first galaxies on Local Volume, $5-10$ Mpc, scales, we have developed a new method for generating initial conditions for ΛCDM N-body simulations which provides the necessary dynamic range. The initial distribution of particles represents the position, velocity and mass distribution of the dark and luminous halos extracted from pre-reionization simulations. We find that ultra-faint dwarfs have properties compatible with well preserved fossils of the first galaxies and are able to reproduce the observed luminosity-metallicity relation. However, because the brightest pre-reionization dwarfs form preferentially in overdense regions, they have merged into non-fossil halos with $v_{max} > 20-30$ km s^{-1}. Hence, we find a luminosity threshold of true-fossils of $< 10^6 L_{\odot}$, casting doubts on the classification of some classical dSphs as fossils. We also argue that the ultra-faints at $R < 50$ kpc, have had their stellar properties significantly modified by tides, and that a large population of fossils remains undetected due to $\log(\Sigma_V) < -1.4$. Next, we show that fossils of the first galaxies have galactocentric distributions and cumulative luminosity functions consistent with observations. We predict there are ~ 300 luminous satellites

orbiting within R_{vir} of the Milky Way, $\sim 50-70\%$ of which are fossils. Despite our multidimensional agreement at low luminosities, our primordial model produces an overabundance of bright dwarf satellites ($L_V > 10^5 L_\odot$), with this "bright satellite problem" most evident in the outer parts of the Milky Way. We estimate that, although relatively bright ($L_V > 10^5 L_\odot$), these ghostly primordial populations are very diffuse, producing primordial populations with surface brightnesses below surveys' detection limits. Although we cannot yet present unmistakable evidence for the existence of the fossils of first galaxies in the Local Group, we suggest observational strategies to prove their existence. (i) The detection of "ghost halos" of primordial stars around isolated dwarfs. (ii) The existence of a yet unknown population of ~ 150 Milky Way ultra-faints with half-light radii $r_{hl} \approx 100-1000$ pc and luminosities $L_V < 10^4 L_\odot$, detectable by future deep surveys.

The Fossils of the First Galaxies in the Local Universe

by

Mia Sauda Bovill

Dissertation submitted to the Faculty of the Graduate School of the
University of Maryland at College Park in partial fulfillment
of the requirements for the degree of
Doctor of Philosophy
2011

Advisory Committee:

Professor Massimo Ricotti, chair
Professor Thomas Cohen (Dean's Representative)
Professor Stacy McGaugh
Professor Eve Ostriker
Professor Derek Richardson
Professor Rosemary Wyse (JHU, External Member)

Preface

The content of this thesis is drawn, sometimes verbatim, from three papers. These are Bovill and Ricotti (2009), Bovill and Ricotti (2010a), and Bovill and Ricotti (2010b) with portions of the introduction coming from Mia Bovill's second year project. They are incorporated as follows. Chapter 1 uses text from the introductions of all three papers. Chapter 2, with a few small modifications, is Bovill and Ricotti (2009) verbatim. Bovill and Ricotti (2010a) is split between the method description and tests in Chapter 3 and the discussion of the fossil properties in the first half of Chapter 4. The distribution of the fossils in Bovill and Ricotti (2010b) is the second half of Chapter 4 and the bright satellite problem discussion is Chapter 5. The observational tests presented in the two 2010 papers are compiled in Chapter 6.

As of July 22, 2011, Bovill and Ricotti (2009) is published and Bovill and Ricotti (2010a) and Bovill and Ricotti (2010b) are revised and accepted to ApJ. The versions of the latter two papers used in this dissertation are verbatim what will be published in ApJ.

In loving memory of my grandfathers, Edwin “New Daddy” Bovill and Jack “Poppa” Sauda, who have been with me every step of the way. And for my great-grandmother, Mabel “Mimer” Bovill, whom I never met, but in whose steps I walk.

Acknowledgements

"If the universe puts a mystery in front of us as a gift, then politeness requires that we at least try and solve it."

- Delenn, Babylon 5

First and foremost, grazie mille to Massimo Ricotti for his knowledge and guidance over the last six years. As a second year project turned into a PhD thesis, he has taught me immense amounts about cosmology, galaxy evolution and fortran, but also about the kind of astronomer I want to be, as a researcher and as a member of the community.

Thank you as well to my departmental committee: Derek Richardson, for his help with many of the computational aspects of the project, and explaining hockey; Stacy McGaugh, for providing an observer's perspective and teaching me to question everything, even the dominate paradigms; and Eve Ostriker, for expecting excellence and pushing me in the classroom and in my thesis. The work in this dissertation is better because of their input.

After over a decade enrolled at the University of Maryland, the Department of Astronomy has become a second home and members of the community have supported me in many ways. In particular, many thanks to Doug Hamilton, for teaching me how to teach, Cole Miller for taking on a young grasshopper, and Grace Deming, who never stopped advising me. Thanks as well to Chris Reynolds, Richard Mushotzky, Stuart Vogel, Mark Wolfire, Ed Shaya, Eric McKenzie, Tamara Bogdanovic, Peter Teuben, Leslie Sage and Stef McLaughlin (and Kisses).

No one makes it through graduate school as an island. I am indebted to my fellow graduate students, past and present; Megan Decesar, John Vernaleo, Jessica Donaldson, Jonathan Fraine, Katie Phillpot, Ashley Zauderer, Rodrigo Herrera Camus, Sid Kumar, Anne Lohfink, Lisa Winter, Randall Perinne, Holly Sheets and my fellow "Mo's", KwangHo Park, Emil Polisensky, and Kari Helgason.

To my non-astronomy friends, Jocelyn Knauf, Alix Watson, Beth Vernaleo, Caroline Crow, Solomon and Johanna Granor, Josh Pilachowski, Kaveh Pahlevan, and especially Erin "Angela" Branigan, you have been my sanity through the entire process and I cannot imagine going through graduate school without you.

I owe a huge debt of gratitude, not only to my parents, Jean Sauda and Carl Bovill, who have kept me fed, laundered and encouraged since I decided to get a PhD in astronomy 17 years ago, but to my entire extended family for their unyielding faith. Especially, Jeanne Bovill, Ted Bovill, Suzanne Knauf, and my second mom, Susan Latchem.

Finally, while many people have contributed to the finishing of this PhD, it began in 1998 when Debora Katz took a 15 year old's dream and gave it form. I hope to pay her gift forward for the rest of my career.

Contents

List of Tables

List of Figures

Chapter 1

Introduction

We currently live in an epoch dominated by large spiral and elliptical galaxies; however such was not always the case. In the cold dark matter paradigm (CDM), the galaxies that populate the modern universe were formed from lower mass building blocks via hierarchical merging. At the time of reionization ($z = 6 - 15$), the majority of the universe‘s stellar mass was contained in these dwarf galaxies with masses no greater than $10^9 M_\odot$. While many of these early dwarfs merged to form the array of larger galaxies seen today, not all of them became part of spirals and giant ellipticals. Those that survived unmolested to the modern epoch are very faint (Gnedin and Kravtsov 2006; Ricotti and Gnedin 2005), and nearly impossible to see beyond the Local Group. Therefore, in the quest to better understand the formation of the first galaxies, the best place to look is in our cosmic backyard.

Hierarchical formation scenarios predict that most of the galactic halos formed before reionization in minihalos which had masses below $10^8 - 10^9$ $\mathrm{M}_\odot$. During the epoch of reionization ($z \sim 15 - 6$), the intergalactic medium (IGM) transitioned from neutral H I to ionized H II. We know reionization ended by $z \sim 6$ because of the lack of a Gunn-Peterson trough in quasars with $z < 6$ (Becker et al. 2001; Fan et al. 2002, 2006), showing no evidence of a neutral absorbing medium on the line of sight between the quasar and Earth. While we can determine the end point of reionization from quasar spectra, its extent and the sources that began it are determined by τ, the optical depth of the universe (Shull and Venkatesan 2008), derived from the CMB. The WMAP 7 value of $\tau = 0.088 \pm 0.015$ (Komatsu et al. 2011).

In addition to turning the IGM transparent to H ionizing radiation, reionization reheated the IGM to $\sim 10^4$ K, cutting off the gas supply to minihalos. Those minihalos, which formed stars at high redshift and survived to the modern epoch, constitute a sub-population of dwarf satellites orbiting larger halos. CDM N-body simulations predict a number of dark matter halos around the Milky Way and M31 that is two orders of magnitude greater than the number of observed luminous satellites (Klypin et al. 1999; Moore et al. 1999), the missing galactic satellite problem. This may indicate a problem with the CDM paradigm or that feedback processes are very efficient in suppressing star formation in the mass halos.

New observations (Belokurov et al. 2007, 2006; Geha et al. 2009; Ibata et al. 2007; Irwin et al. 2007; Kalirai et al. 2010; Majewski et al. 2007; Martin et al. 2006; McConnachie et al. 2009; Walsh et al. 2007; Willman et al. 2005a,b; Zucker et al. 2006a,b) and recent simulations (Ricotti et al. 2002a,b, 2008) require not only a revisitation of the missing galactic satellite problem, but an extensive study of what the smallest dwarfs can tell us about the epoch of the first galaxies. Cosmological simulations of the formation of the first galaxies (Ricotti et al. 2002a,b, 2008) (hereafter the pre-reionization simulations) have shown most previously known dwarf spheroidals (dSphs) to have properties consistent with the surviving fossils of the first galaxies, and predicted the existence of an undiscovered, lower surface brightness population of dwarfs (Ricotti and Gnedin 2005) (hereafter, RG05). In RG05, the members of the Local Group were sorted into three categories: non-fossils, polluted fossils and true fossils. Non-fossils are galaxies whose total mass today exceeds $10^9 M_{\odot}$, a scale set by the filtering mass of the IGM Gnedin (2000). These galaxies have continued to undergo star formation after reionization and today have multiple stellar populations with at least a fraction of their gas retained. The less massive, gas free dwarfs are designated as two types of fossils, with polluted fossils being galaxies that formed more than 30% of their stars after reionization, and true fossils which formed the majority ($> 70\%$) of their stars before reionization. It is this last group on which this work concentrates and, for the remainder of this work, "fossil" refers to the true fossils only.

1.1 The First Galaxies

The formation of the first dwarf galaxies - before reionization - is regulated by complex feedback effects that act on cosmological scales. Primarily, this involves the self-regulating interplay of ionizing and non-ionizing UV radiation, and the resulting formation and destruction of H_2, the only coolant available in the early universe. As the first stars and galaxies formed, the gas was unenriched with a primordial composition ($75\% H 25\% He$). Since no metals were available for cooling, the presence of H_2 was required for star formation. The self-regulation mechanisms governing the formation and destruction of H_2 during these epochs therefore have dramatic effects on the number and luminosity of the first, small mass galaxies, and yet, are unimportant for the formation of galaxies more massive than 10^8 $\mathrm{M}_{\odot}$. The mass scale is set by the mass required for $T_{vir} > 10^4$ K, allowing the gas to initially cool via Lyman-α emission, allowing them to cool gas below their virial temperature. In addition these more massive halos will retain a sufficient column density of H_2 to self shield from FUV dissociating radiation, retaining their coolant for the first generation of stars.

Galaxy formation in the high redshift universe is peculiar due to (i) the lack of important coolants, such as carbon and oxygen, in a gas of primordial composition and (ii) the small typical masses of the first dark halos. The gas in halos with maximum circular velocities (v_{max}) smaller than 20 km s^{-1} (roughly $M \lesssim 10^8 M_\odot$ at $z_{vir} \sim 10$, the virialization redshift of a halo with $M \sim 10^8 M_\odot$) is shock heated to temperatures $\lesssim 10,000$ K during virialization. At this temperature, a gas of primordial composition is unable to cool and initiate star formation unless it can form a sufficient column density of H$_2$ ($x_{H_2} \gtrsim 10^{-4}$). Although molecular hydrogen is easily destroyed by far ultraviolet (FUV) radiation (negative feedback), its formation can be promoted by hydrogen ionizing radiation emitted by massive stars, via the H$^-$ pathway (positive feedback) (Haiman et al. 1996).

$$H + e^- \Rightarrow H^- + H \Rightarrow H_2 + e^- \tag{1.1}$$

This primarily takes place on the edges of Strömgren spheres and inside relic H II regions. Since, by definition, the first, massive stars form in pristine regions, their halos would be able to retain enough H_2 due to the inital lack of negative feedback in those regions. The ionizing radiation from these stars will in turn allow molecular hydrogen to form in regions where it otherwise would not.

It is difficult to determine the net effect of radiative feedback on the global star formation history of the universe before reionization. At $z > 6$, the IGM is optically thick to ionizing UV radiation, requiring a 3D treatment of radiative transfer to address the formation of stars in minihalos. Without radiative transfer, we would be left with only the effects of a dominant FUV background (at energies between 11.34 eV and 13.6 eV), which destroys H$_2$. Radiative transfer is required to simulate the H^- formation pathway for H^2 in the high redshift universe since the IGM is opaque to ionizing UV radiation before the epoch of reionization. The FUV radiation emitted by the first few Population III stars would be sufficient to suppress or delay galaxy formation in halos with maximum circular velocities, $v_{max} \lesssim 20$ km s^{-1}. A less top heavy Pop II IMF would produce stars with softer SEDs and less ionizing and dissociating UV radiation. While this would produce fewer and smaller positive feedback regions, the net effect would a decrease in the suppression of star formation before reionization due to the drop in dissociating radiation and the resulting higher survival rates of H_2 (Ricotti et al. 2008).

Without the positive feedback, the gas in most halos with masses $< 10^8 - 10^9$ M$_\odot$ (below the Lyman limit) will not create or retain sufficient column densities of H_2 to self shield, cool and form stars. They will remain dark. Therefore, the number of pre-reionization fossils in the Local Group would be expected to be very small or zero. In the "tidal scenario," the Local Group's dwarf spheroidals (dSphs) are tidally stripped remnants of more massive dwarf irregulars (dIrrs). However, this model does not take into account the effect of ionizing radiation and "positive feedback regions" at high redshift (Ahn et al. 2006; Ricotti et al. 2001; Whalen et al. 2008), that may have a dominant role in regulating galaxy formation before reionization (Ricotti et al. 2002a,b).

1.1.1 Description of the Pre-reionization Simulation

For a given cosmological model, simulating the formation of the first stars is a well defined problem. However, these simple initial conditions become unrealistic once a few stars form within a volume of several thousand co-moving Mpc^3.

The pre-reionization simulations used in this work differ from many other studies because they self-consistently include "positive feedback" from ionizing radiation (Ricotti et al. 2002a,b, 2008). The pre-reionization simulations have a spatial resolution of 156 pc h^{-1} comoving (about 15 pc physical at $z = 10$) and a mass resolution

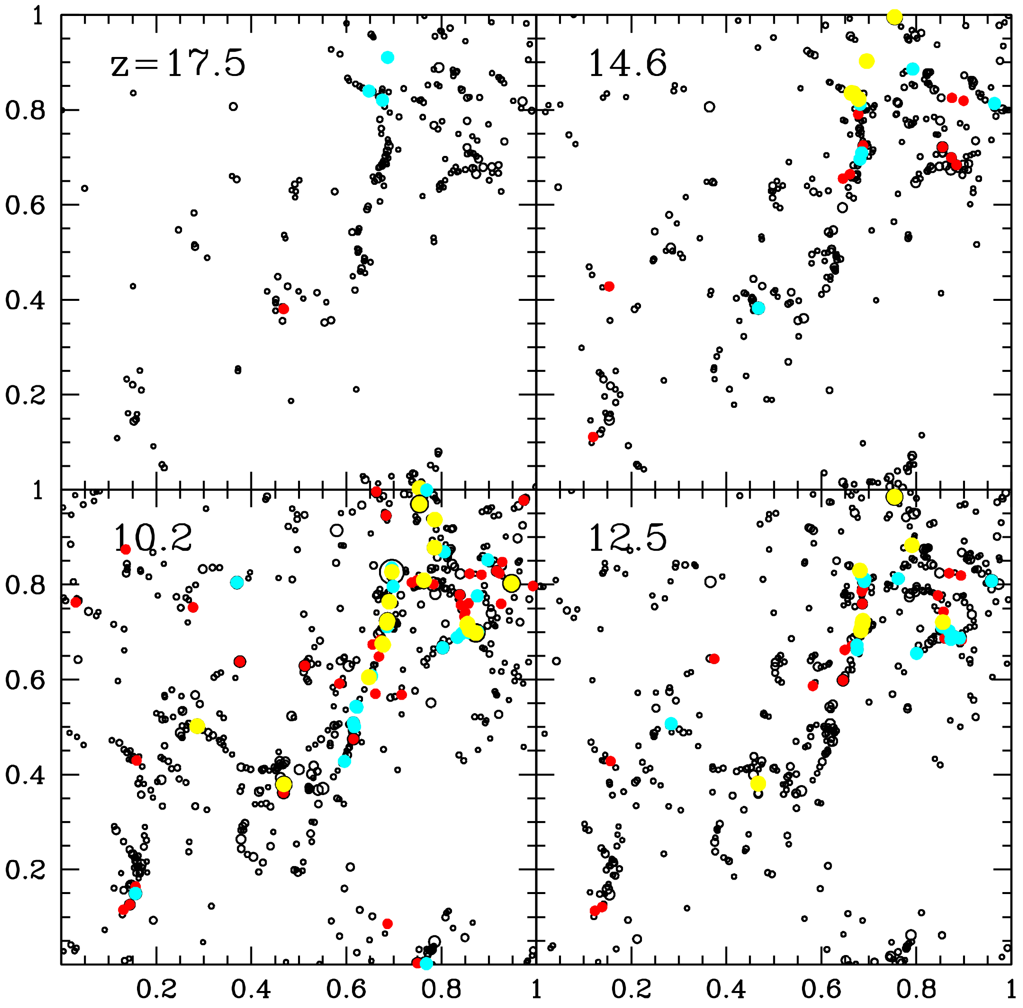

Figure 1.1: Figure 2 from Ricotti et al. (2008) showing the clustering properties of first luminous galaxies. We show positions of dark halos with $M_{dm} > 10^6 M_\odot$ in the simulation projected on the x-y plane in a slice with $\Delta d = 0.2h^{-1}$ Mpc at $z = 17.5, 14.6, 12.5$, and 10.2 (clockwise from top left panel). The $10^6 M_\odot$ scale is set by the resolution limit of the Ricotti et al pre-reionization simulations. Below these masses the parameters found by the halo finder cannot be trusted. Black circles show halo virial radii, and colored symbols mark halos hosting a luminous galaxy with $L_V > 5 \times 10^5 L_\odot$ (yellow), $5 \times 10^4 L_\odot < L_V < 5 \times 10^5 L_\odot$ (cyan), and $L_V < 5 \times 10^4 L_\odot$ (red). We assume $M_*/L_V = 1/50$ (solar), appropriate for a young stellar population. Most luminous galaxies seem to form in groups or filaments, with few in isolation in the lower density IGM.

of 4.93×10^3 $M_\odot$ h^{-1} for dark matter and ≈ 657 $M_\odot$ h^{-1} for the baryons. The stellar masses are always smaller than the baryon mass resolution and can vary from ~ 0.6 $M_\odot$ h^{-1} to 600 $M_\odot$ h^{-1} with a mean of 6 $M_\odot$ h^{-1}. Note that the stellar particles do not represent real stars. Instead they are subgrid patches of gas which formed stars with a local efficiency, ϵ_*, according to the Schmit law. Note, that this local star formation efficiency, which is set by hand, is different than the global star formation efficiency of the galaxy. The global star formation efficiency is not set by hand, but is dominated by the ability of a halo to form and retain H_2. In addition to primordial chemistry and 3D radiative transfer, the pre-reionization simulations include a recipe for star formation, metal production by SNe and metal cooling (see Ricotti et al. (2002a) for details). The code also includes mechanical feedback by SN explosions. The effect of SN is somewhat model dependent and uncertain because it is treated using a sub-grid recipe. Hence, the pre-reionization simulation analyzed in this work includes metal pollution but not mechanical feedback by SNe. Simulations show that while mechanical feed back from supernova is the dominant mechanism for expelling gas in halos with $M > 10^{8.5} M_\odot$ (Wise and Cen 2009), it is only one of several mechanisms for halos in our mass range ($M < 10^8 M_\odot$).

The pre-reionization simulation data used in this work is from the highest resolution run in Ricotti et al. (2002b), evolved further to redshift $z = 8.0$ after the introduction of a bright source of ionizing radiation that completes reionization at $z \sim 9$ (see RG05 for details). The need for introducing a bright ionization source is dictated by the small volume of the simulation (1.5^3 Mpc^3); otherwise the volume would be reionized too late. The H I ionizing source removes all the remaining gas and shuts down star formation in halos with $v_{max} < 20$ km s^{-1}. As the ionization front moves through the minihalo, it is trapped and slowed by the neutral gas, producing a D-type front proceeded by shock waves. The heating of the gas by those shockwaves produces a wind which expels the gas into the IGM. removing the halo's ability to form stars (Shapiro et al. 2004).

Simulations, including positive feedback, produce galaxies that are extremely faint and with very low surface brightnesses. Since H_2 cooling is inefficient, gas does not cool quickly and collapse towards the center of the halo. Star formation occurs throughout the halo at a slow rate and the Ricotti et al simulations do not have the resolution to determine whether those stars formed in isolated Bok globules or in clusters, thus producing a low luminosity population extending out to R_S, where

$$\rho(r) = \frac{\rho_o}{\frac{r}{R_S}\left(1+\frac{r}{R_S}\right)^2} \tag{1.2}$$

is the NFW profile (Navarro et al. 1996), r is the distance from the center, R_S is the scale radius of the halo, and ρ_o is the density parameter unique to each halo. If a minihalo is able to form stars, the number and properties of that population are determined by, among other things, feedback and enrichment by supernova, the choice of the initial mass function (IMF) and the star formation efficiency, ϵ_*. In § 5.1.3 we address the effects which changing ϵ_* has at $z = 0$ on the primordial populations in the Milky Way satellites and isolated dwarfs.

1.2 Reionization to the modern epoch

We would like to be able to test simulations of the first galaxies against observations, but with $L_V < 10^6 L_\odot$ (Ricotti et al. 2002a,b, 2008), these objects may be beyond the reach of even JWST (Johnson et al. 2009; Ricotti et al. 2008). Therefore, observing the first galaxies during their epoch of formation is not possible, even with ALMA (Sheth 2011), but we *can* detect their remnants in the local universe. The minihalos in which the first galaxies formed have shallow gravitational potentials and are easily affected by the properties of the surrounding intergalactic medium (IGM). Imagine a dwarf galaxy before reionization ($z > 8$) in a halo of a few $10^7 M_\odot$. It has been able to form enough H_2 via the H^- pathway to form $\sim 10^5 M_\odot$ of stars. When its local IGM is reionized at $z \sim 9$ the temperature of the surrounding gas is heated to $T_{IGM} \sim 10^4$ K, greater than the virial temperature, T_{vir}, of our minihalo. The faster moving gas particles in the hotter IGM are unable to fall into the dwarf's shallow potential well, and within a few hundred Myr star formation has ceased. The threshold for accretion from the IGM and therefore the ability of a halo to form stars after reionization is set by T_{vir} of the halo, where gas can only accrete if $T_{IGM} < T_{vir}$. Since

$$T_{vir} = 10500K \left(\frac{\Omega_m h^2}{0.147}\right)^{-1/3} \left(\frac{M_{dm}}{10^8 M_\odot}\right)^{2/3} \left(\frac{1+z_{vir}}{10}\right) \tag{1.3}$$

where Ω_m and h are the fraction of matter in the universe and the dimensionless hubble constant in units of (H_o/100 km s^{-1}/Mpc), M_{dm} is the mass of the dark matter halo in solar masses, and z_{vir} is the redshift of virialization. The temperature threshold is equivalent to a mass threshold for a given redshift of virialization. We also know that

$$v_{max} \propto M^\beta \tag{1.4}$$

where $\beta \simeq 1/3$ and v_{max} is the maximum circular velocity of a halo with total mass, $M \sim M_{dm}$, since the baryonic component is insignificant. The $\beta \sim 1/3$ is derived by equating gravity and centripical acceleration for a particle moving in a circular orbit in a spherical halo.

$$a_c = a_g \tag{1.5}$$

$$\frac{\sigma}{R} \propto \frac{M}{R^2} \tag{1.6}$$

where σ is the velocity dispersion of particles moving at a radius R inclosing a mass M. Since $R \propto M^{1/3}$ and at the edge of the halo $\sigma = v_{max}$

$$v_{max}^2 \propto \frac{M}{M^{1/3}} = M^{2/3} \tag{1.7}$$

$$v_{max} \propto M^{1/3} \tag{1.8}$$

. However, dark matter halos are triaxial rather than spherical so rather than $\beta = 1/3$, $\beta \sim 1/3$.

Throughout this work, we express the threshold for accretion from the IGM in terms of a filtering velocity, v_{filter}, where a halo is only able to accrete additional gas if $v_{max} > v_{filter}$. A dwarf is defined as a pre-reionization fossil if its maximum circular velocity has never been greater than the filtering velocity from reionization to the modern epoch. For the majority of this work, we use a $v_{filter} = 20$ km s $^{-1}$, which corresponds to $T_{IGM} \sim 10^4$ K. Like Gnedin and Kravtsov (2006) (hereafter GK06), we assume the filtering velocity is constant in space and time. While this is not a valid assumption given the dynamic and highly structured nature of the IGM, the choice of a constant $v_{filter} = 20$ km s^{-1} provides the most conservative definition for the fossil population. GK06 used $v_{filter} = 30$ km s^{-1} and the temperature of the warm-hot intergalactic medium (WHIM with $T_{WHIM} \sim 10^5$ K) corresponds to an even higher $v_{filter} \sim 40$ km s^{-1}. These higher filtering velocities will increase the number and luminosity range of the fossil population. We discuss this in more detail in § 4.6.

An additional caveat is that *isolated* fossils may undergo a second stage of gas accretion and star formation at $z \lesssim 2$. This late stage accretion onto concentrated minihalos is permitted by the lower T_{IGM} after He reionization. The hallmark of this late accretion would be a dwarf galaxy dominated by an old (> 12 Gyr) population with either an H I reservoir or a small burst of star formation at low redshift (Ricotti

2009). This characteristic star formation history is seen in the isolated dwarf UGC 4879 (Jacobs et al. 2011).

However, this late stage accretion would not take place within the WHIM or near the Local Group, and dwarf galaxies in those regions remain red and dead. This allows us to connect the smallest dwarf spheroidals (dSphs) in the Local Group and Local Volume to the high redshift universe, and it has been a great six years for the Local Group!

The doubling of the Local Group satellite population, and the properties of those satellites have provided a new laboratory in which we can test our understanding of star formation on the smallest scales and the substructure "crisis" in CDM. Unfortunately for the latter, we cannot just match a theoretical mass function to the one derived from observations since it is only possible to derive the dynamical mass within the furthest stellar orbit within the dwarfs (Illingworth 1976; Walker et al. 2009). The dark matter halo extends well beyond that. In addition, the observed dark matter mass assumes an NFW profile in equilibrium, neither of which may be true for dwarf galaxies near our Milky Way (Ricotti 2003; Walker et al. 2010).

For the local dwarfs, we have luminosity, L_V, the line of sight velocity dispersion, σ_{los}, the half-light radius, r_{hl}, the metallicity, $[Fe/H]$, the metallicity spread, $\sigma_{[Fe/H]}$, and various alpha element abundances $[\alpha/H]$.

From the pre-reionzation simulations we have derived values for the luminosity, L_V, line of sight velocity dispersion, σ_{los}, half-light radius, r_{hl}, metallicity, $[Fe/H]$, and metallicity spread, $\sigma_{[Fe/H]}$ for the simulated fossils. Independent alpha abundances are computationally complex and were not included in the pre-reionization simulations. These data allow us to compare "apples to apples" and test our models against the real universe. As with all simulations, the values used in this work are dependent on the assumptions and physics in the pre-reionization simulations.

In a more general context, our theoretical model assumes a primordial formation scenario for the smallest Milky Way and M31 satellites.

1.3 The Local Group

Data mining of the Sloan Digital Sky Survey (SDSS) has roughly doubled the census of Local Group dwarfs. Before 2005, the Local Group looked muck like it had in Mateo (1998). Two massive spirals, the Milky Way and Andromeda were surrounded by 18 dwarf satellites (LMC, NGC 55, Sextans A & B, SMC, WLM, Carina, Fornax, GR8, Leo I, II & A, Sagittarius, Sculptor, Draco, Phoenix, Sextans and Ursa Minor) and 17 dwarf satellites (IC 10, IC 1613, IC 5152, M32, NGC 185, NGC 205, NGC 3109, NGC 6922, DDO 210, LGC3, Pegasus, And I, II, II, VI & V and Antila) respectively, with three additional dwarf spheroidals (Tucana, Cetus and KKR 25) associated with neither galaxy but bound to the Local Group and the smaller, bulgeless spiral M33 near M31. Of those 38 dwarfs, 12 were identified as fossil candidates in RG05, Sculptor, Draco, Phoenix, Sextans and Ursa Minor around the Milky Way and And I, II, II, VI, & V, and Antila around M31 in addition to the isolated Cetus, KKR 25 and Tucana. All these dwarfs are void of gas and dominated by old, metal poor stellar populations.

Starting in 2005, data mining of the Sloan Digitial Sky Survey expanded our picture of the Local Group. This has resulted in the discovery of 15 “new” ultra-faint Milky Way satellites (Belokurov et al. 2010, 2009, 2007, 2006; Geha et al. 2009; Irwin et al. 2007; Walsh et al. 2007; Willman et al. 2005a,b; Zucker et al. 2006a,b). At the same time, deep surveys of the halo of M31 have found 17 new Andromeda satellites (Ibata et al. 2007; Kalirai et al. 2010; Majewski et al. 2007; Martin et al. 2006; McConnachie et al. 2009). All of the new dwarfs, with the exception of Leo

T, are dSphs, devoid of gas and dominated by what appear to be old, metal poor populations. In addition to doubling the census of Local Group dwarfs, the new satellites have more than tripled the number of potential pre-reionization fossils within 1 Mpc of the Milky Way. Detailed properties of this new population as of March 2011 are in Tables 2.1 to 2.6.

We now have an excellent observational sample in the Local Group with which to test models of the first galaxies and begin to ask and answer questions about our local satellite population, and ΛCDM itself. Since we will compare our results to the observed distributions in the Local Volume, a brief inventory and overview of the current observational and theoretical work on this region is useful.

1.4 The Local Volume

The Local Volume consists of seven large groups of galaxies made primarily of dwarfs centered around larger, Milky Way-type spirals, and ten groups composed entirely of dwarfs, all within 5.5 Mpc of the Milky Way and bordering the Local Void. The majority of these galaxies are concentrated near the super galactic plane (SGP) (Karachentsev et al. 2003). The distribution is shown looking down from above and into the SGP plane in Figure 1.2.

The seven major groups are centered around the Milky Way and Andromeda, M81/M82, Cen A, M83, IC 342 and Maffei respectively. Cen A and M83, and IC 342 and Maffei can be further grouped into dynamical pairs similar to the Local Group. Excepting Cen A (0.33 Mpc below the SGP), every group is within 0.1 Mpc of the SGP (Figure 1.2). Typical distances of a group member from the central galaxy range from 104 to 385 kpc. Each group shows evidence for a population of dwarf spheroidal galaxies, bereft of neutral hydrogen gas, overwhelmingly located near the

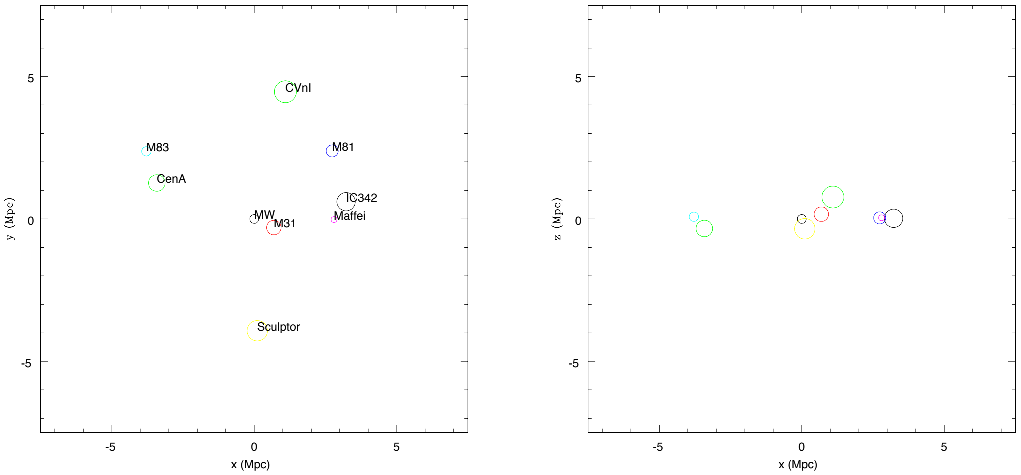

Figure 1.2: The major groups of the local volume from above (left) and into (right) the super galactic plane. The size of the circle around each massive host represents its mass.

massive galaxy at the center of group. In the entire Local Volume, only four isolated early-type dwarfs are observed, suggesting these galaxies are preferentially located near the more massive halos (Karachentsev 2005).

The ten minor groups show no evidence for central galaxies. These dwarf groups contain between two and five galaxies, with a median group population of four galaxies but have the same typical size (179 kpc) as the groups dominated by a massive galaxy (Karachentsev et al. 2003).

On the theoretical side we use our knowledge of the Local Volume to ask: Is the "primordial scenario" consistent with observations when we move beyond the virial radius of our own galaxy and peer into the voids? Unless the local component of galaxy feedback is very strong, star formation should proceed similarly in small mass halos regardless of a halo's location relative to the Local Group. Therefore, the voids should be populated with luminous objects (see Figures 3.5 and 3.6). As first noted in Peebles (2001), they are not. The number of dwarf galaxies with absolute magnitude $M_V > -16$ ($L_V < 2 \times 10^8 L_\odot$) observed in the voids is smaller than expected in CDM cosmology (Karachentsev et al. 2006, 2004; Tully et al. 2006). This discrepancy has been named the "void phenomenon."

According to Tikhonov and Klypin (2009), the luminosity function can only be reconciled if halos with $v_{max} < 35$ km s^{-1} are dark. However, such a large mass threshold for star formation would produce less than 35 luminous satellites between 100-200 kpc of the Milky Way. That is inconsistent with observations unless satellites with $L_V < 10^4$ L$_\odot$ do not exist beyond 100 kpc (see Figure 4.19).

Alternatively, if the star formation rate is primarily determined by halo mass, the void phenomenon can be reconciled with CDM by using a halo occupation distribution for which the M/L ratio increases with decreasing halo mass. However, this solution has only been tested for halos with $M > 10^{10}$ M$_\odot$ (Tinker and Conroy 2009), two to three orders of magnitude more massive than our fossils. When we extend their $M/L \sim M^{-1}$ relation to our fossil mass range, we obtain a M/L ratio $\gtrsim 10^5$ for the fossil population ($M \lesssim 10^8 M_\odot$). This would produce "mega-faint" dwarfs with $M/L \sim 2-3$ orders of magnitude greater than those seen for the fossils in RG05 and observed for the ultra-faint dwarfs.

This dissertation is an investigation of the fate and distribution of the fossils of the first galaxies near the Milky Way and throughout the Local Volume. Chapter 2 presents the observational motivation provided by the discovery of the ultra-faint dwarfs and the comparison of their numbers and properties to the simulated first galaxies at reionization, assumed to take place at $z = 8.3$. Chapter 3 describes the new set of N-body simulations we use to trace the fossils of the first galaxies to the modern epoch. Here, we also present tests of our simulations, proving our method works, and refining the observational definition of a fossil. Chapters 4 & 5 show the results of the simulations for the fossils and non-fossils respectively. These simulations ask a series of questions about the Milky Way's satellite population and the dwarfs inhabiting the nearby void.

First, we want to know if the ultra-faint dwarfs are fossils of the first galaxies and how many fossils remain undiscovered in the halo of the Milky Way. Then, what can the Local Group dSphs tell us about star formation in the early universe? Finally, we investigate the following conundrum: Can we simultaneously account for the predicted and observed subhalo population around the Milky Way and the lack of isolated galaxies with $M_V > -16$ in the voids?

Chapter 2

Local Group Cosmology

Over the last six years, the census of the Local Group dwarfs has doubled with the addition of ultra-faint, ultra-low surface brightness satellites around the Milky Way and M31. These new dSphs provide an excellent opportunity for near field cosmology in our Local Group, specifically an investigation of the physics of the formation of the first stars and galaxies. Before we trace the fossil remnants of these galaxies from reionization to the modern epoch, we compare the new ultra-faint dwarfs to luminous halos in the $z = 8.3$ output from the pre-reionization simulations. We extended the work in RG05 to include the new ultra-faint dwarfs in Bovill and Ricotti (2009) (hereafter, BR09), from which parts of this chapter are taken verbatim.

This chapter is laid out as follows. In § 2.1, we collect published data on the new dwarf population and, after correcting for completeness of the surveys, we estimate the total number of Local Group satellites (which increases from 38 to ~ 70). Using the results of published N-body simulations in GK06, we compare the observed number of luminous satellites to the estimated number of dark satellites that have or had in the past a maximum circular velocity $> v_{filter}$. Using the results of published N-body simulations, we conclude that some ultra-faint dwarfs are likely pre-reionization fossils. In § 2.2 we show that the properties of the new Milky Way and M31 dwarfs are in remarkable agreement with the theoretical data on the "fossils" from RG05 and with their Galactocentric distribution around the Milky Way calculated in GK06. In § 2.3 we discuss the implications of the new dwarfs on the formation of the first galaxies and the missing galactic satellite problem.

2.1 Data and Completeness Corrections

In Tables 2.1 to 2.6, we summarize the observed properties of the new dwarfs as of March 2011. The new Milky Way satellites were discovered using SDSS Data Release 4, 5, 6 and 7, including SEGUE (Abazajian et al. 2009; Adelman-McCarthy et al. 2008, 2007, 2006; Yanny et al. 2009). When multiple references are available for a dwarf property, we defer to the measurement with the smallest error bars. Excepting Bootes I and II, Canes Venatici I and Leo T, where central surface brightness measurements were available, the average surface brightness inside the half light radius, r_{hl}, was used: $\Sigma_V = L_V/(2\pi r_{hl}^2)$.

Recent surveys of M31 (Ibata et al. 2007; Kalirai et al. 2010; Martin et al. 2006; McConnachie et al. 2009) have covered much of the space around the M31 spiral. The surveys have found 19 new M31 satellites. The Pandas survey, which was responsible for most of the new M31 dwarfs, is complete around M31 and M33 to a $\sim$ 150 kpc projected distance from Andromeda. Any satellite counts within 150 kpc and with $M_v < -6$ and $\mu_V < 29$ are complete (Brasseur 2011).

Two new M31 satellites, And XII and And XIV, have velocities near or above their host's escape velocity (Chapman et al. 2007; Majewski et al. 2007). Both galaxies are classified as dwarf spheroidals and show a lack of H I gas, and both are likely on their first approach towards a massive halo. Their σ_* of $2.6^{+5.1}_{-2.6}$ km s^{-1}

(Collins et al. 2010) and 5.4 ± 1.3 km s $^{-1}$ (Kalirai et al. 2010), respectively, place them below the 20 km s^{-1} threshold, and their currently known properties meet the RG05 criteria for fossils.

In estimating the completeness correction for the number of the Milky Way dwarfs, one should also account for selection effects from the limiting surface brightness sensitivity of the Sloan of ∼30 mag arcsec^{-2} (Koposov et al. 2008). The sensitivity limit is shown as a solid line in Figure 2.1. Identification of new satellites depends on the visibility of the horizontal branch in the color-magnitude diagram, which, for the typical luminosity of the new faint dwarfs ($M_V \approx -4$) drops below SDSS detection limits at Galactocentric distances beyond $\sim 200 - 250$ kpc (Koposov et al. 2008). Of the new Milky Way dwarfs, only Leo T is well beyond this distance threshold and thirteen of the fifteen new Milky Way satellites are within 200 kpc. We make the most conservative estimate, by assuming that we have a complete sample of dwarfs within 200 kpc. Additional selection bias for the new dwarfs comes primarily from the limits of the SDSS coverage on the sky. To account for this, we apply the zero-th order correction of multiplying the number of new dwarfs by 5.15. This correction assumes an isotropic distribution of satellites when observed from the Galactic center. With these simple assumptions we estimate that the number of Milky Way satellites with galactocentric distance < 200 kpc is about 85 ± 14, including the 29 previously know satellites. The error estimate is due to shot noise. When we add in the post 2009 data the completeness drops to 3.56 *decreasing* the number of Milky Way satellites to 65 ± 10. However, bright satellites of the Milky Way are distributed very anisotropically (Bozek et al. 2011; Kroupa et al. 2005; Metz et al. 2007, 2009; Zentner et al. 2005), so the assumption of isotropy may not be a good one. Our assumption of isotropy is a 0^th order representation of the distribution of satellites around our Milky Way. While it is consistent with results from our CDM N-body simulations (Chapter 3), observations suggest that the distribution is not isotropic, but rather in a plane roughly perpendicular to the disk (Kroupa et al. 2005; Metz et al. 2007, 2009; Zentner et al. 2005). If we assume a planar distribution of satellites relatively symmetric about the disk then the correction number of Milky Way satellites drops to 37 ± 8.

In addition, the luminous satellites can be radially biased, so the abundance of the faintest satellites within 50 kpc may not be easily corrected to larger distances without prior knowledge of this bias. And, of course, satellites of different luminosity and surface brightness will have different completeness limits. These selection biases have been considered in detail in recent papers by Tollerud et al. (2008) and Walsh et al. (2009). These studies find that there may be between 300 to 600 luminous satellites within the virial radius of the Milky Way. Their estimate for the number of luminous satellites within a galactocentric distance of about 200 kpc is 229^{330}_{176}, twice as large as our simple (and more conservative) estimate.

Name	Type	(l, b) $(^o)$	d_{MW} (kpc)
Bootes I	dSph	$(358.1, 69.6)$ [B06b]	66 ± 3 [D06]
Bootes II	dSph	$(353.7, 68.9)$ [W08]	42 ± 8 [W07b]
CVn I [Z06a]	dSph	$(74.3, 79.8)$ [Z06a]	218 ± 10 [M08]
CVn II [B07]	dSph	$(113.6, 82.7)$ [B07]	160^{+5}_{-4} [M08]
Coma Ber. [B07]	dSph	$(241.96, 83.6)$ [B07]	44 ± 4 [B07]
Hercules [B07]	dSph	$(28.7, 36.9)$ [B07]	133 ± 6
Leo IV [B07]	dSph	$(265.4, 56.5)$ [B07]	160^{+15}_{-14} [B07]
Leo V [B08]	dSph	$(261.86, 58.54)$ [B08]	~ 180 [B08]
Leo T [I07]	dSph[1]	$(214.9, 43.7)$ [I07]	407 ± 38 [dJ08]
Pisces II [B10]	dSph	$(79.21, -47.11)$ [B10]	~ 180 [B10]
Segue 1 [B07]	dSph[2]	$(151.763, 16.074)$	23 ± 2 [B07]
Segue 2 [B09]	dSph	$(149.4, -38.1)$	35 [B09]
Ursa Major I [W05b]	dSph		97 ± 4 [O08]
Ursa Major II	dSph	$(152.5, 37.4)$	32 ± 4 [Z06b]
Willman 1	dSph[2]	$(159.57, 56.78)$	38 ± 7 [W05a]

Table 2.1: Positions and distance of the Milky Way ultra-faint dwarfs. As a note on the classification of the new objects as dSph, (1) Leo T has a $\sim 10^5 M_\odot$ of H Igas and a young stellar population and (2) Willman 1 and Segue 1 may be star clusters instead of dSph. The references are as follows: (B06a) - Belokurov et al. (2006), (B07) - Belokurov et al. (2007), (B08) - Belokurov et al. (2008), (B09) - Belokurov et al. (2009), (B10) - Belokurov et al. (2010), (D06) - Dall'Ora et al. (2006), (dJ08) - de Jong et al. (2008), (I07) - Ibata et al. (2007), (M08) - Martin et al. (2008), (O08) - Okamoto et al. (2008), (W08) - Walsh et al. (2008), (W05a) - Willman et al. (2005a), (W05b) - Willman et al. (2005b), (Z06a) - Zucker et al. (2006b), (Z06b) - Zucker et al. (2006a)

Name	L_V ($10^3 L_\odot$)	r_{hl} ($L_\odot$ pc $^{-2}$)	σ_{los} (pc)	$[Fe/H]$ (km s^{-1})	$\sigma_{[Fe/H]}$
Bootes I	28 ± 5	$242^{+22}_{-20}\ ^{M08}$	6.5 ± 2.0	-2.1 ± 0.3	—
Bootes II	$1.0 \pm 0.8\ ^{M08}$	$36 \pm 9\ ^{W08}$	$10.5 \pm 7.4\ ^{K09}$	$-1.79 \pm 0.05\ ^{K09}$	$0.14\ ^{K09}$
CVn I	$230 \pm 40\ ^{M08}$	546 ± 36	$7.6 \pm 0.4\ ^{SG07}$	$-2.08 \pm 0.02\ ^{K08}$	$0.46\ ^{K08}$
CVn II	$7.9 \pm 3.7\ ^{M08}$	$74^{+14}_{-10}\ ^{M08}$	$4.6 \pm 1.0\ ^{SG07}$	$-2.19 \pm 0.05\ ^{K08}$	$0.58\ ^{K08}$
Coma Ber.	$3.7 \pm 1.8\ ^{M08}$	$77 \pm 10\ ^{M08}$	$4.6 \pm 0.8\ ^{SG07}$	$-2.53 \pm 0.05\ ^{K08}$	$0.45\ ^{K08}$
Hercules	11 ± 4	229 ± 19	3.7 ± 0.9	$-2.58 \pm 0.04\ ^{K08}$	$0.51\ ^{K08}$
Leo IV	$8.7 \pm 4.5\ ^{M08}$	$116^{+26}_{-34}\ ^{M08}$	$3.3 \pm 1.7\ ^{SG07}$	$-2.58 \pm 0.08\ ^{K08}$	$0.75\ ^{K08}$
Leo V	$4.5\ ^{B08}$	$42\ ^{B08}$	$2.4^{+2.4}_{-1.4}$	$-2.0 \pm 0.25\ ^{W09}$	—
Leo T	140 ± 10	115 ± 17	$7.6 \pm 1.6\ ^{SG07}$	$-2.02 \pm 0.05\ ^{K08}$	$0.54\ ^{K08}$
Pisces II	$8.0\ ^{B10}$	$60\ ^{B10}$	—	—	—
Segue 1	$0.34 \pm 0.23\ ^{M08}$	$29^{+8}_{-5}\ ^{M08}$	$3.7^{+1.4}_{-1.1}\ ^{S10}$	$-3.3 \pm 0.2\ ^{G09}$	—
Segue 2	$0.86\ ^{B09}$	$34\ ^{B09}$	$3.4 \pm 2.0\ ^{B09}$	$-2.0 \pm 0.2\ ^{B09}$	—
Ursa Major I	$14 \pm 0.4\ ^{M08}$	$318^{+50}_{-39}\ ^{M08}$	11.9 ± 3.5	$-2.29 \pm 0.04\ ^{K08}$	$0.54\ ^{K08}$
Ursa Major II	$4.0 \pm 2.0\ ^{M08}$	$140 \pm 25\ ^{M08}$	5.7 ± 1.4	$-2.44 \pm 0.06\ ^{K08}$	$0.57\ ^{K08}$
Willman 1	$1.0 \pm 0.9\ ^{M08}$	25^{+5}_{-6}	4.0 ± 0.9	$-2.2\ ^{S08}$	—

Table 2.2: Observed properties of the Milky Way ultra-faint dwarfs. Citations are as follows, B08 - (Belokurov et al. 2008), B09 - (Belokurov et al. 2009), (G09) - Geha et al. (2009), (K08) - Kirby et al. (2008), (K09) - Koch et al. (2009), (S08) - Siegel et al. (2008), (S10) - Simon et al. (2010), (W08) - Walsh et al. (2008), (W09) - (Walker et al. 2009)

Name	Type	(l, b) (^{o})	d_{MW} (kpc)	r_{M31} (kpc)	r_{M33} (kpc)
And IX [Z04]	dSph	$(123.2, -19.7)$	765^{+5}_{-150} [C10]	45 [H05]	—
And X [Z07]	dSph	$(125.8, -18)$	621 ± 20 [B11]	174 ± 29 [B11]	—
And XI [M06]	dSph	$(112.57, -28.0)$	760^{+10}_{-150} [C10]	—	—
And XII [M06]	dSph	$(112.72, -27.4)$	830^{+170}_{-30} [C10]	—	—
And XIII [M06]	dSph	$(112.46, -28.8)$	910^{+30}_{-160} [C10]	—	—
And XIV [M07]	dSph	$(111.63, -32)$	871 ± 87	162.5	—
And XV [I07]	dSph	$(113.95, -23.9)$	770 ± 70 [L09]	90 [L09]	—
And XVI [I07]	dSph	$(112.43, -29.4)$	525 ± 50	130 [L09]	—
And XVII [I08]	dSph	$(120.23, -18.47)$ [I08]	734 ± 23 [B11]	73^{100}_{49} [B11]	—

Table 2.3: Positions and distance of the Andromeda ultra-faint dwarfs. Citations are as follows: (B11) - Brasseuretal:11, (C10) - Collins et al. (2010), (H05) - Harbeck et al. (2005), (I07) - Ibata et al. (2007), (I08) - Irwin et al. (2008), (L09) - Letarte et al. (2009), (M07) - Majewski et al. (2007), (M06) - Martin et al. (2006), (Mc09) - (Z04) - Zucker et al. (2004), (Z07) - Zucker et al. (2007).

Name	Type	(l,b) $(^o)$	d_{MW} (kpc)	r_{M31} (kpc)	r_{M33} (kpc)
And XVIII	dSph	$(113.9, -16.9)$	1355 ± 88	—	—
And XIX ^{Mc09}	dSph	$(115.6, -27.6)$	933 ± 61	—	—
And XX ^{Mc09}	dSph	$(112.9, -26.9)$	802 ± 197	—	—
And XXI ^{M09}	dSph	$(111.9, -19.2)$ ^{M09}	859 ± 51 ^{M09}	152 ± 31 ^{M09}	—
And XXII ^{M09}	dSph	$(132.6, -34.1)$ ^{M09}	$[794] \lesssim 1033$ ^{M09}	$[224] \lesssim 315$ ^{M09}	$[42] \lesssim 227$ ^{M09}
And XXIII ^{R11}	dSph	$(131.0, -23.6)$ ^{R11}	767 ± 44 ^{R11}	$\sim 126 \pm 44$ ^{R11}	—
And XXIV ^{R11}	dSph	$(127.8, -16.3)$ ^{R11}	600 ± 33 ^{R11}	$\sim 197 \pm 33$ ^{R11}	—
And XXV ^{R11}	dSph	$(119.2, -15.9)$ ^{R11}	812 ± 46 ^{R11}	$\sim 97 \pm 47$ ^{R11}	—
And XXVI ^{R11}	dSph	$(118.1, -14.7)$ ^{R11}	762 ± 42 ^{R11}	$\sim 101 \pm 42$ ^{R11}	—
And XXVII ^{R11}	dSph	$(120.4, -17.4)$ ^{R11}	757 ± 45 ^{R11}	$\sim 86 \pm 48$ ^{R11}	—

Table 2.4: Positions and distance of the Andromeda ultra-faint dwarfs. Citations are as follows: (M09) - Martin et al. (2009), McConnachie et al. (2009), (R11) - Richardson et al. (2011)

Name	L_V ($10^3 L_\odot$)	r_{hl} (pc)	σ_{los} (km s^{-1})	$[Fe/H]$	$\sigma_{[Fe/H]}$
And IX	149	552^{+22}_{-110} ^{C10}	$4.5^{+3.6}_{-3.4}$ ^{C10}	-2.2 ± 0.2 ^{C10}	—
And X	75	339 ± 6	3.9 ± 1.2	-1.93 ± 0.11	0.23 ± 0.04 ^{B11} / 0.48
And XI	49 ^{C10}	145^{+24}_{-20} ^{C10}	4.6 ^{C10}	-2.0 ± 0.2 ^{C10}	—
And XII	31 ± 33	289^{+70}_{-47} ^{C10}	$2.6^{+5.1}_{-2.6}$ ^{C10}	-2.1 ± 0.2 ^{C10}	—
And XIII	41 ^{C10}	203^{+27}_{-44} ^{C10}	$9.7^{+8.9}_{-4.5}$ ^{C10}	-1.9 ± 0.2 ^{C10}	
And XIV	180 ± 90	413 ± 41	5.4 ± 1.3	-2.26 ± 0.05	—
And XV	711	220 ± 22	$11.5^{+5.3}_{-4.4}$ ^{C11}	-1.58 ± 0.2 ^{L09}	~ 0.08
And XVI	410 ± 200	136 ± 14	$9.4^{+3.2}_{-2.4}$ ^{C11}	-1.3 ± 0.14 ^{C11}	~ 0.12
And XVII	238	254 ± 25	—	-2.0	0.31 ± 0.03
And XVIII	649	363 ± 36	—	-1.8 ± 0.1	—
And XIX	450 ± 260	2065 ± 206	—	-1.9 ± 0.1	—
And XX	28 ± 26	146 ± 15	—	-1.5 ± 0.1	—
And XXI	780 ± 190 ^{M09}	875 ± 127 ^{M09}	—	-1.8 ^{M09}	—
And XXII	$[30 \pm 10] \lesssim 60$ ^{M09}	$[217] \lesssim 282$ ^{M09}	—	-2.5 ^{M09}	—

Table 2.5: Observed properties of the Andromeda ultra-faint dwarfs. Citations are as follows: C11 - Collins et al. (2011), K10 - Kalirai et al. (2010).

Name	L_V $(10^3 L_\odot)$	r_{hl} (pc)	σ_{los} (km s^{-1})	$[Fe/H]$	$\sigma_{[Fe/H]}$
And XXIII	$1028\ ^{R11}$	$1035 \pm 50\ ^{R11}$	—	$-1.8 \pm 0.2\ ^{R11}$	—
And XXIV	$94\ ^{R11}$	$378 \pm 20\ ^{R11}$	—	$-1.8 \pm 0.2\ ^{R11}$	—
And XXV	$649\ ^{R11}$	$732 \pm 60\ ^{R11}$	—	$-1.8 \pm 0.2\ ^{R11}$	—
And XXVI	$59\ ^{R11}$	$230 \pm 20\ ^{R11}$	—	$-1.9 \pm 0.2\ ^{R11}$	—
And XXVII	$124\ ^{R11}$	$455 \pm 80\ ^{R11}$	—	$-1.7 \pm 0.2\ ^{R11}$	—

Table 2.6: Observed properties of the newest Andromeda ultra-faint dwarfs. Citations are as follows: R11 - Richardson et al. (2011).

2.1.1 Number of non-fossil satellites in the Milky Way

In this section, we use the results of published high resolution N-body simulations (Via Lactea I (Diemand et al. 2007) & II (Diemand et al. 2008), Aquarius (Springel et al. 2008) and Kravtsov et al. (2004)) to estimate the number of dark halos in the Milky Way that have, or had, a circular velocity $v_{max} > 20$ km/s. By definition, dwarf galaxies in these more massive dark halos are non-fossils and polluted fossils. If we find that the number of observed Milky Way satellites exceeds the estimated number of these massive halos in CDM we must conclude that at least a fraction of the observed Milky Way satellites are pre-reionization fossils, assuming CDM simulations reflect the real universe. GK06 have estimated that pre-reionization fossils may constitute about 1/3 of Milky Way dwarfs, based on detailed comparisons between predicted and observed Galactocentric distributions of dwarf satellites.

It is clear that if we simply count the number of dark halos within the Milky Way virial radius with $v_{max} \gtrsim 20$ km/s, their number is much smaller than the current number of observed luminous satellites. However, a significant fraction of dark halos that today have $v_{max} < 20$ km/s were once more massive, due to tidal stripping (Kravtsov et al. 2004). If the stars in these halos survive tidal stripping for as long as the dark matter, they may indeed account for a fraction or all of the newly discovered ultra-faint dwarfs. Kravtsov et al. (2004) favor the idea that tidal stripping of the dark matter halo does not affect the stellar properties of the dwarf galaxy. Thus, this model is qualitatively similar to our model for pre-reionization fossils, save a rescaling of the mass of the dark halos hosting the dwarfs.

However, once tidal stripping of dark matter halos reaches the outer most stellar radii, they lose their stars more rapidly than they lose their dark matter since the cuspy dark matter profile is more resilient to stripping than the flatter King profile of the stars. (Peñarrubia et al. 2008b). Thus, they may quickly transform from luminous to dark halos. According to this scenario, tidally stripped dark halos may not account for the observed ultra-faint population. To summarize, if the number of dark halos that have or had in the past $v_{max} \gtrsim 20$ km/s is smaller than the number of luminous Milky Way satellites, we may conclude that some dwarfs are fossils. Vice versa, if the number is larger, we cannot make any conclusive statements about the origin of Milky Way satellites.

High resolution N-body simulations of the Milky Way system give the number of dark halos in the Milky Way as a function of their circular velocity v_{max} at $z = 0$. The "Via Lactea" simulation by Diemand et al. (2007) finds:

$$N_{dm}(> v_{max}) = N_{dm,20} \left(\frac{v_{max}}{20 km/s} \right)^{-\alpha}, \tag{2.1}$$

with the number of dark matter halos with $v_{max} = 20$ km s^{-1}, $N_{dm,20} \approx 27.7$ and $\alpha \approx 3$. However, the Aquarius simulations (Springel et al. 2008) finds a factor 2.5 more satellites at any given v_{max}, *i.e.*, $N_{dm,20} \approx 69$ and $\alpha \approx 3.15$. Although the Aquarius simulations have higher resolution than the Via Lactea simulation, the large disagreement between the two works is due to a systematic difference, possibly related to the creation of the initial conditions, and it is not due to the improved resolution. The high σ_8 (0.9) used in Aquarius versus Via Lactea ($\sigma_8 = 0.74$) results in a higher normalization of the cosmological power spectrum and more power on small scales (Polisensky and Ricotti 2010). Therefore the Aquarius simulation will produce more halos with a given v_{max} than Via Lactea or this work.

To determine the importance of tidal mass loss for satellites around the Milky Way, we use results from Kravtsov et al. (2004). Figure 5 in Kravtsov et al. (2004) gives the fraction of halos, $f(v_{max})$, that presently have maximum circular velocity v_{max}, but some time in the past had a circular velocity $\leq v_{filter} = 20$ km/s, where

	Number of Dwarfs		Number of Halos with $v_{max}^{max} > v_{filter}$		
v_{filter} (km/s)	this work	Tollerud	VL I	VL II	Aquarius
20	65 ± 10	$\sim 300 - 600$	73 ± 16	100 ± 10	182 ± 40
30			20	29	59
40			7.3	12	35

Table 2.7: Table showing the number of non-fossils calculated using Equation 2.2 for three different filtering velocities. The columns are (1) filtering velocity in km s^{-1}, (2) the corrected number of dwarfs assuming an isotropic distribution of satellites, (3) the number estimated by Tollerud et al. (2008) within R_{vir}, and the number of non-fossils derived from the mass functions of (4) Via Lactea I, (5) Via Lactea II, and (6) Aquarius.

$v_{max}^{max} \equiv \max(v_{max}(t))$. We approximate the Kravtsov et al. (2004) results for $f(v_{max})$ with the power law $f(v_{max}) \approx (v_{max}/20 \text{ km s}^{-1})^{\beta}$, with $\beta \approx 3.7$. We then calculate the number of dark halos $N_{dm}(v_{max}^{max} > 20 \text{ km s}^{-1})$ analytically:

$$N_{dm}(v_{max}^{max} > 20 \text{ km s}^{-1}) = N_{dm}(v_{max}(z=0) > 20 \text{ km s}^{-1}) + \int_{v_{min}}^{20\ km/s} dv \frac{dN}{dv} f(v)$$

$$N_{dm}(v_{max}^{max} > 20 \text{ km s}^{-1}) = N_{dm,20} \left[1 + \frac{\alpha}{\beta - \alpha}(1 - x_{min}^{\beta-\alpha}) \right] \approx 2.64 N_{dm,20} \quad (2.2)$$

where $x_{min} = v_{min}/20$ km/s, and $v_{min} \gtrsim \; < \sigma_* > \approx 10$ km s^{-1} roughly equals the mean observed velocity dispersion of the stars, $< \sigma_* >$, of ultra-faint dwarf satellites. The rationale for integrating to v_{min} is that observed satellites are dark matter dominated and cannot be hosted in dark halos that have $v_{max} < \sigma_*$, unless σ_* is not a tracer for the dark matter content of the halo (*e.g.*, due to tidal heating).

Using the above equation, we find 73 ± 16 and 182 ± 40 halos with $N_{dm}(v_{max}^{max} > 20 \text{ km s}^{-1})$ within R_{vir}, for the Via Lactea I and Aquarius simulations respectively. Both these numbers are smaller than the $300 - 1000$ luminous Milky Way satellites estimated by Tollerud et al. (2008). Taken at face value, these numbers indicate that if the Via Lactea II simalations are correct, a fraction of Milky Way satellites must be true pre-reionization fossils. However, the number of luminous satellites that exist within the Milky Way's virial radius is highly uncertain beyond a distance from the Galactic center of 50 kpc.

Based on Figures 11 and 12 in Springel et al. (2008) (Aquarius) and Figure 5 in Tollerud et al. (2008) (Via Lactea II), we estimate that roughly half of the Milky Way satellites (within the virial radius R_{vir}) are < 200 kpc from the Galactic center. Therefore, within 200 kpc we estimate 36 ± 8 and 91 ± 20 dark halos with $N_{dm}(v_{max}^{max} > 20 \text{ km s}^{-1})$ for the Via Lactea and Aquarius simulations respectively. These numbers can be compared to our estimated number of luminous satellites with $d < 200$ kpc (85 ± 14 satellites) and to the estimate from the Via Lactea II simulations by Tollerud et al. (2008) (229 satellites). Using the Via Lactea I simulation, we still find that some dwarfs are true pre-reionization fossils but the argument is weak if we use the Aquarius simulation results. In Table 2.7 we summarize the counts for dark matter and luminous satellites discussed in this section.

Although there is considerable uncertainty in our estimates, it can be safely concluded that, using the results of the Via Lactea I simulation, at least a fraction of Milky Way dwarfs are fossils. However, this argument is weakened by results from the Aquarius simulations, showing a factor 2.5 increase for the number of Milky Way dark matter satellites in any mass range.

2.1.2 The strange case of Leo T

Almost all the newly discovered dwarfs are dSphs with a dominant old population of stars and virtually no gas, which makes them viable candidates for being pre-reionization fossils. However, there is one notable exception that we discuss below.

With the gas and young stars of a typical dIrr and the radius, magnitude, mass and metallicity of a dSph (Irwin et al. 2007; Simon and Geha 2007), Leo T presents a puzzle. Leo T has a stellar velocity dispersion of $\sigma_{LeoT} = 7.5 \pm 1.6$ km s^{-1} (Simon and Geha 2007), or an estimated dynamical mass of 10^7 M$_\odot$ within the stellar spheroid (although its total halo mass may be much larger). Leo T shows no sign of recent tidal disruption by either the Milky Way or M31 (de Jong et al. 2008) and is located in the outskirts of the Milky Way at a galactocentric distance of 400 kpc. Leo T's photometric properties are identical to those of pre-reionization fossils. However, if we assume that Leo T is a pre-reionization fossil, it is not expected to retain significant gas or form stars after reionization.

How did Leo T keep its H I and how did its < 9 Gyr old stellar population form? Work by Stinson et al. (2007) suggests cyclic heating and re-cooling of gas in dwarf halos can produce episodic bursts of star formation separated by periods of inactivity. The lowest simulated dwarf to form stars has $\sigma = 7.4$ km s^{-1}, similar to Leo T. However, the increasing of the IGM Jeans mass after reionization should prevent gas from condensing back onto halos with circular velocity $v_{max} < 20$ km s^{-1}. Another proposal (Ricotti 2009) is that, although the mass of Leo T at formation was $\sim 10^7 - 10^8$ M$_\odot$ ($i.e.$, a fossil), as indicated by its stellar velocity dispersion, its present dark matter mass and the halo concentration has increased after virialization by roughly a factor of $10/(1+z)$. This is expected if Leo T has evolved in isolation after virialization, as seems to be indicated by its large distance from the Milky Way. In this scenario, Leo T stopped forming stars after reionization, but it was able to start accreting gas again from the IGM very recently (at $z \lesssim 1 - 2$). This can explain the < 9 Gyr old stellar population and the similarity of Leo T to the other pre-reionization fossils.

2.2 Comparison with Theory

In this section, we compare the properties of the new dwarf galaxies discovered in the Local Group to the theoretical predictions of the pre-reionization simulations. We remind the reader of the argument that justifies this comparison.

After reionization, due to IGM reheating, the formation of galaxies smaller than 20 km s^{-1} is inhibited because the thermal pressure of the IGM becomes larger than the halo gravitational potentials (*e.g.*, Gnedin 2000). Galaxies formed before reionization stop forming stars due to the progressive photo-evaporation of their interstellar medium by the ionizing radiation background (Shapiro et al. 2004) (although most of the ISM was already lost due to UV driven galactic winds and SN explosions). Hence, if pre-reionization dwarfs do not grow above $v_{max} = 20$ km s^{-1} by mergers, their stellar population evolves passively, as calculated by stellar evolution models such as Starburst99 (Leitherer et al. 1999). We define such galaxies as pre-reionization "fossils".

Clearly, we do not expect two perfectly distinct populations of fossils with $v_{max} <$ 20 km s^{-1} and non-fossils with $v_{max} >$ 20 km s^{-1}, but a gradual transition of properties from one population to the other. Some fossils may become more massive than $v_{max} \sim$ 20 km s^{-1} after reionization, accrete gas from the IGM, and form a younger stellar population. If the dark halo circular velocity remains close to 20 km s^{-1} the young stellar population is likely to be small with respect to the old one. We call these galaxies "polluted fossils" because they have the same basic properties of "fossils" with a sub-dominant young stellar population (see RG05).

Vice versa, some non-fossil galaxies with $v_{max} >$ 20 km s^{-1} may lose a substantial fraction of their mass due to tidal interactions. If they survive the interaction, we cannot assume that their properties, such as surface brightness and half light radius, stayed the same. Kravtsov et al. (2004) estimate that 10% of Milky Way dark matter satellites were at least ten times more massive at their formation than they are today and more were $\sim 2-3$ times more massive than they are today. Although their simulation does not include stars, they favor the idea that the stellar properties of these halos would be unchanged. Conversely, a recent work of Peñarrubia et al. (2008b) looks at tidal stripping of dark matter and stars, achieving some success in reproducing the observed properties of ultra-faint dwarfs assuming that they are tidally stripped dIrrs. Using our simulations, we cannot make predictions of the internal properties of non-fossil dwarfs, which are too massive to be present in significant numbers in the small volume of our simulation. However, using the pre-reionization simulation data (in RG05), GK06 finds that about one third of Milky Way satellites may be fossils based on comparisons between observed and simulated galactocentric distribution of the satellites.

2.2.1 Statistical properties of simulated "fossils" vs observations

Here we compare the RG05 predictions from the Ricotti et al. (2002a,b) pre-reionization simulations for the fossils of primordial galaxies at reionization to the observed properties (see Tables 2.1 to 2.6) of the new ultra-faint Milky Way and M31 dwarfs. The symbols and lines in Figs. 2.1-2.7 have the following meanings. All known Milky Way dSphs are shown by circles; Andromeda's dSphs satellites are shown by triangles; simulated fossils are shown by the small solid squares. The solid and open symbols refer to previously known and new dSphs, respectively. The transition between fossils and non-fossil galaxies is gradual. In order to illustrate the different statistical trends of "non-fossil" galaxies we show dwarf irregulars (dIrrs) with asterisks and the dwarf ellipticals (dE) as crosses, and we show the statistical trends

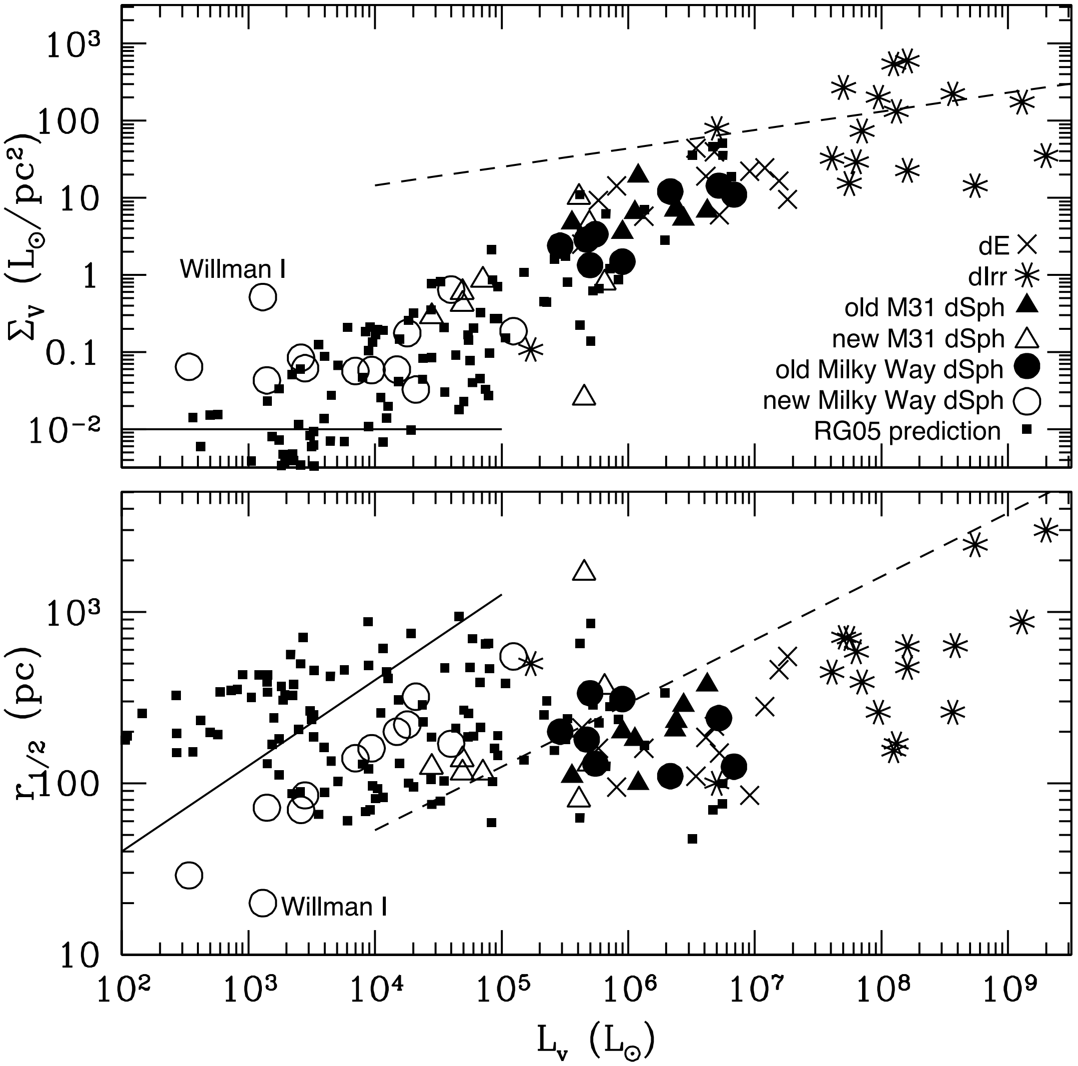

Figure 2.1: An extension of Figure 7 from RG05 to include new dwarfs in the SDSS (Belokurov et al. 2007, 2006; Geha et al. 2009; Irwin et al. 2007; Walsh et al. 2007; Willman et al. 2005a,b; Zucker et al. 2006a,b) and recent surveys of Andromeda (Ibata et al. 2007; Majewski et al. 2007; Martin et al. 2006). Surface brightness and half-light radius are plotted vs. V-band luminosities. Small filled squares are the RG05 predictions, asterisks are known survivors, crosses are known polluted fossils, closed circles are the previously known dSph around the Milky Way, closed triangles are previously known dSph around M31, and open circles and triangles are new dSph around the Milky Way and M31 respectively. The solid lines show the SLOAN surface brightness limits and the dashed lines show the scaling relationships for more luminous Sc-Im galaxies ($10^8 L_\odot \lesssim L_B \lesssim 10^{11} L_\odot$) derived by Kormendy and Freeman (2004).

for more luminous galaxies as thick dashed lines on the right side of each panel.

Figure 2.1 shows how the surface brightness (top panel) and half light radius (bottom panel) of all known Milky Way and Andromeda satellites as a function of V-band luminosity compares to the simulated fossils. The surface brightness limit of the SDSS is shown by the thin solid lines in both panels of the figure. The new dwarfs agree with the predictions up to this threshold, suggesting the possible existence of an undetected population of dwarfs with Σ_V below the SDSS sensitivity limit. The new M31 satellites have properties similar to their previously known Milky Way counterparts (*e.g.*, Ursa Minor and Draco). Given the similar host masses and environments, it is reasonable to assume a similar formation history for the halos of M31 and the Milky Way. This suggests the existence of an undiscovered population of dwarfs orbiting M31 equivalent to the new SDSS dwarfs.

Extreme Mass-to-Light ratios

The large mass outflows due to photo-heating by massive stars and the consequent suppression of star formation after an initial burst, make reionization fossils among the most dark matter dominated objects in the universe, with predicted M/L ratios as high as 10^4 and $L_V \sim 10^3 - 10^4$ $L_\odot$ (Bovill and Ricotti 2009; Ricotti and Gnedin 2005).

Figure 2.2 shows the velocity dispersion (bottom panel) and mass-to-light ratios, M/L_V (top panel), as a function of V-band luminosity of the new and old dwarfs from observations in comparison to simulated fossils. The symbols are the same as in the previous figures. While derived mass data is available for all the previously known dwarfs, we found no published σ values for 9 dIrr, 4 dE and 3 dSph (Antila, Phoenix and SagDIG) (Mateo 1998; Strigari et al. 2008). We observe a good agreement between the statistical properties of the new dwarf galaxies and

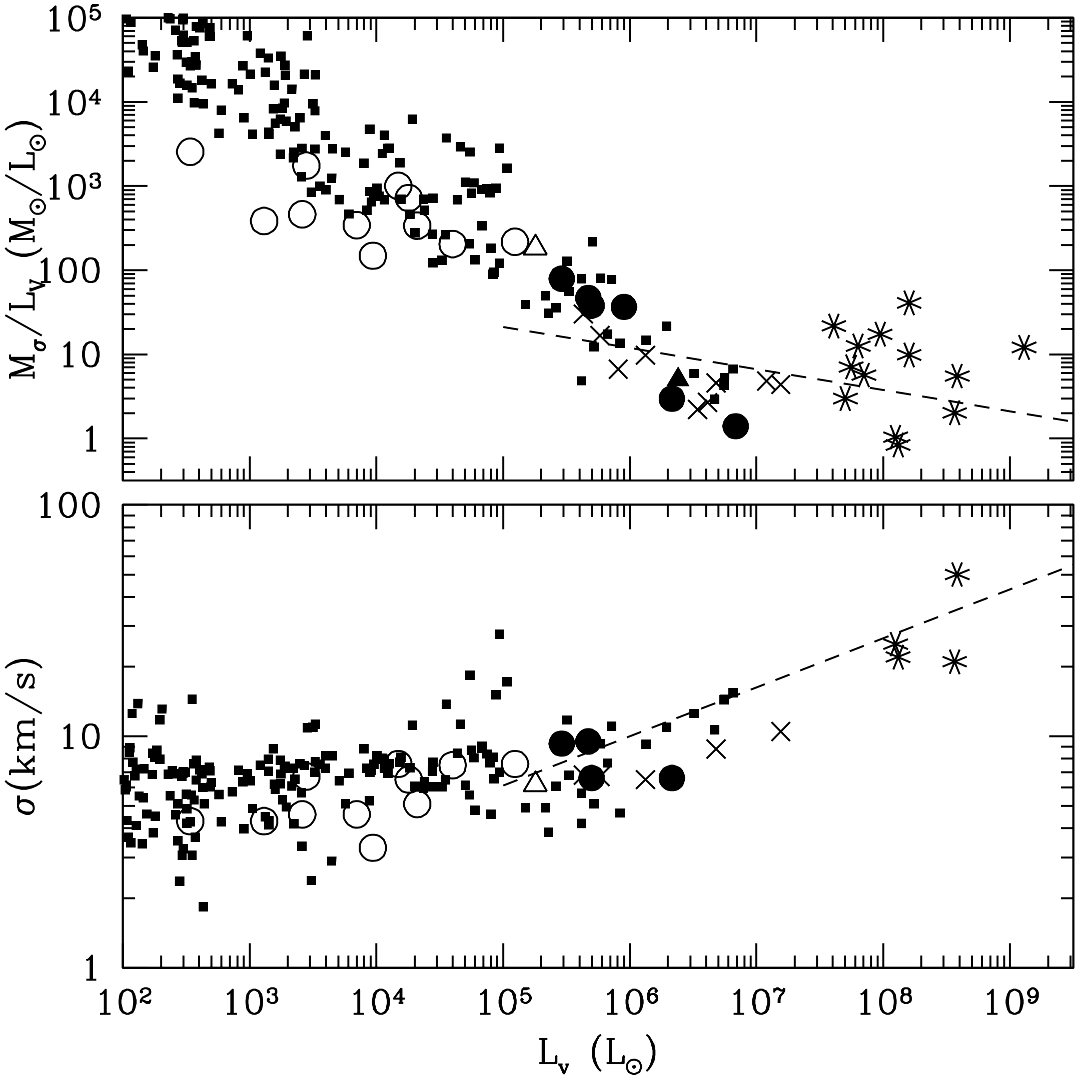

Figure 2.2: Mass-to-light ratio and velocity dispersion of a subset of the new dwarfs (Martin et al. 2007; Simon and Geha 2007) plotted with values for previously known dwarfs and RG05 predictions. The dashed lines show the scaling relationships for more luminous Sc-Im galaxies ($10^8 L_\odot \lesssim L_B \lesssim 10^{11} L_\odot$) derived by Kormendy and Freeman (2004).

the RG05 predictions for the fossils, although simulated dwarfs show slightly larger mass-to-light ratios than observed ones at the low luminosity end, $L_V < 10^4$ L$_\odot$. Theoretical and observed derived masses are calculated the same way, from the velocity dispersions of stars (*i.e.*, $M = 2r_{hl}\sigma^2/G$) (Illingworth 1976), and do not necessarily reflect the total mass of the dark halo at virialization. Indeed, the simulation provides some insight on why the derived value of the dynamical mass, $M \sim (1 \pm 5) \times 10^7$ M$_\odot$, remains relative constant as a function of L_V. Simulations show that in pre-reionization dwarfs, the ratio of the radius of the stellar spheroid to the virial radius of the dark halo decreases with increasing dark halo mass. The lowest mass dwarfs have stellar spheroids comparable in size to their virial radii (see Ricotti et al. (2008)). As the halo mass and virial radius increases, the stellar spheroid becomes increasingly concentrated in the deepest part of the potential well, thus the ratio of the dynamical mass within the largest stellar orbits to total dark matter mass is reduced. This is because cooling is less efficient in the lower mass halos, preventing the gas from cooling rapidly and falling to the center of the halo before it fragments and forms stars. This effect keeps the value of the dynamical mass within the stellar spheroid (measured by the velocity dispersion of the stars) remarkably constant even though the total mass of the halo increases.

If dwarfs are undergoing tidal disruption (*e.g.*, Ursa Major II), the velocity dispersions could be artificially inflated right before destruction (Walker et al. 2009). However, the agreement with theory is rather good for all the new ultra-faint dwarfs. The data on the lowest luminosity dwarfs in our simulations are the least reliable, because they are very close to the resolution limits of the pre-reionization simulation (we resolve halos of about 10^5 M$_\odot$ with 100 particles). Let us assume we can trust the simulation and the observational data, even for the lowest luminosity dwarfs and the discrepancy between simulation and observation at the low luminosity end is real. The dynamical mass is $M \propto r_{hl}\sigma^2$. There is good agreement between observations and simulations for σ in faint dwarfs. Thus, it is likely that the the reason for disagreement in M/L_V is due to the value of r_{hl}, being smaller for the observed dwarfs than the simulated ones. This could be partly due to an observational bias that selects preferentially dSphs with higher surface brightness and smaller r_{hl} (see Figure 2.1). Another explanation is a dynamical effect, not included in our simulations that reduces the stellar radius of dwarfs after virialization; for instance, tidal stripping. A larger sample size of distant dwarfs, including kinematics of And XII and And XIV, both believed to be on their first approach to M31, would be useful to better characterize this discrepancy.

The velocity dispersions of the stars for the observed new dwarfs and the simulated pre-reionization fossils are just below 10 km s^{-1} for luminosities $< 10^6$ L_V. The scatter of the predicted velocity dispersions as a function of dwarf luminosity and the agreement between our simulations and the observed distribution suggests that observed dwarfs with the same luminosity may be hosted in dark matter halos with a broad distribution of masses. These results are in agreement with Figure 2.5, showing that the faintest simulated primordial galaxies of a given luminosity may form in halos with a total mass at virialization between $10^6 - 10^7$ $M_\odot$ to a few times 10^8 $M_\odot$. This is because at these small masses the star formation efficiency is not necessarily proportional to the dark halo mass and there is a large scatter in f_* at any given mass. This is due to the nature of feedback effects that are local and depend on the environment (*e.g.*, positive feedback on the formation of H_2). Ricotti et al. (2008) finds that pre-reionization dwarfs that form in relative isolation have a typically smaller value of f_* than dwarfs of the same total mass that form in the vicinity of other luminous dwarfs (see Fig. 4 in Ricotti et al. (2008)).

Understanding the luminosity-metallicity relation

The metallicity-luminosity relation of the observed and simulated dwarfs is shown in Figure 2.4. [Fe/H] is plotted against V-band luminosity in solar units. Symbols for the previously known dwarfs, the new, ultra-faint dwarfs, and simulated fossils are the same as in Figure 2.1. In this plot, we also color code simulated fossils according to their star formation efficiency, f_*, defined as $f_* = M_*/M_{bar}$, where M_* is the mass in stars and $M_{bar} \approx M_{dm}/6$ is the baryonic mass of the halo assuming cosmic baryon abundance. Red symbols show simulated dwarfs with $f_* < 0.003$, blue $0.003 \leq f_* \leq 0.03$ and green $f_* > 0.03$.

The new ultra-faint dwarfs do not follow a tight luminosity-metallicity relationship observed in more luminous galaxies (but see Geha et al. (2009)). This behavior is in good agreement with the predictions of our simulation. The contentious "dwarf galaxy" Segue 1 with luminosity of $340L_\odot$ and metallicity of [Fe/H]~ -2.8 fills a gap in the luminosity-metallicity plot that was previously devoid of observed dwarfs, present instead in the simulation (Geha et al. 2009). However, Segue 1, Segue 2, Willman 1, and, to a lesser extent, Pisces II and Leo V, have half light radii smaller than what our simulation predicts. In Figure 4.6 they are the filled green circles which have $[Fe/H]$ abundances too high for their luminosities. In general, when compared to their previously known counterparts, the new ultra-faint dwarfs have a slightly lower metallicity but much lower luminosities.

There are several physical mechanisms that may produce the observed scatter in metallicities of dwarfs at a given constant luminosity. Here, we identify the two mechanism that are dominant in our simulation for primordial dwarf galaxies: 1) the large spread of star formation efficiencies producing a dwarf of a given luminosity is the dominant mechanism (to zero-th order approximation, in a closed box model, we have $Z \propto f_*$) and 2) the existence of dwarfs experiencing either a single or multiple episodes of star formation contribute to the metallicity spread as well. Metal pollution from nearby galaxies at formation might also play a role. For more massive dwarfs that form after reionization, there may be different processes that dominate metal enrichment. See Tassis et al. (2008) for a discussion.

Let's start with the first mechanism. Contrary to what is usually the case for more massive galaxies, the Ricotti et al pre-reionization simulations find that in primordial dwarfs with masses $\lesssim 5 \times 10^7$ M$_\odot$ the star formation efficiency f_* does not monotonically increase with halo mass (*i.e.*, f_* has a large spread for a given halo mass or for a given mass in stars, M_*, see Figure 4 and Figure 7 in Ricotti et al. (2008)). The wide range in values results from the sensitivity of f_* on a halo's environment and is due to local feedback effects that are of fundamental importance in determining star formation in the shallow potential wells typical of pre-reionization dwarfs. Figure 2.5 (Figure 7 in Ricotti et al. (2008)) shows that below a few 10^7 M$_\odot$, halos with the same dark mass can be dark or luminous (depending on the environment). Thus, feedback from non-ionizing and ionizing UV radiation, mechanical feedback and chemical enrichment can produce two halos with the same dark mass and very different star formation efficiencies. This appears to be the main effect responsible for the observed spread in metallicity for a given luminosity, in the new dwarfs. In Figure 2.6, we plot the metallicity as a function of the mean star formation efficiency for the halo, f_*. As expected, simulated dwarfs with higher values of the star metallicity are the ones with the larger value of f_*.

However, this effect alone cannot account for all the observed scatter of the metallicity as illustrated by the color coding of simulated dwarfs in Figure 2.4. It appears that the metallicity is not simply proportional to f_* (otherwise the boundaries between symbols of different colors would be horizontal). Instead, for a given value of f_*, the metallicity is larger for fainter dwarfs. It is not too surprising that

Z is not simply proportional to f_*. Even when using a very simple chemical evolution model, neglecting gas inflows and assuming instantaneous metal recycling, the mean metallicity of the stars is proportional to M_*/M_{gas} rather than $f_* = M_*/M_{bar}$, where M_{gas} is the initial value of the gas mass available for star formation. Thus, $Z \propto f_*(M_{bar}/M_{gas})$. If feedback effects reduce the value of M_{gas}/M_{bar} below unity in the smallest and lowest luminosity primordial dwarfs, the metallicity of the stars will be larger for a fixed value of f_*, as observed in Figure 2.6 and Figure 2.4. The reduction of M_{gas}/M_{bar} below unity can be produced by three effects: the increase of the Jeans mass of the IGM over the virial mass of the halo due to reheating (see Figure 6 in RGS08), heating of the gas via ionizing radiation from stars within the halo, and by multiple episodes of star formation with a first burst that lowers M_{gas} substantially, but does not produce sufficiently large values of f_* and Z when compared to subsequent bursts.

Figure 2.7 shows [Fe/H] versus the surface brightness in the V-band, Σ_V. The symbols are the same as in Fig. 2.1 and the solid line shows the SDSS sensitivity limit. No trend is observed between metallicity and Σ_V for the simulated dwarfs. Observed dwarfs show less scatter for Σ_V-metallicity relation than for the luminosity-metallicity relation in Figure 2.4. There is one dwarf with metallicity below [Fe/H]$= -2.5$: Segue 1 that has [Fe/H]$= -2.8$. Since the spectral synthesis method used in Kirby et al. (2008) and Geha et al. (2009) may not be subject to the overestimation of metallicities seen with measurements using the CA triplet, the lack of dwarfs with [Fe/H]< -3.0 could be a sign of a change in the IMF at very low [Fe/H].

Finally, in Figure 2.3 we have examined whether there is a dependence of the metallicities on the distance of the galaxy from the Milky Way or Andromeda. For the new Milky Way dwarfs there is a slight trend of higher metallicities at smaller galactocentric distances; however, the upward trend is dominated by Ursa Major II

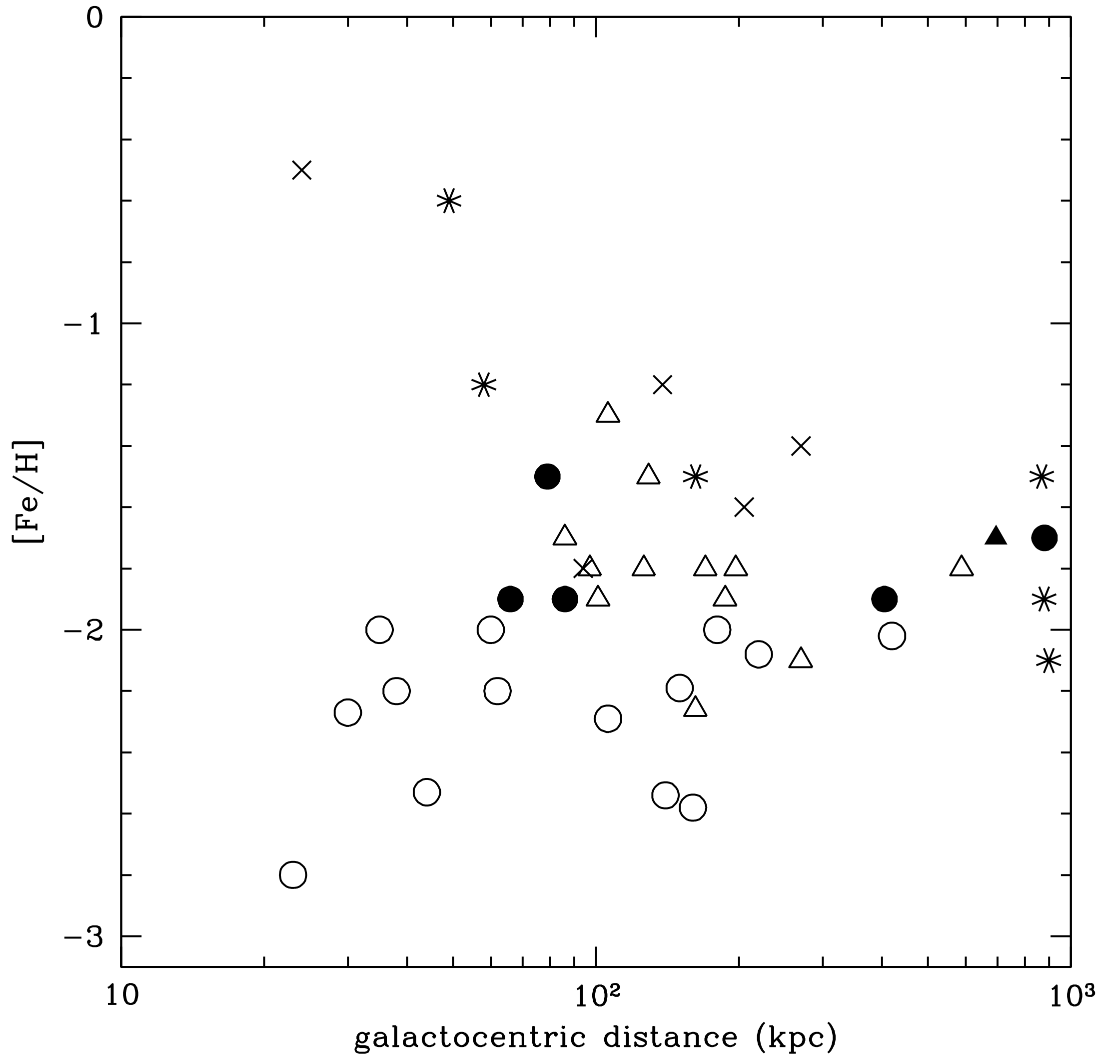

Figure 2.3: The galactocentric distance vs. metallicity for the ultra-faint dwarfs as of March 2011. The black symbols have the same meaning as in Figure 2.1.

and Coma Ber., both of of which show evidence for tidal disruption. For the M31 dwarfs, no trend was observed.

Figures 2.8 show the scatter of the metallicity of the stars, $\sigma_{[Fe/H]}$, plotted against V-band luminosity and [Fe/H] respectively. Once more, the various point types and colors are the same used in Figure 2.4. The observational data for the new dwarfs matches the predictions, though Figure 2.8 shows a lack of low L_V objects with

$\sigma_{[Fe/H]} < 0.4$. However, given the small number of data points available, it is not possible to rule out selection effects of small number statistics as an explanation. Dwarfs with low values of $\sigma_{[Fe/H]}$ tend to have higher luminosities and are equally likely to be a dE or dSphs. However, dwarfs with the highest $\sigma_{[Fe/H]}$ are faint dSphs with $L_V < 10^6$ $\mathrm{L}_\odot$, and occupy the lowest mass dark matter halos. It is not clear at this point how reliable the simulation data for $\sigma_{[Fe/H]}$ is for dwarfs with luminosities $L_V < 10^3 - 10^4$ $\mathrm{L}_\odot$. However, all the dwarfs we analyze have at least 10 stellar particles and 100 dark matter particles. The masses of stellar particles vary, depending on the star formation efficiency and the duration of the star burst.

As with the metallicities, we looked at how the metallicity spread depends on the distance from the host. For both previously known and ultra-faint dSphs there is no dependence on distance within the virial radius of the Milky Way. There is a lack of dwarfs with high $\sigma_{[Fe/H]}$ beyond 400 kpc; however, given the small number of data points and the luminosity and surface brightness limits of current surveys, the trend is not statistically significant.

2.2.2 The Missing Galactic Satellite Problem, Revisited

In order to simulate a representative sample of the universe, the size of cosmological simulations must be significantly larger than the largest scale that becomes non-linear at the redshift of interest. At $z = 0$, this scale is at least 50 to 100 Mpc. Current computational resources are not able to evolve a cosmological simulation of this size, including all relevant gas and radiation physics, to $z = 0$. However, as argued in § 2.2, the properties of those fossil galaxies that survive tidal destruction change only through passive aging of their stars formed before reionization (but see Ricotti (2009)), allowing their properties at $z = 0$ to be simply related to their properties at reionization. GK06 uses this approximation in conjunction with high-

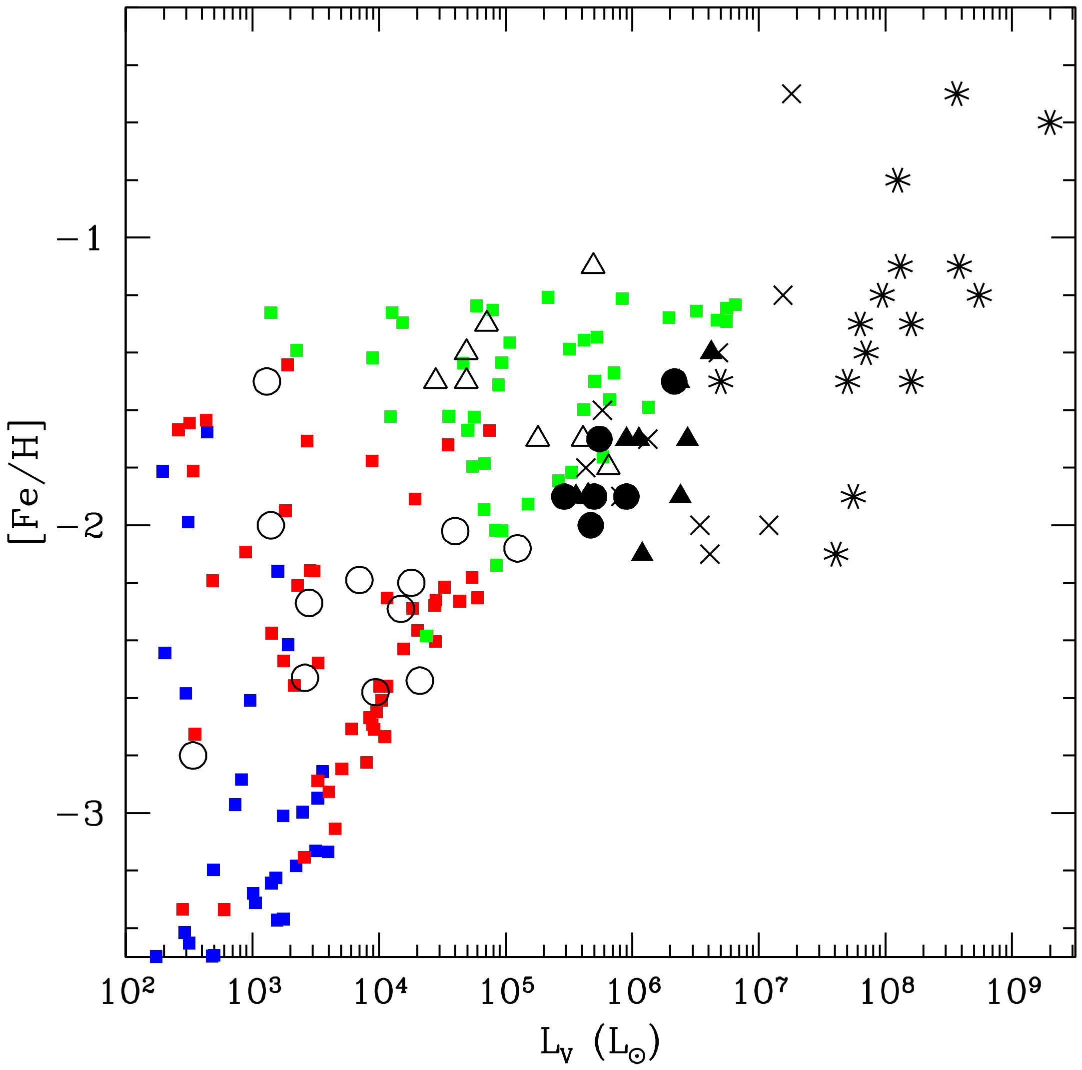

Figure 2.4: Metallicity vs. luminosity for the new and old dwarfs plotted with the RG05 predictions.

resolution N-body simulations of the Local Group, to evolve a population of dwarf galaxies around a Milky Way mass halo from $z = 70$ to $z = 0$. For details of the simulations, see § 2 in GK06.

GK06 defines a fossil as a simulated halo which survives to $z = 0$ and remains below the critical circular velocity of 20 km s^{-1} with no appreciable tidal stripping. They calculate the probability, $P_S(v_{max}, r)$, of a luminous halo with a given

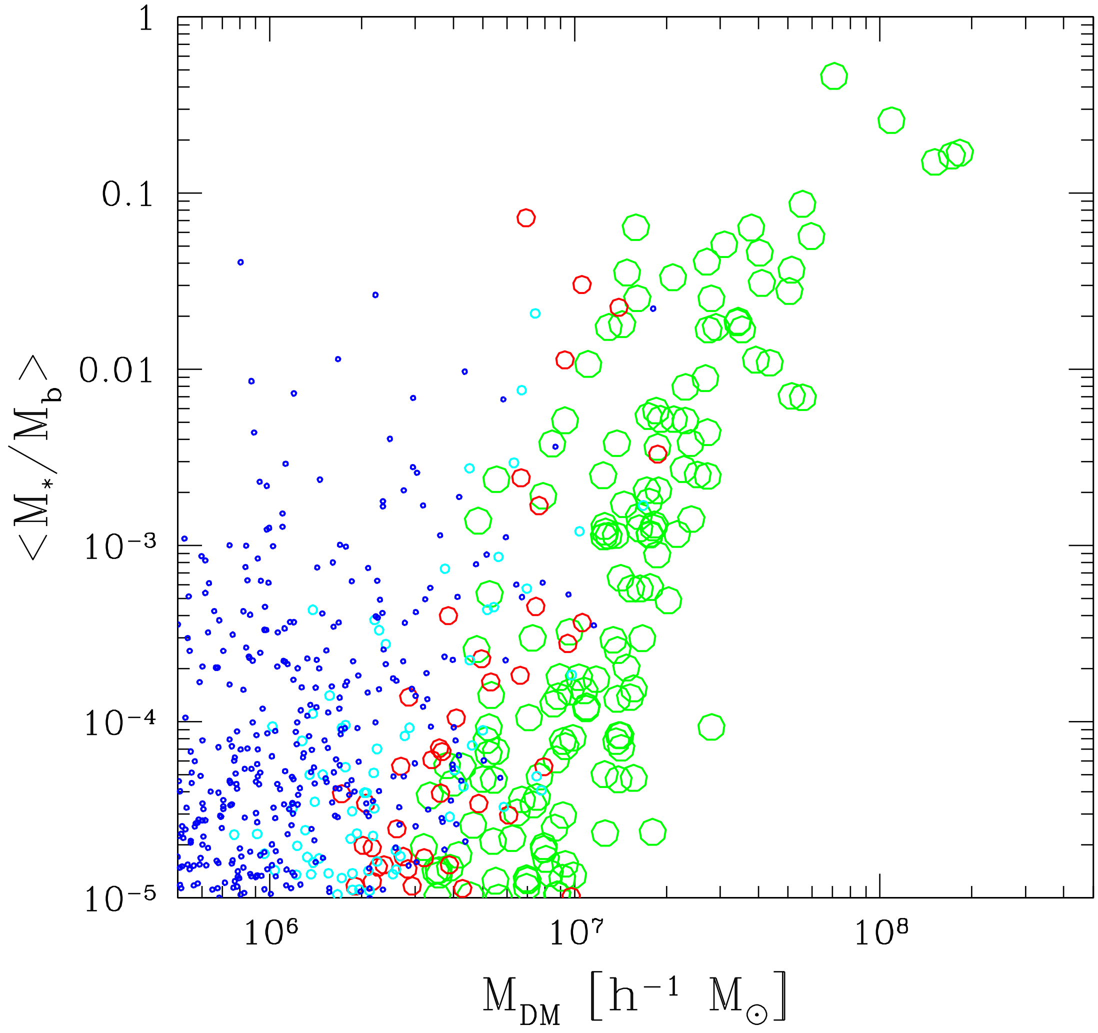

Figure 2.5: Figure 7 from Ricotti et al. (2008) showing the fraction of baryons converted into stars as function of halo mass of the galaxy at $z = 10$. Circles, from smaller to the larger, refer to galaxies with gas fractions $f_g = M_{gas}/M_b < 0.1\%$ (blue), $0.1\% < f_g < 1\%$ (cyan), $1\% < f_g < 10\%$ (red) and $f_g > 10\%$ (green), respectively.

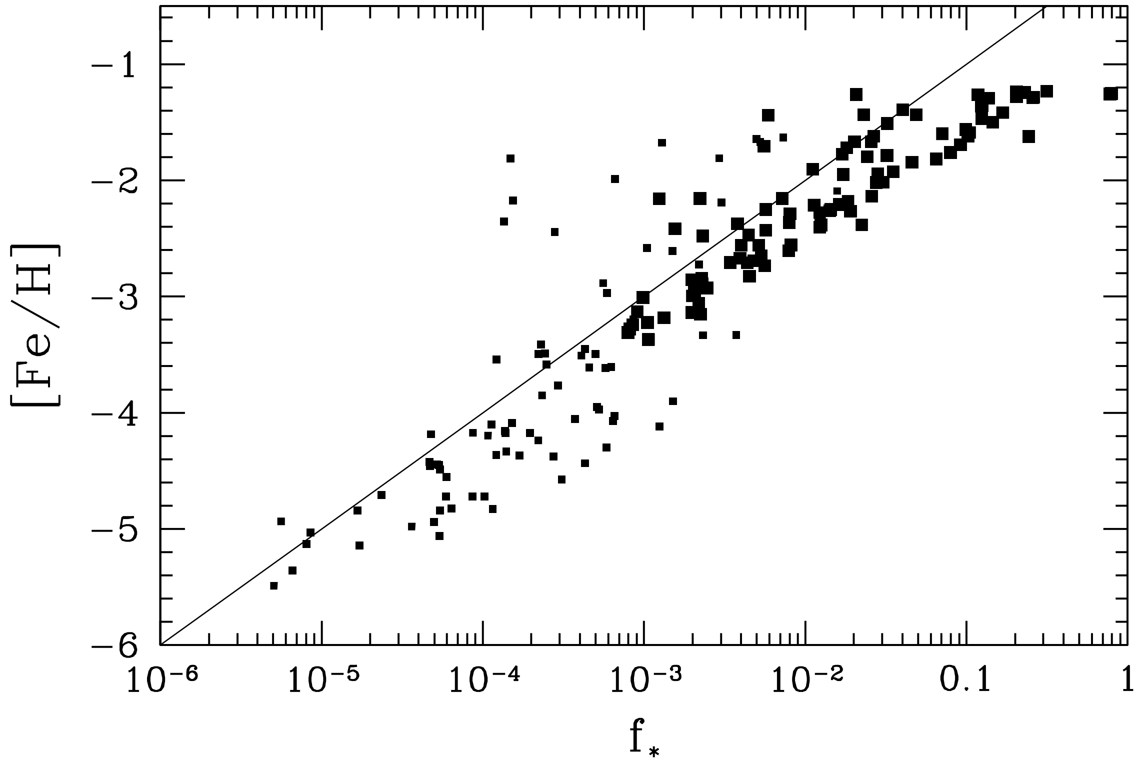

Figure 2.6: Metallicity versus star formation efficiency $f_* = M_*/M_b$ for the simulated fossils from Ricotti et al. (2008). The large squares show galaxies with $L_V \geq 10^3$ L$_\odot$, and the small squares galaxies with $L_V < 10^3$ L$_\odot$.

maximum circular velocity v_{max} to survive from $z = 8$ (the final redshift of the RG05 simulation) to $z = 0$. For a given v_{max}, the number of dwarfs at $z = 0$ is $N(v_{max}, z = 8)P_S(v_{max}, r)$. The surviving halos are assigned a luminosity based on the L_V versus v_{max} relationship from RG05. At $z = 0$, GK06 has a population of dwarf galaxies with a resolution limit of $v_{max} = 13$ km s^{-1}. Unfortunately, this limit corresponds to a lower luminosity limit of $L_V \sim 10^5$ L$_\odot$, which includes Leo T and

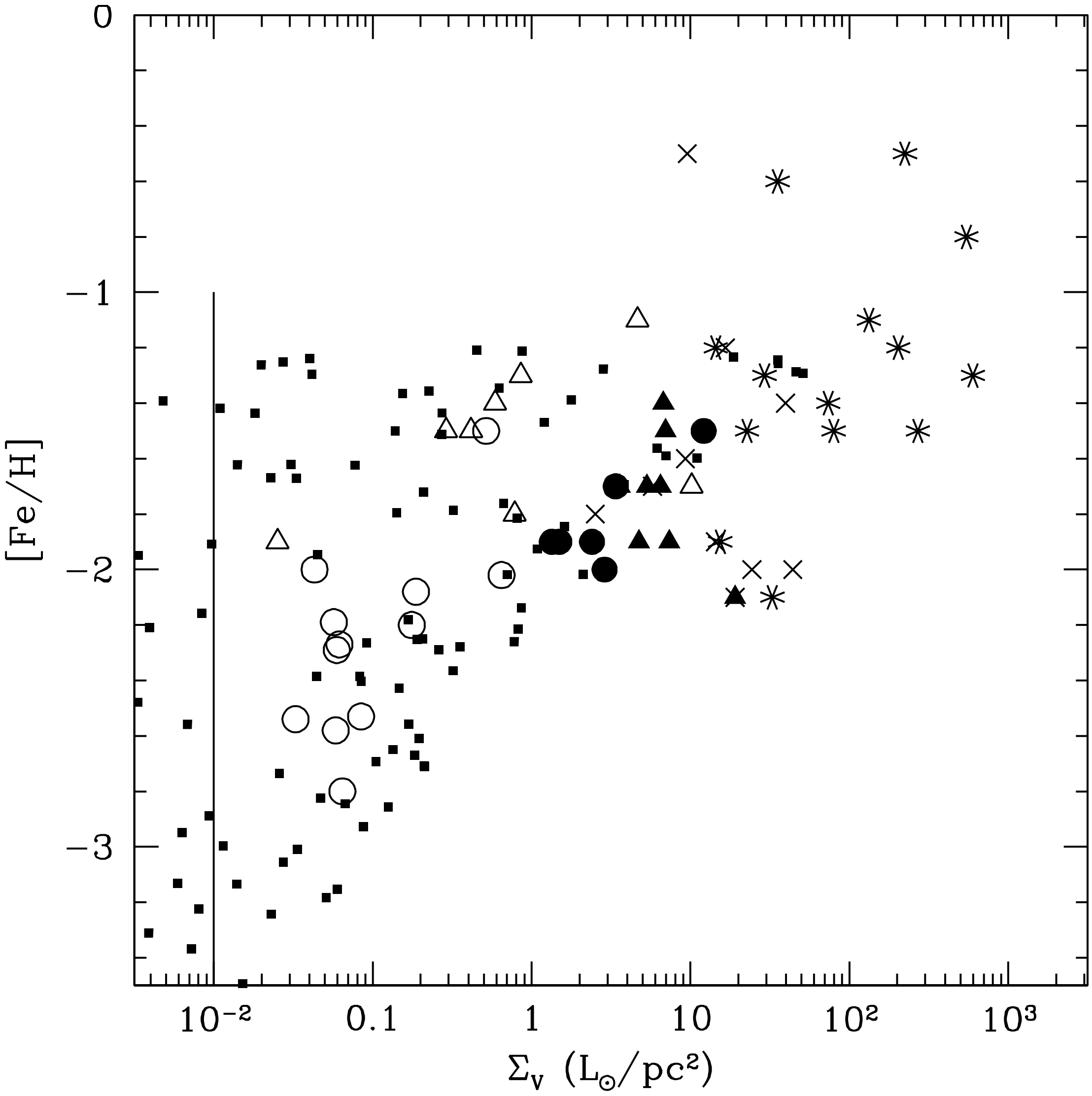

Figure 2.7: Metallicity vs. surface brightness for the new and old dwarfs. The surface brightness limit of the SDSS is shown by a solid vertical line. Note the predicted dwarfs with Z<-2.5 and surface brightnesses above Sloan detection limits.

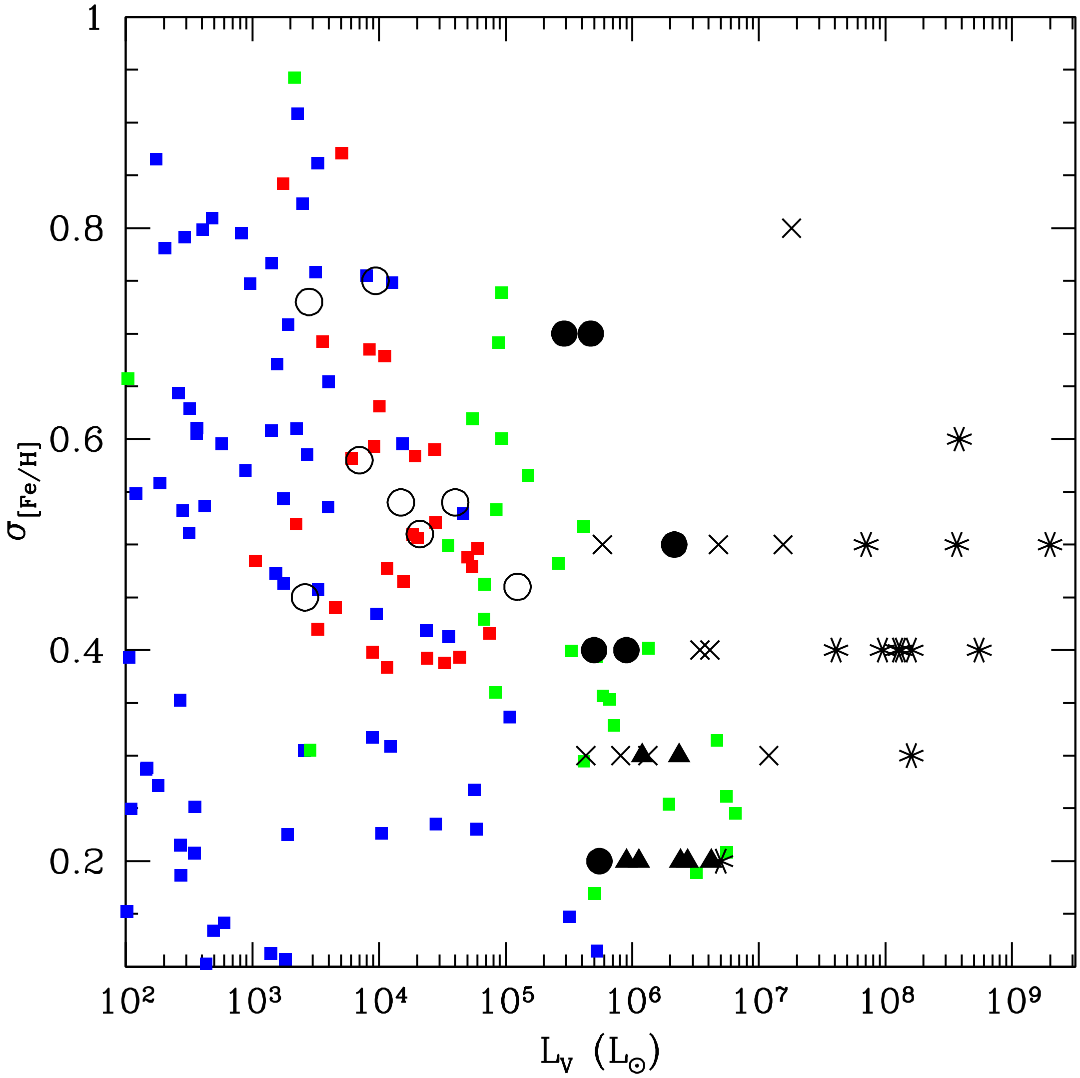

Figure 2.8: Metallicity spread vs. V-band luminosity for the new and old dwarfs. Simulation data for the metallicity spread may be unreliable for dwarfs with luminosities $L_V < 10^3 - 10^4$ $L_\odot$, due to the small number of stellar particles in the galaxies.

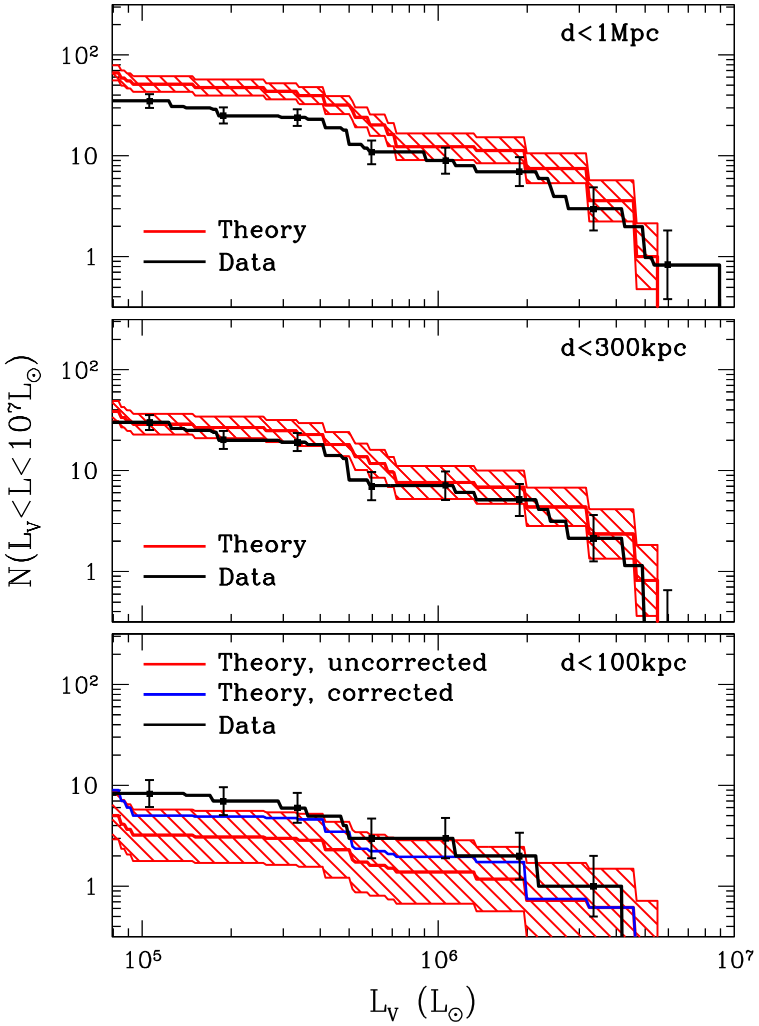

Figure 2.9: Luminosity function of pre-reionization fossil dwarfs predicted in GK06 (red) plotted with the luminosity function for the new and old Local Group dSphs. The black lines are the observations corrected for completeness as discussed in Section 2. Corrections to the theory account for an under-abundance of small halos near the hosts due to numerical effects (GK06).

Canes Venatici I, but excludes all the other new ultra-faint Milky Way satellites. We do not show the prediction of the GK06 model below this lower luminosity limit. A new N-body method with a resolution limit of $L_V \sim 10^3$ L$_\odot$ that follows the merger histories for the halos will be presented in Chapter 3 of this work.

In Figure 2.9, we show the cumulative luminosity function from GK06 for the Milky Way and M31 satellites with the addition of the new ultra-faint dSphs. The lower panel shows satellites with distance from their host $d < 100$ kpc, the middle panel $d < 300$ kpc and the upper panel $d < 1$ Mpc. The gray lines show the GK06 predictions, and the shaded region encompasses the error bars. Since, the resolution limits of GK06 causes halos with $v_{max} < 17$ km s^{-1} to be preferentially destroyed by tidal effects, the predicted luminosity function is corrected. Both the uncorrected (lower) and corrected (upper) luminosity functions are plotted in the lower panel. On all three panels, the black histogram and the points with error bars represent the observed luminosity function of fossil dwarfs around the Milky Way and M31. Their numbers have been corrected for completeness as discussed in § 2. For the purposes of this plot, we are considering all the new dwarfs to be fossil candidates.

For $d < 100$ kpc (bottom panel), there is an overabundance of observed satellites with respect to the simulated luminosity function from 10^5 to 10^6 L$_\odot$. This discrepancy is likely due to excessive destruction rate of satellites caused by the insufficient resolution of the GK06 N-body simulations. At distances $d < 300$ kpc (middle panel), there is excellent agreement between theory and observation. Canes Venatici I and the new Andromeda satellites are included in the latter panel. The upper panel shows the luminosity function for all dwarfs within 1 Mpc of the host, including Leo T. Note, that GK06 assumes an isolated Milky Way type galaxy (with total mass comparable to the Local Group mass), while observations with $d < 1$ Mpc of the Milky Way include the satellite system around M31. For $d < 1$ Mpc, there is an under-abundance of observed satellites between 10^5 to 10^6 $L_\odot$ with respect to the simulation predictions. However, this is consistent with the theory since beyond 250 kpc dwarfs with $L_V \sim 10^5 L_\odot$ drop below SDSS detection limits (Koposov et al. 2008). Hence, the under-abundance of observed dwarfs at large distances may be due to the completeness limit of the survey.

2.3 Discussion

There are two main ideas for the origin of dSphs in the Local Group. Most importantly, these two ideas have very different implications for models of galaxy formation, and the minimum mass a dark halo needs to host a luminous galaxy. The "tidal scenario" holds the dwarfs we see today were once far more massive, having been stripped of most of their dark matter during interactions with larger galaxies (*e.g.*, Kravtsov et al. 2004). In this model, we would expect the halos with original dark matter masses below 10^8 $M_\odot$ to be mostly dark at formation and at the modern epoch. The "primordial scenario," has dwarf galaxies starting with close to their current stellar mass of about $10^3 - 10^6$ $M_\odot$ and, with several dark halos with mass at formation below the threshold of about 2×10^8 $M_\odot$ hosting a luminous galaxy. Star formation in halos this small is possible only before reionization and is widespread if "positive" feedback plays a significant role in regulating star formation in the first galaxies (Ricotti et al. 2001, 2002a,b).

In this chapter, we argue that the recent discovery of the ultra-faint dwarfs in the Milky Way and M31 supports the "primordial scenario". The existence of the ultra-faint dwarfs was predicted by simulations of the formation of the first galaxies (see RG05) and, as shown in the present work, the observed properties of this new population are consistent with them being the "fossils" of the first galaxies.

While tidal stripping can reproduce properties of an individual galaxy, it is unable to completely reproduce all the trends in the ultra-faint population. This is primarily seen in the kinematics of the ultra-faint dwarfs. Tidal stripping predicts a steeper drop in σ with L_V than is observed for the ultra-faint dwarfs (Peñarrubia et al. 2008b; Wadepuhl and Springel 2010), while our simulations show primordial dwarfs which match the observed trends in σ extremely well. It has not been shown yet that star formation in dwarf galaxies more massive than $10^8 - 10^9$ $\mathrm{M}_\odot$ can reproduce the observed properties of ultra-faint dwarfs without requiring tidal stripping of stars.

The tidal model predicts that gas rich dIrr lose their gas and transform into dSphs due to tidal or ram pressure interaction with a host halo. And XII, which shows a proper motion close to current published escape velocity of M31, may be on its first approach to the Local Group (Chapman et al. 2007; Martin et al. 2006). A similar situation exists for And XIV. With a dynamical mass of $M \sim 3 \times 10^7 M_\odot$, And XIV has $v_{dwarf} > v_{esc,M31}$, suggesting it is also just entering the Local Group (Chapman et al. 2007). In the tidal model (Mayer et al. 2007, 2006), And XII and And XIV would be expected to still harbor significant reservoirs of gas, however, observations show And XIV has $M_{HI} < 3 \times 10^3 M_\odot$ (Chapman et al. 2007) and And XII has no detected H I (Martin et al. 2006). If neither of these dwarfs have undergone significant tidal interactions with their hosts, as their velocities suggest, how did they lose their gas? Though its velocity is unknown, the recently discovered And XVIII (McConnachie et al. 2008), shows the same characteristics. At a distance of 600 kpc from M31 and 1.35 Mpc from the Milky Way, it is unlikely that And XVIII has undergone significant interaction with either Local Group spirals. And XVIII is classified as a dSph with no detected H I and is similar to the Cetus and Tucana dwarfs (McConnachie et al. 2008), both of which are good candidate fossil galaxies (Ricotti and Gnedin 2005).

On the opposite end of the spectrum is the strange case of Leo T, the properties of which are discussed in Section 2.1.1. While, Leo T has an H I mass fraction typical of dIrr, its other properties are indistinguishable from the other newly discovered ultra-faint dwarfs (Simon and Geha 2007), all of which are dSph and potential fossils. Leo T's large distance from its host, H I reservoir and low probability of recent tidal interactions (de Jong et al. 2008) make it a good candidate for a precursor to a dSph in the tidal scenario. Particularly given that Leo T's dynamical mass within the stellar spheroid is small: 8.2×10^6 $M_\odot$ (Simon and Geha 2007), its gas is unlikely to survive a single tidal encounter intact. Therefore, Leo T may have formed at or near its current mass, and the striking similarity of Leo T to its ultra-faint counterparts suggests that they too could have formed as primordial dwarfs at their current masses.

By our definition, pre-reionization fossils are dwarfs that form before reionization in dark halos with $v_{max} < v_{filter} \sim 20$ km s^{-1}, while non-fossils dwarfs form in halos with $v_{max} > v_{filter}$ before and after reionization. The value $v_{filter} \sim 20$ km s^{-1} that we use to define a fossil is primarily motivated by fundamental differences in cooling and feedback processes that regulate star formation in these halos in the early universe. This value of the circular velocity is also very close to estimates based on the suppression of star formation in dwarfs after reionization (Gnedin 2000; Okamoto et al. 2008). However, as argued in (Ricotti 2009), fossil dwarfs can have a late phase of gas accretion and star formation well after reionization, at redshift $z < 1-2$. Thus, a complete suppression of star formation after reionization is not necessarily what defines a "fossil galaxy".

The number of Milky Way dark satellites that have or have had $v_{max} > v_{filter}$ can be estimated using the results of published N-body simulations (see § 2.1.1). We find that using the Via Lactea I N-body simulation there are approximately

$N_{dark} \approx 73 \pm 16$ halos with $v_{max} > 20$ km s^{-1} within the virial radius (Diemand et al. 2007). The Aquarius simulations (Springel et al. 2008), however, show a factor of 2.5 increase in the number of halos with $v_{max} > 20$ km s^{-1}, *i.e.*, $N_{dark} \sim 182 \pm 40$ dark halos. Within a distance of 200 kpc we estimate $N_{dark} \approx 36 \pm 8$ for the Via Lactea and $N_{dark} \approx 91 \pm 20$ for the Aquarius simulation.

If the number of observed dwarf satellites within the Milky Way (after applying completeness corrections) is larger than N_{dark} we must conclude that some satellites are fossils. Twelve new ultra-faint dwarfs have been discovered around the Milky Way by analyzing SDSS data in a region that covers about 1/5 of the sky. Applying a simple correction for the sky coverage we estimate that there should be about at least 85 ± 14 Milky Way satellites. However, the data becomes incomplete for ultra-faint dwarf that are further than about 200 kpc from the Galactic center. Comparing this number of luminous satellites to N_{dark} within 200 kpc we cannot conclusively conclude that some ultra-faint dwarfs are fossils because N_{dark} for the Aquarius simulation is comparable to the estimated number of luminous satellites.

Once both sensitivity and survey area corrections are applied, Tollerud et al. (2008) estimates the existence of 300 to 600 luminous satellites within the virial radius ($R_{vir} \sim 400$ kpc) of the Milky Way and 229^{330}_{176} within 200 kpc. Comparing N_{dark} to the Tollerud et al. (2008) estimates of the number of luminous Milky Way satellites implies that a significant fraction of them are fossils (regardless if we use the Via Lactea I, II or the Aquarius simulations estimates for N_{dark}). In Table 2.7 we have summarized the aforementioned results.

Another argument for the existence of fossils is provided by detailed comparison of the galactocentric distribution of fossils in the Milky Way (GK06). Based on these comparisons GK06 finds that about 1/3 of Milky Way dwarfs may be fossils. In this paper, we show the GK06 theoretical results in comparison to updated observational data, including the new ultra-faint dwarfs found using SDSS data, and applying completeness correction due to the limited area surveyed by the SDSS (about 1/5 of the sky). Assuming that the Local Group has a mass of 3×10^{12} $M_\odot$, as in the GK06 simulation, we find that there are no "missing galactic satellites" with $L_V \geq 10^5$ $L_\odot$ within the virial radius of the Milky Way. When the new dwarfs are included, the observed and predicted numbers of satellites agree near the Milky Way, however, for distances greater than 200 kpc, it is clear that there is still a 'missing' population of dwarfs. However, given that for $d > 200$ kpc, dwarfs with $L_V \sim 10^5$ $L_\odot$ drop below SDSS detection limits (Koposov et al. 2008), the underabundance of observed dwarfs at large distances is not surprising and likely due to the SDSS sensitivity limit.

A final comment regarding the cosmological model. The RG05 and GK06 simulations use cosmological parameters from WMAP 1. N-body simulations show that the number $N(M)$ of Milky Way dark matter satellites as a function of their mass is not overly sensitive to the cosmology, although there are some differences on the number of the most massive satellites (Madau et al. 2008). However, $N(v_{max})$ should be sensitive to the cosmology (Zentner and Bullock 2003), and changes of σ_8 and n_s may affect the occupation number and galactocentric distribution of luminous halos. The collapse time of small mass halos in high density regions probably dominates the 20% variations in σ_8 between WMAP 1 and WMAP 3, limiting effects due to the cosmology near large halos. A decrease in luminous dwarf numbers, due to the lower σ_8, could be evident in the distribution of the lowest mass luminous halos in the voids.

In conclusion, the number of Milky Way and M31 satellites provides an indirect test of galaxy formation and the importance of positive feedback in the early universe. Although the agreement of the SDSS and new M31 dwarfs' properties with predictions from the RG05 and GK06 simulations does not prove the primordial origin of the new ultra-faint dwarfs; it supports this possibility with quantitative data and more successfully than any other proposed model has been able to do thus far. At the moment, we do not have an ultimate observational test that can prove a dwarf galaxy to be a fossil. Even a test based on measuring the SFH of the dwarf galaxies may not be discriminatory because, as has been recently suggested, fossil galaxies may have a late phase of gas accretion and star formation at $z < 1 - 2$, during the last $9 - 10$ Gyrs (Ricotti 2009). The distinction between fossils and non-fossils galaxies thus is quite tenuous and linked to our poor understanding of star formation and feedback in dwarf galaxies. Arguments based on counting the number of dwarfs in the Local Universe probably provide the most solid argument to prove or disprove the existence of fossil galaxies. In the future, a possible test may be provided by deep surveys looking for ultra-faint or dark galaxies in the local voids. Some fossil dwarfs should be present in the voids if they formed in large numbers before reionization.

To extend our argument that the new ultra-faint dwarfs represent the high luminosity and surface brightness tip of a fossil distribution, we need to trace these first galaxies from reionization to the modern epoch. The simulations described in the next chapters were designed to do exactly that.

Chapter 3

Method and Tests

In this chapter, we present a novel method for generating initial conditions for a set of cosmological N-body simulations. These runs allow us to *directly* trace the distribution and evolution of the fossils of the first galaxies from reionization to the modern epoch.

GK06 uses the filtering velocity approximation, in conjunction with high-resolution N-body simulations of the Local Group, to evolve a population of dwarf galaxies around a Milky Way mass halo from $z = 70$ to $z = 0$. For details of the simulations, see § 2 in GK06. GK06 defines a fossil as a simulated halo which survives to $z = 0$ and remains below $v_{filter} = 30$ km s^{-1} with no appreciable tidal stripping. They calculate the probability, $P_S(v_{max}, r)$, of a luminous halo with a given maximum circular velocity v_{max} to survive from $z = 8$ (the final redshift of the RG05 simulation) to $z = 0$. For a given v_{max}, the number of surviving dwarfs at $z = 0$ is $N(v_{max}, z = 8)P_S(v_{max}, r)$, where P_S is the survival probability for a satellite a distance, r, from the host halo. The surviving halos are assigned a luminosity based on the L_V versus v_{max} relationship from RG05. At $z = 0$, GK06 has a population of dwarf galaxies with a resolution limit of $v_{max} = 13$ km s^{-1}. Unfortunately, this limit corresponds to a lower luminosity limit of $L_V \sim 10^5$ L$_\odot$, which includes Leo T and

Canes Venatici I, but excludes all the other new ultra-faint Milky Way satellites.

Here, we describe and test a new method of generating N-body initial conditions which allows us to follow the evolution, merger rates and tidal destruction of pre-reionization halos to present day and to overcome some of the limitations of the GK06 method. The initial distribution of particles in the N-body simulations represents the position, velocity and mass distribution of the dark and luminous halos extracted from pre-reionization simulations. Our simulations have a sufficiently large volume and dynamical range to explore the distribution of fossil galaxies outside the Local Group, in nearby filaments and voids using limited computational resources.

Our method improves on the GK06 work by removing the constraints that preclude a comparison of the GK06 simulations with the observed distributions of the ultra faints: (1) Due to the resolution of their N-body simulations, GK06 cannot resolve dwarfs with circular velocity, v_{max}, < 13 km s^{-1} which roughly corresponds to a simulated dwarf with $L_V < 10^5 L_\odot$. With two exceptions, no ultra faint dwarfs have $L_V > 10^5 L_\odot$ (CVn I (Zucker et al. 2006b) and Leo T (de Jong et al. 2008)). (2) The statistical matching of the baryonic properties of the pre-reionization halos to equivalent $z = 0$ halos in their N-body simulation does not allow GK06 to account for mergers of pre-reionization halos after reionization. For $z = 0$ halos which contain only one primordial galaxy the lack of mergers is not significant since not accounting for them will not change the baryonic properties of the halo. However, for the $z = 0$ halo which contain > 1 primordial galaxies the mergers of luminous components will change the baryonic properties of the fossils at $z = 0$. While the majority of mergers would not involve two luminous pre-reionization halos, the effect cannot be ruled out *a priory.* (3) The GK06 statistical matching also does not account for the clustering bias of the most luminous pre-reionization halos. The formation efficiency of H_2 is dependent on stochastic effects, so the most luminous pre-reionization halos form in the highest density regions of the Ricotti et al. (2002b) simulations and are more likely to have undergone a merger with another massive, luminous pre-reionization halo. (4) Extracting the baryonic properties of their fossils at $z = 0$ from the final output of the pre-reionization simulation does not allow GK06 to account for cosmic variance. By $z = 0$, the faster evolution of structure in over-dense regions (ie. Local Group) and the slower structural evolution of under-dense regions (ie. Local Void) have produced significant variance in the numbers and types of objects seen in both.

This chapter is laid out as follows. § 3.1 describes the simulations and § 3.2 show the variety of test we performed to ensure that our method produced results equivalent to those of other published N-body simulations. Finally, in § 3.2.4 we present a more detailed definition of a fossil and refine the observational criterion for the “fossil” Local Group satellites.

3.1 Numerical Method

To achieve the resolution necessary to study the ultra-faint dwarfs in a $z = 0$ volume equivalent to the Local Volume, we developed a method for generating initial conditions for N-body simulations which provides the required mass resolution, while using only limited computational resources. Our simulations allow us to trace the merger rate and tidal stripping of the first galaxies from reionization to the modern epoch. Traditional initial conditions for CDM simulations begin with an evenly distributed grid of uniform mass particles before the positions and velocities are perturbed according to a given power spectrum. Our method follows the same concept, except the initial distribution of the particles is not a uniform grid, but represents the distribution of halos in the final outputs of a 1Mpc^3 high resolution cosmological hydrodynamical simulation run to $z = 8.3$ (Ricotti et al. 2002b) (we refer to these as the pre-reionization simulations and the halos found in their 1 Mpc^3 outputs as pre-reionization halos). Thus, each particle represents a dark or luminous halo with a different mass and given stellar properties.

All of the initial conditions described in this section were run from their initial redshift, z_{init}, to $z = 0$ using Gadget 2 (Springel 2005) on the University of Maryland HIPCC Deepthought and analyzed with the Amiga halo finder AHF (Knollmann and Knebe 2009). A more complete discussion of the various halo finders used in this thesis is provided in § 3.1.2.

Figure 3.1 shows how we construct our high resolution region. We produce a lattice of the pre-reionization simulation $z = 8.3$ output. This gives us a grid similar to that used in traditional CDM, except power on scales below 1 Mpc is already present through the positions of the pre-reionzation halos. To add the larger scale power, we perturb the particle positions and velocities of the pre-reionization halos according to a power spectrum with no power for modes $l < 1$ Mpc. This method, similar to the one described in Tormen and Bertschinger (1996), is described in detail below.

The hybrid initial conditions are set using the following steps. (1) We locate an analog to the Local Volume within a low resolution 50^3 Mpc^3 volume run from $z = 40$ to $z = 0$. (2) A high resolution region is built out of the final outputs from the pre-reionization simulations at $z_{init} = 8.3$. (3) Finally, we insert our high resolution, 'Local Volume' into the larger low resolution simulation at $z_{init} = 8.3$ and run it to $z = 0$ using Gadget 2 (Springel 2005). We now explain these steps in more detail.

We need to generate and run a volume large enough to contain at least one sub-

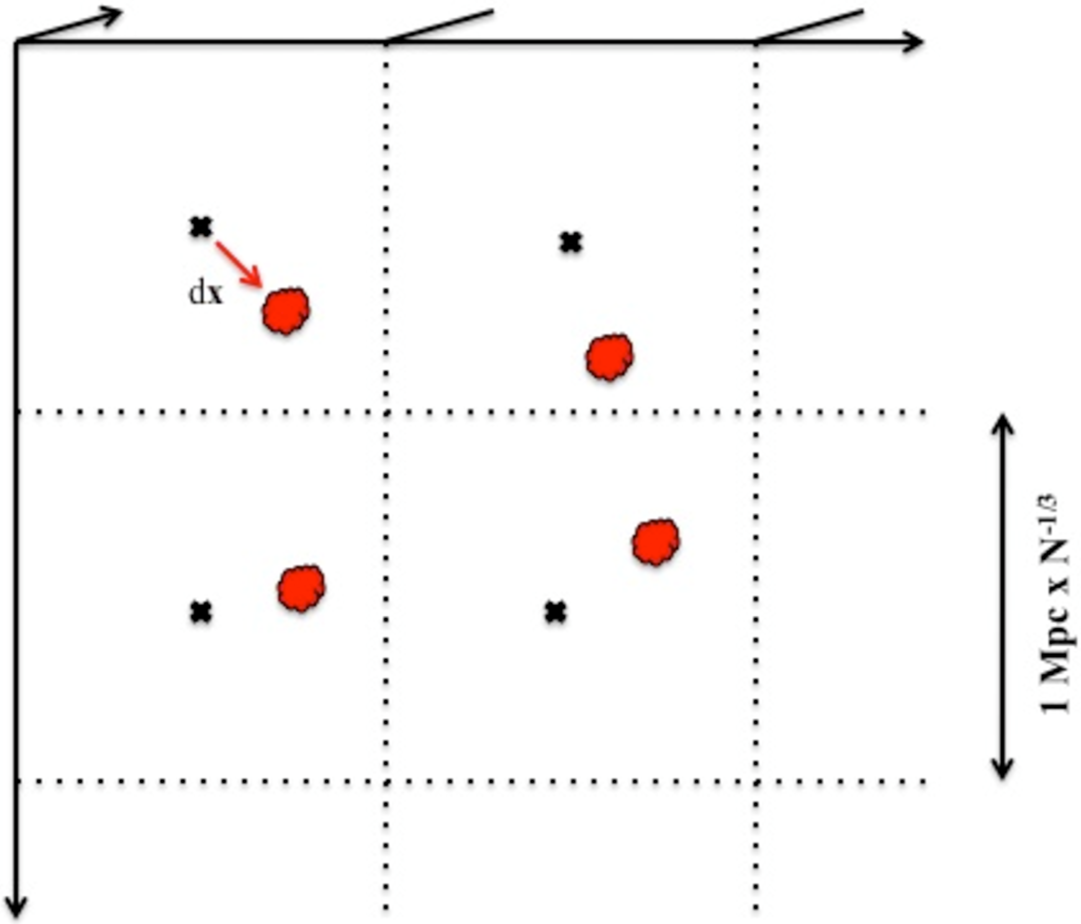

Figure 3.1: Diagram of how we add the large scale density perturbations to our high resolution region. In this diagram we show the upper, front, left-hand corner of our high resolution region. The size of each box enclosed by the dotted lines is 1 Mpc$\times N_{Mpc}^{-1/3}$ on a side where N is the number of course particles per Mpc^3. In each box, the black cross shows the position of an unperturbed, low resolution particle and the red blob shows that particle after the large scale positions and velocity perturbations have been applied. A pre-reionization halo at the same location as the black cross will have its position perturbed as shown. If the pre-reionization halo is between the black crosses, the perturbation on its position will be a linear interpolation between those of nearby black crosses, representing the perturbed positions of the low resolution particles.

volume analogous to the Local Volume. Our low resolution simulation is a 50^3 Mpc^3 volume with 250^3 particles run from $z = 40$ to $z = 0$. The power spectrum at $z = 40$ is generated by the cosmological initial conditions generator P-GenIC. At $z = 0$, we use the friend-of-friend halo finder HOP (Eisenstein and Hut 1998) to locate potential Milky Ways. In our 'Local Volume,' we look for a filament between two Virgo-like clusters with $2-3$ halos with $M \sim 10^{12} M_\odot$ within a $7^3 - 10^3$ Mpc^3 volume. Ideally, one of our Milky Ways has an equal mass companion within 1 Mpc, however, we were not able to find such a pair in our volume. Since the Milky Way and M31 are on first approach, within the virial radius where we can make the most accurate comparisons, the effect of the companion is minimal.

From the location of our Milky Ways, we define our 'Local Volume' as a region $\sim 5-10$ Mpc across, centered on one of our Milky Ways. Once we have a 'Local Volume' at $z = 0$, we estimate its equivalent volume at $z_{init} = 8.3$. We do this via tagging the low resolution particles in our present day Local Volume, and, using their positions at $z = 8.3$, determine the equivalent rectangular prism containing the majority of the tagged particles. At this point, we have defined a high resolution region with dimensions $m \times n \times p$.

We turn the 1 Mpc^3 $z = 8.3$ output from the pre-reionization simulations to an equivalent cube of N-body particles as follows. First, any pre-reionization halo in the output becomes an N-body particle with that halo's position, velocity, mass and, critically, unique ID. We then choose a mass resolution, m_{trun}, for our high resolution simulations and truncate the mass function of the pre-reionization halo at that resolution. To account for the additional mass needed to bring each 1 Mpc^3 to the average density of the universe, we add a population of lower mass dark particles. Hereafter we will refer to this population as tracer particles. These tracer particles have a mass, $m_{trace} \lesssim m_{trun}$. The positions and velocities of the tracer particles are determined from the position and velocities of the pre-reionization halos with masses below the truncation mass. This dark tracer population preserves our mass budget while allowing us to follow the dynamical evolution and locations of the lowest mass minihalos which were unable to from stars even with positive feedback.

At the end of this process we have a 1 Mpc^3 cube of N-body particles with $m_{min} \sim m_{trace}$, where positions, velocities and masses are determined by the $z = 8.3$ output of the pre-reionization simulations. The mass function produced by this method is shown in the upper left panel of Figure 3.2. The spike in the lowest mass bin shows the mass of the tracer particles. Critically, each particle has a unique ID allowing us to trace each pre-reionization halo to $z = 0$ and retrieve its baryonic properties in the modern epoch.

We have generated a 1 Mpc^3 cube for which each particle is a tracer for a pre-reionization halo. From the location of our Local Volume, we have a rectangular prism at $z = 8.3$ where our high resolution region will go. We duplicate the 1 Mpc^3 box to form the $m \times n \times p$ prism used for the high resolution region. We now have a $m \times n \times p$ prism with power on $l <$ Mpc scales. We add power on $l >$ Mpc scale using the position shift, $\delta \mathbf{x}$, of the low resolution particles via linear interpolation between them. Once we have $\delta \mathbf{x}$, we use the linear relation, $\delta \mathbf{v} = A(z) \delta \mathbf{x}$ to calculate the velocity perturbation, $\delta \mathbf{v}$, for our high resolution particles where $A(z)$ is the ratio of the $\delta \mathbf{v} / \delta \mathbf{x}$ at a given redshift. We now have a high resolution region with $m \times n \times p$ embedded inside a 50^3 Mpc^3 simulation at $z = 8.3$. In the low resolution region, all power comes from the power spectrum, and in the high resolution region the power comes from the power spectrum on $l >$ Mpc scales and from the $z = 0$ mass function of the pre-reionization simulations on $l <$ Mpc scales. This mass function matches the Press-Schetcher at high redshifts.

The high resolution region $\sim$ 10 Mpc on a side, with a mass resolution of

$\sim 3.2 \times 10^5 M_\odot$, is embedded in a low resolution volume 50 Mpcs on a side containing 250^3 particles at $z = 8.3$.

When compared to traditional zoom simulations, our high resolution region has several key differences. Primarily, each of our particles represents a resolved halo from the pre-reionization simulations. Each of these pre-reionization halos has a set of dark matter and stellar properties derived at $z = 8.3$. This technique allows us to push our simulations to higher mass resolutions over a 'Local Volume' sized region without a prohibitive increase in the number of particles. However, this technique precludes us from determining detailed density profiles of pre-reionization halos at $z = 0$. Since we assume the primordial galaxies have been relatively unaffected by tidal forces and significant mergers, their baryonic properties at reionization can be simply mapped to their stellar properties at $z = 0$ by accounting for the evolution of their stellar properties. The stellar properties of the pre-reionization halos are preserved through the unique IDs of each particle in our simulation. If, in the modern epoch, a given pre-reionization halo is in a halo whose maximum circular velocity has never exceeded the filtering velocity, it has not accreted gas from the IGM after reionization. If a halo has gone above the filtering mass it may have accreted gas and likely formed stars. Since we do not simulate baryonic evolution after reionization, we have only limited information on the primordial populations of these more massive halos and none on the younger ($\lesssim$ 12.5 Gyr) stars and gas. This filtering velocity, v_{filter} is the point below which star formation is suppressed by the reheating of the IGM via reionization feedback (Babul and Rees 1992; Benson et al. 2006; Efstathiou 1992; Gnedin 2000; Hoeft et al. 2006; Navarro and Steinmetz 1997; Quinn et al. 1996; Shapiro et al. 1994, 2004; Susa and Umemura 2004; Thoul and Weinberg 1996). The subsequent lack of star formation in these low mass halos allows us to approximate its present day observable properties from those at reionization. If a halo is able to exceed the filtering mass and accrete gas after reionization, it is not considered a fossil and we have only very limited information on its $z = 0$ baryonic properties. We consider the initial conditions built using the method described above as our first order simulations, specifically, runs A, B and C (Table 3.1). The initial conditions for run D, which are significantly different than those described for runs A-C, are described in the next section. For the remainder of this work we focus on Run C since Runs A and B do not have the resolution necessary to study the dwarf populations inside the Milky Way's virial radius.

3.1.1 Approximating Cosmic Variance

For our first order simulations (see Table 3.1), we assume that every part of our 'Local Volume' evolves at the rate associated with the mean density of the universe, before and after reionization. However, there are deviations from this mean due to linear perturbations on large (> 1 Mpc) scales . The evolution of a given region depends on its mean density with regions of higher density evolving faster than their lower density counterparts (Cole 1997; Crain et al. 2009; Reed et al. 2007). As a result, halos will collapse, and form stars, at later times in the voids compared to the filaments. To account for this effect, we relate the over-density or under-density of each region of our high resolution region to the speed of its evolution. We express the evolution of a region as a function of its densities as $z_{eff} = z_{init} + \Delta z$, where z_{eff} is the effective redshift, z_{init} is the redshift of the simulations, and the effective redshift of a region whose local density is the average density of the universe, $\rho_o(z_o)$, and:

$$\Delta z = (1 + z_{init})[(1 + \delta)^{-0.6} - 1)] \tag{3.1}$$

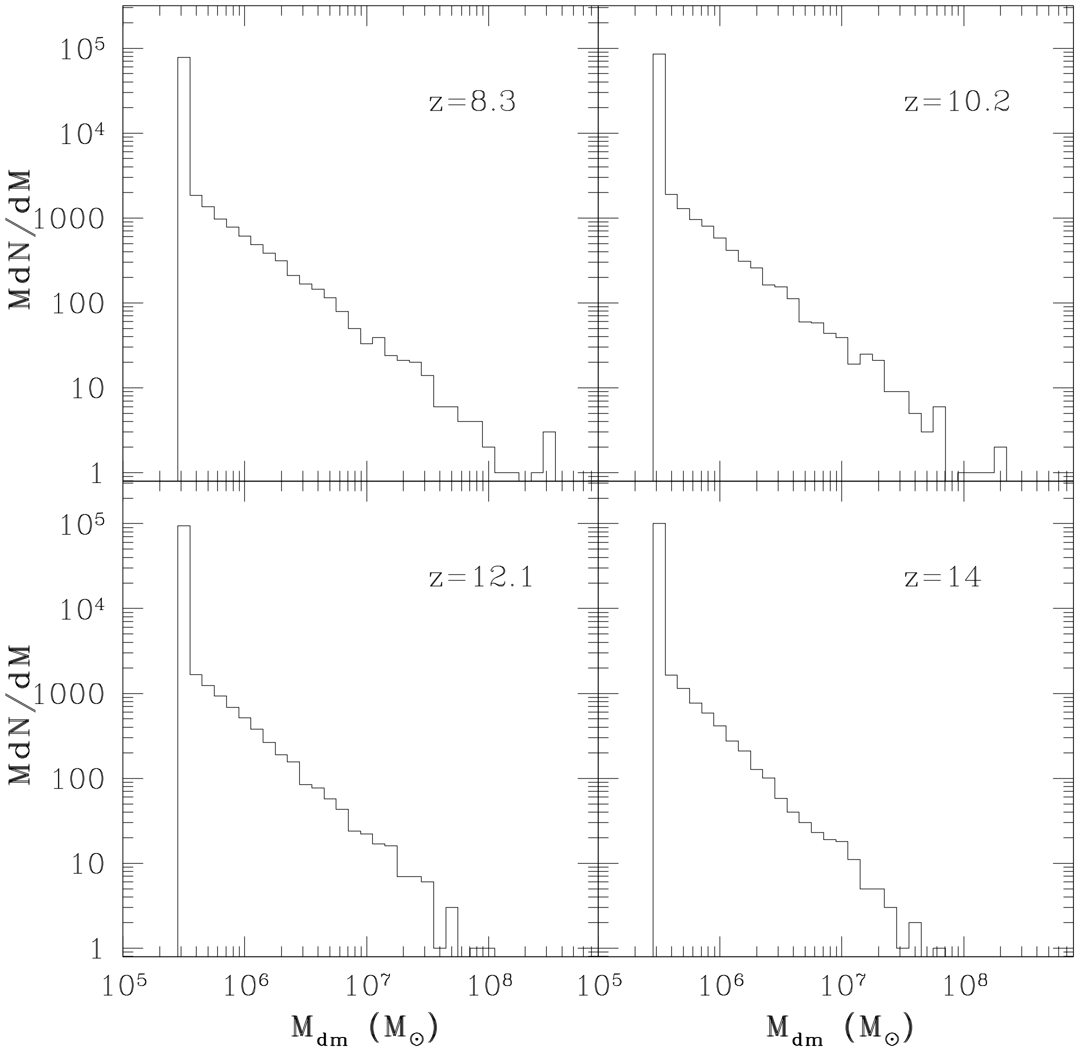

Figure 3.2: Truncated mass function of the pre-reionization outputs from $z = 8.3$ (top left), $z = 10.2$ (top right), $z = 12.1$ (bottom left), and $z = 14$ (bottom right). The spike in the lowest mass bin at all four redshifts is due to the dark tracer particles.

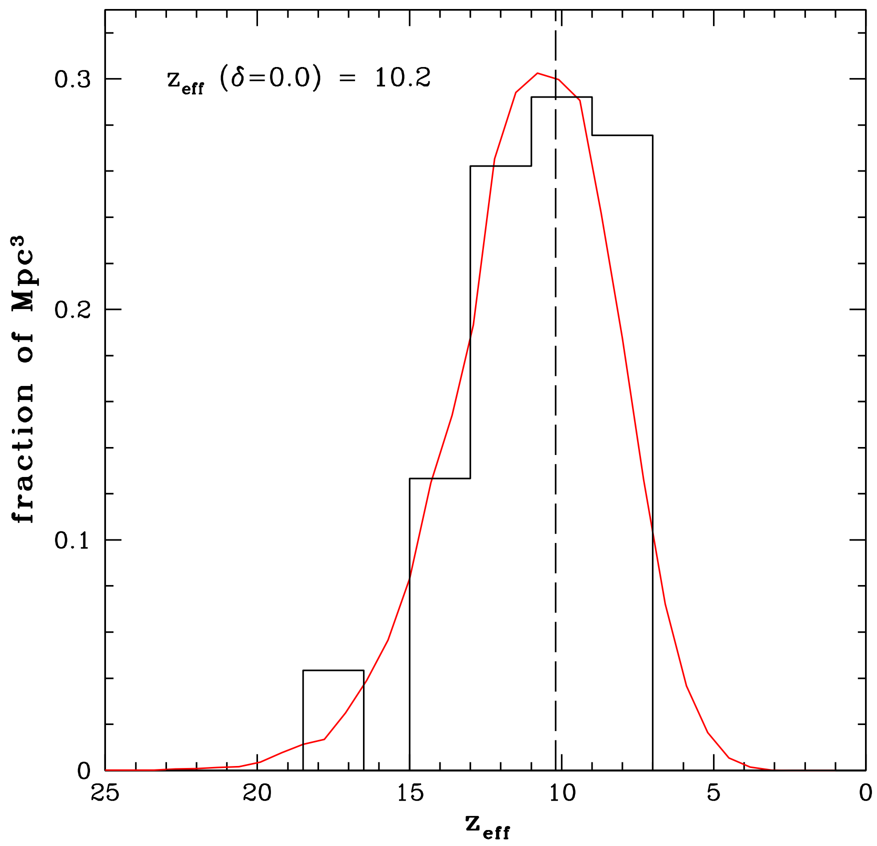

Figure 3.3: Fraction of 1 Mpc^3 cubes with a given effective redshift, z_{eff}. The red curve shows the distribution for all the Mpc^3 cubes in our entire 50^3 Mpc^3, low resolution volume. The black histogram show the fraction of 1 Mpc^3 volumes within the high resolution region which use a given pre-reionization output. Specifically, $z = (8.3, 10.2, 12, 1, 14)$. Sub-regions with $z_{eff} \sim 17$ use the $z_{eff} = 14$ pre-reionization output. The dashed vertical line shows the $z_{init} = 10.2$ for our second order initial conditions.

is the correction to z_{init} due to δ, the local over-density or under-density of a given region.

To approximate this variance effect, we produce a set second order initial conditions as in Cole (1997) (run D). The sole difference between runs D and C lies in the construction of the high resolution volume. Instead of using a single pre-reionization simulation output at $z = 8.3$ (runs A-C), we use outputs at multiple redshifts ($z = 8.3 - 14$) to approximate the differential evolution of the universe up to $z_{init} = 10.2$. Before constructing our high resolution region, we calculate the effective redshift of each 1 Mpc^3 sub-volume. Each sub-volume is then assigned a pre-reionization output based on its effective redshift, with the lowest density voids at $z_{eff} = 14$ and highest density regions at $z_{eff} = 8.3$. The details of this second order method are described below.

To account for the different rates of structure formation, we take the following additional steps when generating our high resolution region. (1) First, for each 1 Mpc^3 cube within our low resolution volume, we calculate local density at $z = z_{init}$. (2) From the density, we use Equation 3.1 to find the shift in effective redshift due the over-density or under-density of each subvolume, and then calculate z_{eff} (Figure 3.3). (3) Since we have a discrete set of pre-reionization outputs at $z = (8.3, 10.2, 12.1, 14)$, we divide the 1 Mpc^3 cubes within our high resolution region into four bins based on their densities and effective redshifts. The fraction of cubic Mpcs within our high resolution region in each effective redshift bin is shown as the black histogram overlaid on the z_{eff} distribution in Figure 3.3. Note, that both the histogram and the smoother curve follow the same general shape. (4) Finally, based on which bin each Mpc^3 falls into, we assign it a pre-reionization output.

To account for the faster evolution in our high density regions, for Run D we use a $z_{init} = 10.2$ instead of the $z_{init} = 8.3$ used in Runs A-C. This allows us to assign a $z_{eff} = 8.3$ to place near Milky Ways in our high density region. Nothing else substantially changes, except for using the $z = 10.2$ output from the low resolution simulation to generate the $l > 1$ Mpc structure in the high resolution region.

All the pre-reionization outputs are truncated to the same mass resolution using the same method described in the previous section. As near as possible, we use tracer particles of the same mass in each pre-reionization output. The truncated mass functions of the three additional pre-reionization outputs used in our second order initial conditions are the additional panels (bottom and top right) in Figure 3.2.

After the high resolution has been built and the large scale modes added at $z_{init} = 10.2$, we embed it inside the low resolution volume region and run to the present with Gadget 2. Run D has two key differences when compared to Runs A-C. First, the 50^3 Mpc^3 snapshot used to generate the $l > 1$ Mpc modes is $z = 10.2$ instead of $z = 8.3$. Second, the $z = 8.3$ pre-reionization output is not used for the entire high resolution volume, but only in the over-dense regions, with outputs from $z = (10.2, 12.1, 14)$ used for the average and under-dense regions.

In addition to accounting for cosmic variance, comparisons of runs A-C and run D allow us to probe two different reionization scenarios. Since we cannot account baryonic evolution after "reionization" when the pre-reionization outputs are transformed into our N-body simulation, we assume no baryonic evolution occurred after reionization in our fossils. During UV reionization we assume our entire volume was reheated to $\sim 10^4$ K (Ricotti and Ostriker 2004). We also assume that the entire volume was reionized by z_{init} and that the photo-evaporation of gas in minihalos completely cuts off star formation in the smallest galaxies. For runs A-C this approximates reheating at $z_{init} \sim 8.3$ by UV photons generated by stars in the first galaxies (Sokasian et al. 2004; Wise and Cen 2009). Since the voids evolve at a slower rate than the filaments, using the same pre-reionization output for our entire simulation is effectively allowing the low density regions to evolve for a longer time before their IGM is reheated to 10^4 K. This is consistent with reionization and reheating beginning in the filaments before spreading into the voids. In this scenario, low mass halos in the voids would have had more time to accrete gas and form stars than their counterparts in the filaments before reionization and reheating cut off their gas supply. We therefore expect the "filaments out" reionization scenario in run C produces brighter voids than the "simultaneous" reionization approximated in run D. This is seen in Figures 3.5 and 3.6

Since each 1 Mpc^3 subvolume in Run D used a pre-reionization output consistent with its effective redshift, the entire high resolution region has been given the same amount of time to evolve. When we transition from the pre-reionization output to our N-body simulations, Run D does not allow low mass halos in the low density regions to continue to evolve as the denser filaments are reheated. Instead, Run D approximates a universe in which all of space is reionized and reheated at approximately the same time by X-rays from the accretion of the ISM onto Pop III stellar remnants. Uniform reheating of the filaments and voids is a characteristic of reionization and reheating from X-rays produced by remnants of the first stars accreting from the ISM at high redshift (Ricotti and Ostriker 2004; Ricotti et al. 2005; Ripamonti et al. 2008; Shull and Venkatesan 2008; Venkatesan et al. 2001). X-rays could also be produced by primordial black hole binaries (Mirabel et al. 2011; Saigo et al. 2004). When compared to the "filaments out" reheating by UV radiation, the simultaneous X-ray reheating scenario produces noticeably darker voids.

3.1.2 All We Have to do is Run the Halo Finder

We use the halo finders to find bound structures within our cosmological simulations at various redshifts. In this thesis we use two codes using different methods, HOP (Eisenstein and Hut 1998), a friend of friend algorithm, and the Amiga halo finder AHF (Knollmann and Knebe 2009), a grid based density method. In this section, we discuss these two methods and codes in more detail.

A friend of friend algorithm (FoF) finds halos by linking all particles closer than

Name	IC Method	Volume (Mpc^3)	HR Volume (Mpc^3)	Mass Res. ($10^6 M_\odot$)	ϵ (kpc)	z_{init}
A	1^{st} order	50^3	$\sim 9^3$	3.16	1	8.3
B	1^{st} order	50^3	$\sim 9^3$	1.0	1	8.3
C	1^{st} order	50^3	$\sim 9^3$	0.316	1	8.3
D	2^{nd} order	50^3	$\sim 9^3$	0.316	1	10.2

Table 3.1: Table of simulation runs. From left to right the columns are (1) the simulation identifier, (2) the type of initial conditions used, (3) the co-moving volume of the larger, low resolution volume, (4) the approximate cubic co-moving volume of the high resolution region in Mpc^3, (5) the minimum mass of the dark particles in $10^6 M_\odot$, (6) the softening length of the high resolution particles in kpc, and (7) the redshift at which the zoom simulation is started.

a given linking length, l (Davis et al. 1985). While it is fast and computationally cheep, pure FoF codes does not find halos based on any physical property and can artificially link halos via filamentary bridges between them. In addition, they do not consider the binding energy of each particle when deriving halo properties. HOP uses a modified FoF algorithm where the density of each particle is calculated base on a smoothed kernel and used to link the particles based on local density as well as location to remove artifacts from the FoF algorithm. However, while HOP is fast and efficient ($\sim$ 30 minutes for 400^3 particles on a single i7 processor with 8 GB of RAM), it is unable to find halos with $N < 100$ particles. Unfortunately many of our fossils have $N < 100$, but HOP works wonderfully to find the locations of the Milky Way mass halos ($N \sim$few100) at $z = 0$ and guide the placement of our high resolution region.

To find the small fossil halos and substructure near the Milky Way we use a gird based density method. Initially we used PMHalos (Klypin), but found it insufficient for our needs for two reasons; (1) using a serial code on a simulation of 83 million particles is not feasible and (2) the spectrum of masses used in our high resolution region and the derivation of baryonic particles at $z = 0$ require a particle to particle

particle matching PMHalos could not supply. We therefore switched to the Amiga halo finder, AHF (Knollmann and Knebe 2009) which is a parallel grid based code. It uses a set of grids supplied by the uses which is then refined via criterion also supplied by the user. Only the refinement criteria used on the already refined grids, RefRef effects the results. A lower value of RefRef uses more memory but produces a more complete distribution of halos with $N < 50$ particles. Once the halos are found, AHF uses the binding energy of each particle and the escape velocity of the halo to "unbind" particles whose energies are too high to belong to the halo. While AHF runs quickly (~ 30 minutes) and finds the fossil halos and substructure required for our work, it requires significantly more memory than HOP (~ 16 GB of RAM) requiring it be run on the Maryland HPCC Deepthought.

In summary, we use HOP, a modified friend of friend (Eisenstein and Hut 1998), to locate the Milky Way mass halos in our large (50-100 Mpc) low resolution boxes and the parallel grid based AHF (Knollmann and Knebe 2009) to locate the fossils within the high resolution of our re-run simulations.

3.1.3 A Note on the Halo Occupation Distribution

The luminosities of the $z = 0$ halos are determined by the luminosity/luminosities of their component pre-reionization halos. These pre-reionization luminosities are taken directly from the Ricotti et al. (2002a,b) pre-reionization simulations and are determined by the feedback prescriptions and star formation efficiencies used in that work. Predictions made based on the resulting luminosity function and galactocentric radial distribution are a result of the primordial formation model we assume for the smallest dSphs. Note, that the match of luminosity and dark matter mass in this simulation is not statistical, but rather a direct result the distribution of the remnants of the first galaxies in the modern epoch.

3.2 Tests of the Method

In this section, we present consistency checks of our method to confirm that it reproduces known results from previous CDM simulations. We also discuss numerical effects introduced by our use of a spectrum of masses in our high resolution region. First, we confirm that the large scale structure and clustering of matter is consistent with traditional CDM simulations run with constant mass per particle. Then, we see that the halo mass function is consistent with the mass function of halos derived from the Press-Schechter formalism (Press and Schechter 1974). Finally, we confirm that the number of subhalos and their galactocentric distribution agree with the published results of the Via Lactea II (Diemand et al. 2008), Aquarius (Springel et al. 2008) and Polisensky and Ricotti (2010) simulations and that mass loss due to tidal stripping of the $z = 0$ halos is also in agreement with Kravtsov et al. (2004).

Figures 3.4 - 3.6 show a region of our Local Volume 5 Mpc across at $z = 0$. In order are the low resolution simulation, Run C and Run D seen from the same viewing angle. For Runs C and D, the luminous pre-reionization halos are shown as large red dots plotted over the white distribution of dark tracer particles. We find both Run C and D reproduce the large scale structure seen in the low resolution simulation. In CDM, the thickness of the filaments in our Local Volume is set by the mass scale we are considering. It is set during pancake collapse and can be thought of as the size of an over-density of $\rho \sim \rho_{ta} \sim 5$, where ρ_{ta} is the over-density at which a halo decouples from the Hubble flow in the top hat collapse model.

The existing differences result in the slight difference between the initial condition generated for run C and run D. There is only one Milky Way mass galaxy in run C because the second over-density which would have produced a Milky Way was

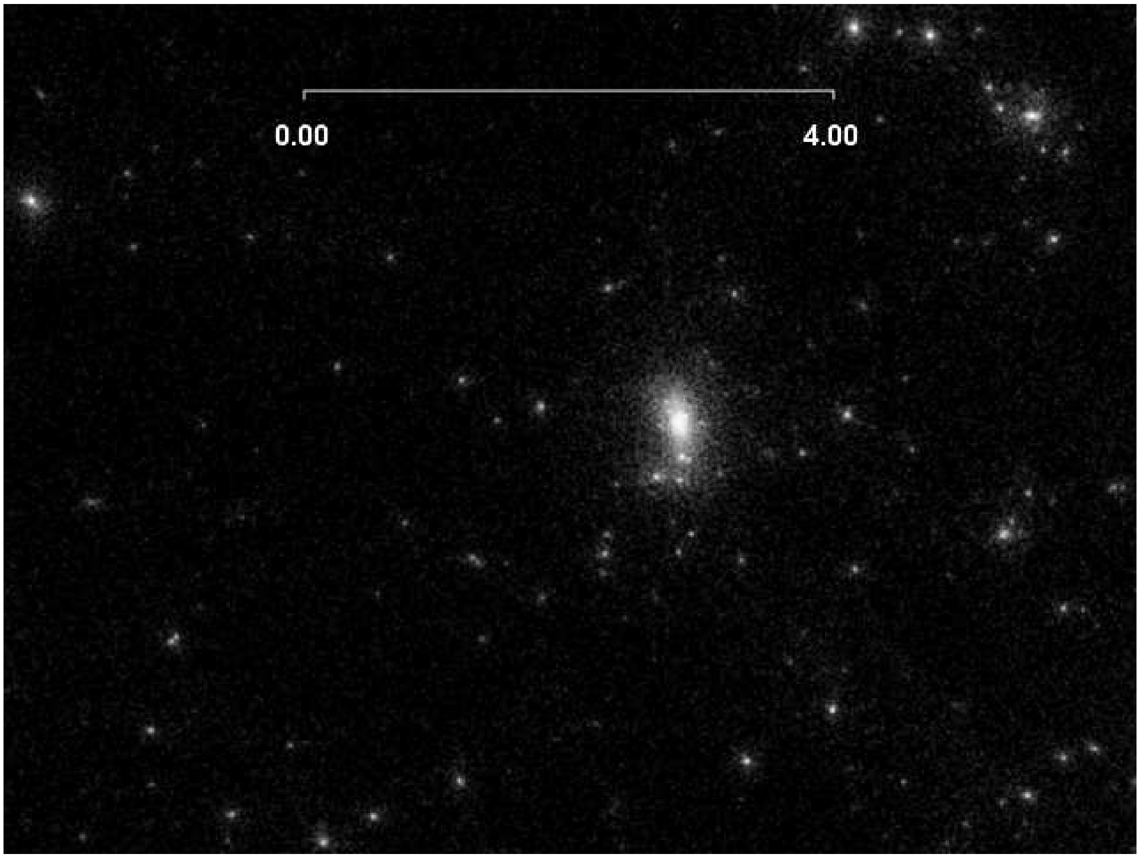

Figure 3.4: Large scale structure of the same region of our simulations for the low resolution simulations. The bar across the top shows the scale in Mpc.

“polluted” with the low resolution particles and thrown out. Of the two Milky Ways in run D one is undergoing an approximately 1:10 merger which its counterpart in run C has completed by $z = 0$. This difference is due to the starting redshift of run C versus run D. Run C was started at $z_{init} = 8.3$ using the $z = 8.3$ pre-reionization outputs. In contrast, while the region around the Milky Ways in run D uses the $z_{eff} = 8.3$ pre-reionization outputs, it is started at $z =_{init}= 10.2$, giving the Milky Ways in that simulation more time to evolve, allowing it to complete the 1:10 merger before $z = 0$. The output $300Myr$ before $z = 0$ shows the Milky Way in Run C undergoing an approximately 1:10 merger.

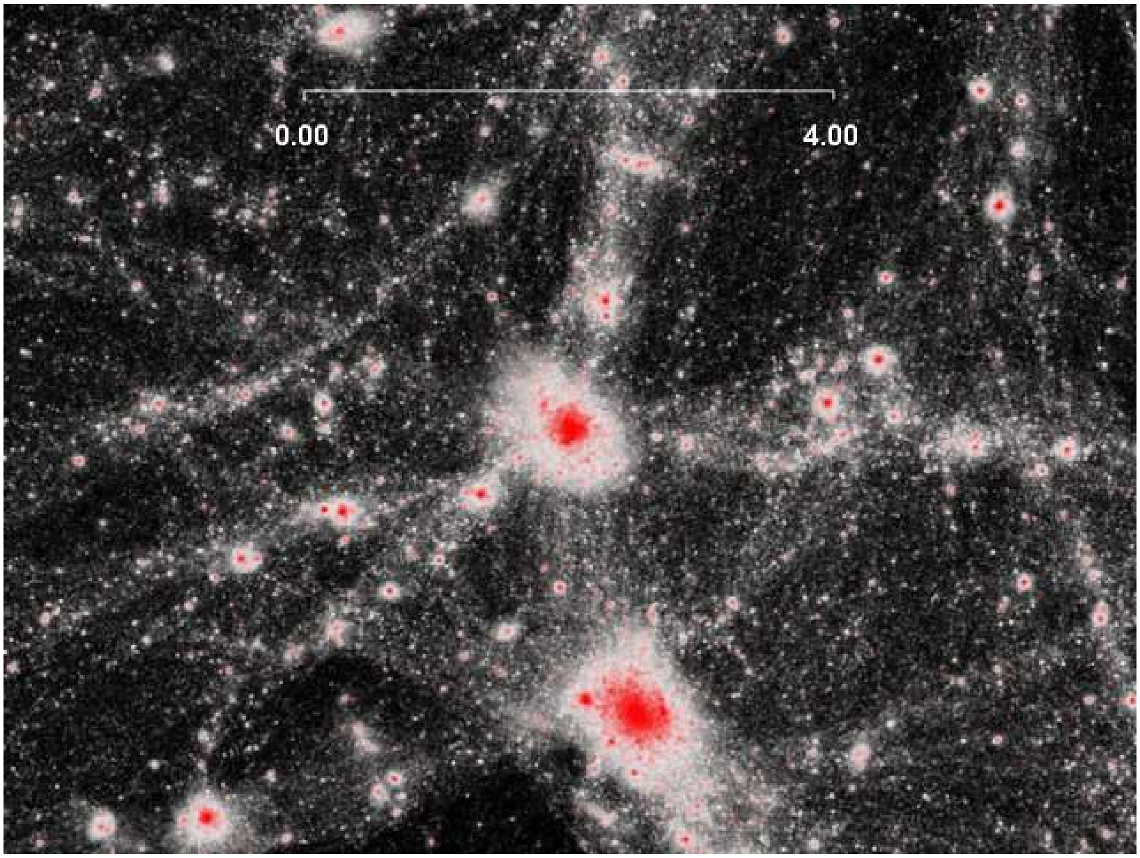

Figure 3.5: Large scale structure of the same region of our simulations for Run C. White shows the halos with no luminous component while the larger, red points show the luminous pre-reionization halos. The color of the latter does not depend on luminosity. The bar across the top shows the scale in Mpc.

3.2.1 Mass Resolution

Our simulations produce maps of the present day distribution and properties of pre-reionization fossils in a 5^3 Mpc^3 volume around a Milky Way type halo and in local filaments and voids. One of our goals is to map the distribution and properties of fossil galaxies outside the large hosts. This is done to quantify the number and properties of luminous dwarfs in the voids if stars formed in minihalos before reionization. These dwarfs would have evolved in relative isolation, and, if found by observations, would represent unambiguous and unperturbed fossils of the first galaxies. However, at this time, the only observational sample to which we can

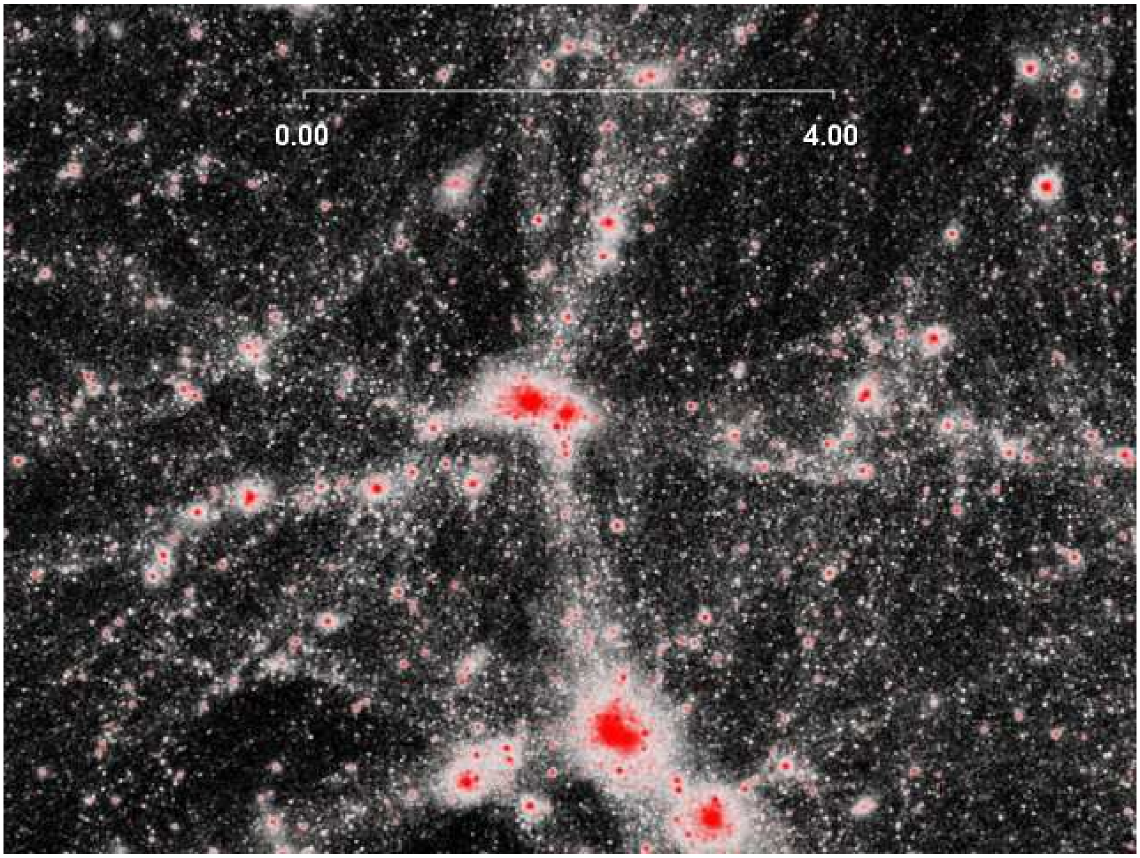

Figure 3.6: Large scale structure of the same region of our simulations for Run D. White shows the halos with no luminous component while the larger, red points show the luminous pre-reionization halos. The color of the latter does not depend on luminosity. The bar across the top shows the scale in Mpc.

compare our simulations is the classical dSphs and ultra-faint dwarfs near the Milky Way and M31. The faintest known dwarfs ($L_V < 10^3 L_\odot$) are found at less than 50 kpc from the Galactic center. Observations are likely incomplete at $R > 50$ kpc with some dependence on luminosity (Koposov et al. 2008; Simon and Geha 2007; Walsh et al. 2009). To compare our simulations to observations of the faintest known dwarfs, we must resolve halos within 100 kpc of the Milky Way center.

Run A, with a minimum particle mass of a $3.5 \times 10^6 M_\odot$, was not able to resolve subhalos within 200 kpc of the Milky Way mass halos. In Run C, we increase our mass resolution to $3.5 \times 10^5 M_\odot$ by increasing the number of pre-reionization halos in the initial conditions. By decreasing our minimum pre-reionization halo mass to $3.5 \times 10^5 M_\odot$ we are able to resolve subhalos at $R > 50$ kpc (see Figure 3.7). At $z = 0$, a luminous pre-reionization halo, evolving in isolation, is surrounded by a cloud of lower mass pre-reionization halos and tracer particles. The number of dark particles increases with the total mass of the luminous pre-reionization halo and the mass resolution of the simulation. The detectability of the lowest mass halos by the halo finder AHF is dependent on the ability of the luminous pre-reionization halos to accrete and retain their clouds of tracer particles. The larger number of low mass pre-reionization halos and tracer particles in runs C and D will allow more pre-reionization halos to accrete large enough clouds to be detected as a present day halo.

Resolving subhalos near a large galaxy is complicated by the background density field of the host halo and the stripping of the clouds of tracer particles during tidal interactions. To resolve a subhalo in the inner 100 kpc of Milky Way mass halo, the pre-reionization halo must retain enough of its cloud to be considered a bound system. In addition, it must have a high enough central density to be seen against the background of the host halo. The effect of the larger mass of the pre-reionization halo on the central concentration of the subhalo will be discussed in § 3.2.2. For AHF, the lower limit to robustly detect halos at $z = 0$ is a cloud of ~ 50 tracer particles (Knollmann and Knebe 2009).

Our simulations cannot provide information on the $z = 0$ stellar properties of a halo for a pre-reionization halo which has undergone significant tidal disruption. Beyond the stripping of the accumulated dark cloud described above, our simulations do not allow for the breaking apart of the pre-reionization halos. We only consider a pre-reionization halo unaffected by tides if its cloud of dark particles remains intact and detectable. This negates comparisons within 50 kpc of a host

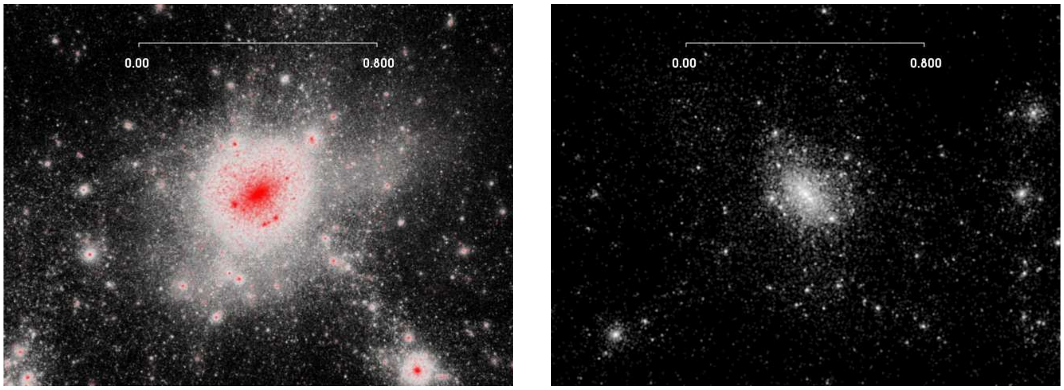

Figure 3.7: We show images MW.1 ($1.82 \times 10^{12} M_{\odot}$) from Run C. In Figure 3.5 it is large galaxy located in the center of the image. The left panel shows both the dark (white) and luminous (red) pre-reionization halos. The right panel shows only the luminous pre-reionization halos in greyscale with the brightest pre-reionization halos in white. In the right panel our Milky Way has been rotated $\sim 180^{o}$ relative to the view in the left hand panel. The bar across the top shows the scale in Mpc.

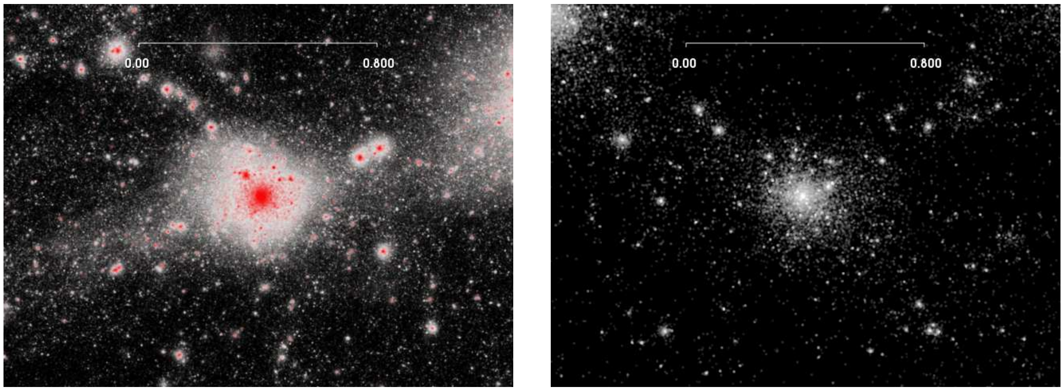

Figure 3.8: We show images of MW.2 ($0.87 \times 10^{12} M_{\odot}$) from Run D. In Figure 3.6 it is large galaxy located in the center of the image. The left panel shows both the dark (white) and luminous (red) pre-reionization halos. The right panel shows only the luminous pre-reionization halos in greyscale with the brightest pre-reionization halos in white. In the right panel our Milky Way has been rotated $\sim 180^{o}$ relative to the view in the left hand panel. The bar across the top shows the scale in Mpc.

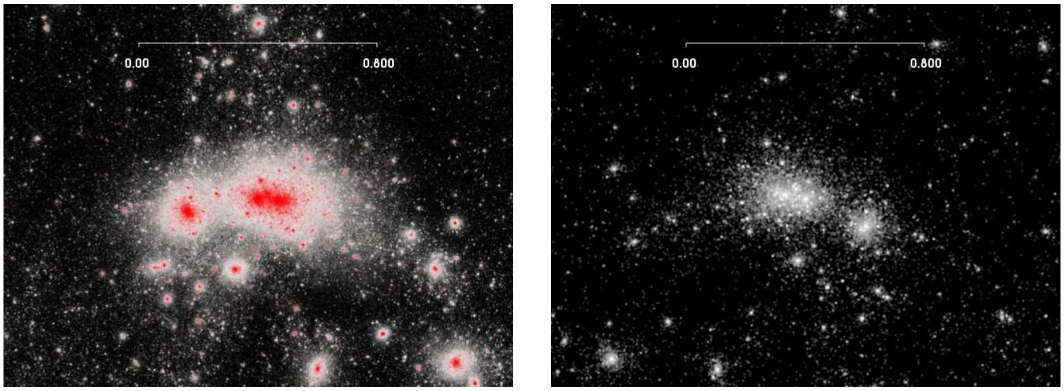

Figure 3.9: We show images of MW.3 ($1.32 \times 10^{12} M_{\odot}$) from Run D. In Figure 3.6 it is large galaxy located in the bottom-center of the image. The left panel shows both the dark (white) and luminous (red) pre-reionization halos. The right panel shows only the luminous pre-reionization halos in greyscale with the brightest pre-reionization halos in white. In the right panel our Milky Way has been rotated $\sim 180^o$ relative to the view in the left hand panel. The bar across the top shows the scale in Mpc.

halo where a significant number of the observed ultra-faint dwarfs have been modified by tides and our luminous pre-reionization halos are stripped of their clouds of tracer particles. In the galactocentric radial distributions and luminosity functions presented in Chapters 4 and 5, we only include the simulated and observed sample at $R > 50$ kpc.

3.2.2 Softening Length

In this section, we discuss one of the most prevalent numerical effects of using a spectrum of particle masses in our high resolution region instead of a uniform particle masses. The effects of this spectrum of masses primarily manifests in the lower mass halos and are sensitive to our choice of the softening length, ϵ. We also show the mass functions from Runs C and D for our chosen softening length.

Typically, the softening length is set at 2% of the average distance between particles in co-moving coordinates. For a representative volume of the universe with particles of uniform mass, $\epsilon = 0.02N^{-1/3}$ Mpc, where N is the number of particles per Mpc^3. For the high resolution region, we have a particle mass range between $3.5\times10^5 M_\odot - 2.5\times10^8 M_\odot$, requiring particle softening lengths from 0.5 kpc to 2 kpc. The public version of Gadget 2 does not have the capability of assigning softening lengths to each particle. Therefore, we must choose a single softening length for all the particles in the high resolution region. To determine the optimal value of ϵ, we have run the same initial conditions with softening lengths in our high resolution region of $\epsilon = 0.1$ kpc, 1 kpc and 5 kpc. We find that the best results for $\epsilon = 1$ kpc (corresponding to a uniform particle mass of $\sim 10^7 M_\odot$).

The right panel of Figure 3.10 shows the mass functions of Runs C and D compared to the Press-Schechter mass function run with $\epsilon = 1$ kpc . For C and D we see a deficit in the number of $10^9 - 10^{11} M_\odot$ halos when compared to the Press-Schechter and an over abundance of $M < 10^7 M_\odot$ halos. The deficit for larger halos may result from the location of our high resolution region. The Press-Schechter is the mass function of a typical volume of the universe. Our high resolution region is under-dense, containing three filaments bordering a void. The overabundance for $M < 10^7 M_\odot$ halos has a slope similar to the initial halo mass function from the pre-reionization simulations. At those masses, the $z = 0$ halos are dominated by one pre-reionization halo. This suggests that the steeper slope of the mass function at low masses is a numerical effect reflecting the behavior of the $z = 8.3$ mass function from the pre-reionization simulations.

When ϵ is set lower than 1 kpc (red curve in Figure 3.10), low mass halos with one or more luminous pre-reionization halos are preferentially destroyed by numerical effects. Statistically, luminous pre-reionization halos are more massive than their dark counterparts, hence they migrate to the centers of their modern halos via dynamical friction. Any two body interaction between a luminous pre-reionization halo and lower mass dark tracer particle will result in artificial heating.

Over the entire simulation, such interactions artificially heat the cloud of tracer particles until is disperses. We find that for $\epsilon = 0.1$ kpc only the most massive pre-reionization halos with the deepest potentials are able to retain their clouds. Isolated pre-reionization halos are surrounded by an extremely tenuous cloud of low mass dark particles, which is not detected by AHF as a bound halo.

Using $\epsilon > 1$ kpc also artificially decreases the number of the low mass halos (blue curve on Figure 3.10). Unlike the deep potentials of the massive halos, the potentials of halos with masses $M < 10^8 M_\odot$ are relatively shallow. If ϵ is too large, the low mass potentials will be flattened to the point where the pre-reionization halos are unable to accrete the tracer particles required for AHF detection. In halos with $M \gtrsim 10^9 M_\odot$, this effect is minimal. However we are primarily interested in halos with $M < 10^9 M_\odot$.

3.2.3 Subhalo Scale Comparisons

In this section, we study the distribution of subhalos around our Milky Ways. We use runs C and D to explore the simulated distribution of $z = 0$ subhalos around our Milky Way mass hosts. Comparisons are made with other CDM simulations and with observations.

In each simulation, we search for Milky Way type halos, using observational and theoretical constraints. This gives us a range of halo masses for candidate Milky Ways of $\sim 0.6 \times 10^{12} M_\odot - 4 \times 10^{12}$ (Kallivayalil et al. 2009; Klypin et al. 2002; Watkins et al. 2010; Zaritsky et al. 1989), and upper mass estimates for the Local Group of $\sim 5.3 \times 10^{12}$ (Li and White 2008; van der Marel and Guhathakurta 2008). These criteria give us three Milky Ways, one in the Run C and two in the Run D, respectively (Table 3.2). All three hosts have masses on the low end of the observed Milky Way mass range.

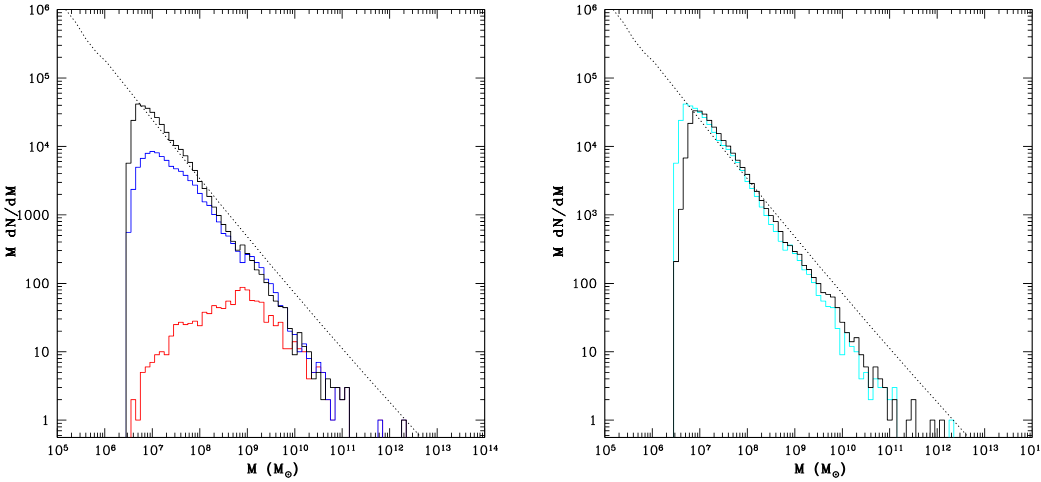

Figure 3.10: *Left* : Mass functions for Run C evolved with three different softening lengths, 100 pc (red), 1 kpc (black) and 5 kpc (blue). Note that while there is a negligible difference at large masses, $\epsilon = 1$ kpc gives us the least residual when compared to the expected mass function. The dotted line is the Press-Schechter for a $\sim$ 7 Mpc^3 volume, equivalent to the mass of the bound halos. *Right* : Mass function of all halos found by AHF in our high resolution region for run C (gray line) and run D (black line). The dotted line is the Press-Schechter for a $\sim$ 7 Mpc^3 volume at $z = 0$, equivalent to the mass of the bound halos. In both mass functions we only include $z = 0$ halos which contain only high resolution particles.

The Milky Way halo in Run C, MW.1, is in one of the highest density regions of our volume, with a companion galaxy of mass $10^{11} M_\odot$ at a distance of 2 Mpc. The Milky Ways in Run D have masses of $0.87 \times 10^{12} M_\odot$ for MW.2 and $1.32 \times 10^{12} M_\odot$ for MW.3. Though they are both in filaments, the nearby environments of MW.2 and MW.3 differ (see Figure 3.6). MW.2 sits at the intersection of three filaments, and there are $\sim 10^{11} M_\odot$ halos within 1.5 Mpc. In contrast, MW.3 is only 1-2 Mpc away from a complex of galaxies with masses $\sim 10^{11} M_\odot$ that appears to be in the process of merging to form another Milky Way mass system. For our comparisons with traditional simulations, and with observations, we use all three Milky Way mass halos. This allows us to explore differences between the first and second order as well as variations introduced by environmental effects.

Name	Run	Mass ($10^{12}M_{\odot}$)	R_{vir} (kpc)	v_{max} (km s^{-1})
MW.1	C	1.82	248.1	203.4
MW.2	D	0.87	222.6	196.6
MW.3	D	1.32	194.7	177

Table 3.2: Table of the three Milky Ways in runs C and D. The columns are (1) the Milky Way identifier, (2) the mass of the host in $10^{12}M_{\odot}$, (3) the virial radius in kpc, and (4) the maximum circular velocity in km s^{-1}.

Before looking at the distribution of satellites around individual Milky Ways, we check the distribution of the number of dark matter subhalos as a function of host mass. In Figure 3.11, we show a linear relation between host mass and the number of satellites for both Runs C and D. There is good agreement with the Via Lactea and Aquarius runs when we adjust their results for our lower mass resolution. Our simulations can robustly resolve halos with $M > 10^7 M_{\odot}$ ($v_{max} \gtrsim 5.5$ km s^{-1}). To scale the number of subhalos within R_{vir} in the Via Lactea and Aquarius simulations, we use $v_{max} \sim 5$ km s^{-1} for Via Lactea and $v_{max} \sim 7$ km s^{-1} for Aquarius (from Figure 27 in Springel et al. (2008)).

We use knowledge of the stellar properties of the pre-reionization halos to investigate the expected number of luminous satellites for a given host mass. We consider a subhalo luminous if it contains at least one pre-reionization halo with $M_* > 10^2 M_{\odot}$, or has a $z = 0$ mass $M > 10^9 M_{\odot}$. To study the distribution of the number of luminous satellites, $N_{sat}(L_V > 10^2 L_{\odot})$ vs. M_{host} we do not need to know the luminosity of the satellite at $z = 0$, only whether it is luminous. We find all of the luminous subhalos in Figure 3.11 formed stars before reionization since we have no $z = 0$ halos above the threshold for post-reionization gas accretion ($10^9 M_{\odot} : v_{max} = 20$ km s^{-1}) which do not contain a primordial stellar population. For Runs C and D, we find the number of luminous satellites increases linearly with host mass. For hosts with $M < 10^{11} M_{\odot}$, we see a larger scatter in the total number of satellites. Additionally,

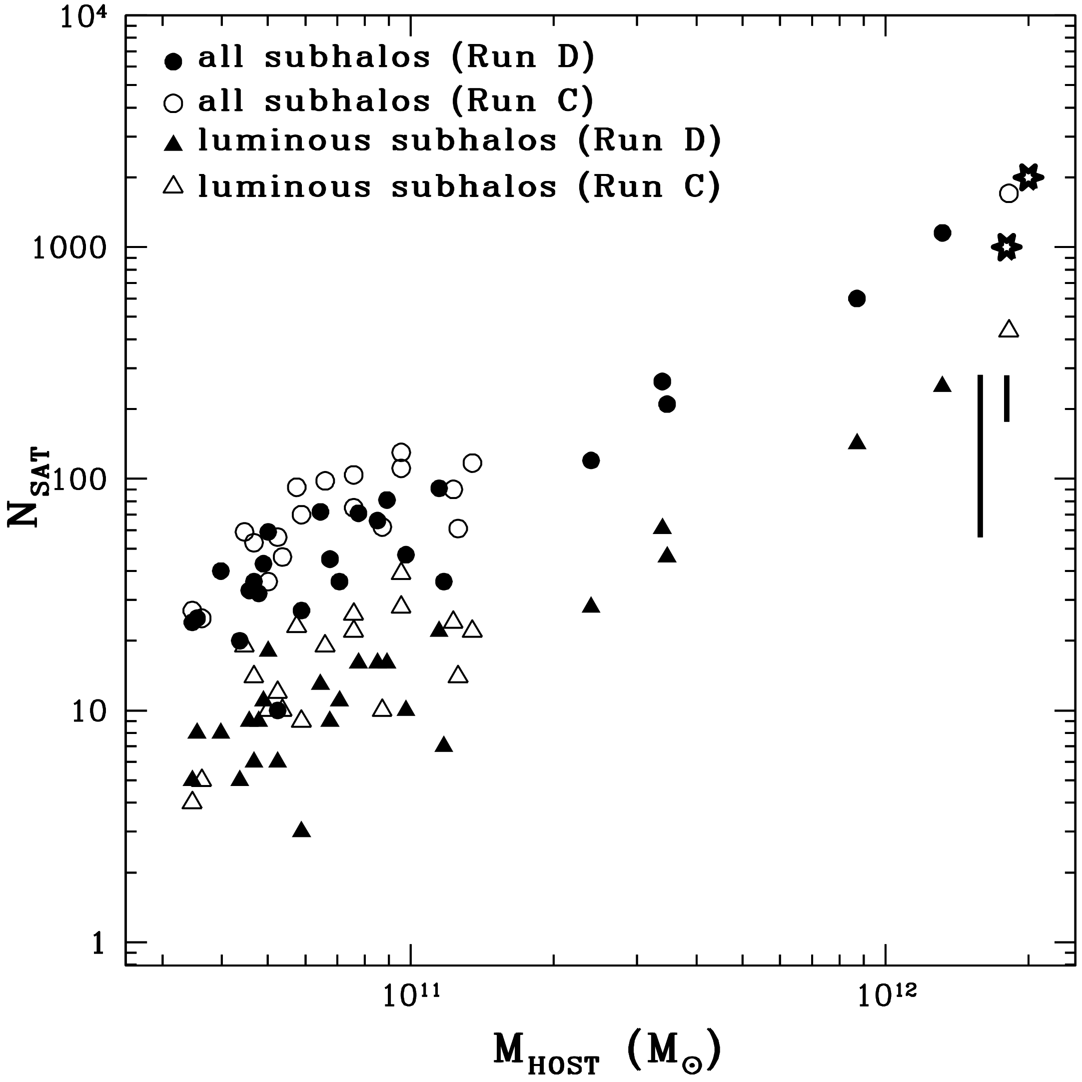

Figure 3.11: Number of satellites as a function of the mass of the host halo. The total number of satellites within R_{vir} for each halo are represented by circles, and the number of luminous satellites within R_{vir} for each halo by triangles. The results from runs C and D are shown as the opened and filled symbols respectively. The predictions from Via Lactea II (Diemand et al. 2008) and Aquarius (Springel et al. 2008), scaled to our mass resolution, are shown as the opened stars. Aquarius is the star with a greater number of satellites within R_{vir}. The ranges of the Tollerud et al. (2008) and Walsh et al. (2009) predictions at 200 kpc are the green and purple barred lines, respectively.

in that host mass range, we see greater scatter in the mapping of the total number of satellites to the number of luminous satellites. Since Runs C and D contain only three Milky Way mass systems, the lack of scatter may also be due to small number statistics. The decrease in scatter may be a function of how dominant the halo is in its environment. In the filaments, a $10^{12} M_\odot$ halo dominates the region around it, negating any environmental effects inside the virial radius. A lower mass host, however, is not able to dominate its environment. Therefore, the number of satellites for low mass hosts will be more sensitive to the environment in which they are embedded.

The current observational sample of the faintest dwarfs with $L_V < 10^3 L_\odot$ is complete only to within 50 kpc with the completeness limit dependent on the detectability of an overdensity of RGB stars against the red dwarfs and red giants of the halo (Koposov et al. 2008; Simon and Geha 2007; Walsh et al. 2009). A more luminous dwarf will have more stars on the red giant branch and therefore be detectable at greater distances than its dimmer counterpart.

Tollerud et al. (2008) used the detection limits of the SDSS and the Via Lactea II simulations to estimate the total number of satellites around the Milky Way given the currently known population and assuming the subhalo distribution in Via Lactea II accurately reflects the true satellite distribution of the Milky Way. They used halos from Via Lactea II (Diemand et al. 2007), assuming a simple relationship between halo mass and luminosity for the subhalos. The range of Tollerud et al. (2008) is shown on Figure 3.11 as the shorter, thick black line. Unlike their work, our simulations do not assume a relationship of luminosity to halo mass. Instead, we draw the stellar properties of the $z = 0$ halos directly from the cosmologically consistent pre-reionization simulations. This accounts for the large scatter in stellar mass as a function of halo mass for the smallest galaxies (Ricotti et al. 2002b). Our results are consistent with the upper end of the Tollerud et al. (2008) range for the number of luminous satellites within ~ 200 kpc. Based on these comparisons, the total number of subhalos and number of luminous satellites around MW.1, MW.2, and MW.3 are in agreement with results of other published works.

We next compare the distribution of maximum circular velocity for all subhalos around a Milky Way for our simulations with other CDM simulations. We find that the satellite mass functions for halos from Runs C and D are consistent with one another, and results from Aquarius, Via Lactea and Polisensky and Ricotti (2010) (Figure 3.12). Based on this, we argue that our simulations can reproduce the number and distribution of subhalos around the Milky Ways, as well as traditional N-body simulations. In the next section, we discuss the observational and theoretical criteria for a halo to be defined as a fossil of the first galaxies.

3.2.4 A More Detailed Definition of a Fossil Dwarf

For observed dwarfs, a fossil is defined as a dSph which underwent $> 70\%$ of its star formation before reionization, and today is a diffuse spherical system devoid of gas (Ricotti and Gnedin 2005). These dim dwarfs populate dark matter halos whose circular velocities have never been above the filtering velocity, preventing them from accreting gas from the IGM after reionization.

In our simulations, we define a fossil halo for which $max(v_{max}(z)) < v_{filter}$. Any halo with $v_{max}(z = 0) < v_{filter}$ is referred to as a *candidate fossil*. However, in regimes where tidal stripping is considerable, there is a significant chance that a halo with a $v_{max} < v_{filter}$ at $z = 0$ had a maximum circular velocity above the threshold for accretion from the IGM at an earlier time (Kravtsov et al. 2004).

Given these criteria, we classify our $z = 0$ halos into three populations as follows. (1) A *non-fossil* is a $z = 0$ halo for which $v_{max}(z = 0) > v_{filter}$. (2) Halos which are

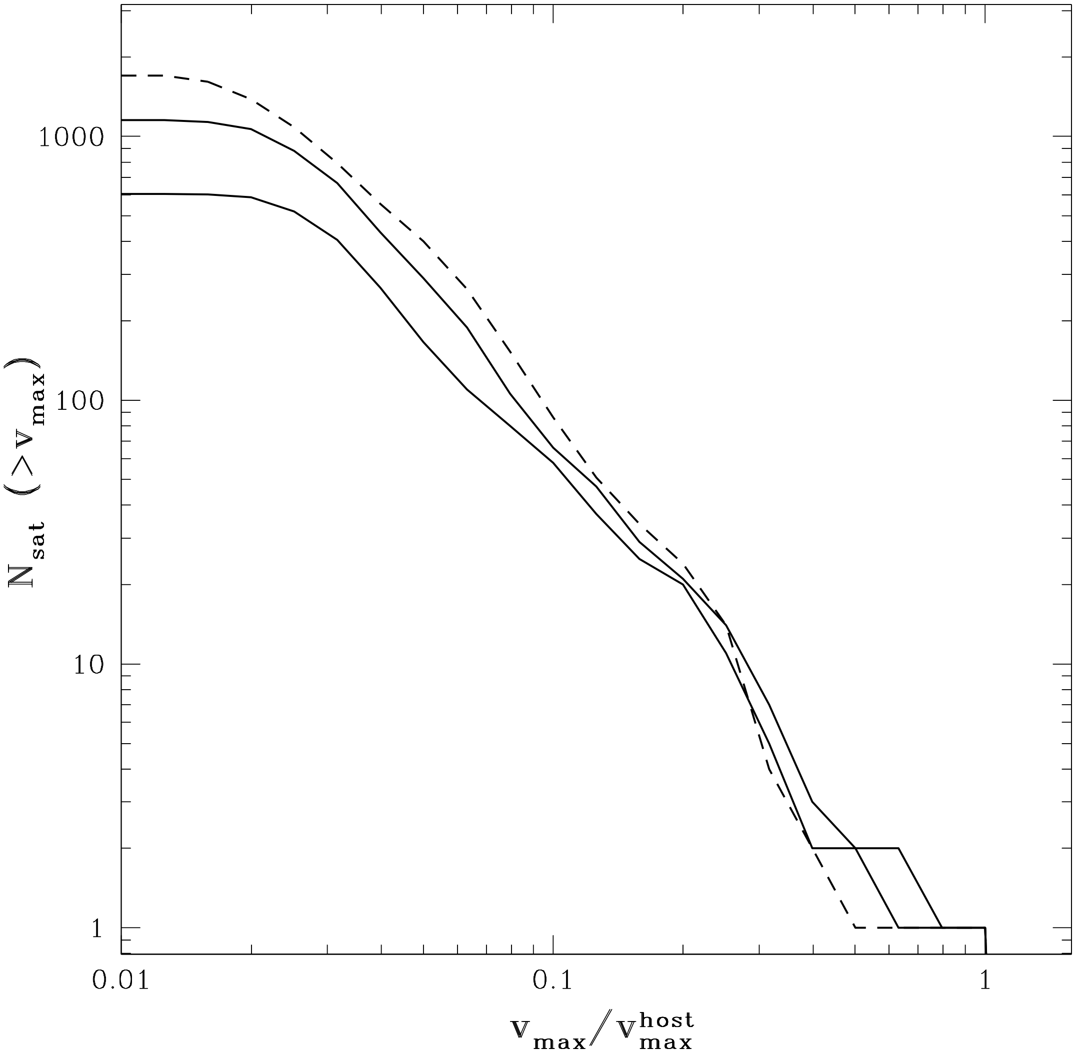

Figure 3.12: Number of satellites within R_{vir} with greater than a given v_{max} for our two second-order (black lines) and one first-order (gray line) Milky Ways. The two versions of our method produce equivalent distributions and match the CDM simulations from Polisensky and Ricotti (2010).

		Fossils		
	Non-fossils	RG05 only	RG05 & BR11a	BR11a only
Milky Way	LMC	Sculptor	Draco	Bootes I & II
	NGC 55		Phoenix	CVn I & II
	Sextans A & B		Sextans	Hercules
	SMC		Ursa Minor	Leo IV & T[1]
	WLM			Pisces II
	Carina			
	Fornax			
	GR8			
	Leo I, II & A			
	Sagittarius			
M31	IC 10	And I & II	And V	And XI XII
	IC 1613	And III		And XIII & IV
	IC 5152	And VI		And XV & XVI
	M32	Antila		And XVII & XVIII
	NGC 185	KKR 25		And XIX & XX
	NGC 205			And XXI & XXII
	NGC 3109			And XXIII & XXIV
	NGC 6822			And XXV & XXVI
	DDO 210			And XXVII
	LGC3			
	Pegasus			

		Fossils		
	Non-fossils	RG05 only	RG05 & BR11a	BR11a only
Isolated	—	—	Cetus[2] Tucana	—

Table 3.3: Classification of the known dwarfs into non-fossils and fossils. We also split the fossils into three groups. The classical fossil candidates from RG05 with $L_V > 10^6 L_\odot$ and $L_V < 10^6 L_\odot$, and the ultra-faint dwarfs discovered since 2005. When we compare our simulated fossils to the observed sample we only use the latter two categories.

candidate fossils but for which $max(v_{max}(z))$ was above the IGM accretion threshold in the past are classified as *polluted fossils*. The non-fossils and a fraction of the polluted fossils accreted gas from the IGM and formed a significant population of stars after reionization. Therefore, our simulations cannot provide robust information on the non-fossil and polluted fossil stellar properties in the modern epoch. (3) For the *true fossils*, we are able to generate detailed information on their stellar properties. A true fossil is defined as any $z = 0$ halo for which v_{max} never exceeded the IGM filtering mass, suppressing gas accretion and star formation after reionization.

To separate the polluted fossils from the true fossils of the first galaxies, we follow the v_{max} evolution for each candidate fossil back from $z = 0$ to z_{init}. We find that $f(v_{max})$, the fraction of candidate fossils which have $max(v_{max}) > v_{filter}$, as a function of their $v_{max}(z = 0)$, is consistent with results found by Kravtsov et al. (2004) (see Figure 3.13). In addition, we find that $f(v_{max})$ does not have a strong dependence on the environment of the fossils. When we compare the results for all the fossils (solid line) with those within 1 Mpc (dotted line) and 400 kpc (dashed line) of MW.2 and MW.3 we do not see a significant difference. These results are

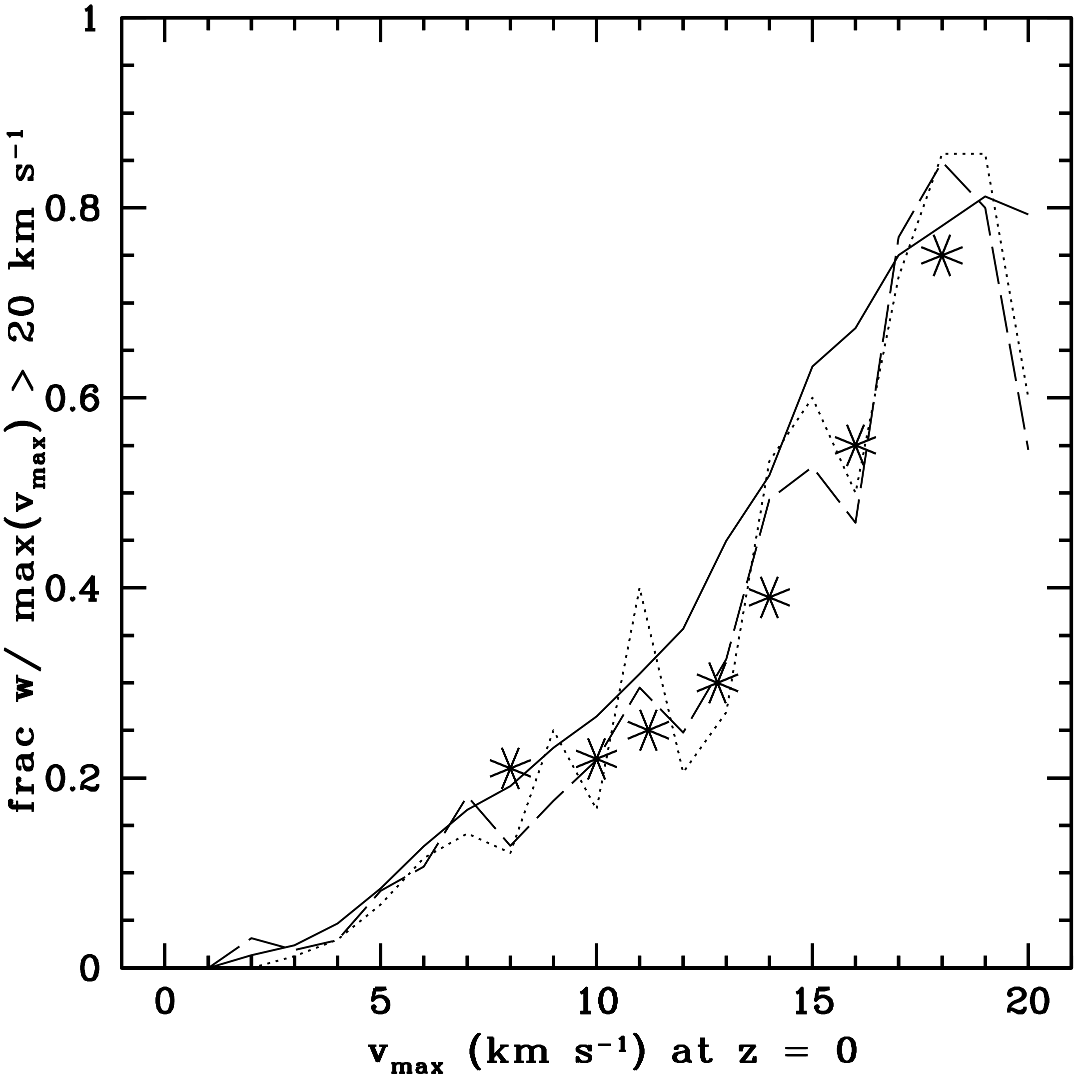

Figure 3.13: Fraction of candidate fossils with $\max(v_{max}(z)) > v_{filt}$ where $v_{filt} = 20$ km s^{-1} for Run D (lines) and Kravtsov et al. (2004) (asterisks). The solid, dashed and dotted lines show the fraction of true fossils for three different subpopulations. The solid line shows the relation for all the candidate fossils in Run D, while the dashed and dotted lines show the fraction of true fossils for candidate fossils within 1 Mpc and 400 kpc of MW.3 respectively.

independent of the choice of the filtering velocity. For the remainder of this work, we use the term fossil in reference to only these true fossils.

In addition to maintaining $v_{max} < v_{filter}$ for its entire evolution, a fossil must also survive to $z = 0$ without being tidally stripped. Objects which have undergone significant tidal stripping are unlikely to retain their pre-reionization stellar properties (Peñarrubia et al. 2008b). Once $\sim 90\%$ of the dark matter is stripped, the stars are stripped preferentially, trending the dwarfs towards lower σ_* and higher M/L. However, our initial conditions do not allow us to simulate tidal effects beyond the stripping of a $z = 0$ halo's tracer particles and our knowledge the baryonic properties of the fossils at $z = 0$ depends on the stellar population of the primordial dwarfs evolving only via stellar evolution, not via tides or additional gas accretion.

The use of N-body particles to represent pre-reionization halos forces the masses of those halos to be conserved. No matter how strong the tidal forces are, the stellar and dark matter properties will not change, inconsistent with the current understanding of the effect of tidal stripping on a satellite's stellar population. While the dark matter halo can be stripped away, leaving the stellar properties relatively intact (Choi et al. 2009; Peñarrubia et al. 2008a), once the mass loss reaches the outer stellar radii, the stripping of the stellar populations will occur at a faster rate than the denser dark matter cusp (Peñarrubia et al. 2008b). We have no way of tracking the mass loss of an isolated pre-reionization halo to determine which components have been disrupted. We address this limitation by using the destruction of a $z = 0$ halo's dark particle cloud to flag halos which have undergone tidal stripping. Any present day halo whose cloud of tracer particles has been destroyed or stripped down to $N \lesssim 50$ particles, will not be robustly detected as substructure and its mass will be added to that of the host galaxy. If $N < 20$, the $z = 0$ halo will not be detected at all (Knollmann and Knebe 2009). Any pre-reionization halo which is not found at $z = 0$ is assumed to be tidally disrupted and is not considered a fossil.

Given these criteria, we can say a few things about our fossil population. For the $v_{filter} = 20$ km s^{-1} used in the majority of this work 82% of the primordial galaxies are in non-fossils with the fraction approaching 70% as v_{filter} nears 80 km s^{-1}. For the $v_{filter} = 30$ km s^{-1} used in GK06 $\sim$ 30% of primordial galaxies are not in non-fossils at $z = 0$. Our fossils are dimmer and less massive than the polluted fossils and non-fossils. As a population, they are less likely to have undergone mergers involving two or more luminous pre-reionization halos (Figure 3.15). We define a merge between two or more luminous pre-reionization halos as a galaxy merger. Using an $v_{filter} = 20$ km s^{-1}, 25% of the fossils have two or more luminous pre-reionization halos compared to 40% of candidate fossils. The majority of true fossils (75%) contain only one luminous pre-reionization halo, however the remainder do not represent a negligible fraction. We find the same result when using the $v_{filter} = 30$ km s^{-1} adopted by GK06. As with the 20 km s^{-1} case, 75% of true fossils have only one luminous pre-reionization halo. Therefore, while the majority of fossils have not undergone galaxy mergers, it is not an effect that can be ignored.

3.2.5 Luminosity Threshold for Fossils

Before making detailed comparisons between our simulations and observations, we compare our work and the N-body simulations in GK06. Unlike our method, which allows us to directly trace the pre-reionization halos to the present day, GK06 statistically matches pre-reionizaion halos to their counterparts at $z = 0$ based on their v_{max} at $z = 8.3$. To make a direct comparison with GK06 we must use our MW.1 from Run C, since GK06 only used the $z = 8.3$ outputs from the pre-reionization simulations.

Figure 3.16 shows the galactocentric radial distribution for GK06 (blue band) and for MW.1 (black lines). Both curves only include the true fossils. For $L_V > 10^5 L_\odot$ (lower panel) we find that our simulations are consistent with GK06, if on the low end of their range. However, the brightest true fossils in GK06 with $L_V > 10^6 L_\odot$ have no counterparts around MW.1. We ascribe this discrepancy to the difference

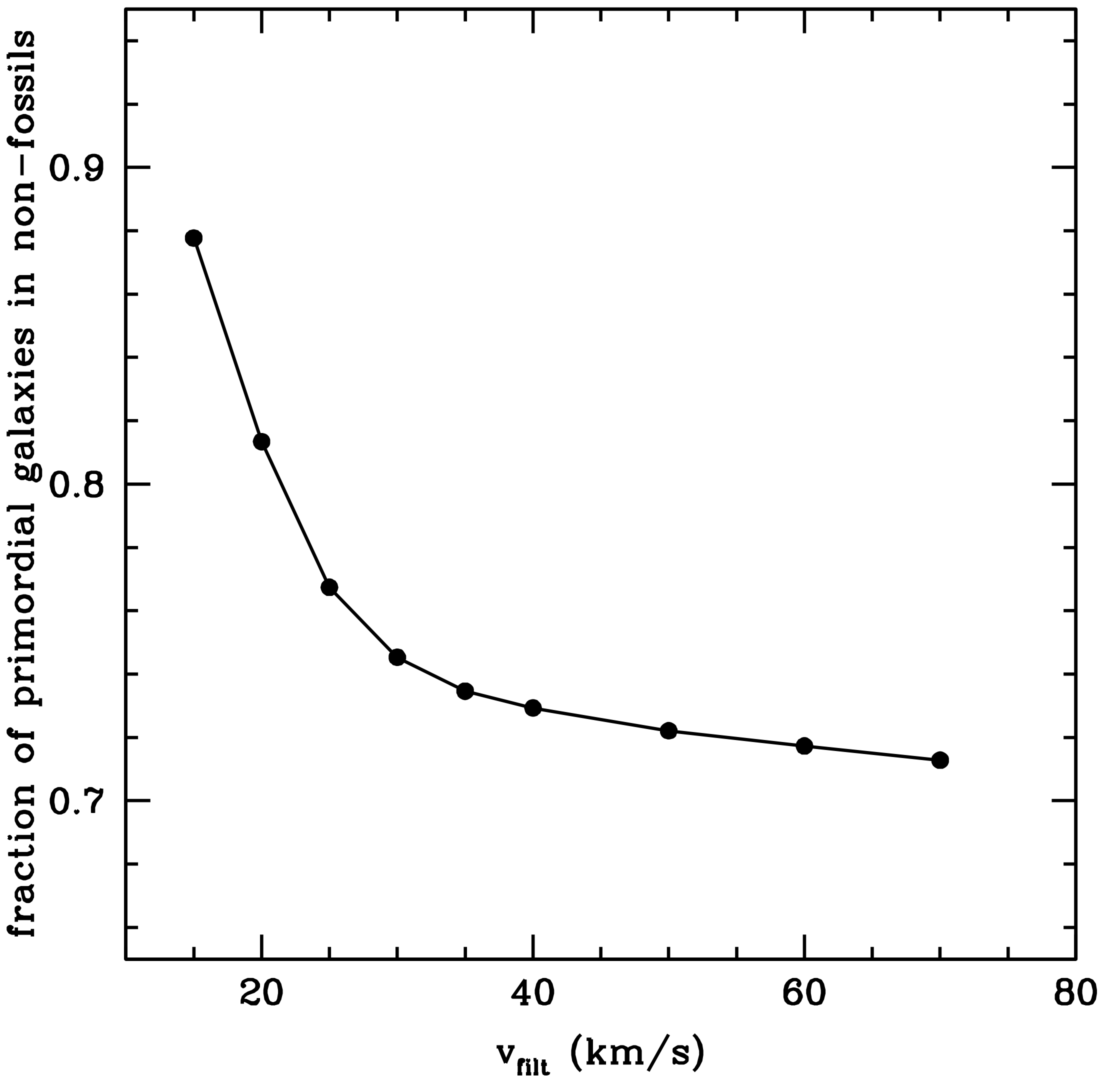

Figure 3.14: The fraction of primordial galaxies in non-fossils as a function of a given filtering velocity. Note, that above 30 km s^{-1} the fraction drops below 75%, approaching 70%, so at least $25 - 30\%$ of the primordial galaxies survive outside massive halos to $z = 0$.

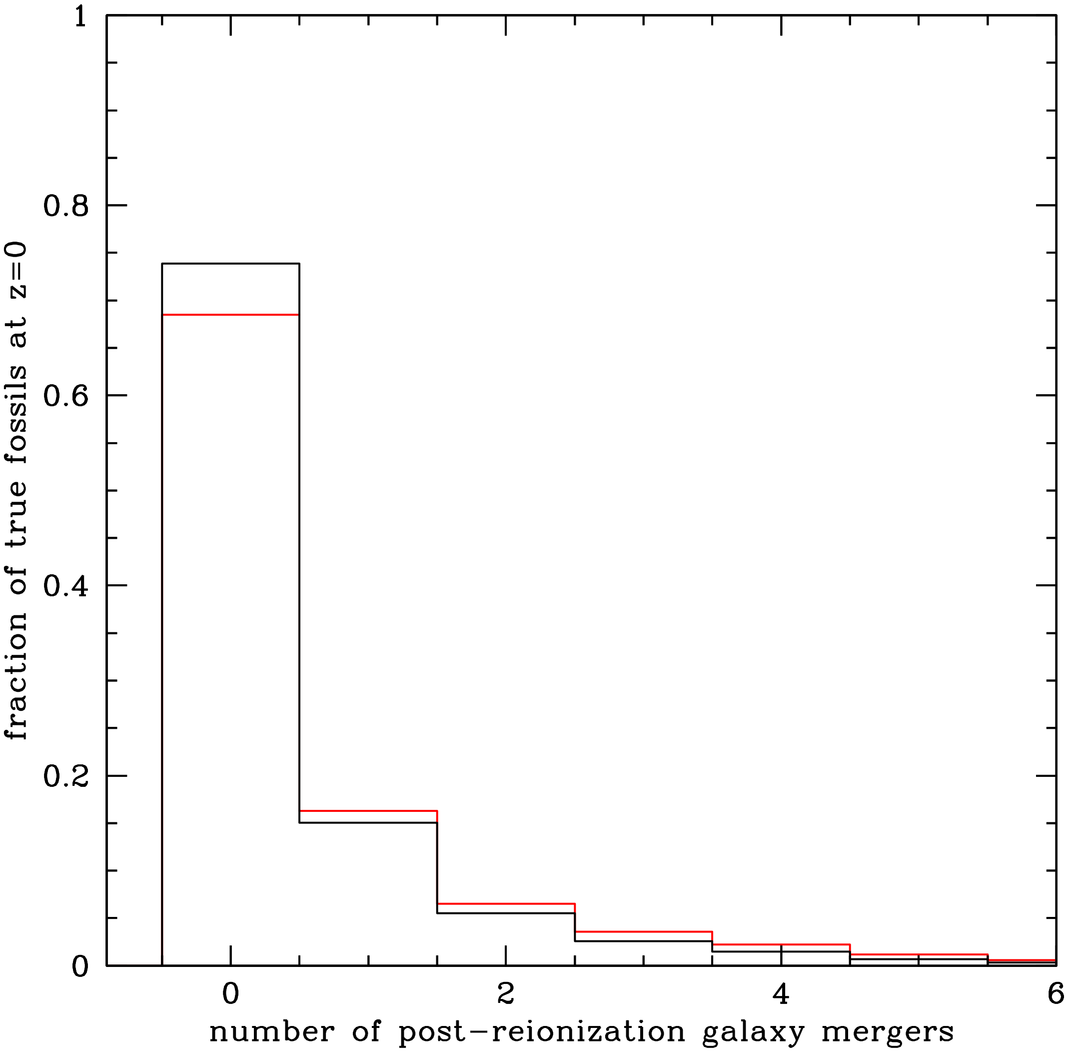

Figure 3.15: Fraction of luminous true fossils which have undergone < 6 galaxy mergers after reionization for $v_{filt} = 20$ km s^{-1} (black) and $v_{filt} = 30$ km s^{-1} (red). We define a galaxy merger as any merger in which two or more of the components contain a luminous population. For $> 4-5$ galaxy mergers, the fraction of $z = 0$ true fossils becomes negligible.

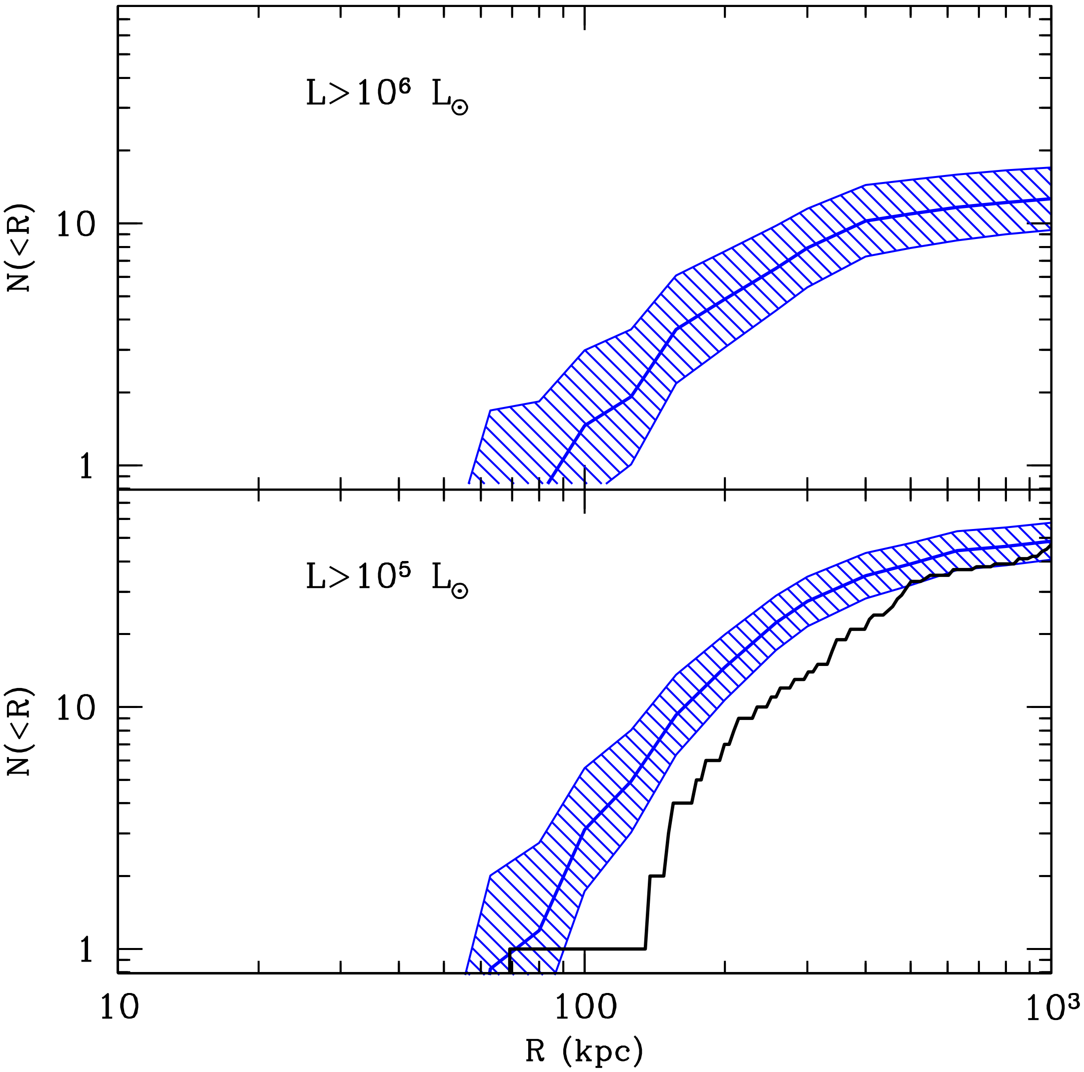

Figure 3.16: The radial distribution of the true fossils around MW.1 in Run C (black lines) and the results from GK06 (blue band) for halos with $L_V > 10^5 L_\odot$ and $L_V > 10^6 L_\odot$. We have used a $v_{filter} = 30$ km s^{-1} threshold to determine whether a $z = 0$ halo is a true fossil.

in how this work follows the pre-reionization halos to the modern epoch.

While both methods allow for the growth and stripping of a halo via accretion and tidal forces, our simulations also account for clustering of the pre-reionziation halos. The most luminous pre-reionization halos correspond to the most massive halos at $z = 8.3$. These $10^7 - 10^8 M_\odot$ galaxies are preferentially located in higher density regions within the 1 Mpc^3 pre-reionization simulation. This increases the probability that the pre-reionization halos with $L_V > 10^5 L_\odot$ will have undergone a galaxy merger relative to those with $L_V < 10^5 L_\odot$. In Figure 3.17, we show the histogram of the number of luminous pre-reionization halos for true fossils with $L_V < 10^5 L_\odot$ (left panel) and $L_V > 10^5 L_\odot$ (right panel). Only $\sim 0 - 5\%$ of the highest luminosity fossils have never undergone a galaxy merger compared to $\sim 90\%$ of fossils with $L_V < 10^5 L_\odot$. This is independent of our choice of filtering velocity.

Why does this explain the discrepancy between our results and GK06 in Figure 3.16? The definition of a true fossil is a dwarf whose maximum circular velocity has never gone above the threshold for accretion for the IGM. In Figures 3.16 and 3.17, we set $v_{filter} = 30$ km s^{-1}. Since the brightest pre-reionization halos are also the most massive, one or two galaxy mergers at high redshift would be enough to push v_{max} above the filtering velocity and classify the halo as a non-fossil. In Run C, there are only 11 true fossils with $L_V > 10^6 L_\odot$, none of which are within 1 Mpc of MW.1.

This gives us a maximum luminosity threshold, $10^6 L_\odot$*, above which an observed dwarf is unlikely to be a primordial fossil.* Of the true fossil candidates identified in RG05, this puts seven into question; And I ($4.49 \times 10^6 L_\odot$), And II ($9.38 \times 10^6 L_\odot$), And III ($1.13 \times 10^6 L_\odot$), And VI ($2.73 \times 10^6 L_\odot$), Antila ($2.4 \times 10^6 L_\odot$) and KKR 25 ($1.2 \times 10^6 L_\odot$) around M31, and Sculptor ($2.15 \times 10^6 L_\odot$) around the Milky Way. The remaining seven, And V, Cetus, Draco, Phoenix, Sextans, Tucana and Ursa

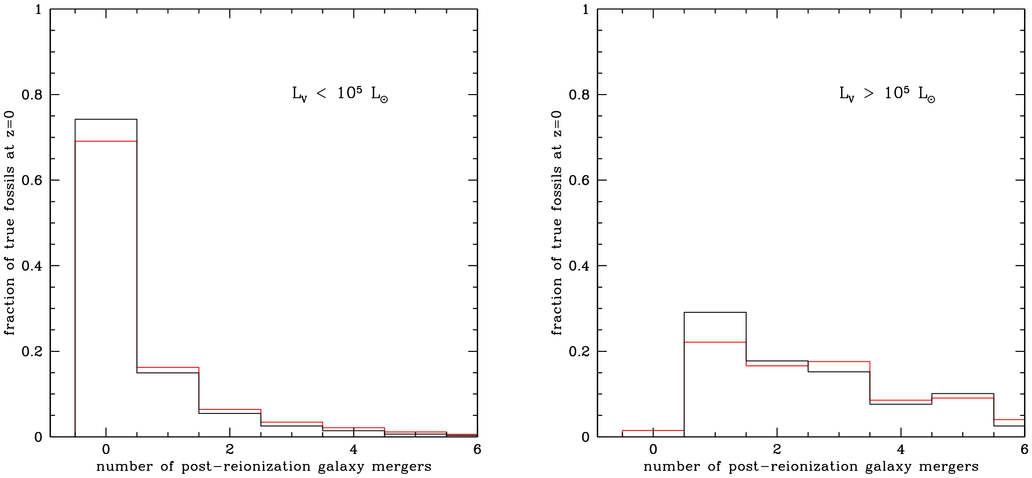

Figure 3.17: *(Left)* Histogram of the fraction of true fossils at $z = 0$ with a given number of galaxy mergers after reionization for $v_{filter} = 20$ km s^{-1} (black line) and $v_{filter} = 30$ km s^{-1} (red line). As in Figure 3.15, the number of galaxy mergers is a proxy for the number of luminous pre-reionization halos in a $z = 0$ halo. In this panel we show only the true fossils with $L_V(z = 0) < 10^5 L_\odot$. *(Right)* The fraction of true fossils with a given number of luminous pre-reionization halos for only those with $L_V(z = 0) > 10^5 L_\odot$ for $v_{filter} = 20$ km s^{-1} (black line) and $v_{filter} = 30$ km s^{-1} (red line). Note the shifted peak and different shape of the histogram in this panel.

Minor all have $L_V < 10^6 L_\odot$ and remain reasonable candidates for the fossils of the first galaxies. The classical Milky Way fossils, Draco, Sextans, Ursa Minor, as well as the ultra-faint Canes Venatici I, all have metallicity distributions suggesting star formation durations < 1 Gyr and populations > 10 Gyr old (Kirby et al. 2011a). These dwarfs, in addition to Sculptor, have star formation histories that are dominated by outflows, in contrast to their brighter counterparts ("polluted fossils" Fornax and Leo I & II) (Kirby et al. 2011b). However, unlike the other outflow dominated dwarfs which have relatively short star formation bursts, Sculptor has undergone star formation over several Gyrs (Babusiaux et al. 2005; Shetrone et al. 2003; Tolstoy et al. 2003) and a fraction of Draco's stars may be of intermediate age (Cioni and Habing 2005).

3.3 Discussion

We have presented a new method for generating initial conditions for cosmological N-body simulations which allows us to create simulated maps of the present-day distribution of fossils in a "Local Volume." In order to produce these maps, we assume pre-reionization fossils do not accrete gas and form stars after reionization. They are hosted in dark halos that maintain circular velocities below a critical threshold, $v_{filter} \sim 20 - 30$ km/s. The precise value of v_{filter} depends on details of the reheating in the local IGM by stars and AGN. Therefore, we explore different values for v_{filter}, but find little variation. For our purposes, we do not need to include gas dynamics. The lack of post-reionization baryonic evolution in the fossils allows us to simply simulate the evolution of the dark matter and stars using N-body techniques.

We have combined the results from previous cosmological simulations of the formation of the first galaxies (Ricotti and Gnedin 2005; Ricotti et al. 2002b, 2008) with N-body simulations in which each particle in the initial conditions represents a pre-reionization minihalo. Our N-body simulations zoom in on a Local Volume containing one to two Milky Ways. We follow the merger history and tidal stripping of pre-reionization fossils as they merge to form more massive galactic satellites of the Milky Way. We also trace the evolution of more massive non-fossil satellites, but we do not account for star formation taking place after reionization.

Our goal is to determine if a widespread population of primordial dwarfs is consistent with the observed population of Milky Way and Andromeda satellites, and, at the same time, if our simulations match observations of dwarfs in the Local Void. It is not well established whether halos with $v_{max} < 20$ km/s, too small to initiate collapse via Lyman-alpha cooling, remain dark or form luminous dwarfs.

Our simulations are a first attempt to constrain the theory of self-regulated galaxy formation before reionization using "near field" observations. Observational tests based on our results can constrain models of star formation in minihalos before reionization.

We present maps of the Local Volume showing the distribution of stars formed before reionization in the present day universe. We find that primordial fossils are present in the voids regardless of the details of reionization, however, reionization by X-rays produces darker voids.

We find that most classical dSph satellites are unlikely true-fossils of the first galaxies, even though they have properties expected of fossils: diffuse, old stellar populations with no gas (Bovill and Ricotti 2009; Ricotti and Gnedin 2005). The reason that true-fossils in the Milky Way have luminosities $< 10^6$ $L_\odot$, is that the most luminous pre-reionization fossils, with $v_{max} \sim 20$ km/s form in over-dense regions and are strongly clustered. Thus, they are likely to merge into more massive non-fossil dwarfs. The surviving fossils found today are a sub-population with lower typical luminosities, and formed in less clustered regions in which feedback effects suppress rather than stimulate star formation.

The results from this chapter are as follows:

- Voids contain many low luminosity fossil galaxies. However they have surface brightnesses and luminosities making them undetectable by SDSS. One possible way to detect these void dwarfs is if they experience a late phase of gas condensation from the IGM as proposed in (Ricotti 2009). Future and present 21cm surveys such as ALFALFA and GALFA may be used to find these objects (Begum et al. 2010; Giovanelli et al. 2005).

- We find a linear scaling relation between the number of luminous satellites and the mass of host halos. The scaling has scatter similar to the relationship between the total number of sub-halos with $M > 10^7$ M$_\odot$ ($v_{max} > 5$ km s^{-1}) and the host mass, although the normalization is $3 - 4$ times lower.

- Due to the dependence of the properties of primordial dwarfs on their formation environment (Ricotti et al. 2008), we find very few true fossils with $L_V > 10^6 L_\odot$, and none within 1 Mpc of our Milky Ways. This places the identification of some of the more luminous classical dSphs fossils in doubt.

Chapter 4

The Properties and Distribution of the Fossils

In this chapter, we present the stellar properties and distribution of our simulated true fossils and compare them with observed stellar properties and distribution of Milky Way satellites. These comparisons include V-band luminosity, L_V, half-light radius, r_{hl}, metallicity, $[Fe/H]$, and mass inside the half-light radius $M_{1/2}$ (Walker et al. 2009). In Chapter 2, we showed strong statistical agreements between the stellar properties of the pre-reionization halos, and the observed distribution of known classical dSph and ultra-faint dwarfs. Here we improve our previous results by relaxing some of the assumptions made in Chapter 2.

As in GK06, Chapter 2 assumed that none of the luminous pre-reionization halos had undergone a galaxy merger. Thus, the present day distribution of stellar properties for the fossils would be identical to that of the pre-reionization halos. In addition, our previous work assumed the voids were reheated to $T \sim 10^4$ K well after the clusters and filaments, as expected for UV reionization by stars. As seen in Figures 3.5 & 3.6, a universe reionized by stars, Run C, produces a larger number of luminous objects in the voids when compared to a universe reionized and reheated by X-rays emitted by accretion from the ISM onto BHs in the early universe (Ricotti and Ostriker 2004; Ricotti et al. 2005) (Run D). As in Chapter 2, for all observed stellar properties, we use the measurements with the lowest error bars.

4.1 Fossil Properties

From hierarchical formation models, we know that all halos have undergone merger and/or accretion events since their epochs of formation. For 60% of our pre-reionization halos, these mergers are with dark halos, producing a daughter halo with the same stellar properties as the parents. We are assuming that the stellar velocity dispersion radial profile of the stars within the fossil halos is undisturbed by these "minor" mergers.

However, for all runs and all halos, fossil and non-fossil, $\sim 40\%$ of the $z = 0$ halos contain more than one luminous pre-reionization halo. These galaxy mergers will change the stellar properties of the systems.

True fossil halos in the modern epoch derive their stellar properties solely from their pre-reionization populations. For the 75% of luminous true fossils which contain only one luminous pre-reionization halo, the $z = 0$ stellar properties are taken directly from those of the pre-reionization halo. We account for the reddening of the stellar population by using a $M_*^{rei}/L \sim 5$. Note that we use such a large stellar mass to light ratio to account for stellar mass lost since reionization. The stellar mass to light ratio of our simulated galaxies at $z = 0$ is,

$$\frac{M_*^{rei}}{L} = \left(\frac{M_*^{today}}{L}\right)\left(\frac{M_*^{rei}}{M_*^{today}}\right) \tag{4.1}$$

where M_*^{rei} and is the mass of the stellar population at reionization, and M_*^{today} is the mass of the stellar population at $z = 0$. The ratio between them, M_*^{rei}/M_*^{today} is between 2 and 20 depending on the IMF of primordial stellar population. RG05 used a range of M_*^{rei}/L ratios and found no dependence of the fossil properties on the choice of mass to light ratio.

For the one-quarter of true fossils which have undergone a galaxy merger, the stellar properties are calculated as follows. Throughout this section, the superscript f will denote the stellar and dark matter properties of the $z = 0$ halo, and the superscript i the properties of the component, luminous pre-reionization halos.

The final V-band luminosity, L_V^f of a fossil halo at $z = 0$, is the sum of the V-band luminosities, L_V^i, of the component pre-reionization halos. We assume stellar mass is conserved during all mergers of luminous pre-reionization fossils, an assumption that will be addressed in future, higher resolution simulations.

We determine the half light radii, r_{hl}^f, for $z = 0$ fossils using the 3D r_{hl} from the pre-reionization simulations, with the following assumptions. (1) The dynamical evolution of the stars is decoupled from that of the dark matter. (2) The kinetic energy of the stars is conserved. Dark matter provides the gravitational potential in which the stars move and the orbits of the stars are not dragged along with the dark matter while it mergers and interacts dynamically. (3) The collision of the luminous pre-reionization halos is elastic with respect to the stars. We assume this for convenience since we were unable to derive a clean analytical expression which included an injection of kinetic energy into the stellar population from the merger or that allowed for the loss of kinetic energy. Since we do not account for this additional source of energy, the final velocity dispersions of the merged fossils, and therefore their half-light radii represent lower limits to what we would expect if a full merger simulation had been run for each interaction. (4) Enough time has passed since the collision for the halo to return to an equilibrium state. Given the kinetic energy conservation of the stars:

$$(\sigma_*^f)^2 = (L_V^f)^{-1} \sum L_V^i \times (\sigma_*^i)^2, \tag{4.2}$$

where σ_*^i and σ_*^f are the 3D stellar velocity dispersions of the parent and daughter halos. For a halo in equilibrium, $r_{hl} \sim \sigma_*^2$, therefore:

$$r_{hl}^f = (L_V^f)^{-1} \sum L_V^i \times r_{hl}^i. \tag{4.3}$$

We use r_{hl}^f to calculate an average surface brightness, $<\Sigma_V>$, for our fossils in units of $L_\odot/$ pc ^{2}. The Σ_V and r_{hl} distributions as a function of luminosity are shown in Figure 4.1.

In Figure 4.1, the black symbols are the observed Milky Way and M31 satellites overlaid on colored contours showing the equivalent distributions for the simulated true fossils. The cyan and red contours show the stellar properties of the fossils above and below the SDSS detection limits, respectively. We see that, as in Chapter 2, our simulations are able to reproduce the observed Σ_V and r_{hl} distributions for the ultra-faint and classical dSphs, with a few exceptions. We are unable to account for the ultra-faints with $r_{hl} < 60$ pc (Segue 1 and 2, Leo V, Pisces II and Willman 1), all but two of which (Leo V and Pisces II) are within ~ 50 kpc of the Milky Way.

In Chapter 2, we called attention to a population of ultra-faints, as yet undetected, with surface brightnesses below SDSS limits. The existence of these dwarfs was independently proposed in Bullock et al. (2010), who named them 'stealth galaxies.' The detection of these ultra-faint dwarfs is a test for the fossil scenario. In this section, we summarize the properties expected of these extremely ultra-faint fossils.

In Figures 4.1 - 4.8, the simulated true fossils are shown as two sets of contours. Up until now, we have been comparing the ultra-faints and a subset of the classical dSphs to the simulated true fossils with $\Sigma_V > 10^{-1.4} L_\odot$ pc^{-2}. These true fossils,

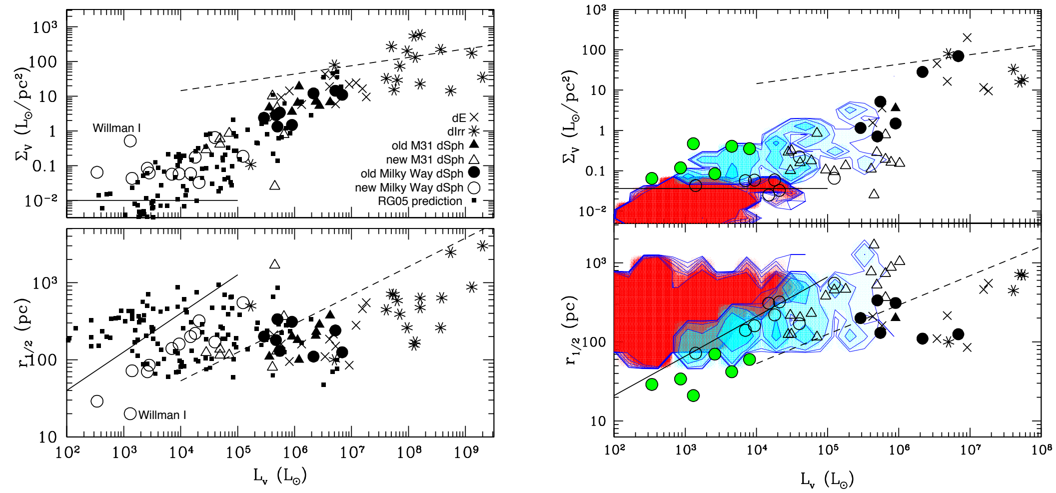

Figure 4.1: *Left* : Figure 2.1. Surface brightness and half-light radii are plotted against V-band luminosity. The small black squares show the properties of the pre-reionization halos at $z = 8.3$. The other black symbols show the dwarf populations for the Milky Way and M31. The asterisks are non-fossils (dIrr), crosses are polluted fossils (dE and some dSph), the filled circles and triangles are the fossils (dSph) known before 2005 for the Milky Way and M31 respectively and the opened circles and triangles are the ultra-faint populations those galaxies found since 2005. *Right* : Surface brightness and half-light radii are plotted against V-band luminosity. The cyan contours show the distribution for the fossils from Run D and the overlaid black symbols show the observed dwarfs. In this panel we color the observed dwarfs whose half-light radii are inconsistent with our simulations green. The magenta contours show the undetectable fossils with Σ_V below the 0^{th} order detection limit of the SDSS, ~ -1.4, (Koposov et al. 2008). In both panels, the solid black lines show the surface brightness limit of the Sloan (Koposov et al. 2008) and the dashed black lines show the trends from Kormendy and Freeman (2004) for luminous Sc-Im galaxies ($10^8 L_\odot < L_B < 10^{11} L_\odot$).

shown by the cyan contours, would be detectable by the SDSS (Koposov et al. 2008). The red contours show the true fossils which would remain undetected by SDSS. In Chapter 6, we present the existence and properties of the true fossils with surface brightnesses below the SDSS detection limits as a test for primordial star formation in minihalos. For the remainder of this section, we direct the reader to the red contours on Figures 4.1- 4.8.

The mass to light ratios and σ_* of the observed and simulated populations are

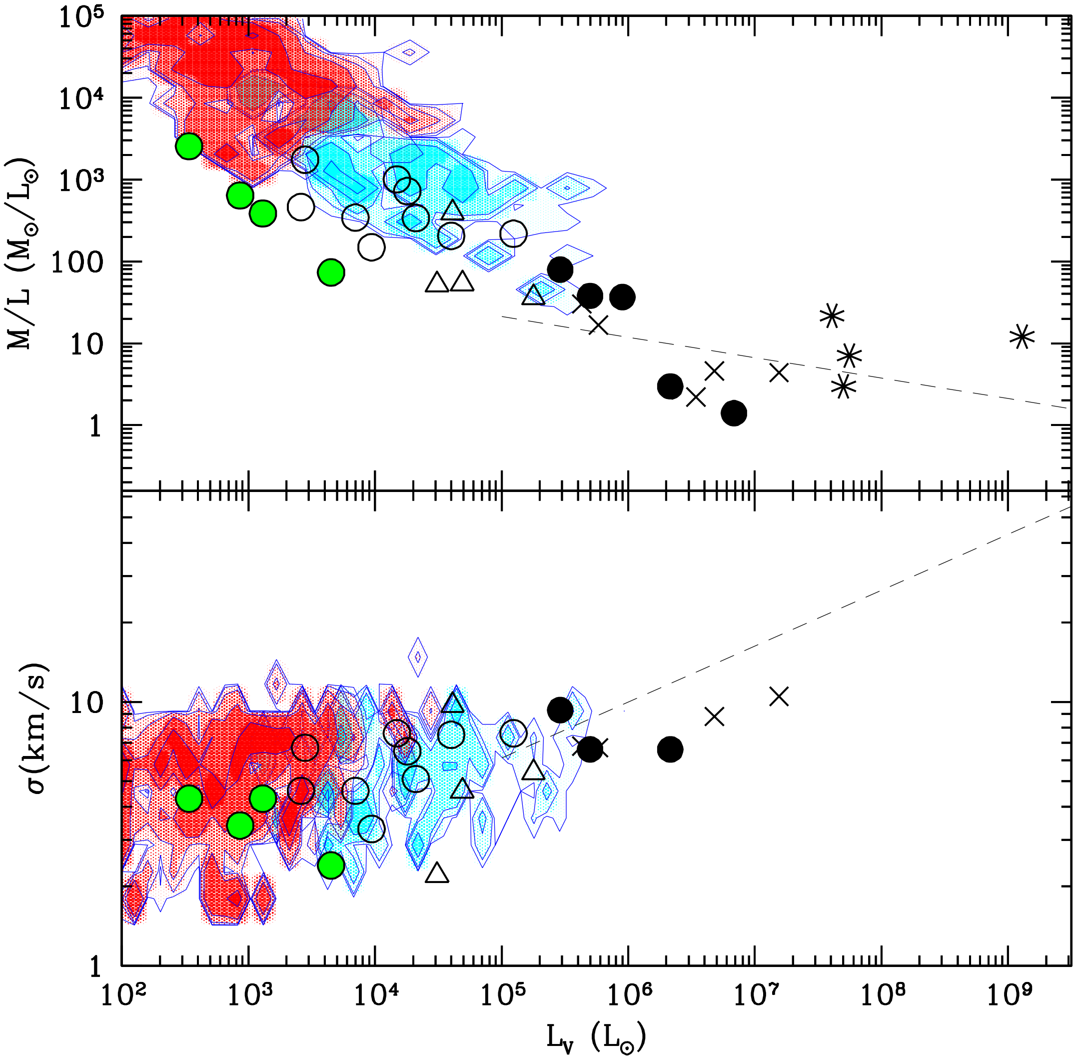

Figure 4.2: The stellar mass to light ratios calculated from Illingworth (1976) and stellar velocity dispersons versus the V-band luminosities for Run D (blue contours) and observations (red symbols). Symbols are the same as in Figure 4.1. Once again, the dashed lines show the Kormendy and Freeman (2004) trends for Sc-Im galaxies with $10^8 L_\odot < L_B < 10^{11} L_\odot$.

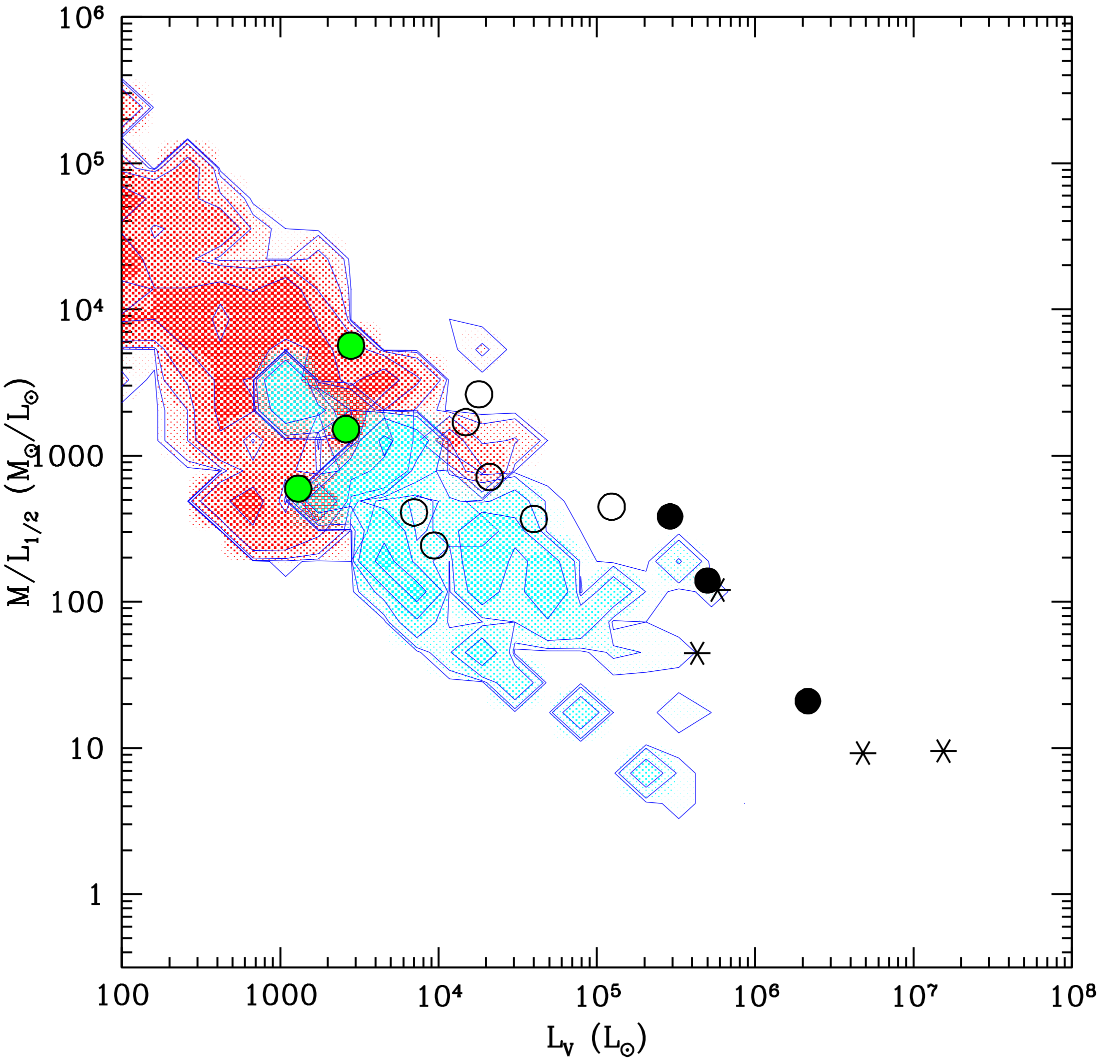

Figure 4.3: The $M/1/2L_V$ versus $1/2L_V$ using the Walker et al. (2009) mass estimator.

shown as the top and bottom of in Figure 4.2. As in Figure 4.1, the five dwarfs which do not match the r_{hl} of the simulated fossils are marked with filled green circles. Excepting this subpopulation, the ultra-faints show the same distribution as the simulated true fossils for both M/L and stellar velocity dispersions. In the left panel of Figure 4.2, the masses of our simulated halos are calculated from the stellar properties using Illingworth (1976). The right panel shows the mass to light ratios inside the half-light radii, $M/L_{1/2}$ versus half the V-band luminosity using the Walker et al. (2009) mass estimator. The latter mass estimator is more accurate for dispersion supported systems, but we note that the agreement between the mass to light ratios of our fossils and ultra-faint dwarfs is independent of the mass estimator we use to calculate $M(\sigma_*, r_{hl})$. As expected, the undetected dwarfs (red contours in Figure 4.2 & 4.3) would have $M/L > 10^3 M_\odot/L_\odot$, higher than even the most dark matter dominated ultra-faint dwarfs. However, the range of their stellar velocity dispersion is $2 - 10$ km s^{-1}, equivalent to the ultra-faint dwarfs and detectable fossils, and shows no evolution with decreasing luminosity.

As seen in the left panel of Figure 4.4 & 4.5, the mass function of the detected fossils peaks at $10^8 M_\odot$ while the undetected fossil peak at $5 \times 10^7 M_\odot$. Note, however, that this mass function is for the total dark matter mass, not the dynamical mass calculated from the velocity dispersion and half-light radius. Our simulations provide us with the information needed to plot a mass function of the dynamical mass, referred to in the right panel of Figure 4.4 & 4.5 as the derived mass. For the observed mass function both the detected and undetected fossils peak at $2 \times 10^7 M_\odot$. This peak corresponds to the 'common mass scale' for dwarf spheriodals (Strigari et al. 2008), however, no such sudden peak is seen in the dark matter mass function. The difference is due to the stochastic star formation in the first galaxies (Ricotti et al. 2008), two dwarfs may have stellar population of the same stellar velocity dispersion and extent, producing the dynamical mass, but those populations can be embedded within halos whose masses vary by an order of magnitude. As discussed in § 2.1.1, while the more massive halo's population is concentrated at the center of its potential, the lower mass halo's stars fill a larger fraction of its dark matter halo.

More specifically, the lower limit in dwarf size of $r_{hl} \sim 100$ pc can be understood by the following. In low mass dark halos cooling is very inefficient. Since the temperature of the ISM in these galaxies remains near the virial temperature after reionization, their gas is more extended during fragmentation and star formation, with the ratio of the temperature of the ISM to the virial temperature setting the outer most stellar radius. Inefficient cooling produces a higher ratio, and the closer T_{ISM}/T_{vir} is to one, the more extended the dwarf's stellar population will be. In hydrostatic equilibrium, the gas density profile of a NFW halo can be described by the beta-model (Makino et al. 1998) with a core radius $r_c \sim 0.22 R_{vir}/c$, where c is the halo concentration and $c \sim 4$. Before stars form, the gas density inside the core radius is $> 100\ cm^{-3}$ and drops as $\propto r^{-3}$ outside of the core radius. To use some numbers, the typical virial radii of the least luminous fossils in these simulations at $z = 0$ is 10-15 kpc, and given $c \sim 4$, $r_c \sim 0.07 R_{vir}$, a core radius of $\sim 70 - 120$ pc. Thus, star formation can extend to a decent fraction of the virial radius in small halos, roughly to $r_{hl} \sim r_c \sim 100$ pc (the pre-reionization simulations use $\rho_* \propto \rho_{gas}^{1.5}$). The net effect of this is that r_{hl} remains nearly constant as a function of the mass, in the first small mass halos. Galaxy-galaxy interactions and merges can increase r_{hl} above the minimum values set by the structure of the ISM in primordial galaxies. For more massive halos, r_c becomes a smaller fraction of R_vir because gas cooling is more efficient, and the ISM in larger galaxies cools rapidly to values below the virial temperature.

For the metallicity distribution, we also use a luminosity weighted average:

$$[Fe/H]^f = log(\sum 10^{[Fe/H]^i} \times L_V^i) - log(L_V^f). \tag{4.4}$$

The distribution of metallicity versus L_V is shown for our $z = 0$ fossils and the known ultra-faint and classical dwarfs. As in Chapter 2, the fossil metallicities from Run D are consistent with the observed distribution for the ultra-faint and classical dSph. We also find our results for $L_V > 10^4 L_\odot$ to be in agreement with

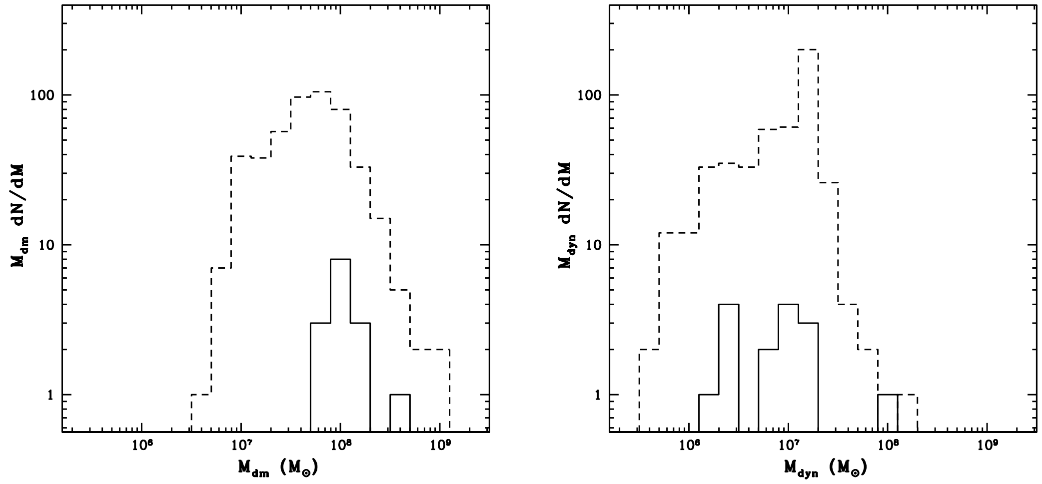

Figure 4.4: *Left* : The mass function of the detected (solid) and undetected (dashed) fossils with $L_V > 10^2 L_\odot$ within 1 Mpc of MW.3 from Run D. *Right* : Same as the left panels except the x-axis is the dynamical mass inside the half light radius (Walker et al. 2009) calculated from the velocity dispersion and half-light radius of our fossils.

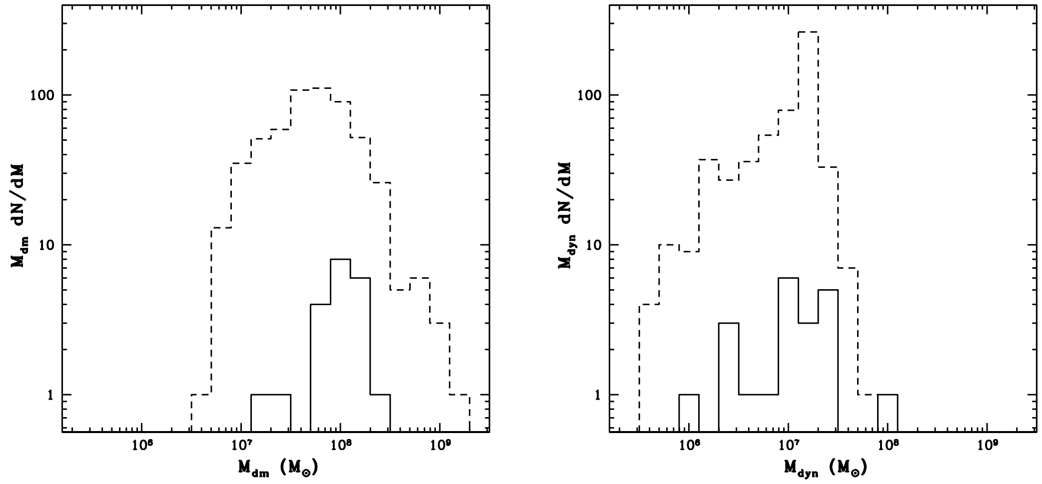

Figure 4.5: *Left* : The mass function of the detected (solid) and undetected (dashed) fossils with $L_V > 10^2 L_\odot$ within 1 Mpc of MW.2 from Run D. *Right* : Same as the left panels except the x-axis is the dynamical mass inside the half light radius (Walker et al. 2009) calculated from the velocity dispersion and half-light radius of our fossils.

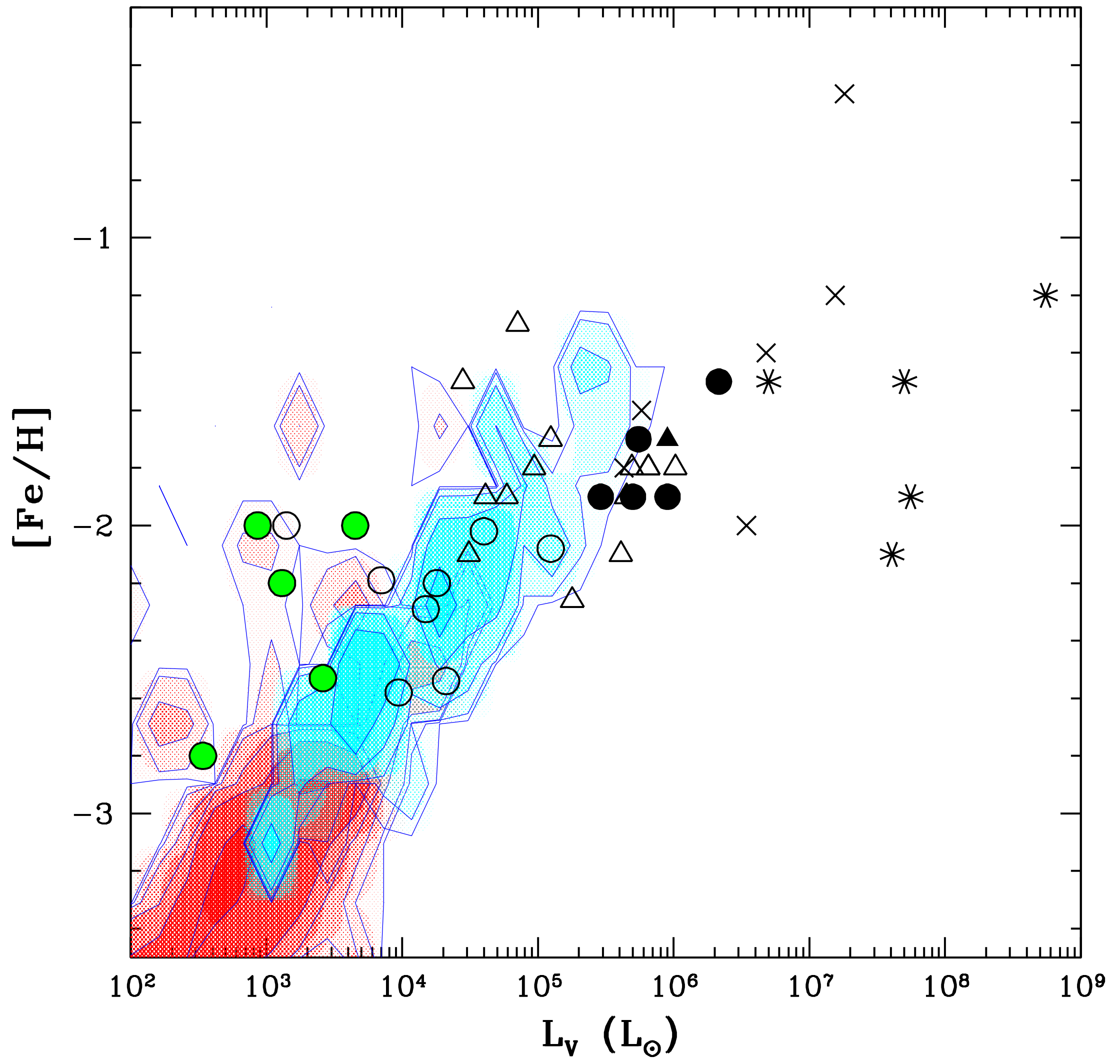

Figure 4.6: The [Fe/H] distribution for the true fossils plotted against the V-band luminosities for Run D (blue contours) and observations (red symbols). Symbols are the same as in Figure 4.1. Our results agree with Salvadori and Ferrara (2009) for $L_V > 10^4$.

Salvadori and Ferrara (2009) while for the dimmest fossils our work finds comparatively lower metallicities. The undetected dwarfs (red contours in Figure 4.6) have $[Fe/H] < -2.5$ and as low as -3.5 with slightly larger scatter than their detectable counterparts.

The maximum circular velocity versus L_V contours for our simulated true fossils are shown in Figure 4.7 to illustrate the following. While v_{max} does decrease by approximately a factor of two over four decades of luminosity, the scatter in v_{max} at a given L_V is large. Though a halo with $v_{max} < 6$ km s^{-1} is likely to have a $L_V < 10^4 L_\odot$, there is, at most, a minimal trend of decreasing v_{max} with decreasing luminosity for the primordial fossils. This highlights a theme across all our stellar property comparisons. Because of the strong dependence of their stellar properties on stochastic feedback effects, there is no baryonic property that shows a strong trend with maximum circular velocity and the size of the dark matter halo.

We now briefly discuss the M31 satellite population. Figure 4.8 shows the σ_* plotted against r_{hl} on a similar scale to the top left panel of Figure 18 in Collins et al. (2010). The circles show the Milky Way dSphs, while the triangles show the dSphs associated with M31. We find that four of the six M31 dSphs plotted are within, albeit at the edges of, the contours of detectable true fossils. Like their Milky Way counterparts, the new M31 dSphs show reasonable agreement with our simulated primordial fossils excepting of r_{hl}, which are higher than expected by our simulations for two of the M31 dwarfs. However, this does not represent a major problem for our model since $\sim 65\%$ of simulated true fossils with $L_V > 10^4 L_\odot$ have undergone one or more major mergers that may have puffed up their stellar populations. Our estimates do not account for extra heating of the stellar populations by the kinetic energy of the collision. A higher σ_* would result in a more extended stellar population in the same mass halo. We will discuss the comparison between the M31 dSphs and our simulated fossil dwarfs in an upcoming paper.

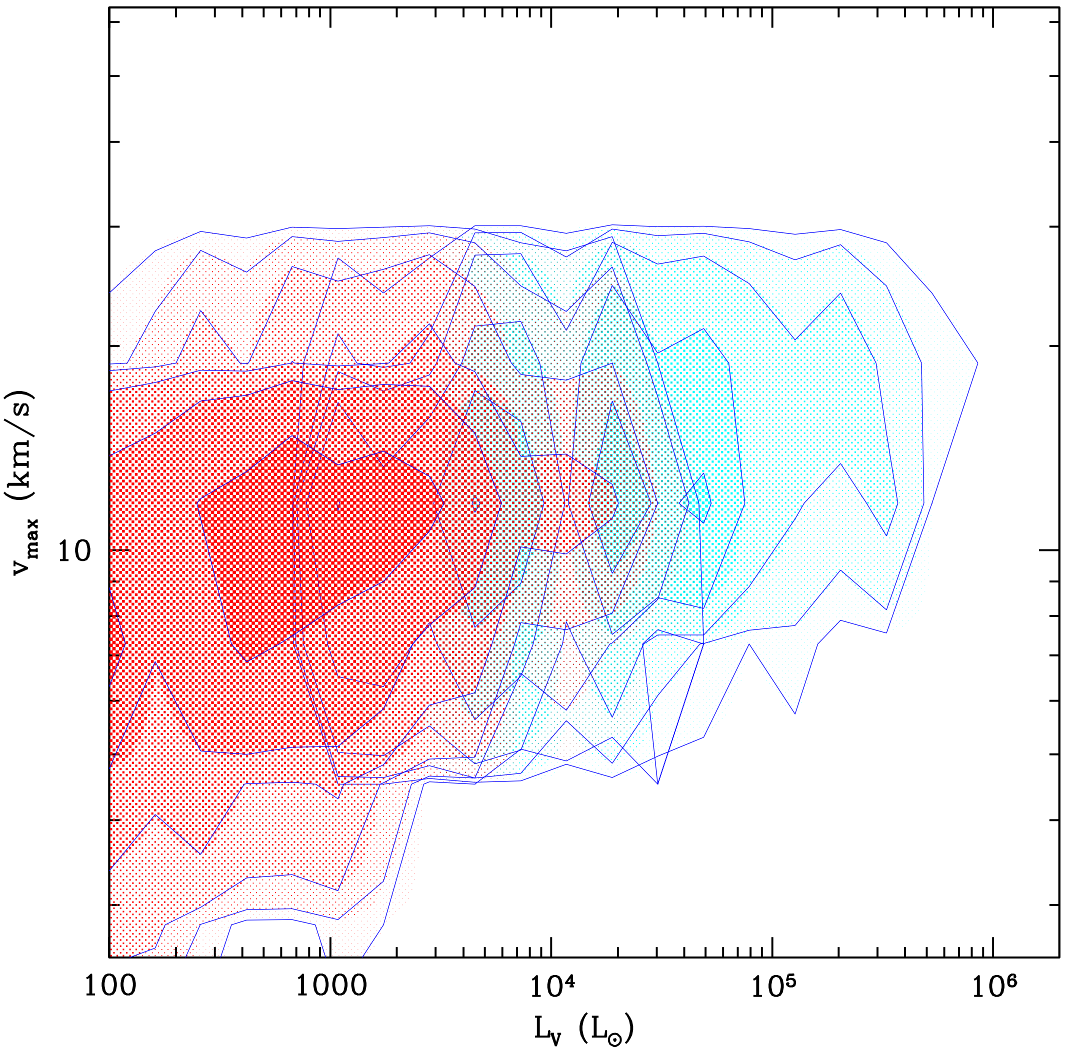

Figure 4.7: The maximum circular velocity, v_{max} of our simulated true fossils plotted against the V-band luminosities. The cyan and red contours are the same as in Figure 4.1. Here we show no observed dwarfs due to the lack of data.

4.1.1 The Inner Ultra-Faints

In this section, we discuss a possible origin scenario for the inner ultra-faint dwarfs, ie. the ultra-faints whose half light radii and mass to light ratios are lower than our true fossils. These dwarfs are, Segue 1 and 2, Leo V, Pisces II and Willman 1, and excepting Leo V and Pisces II (both at ~ 180 kpc) all are within 50 kpc of the

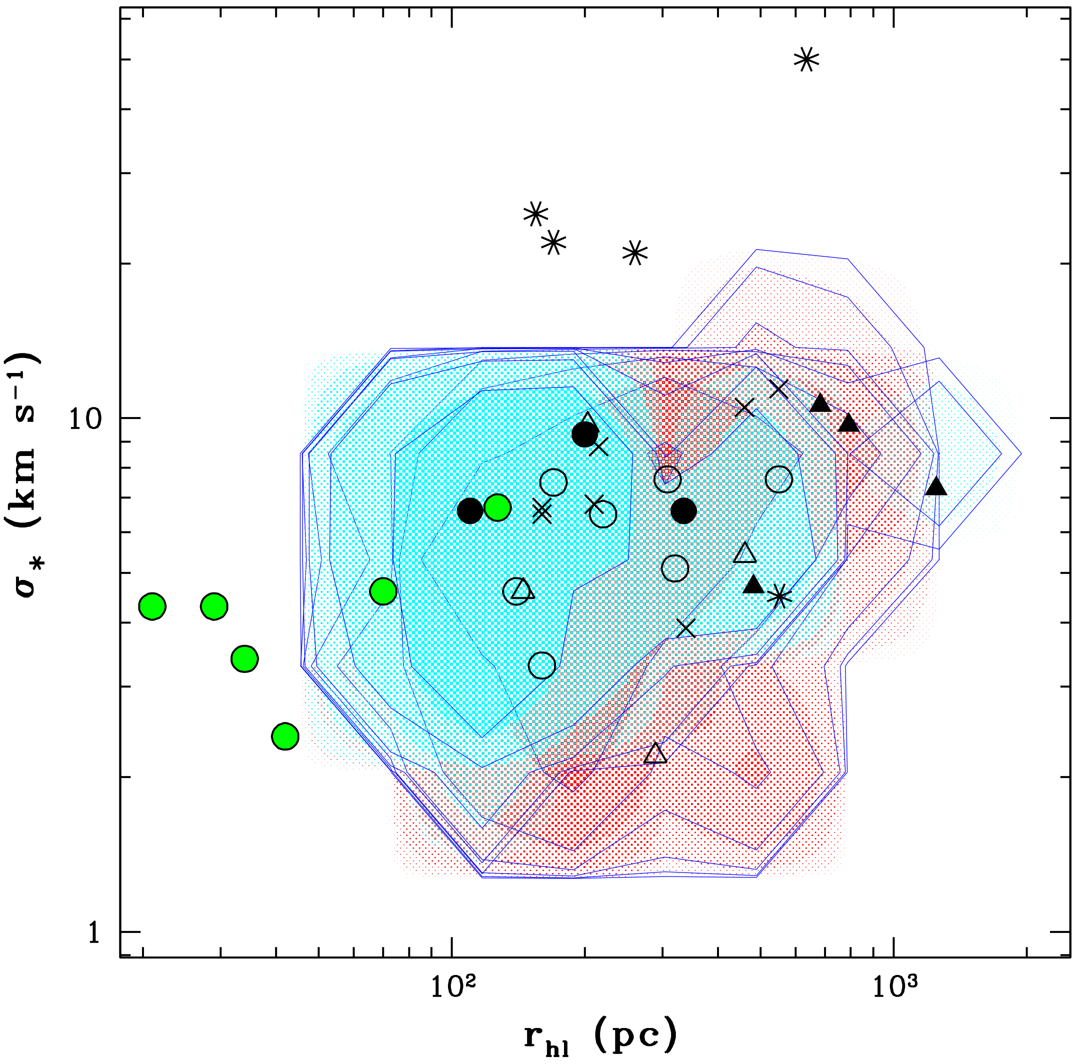

Figure 4.8: The stellar velocity dispersion, σ_* against the half-light radius, r_{hl}. The black symbols are the observed dwarfs and blue and red contours from Run D have the same meanings as in Figure 4.1.

Milky Way.

However, their mass to light ratios follow a shifted power law with a similar slope to the true fossils and more luminous dwarfs. The stellar velocity dispersions are in the range expected for primordial fossils, but the inner ultra-faints show an $L_V - \sigma_*$ combination which would be expected for true fossils below the detection limits of SDSS (red contours on Figure 4.2). These properties are either directly affected by

	$R < 50$ kpc	$R > 50$ kpc
Inconsistent	Segue 1 Segue 2 Willman 1	Pisces II * Leo V *
Consistent	Coma Ber.	Bootes I & II CVn I & II Hercules Leo IV & Leo T Ursa Major I

Table 4.1: Table of Milky Way ultra-faint dwarfs classified by their distance from our galaxy (columns) and whether or not they are consistent with our predictions for the fossils of the first galaxies (row). Note the correlation between distance and consistency. (*) Pisces II and Leo V are both on the lower end of radii expected for fossils, as such they are marked as "inconsistent," but are not as far from predictions as the "inconsistent" ultra-faints within 50 kpc.

tidal stripping (r_{hl} and σ_*) or are derived from affected properties (Σ_V and M/L). However, the metallicity of the stars is not affected by tidal stripping.

Figure 4.6 shows the metallicities of the inner ultra-faint dwarfs do not fall on the luminosity-metallicity relation. However, their scatter is consistent with expectations for true fossils. To place the Segues, Leo V, Pisces II and Willman 1 on the luminosity-metallicity relation traced by the majority of the ultra-faints and our fossils, their luminosities would need to be increased by one to two orders of magnitude. We suggest these dwarfs may be a subset of bright primordial fossils which have been stripped of $90\% - 99\%$ of their stars.

4.2 Baryonic Tully Fisher Relation

In § 4.1 we demonstrated good agreement between the properties expected of primordial galaxies and those observed for a subset of the new ultra-faint dwarfs. We now extend that comparison to the baryonic Tully-Fisher (BTF) relation. The baryonic Tully-Fisher relation is a relatively tight correlation between the rotation

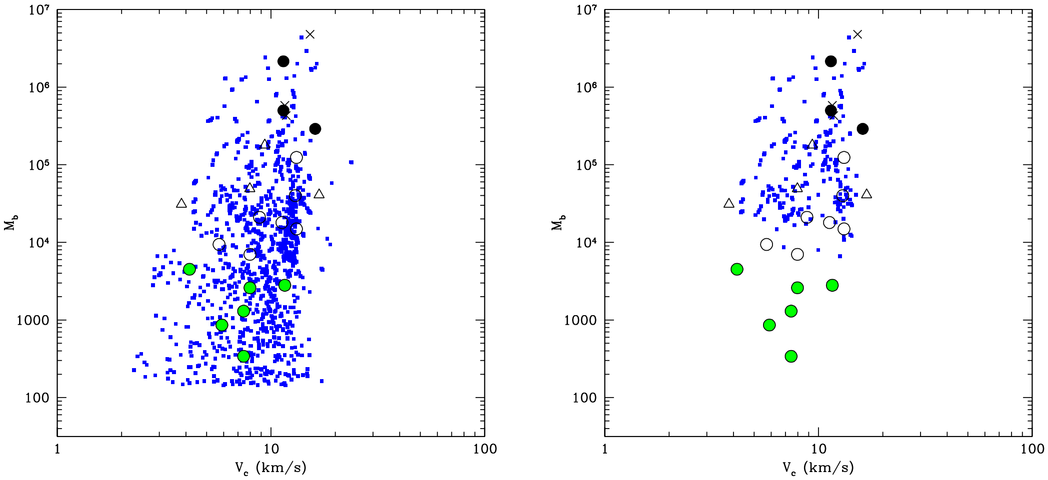

Figure 4.9: (*Left*) : The baryonic Tully-Fisher relation for the observed dwarfs (same symbols as FIgure 4.1) and our simulated fossils (blue points). In this panel we show all the simulated fossils regardless of their detectability by the SDSS. (*Right* : The BTF, except we show only the simulated fossils with $\Sigma > 10^{-1.4} L_\odot$ pc^{-2} (Koposov et al. 2008).

velocity or velocity dispersion of a galaxy and its total baryonic mass which extends from disk galaxies to dwarfs with $V_c = \sqrt{3}\sigma_* = 20$ km s^{-1} (McGaugh et al. 2000; Stark et al. 2009; Trachternach et al. 2009; Verheijen 2001). However, when the Local Group dSphs are plotted on the BTF they do not continue the correlation to lower V_c, instead deviating by up to two orders of magnitude in baryonic mass (McGaugh and Wolf 2010). We now investigate whether the stochastic star formation in the primordial model can reproduce the scatter in the baryonic Tully-Fisher relation seen for the smallest galaxies McGaugh and Wolf (2010).

Figure 4.9 shows the baryonic Tully-Fisher relation for the observations (black and green symbols) and our simulated fossils (blue squares). The left and right panels show all of the fossils and only those with $\Sigma_V < 10^{-1.4} L_\odot$ p^{-2} (Koposov et al. 2008), respectively. Note, that since we can only work with the primordial galaxies produced in the pre-reionization simulations we have a discrete sampling of the fossil properties. This is particularly true for the 75% of fossils which are not the result of one or more galaxy mergers between pre-reionization dwarfs.

We find that we are able to reproduce the scatter of the baryonic Tully-Fisher at $V_c < 20$ km s^{-1} well. However, when we only include the detectable fossils, the inner ultra-faints (green circles) are completely inconsistent with our predictions, more so when we include any other set of properties we have plotted thus far.

McGaugh and Wolf (2010) explored whether the large scatter in the baryonic Tully-Fisher at low masses was correlated with any other properties. To do this, they used the baryonic Tully-Fisher residual, M_b/M_b^{BTF}, where M_b^{BTF} is the expected baryonic content of a halo if it fell directly on the relation. We next see if any of their trends can be reproduced by our fossil population. We look at the BTF residual versus L_V (Figure 4.10), $[Fe/H]$ (Figure 4.11), $V_c = \sqrt{3}\sigma_*$ (Figure 4.12), r_{hl} (Figure 4.13), and galactocentric distance (Figure 4.14). In Figures 4.9 to 4.14, the left and right panels show all and only the detectable simulated fossils (blue squares), respectively.

In general, we are able to reproduce the observed trends quite well with a few exceptions. We are unable to reproduce the $M_b/M_b^{BTF} > 10$ seen for a few of the M31 ultra-faint dwarfs (opened triangles). The pre-reionization simulations do not produce objects which form stars at efficiencies above a few percent (Ricotti et al. 2008), making it unlikely that our model would produce objects which sit that high above the BTF relation.

A more critical discrepancy is the population of inner ultra-faint dwarfs (green circles). Throughout, they are either at the edge of (right panels of Figures 4.10 to 4.12) or clearly distinct from (right panels of Figures 4.13 and 4.14) the detectable fossils. This clearly distinguishes them from their larger, generally more distant counterparts. Note in Figure 4.14 that the M_b/M_b^{BTF} of our simulated fossils shows little evolution with galactocentric distance and the observed population follows this

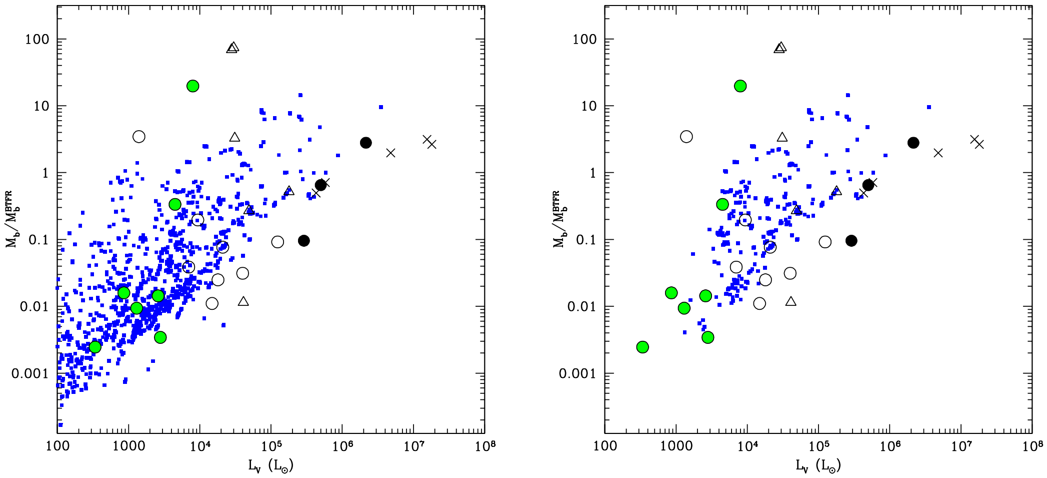

Figure 4.10: (*Left*) : The luminosity versus the residual of the BTF relation for the observed dwarfs (black symbols) and the simulated fossils (blue points). As in Figure 4.9, in this panel we show all of the simulated fossils. (*Right*) : Same as the left panel except with only fossils with $\Sigma > 10^{-1.4} L_\odot$ pc^{-2} (Koposov et al. 2008).

trend for $R \gtrsim 60$ kpc. The distinct properties of the inner ultra-faint dwarfs and the steep evolution of the BTF residuals with galactocentric distance supports the scenario postulated in § 4.1.1, that they are a population which either currently, or in the past has been strongly affected by tides.

4.3 A Note on Observations

As in Chapter 2, we approach the observations as follows. The majority of the information on the classical dwarfs comes from the Mateo (1998) review. For the ultra-faint dwarfs we generally defer to measurements with the smallest error bars with some weight given to more recent work (Wolf et al. (2010) and references therein). We direct the reader to § 2.1 for a more complete discussion of these criteria.

When calculating the observed distributions of dwarfs around the Milky Way, we account for two effects, the sky coverage of the SDSS, and its detection efficiencies

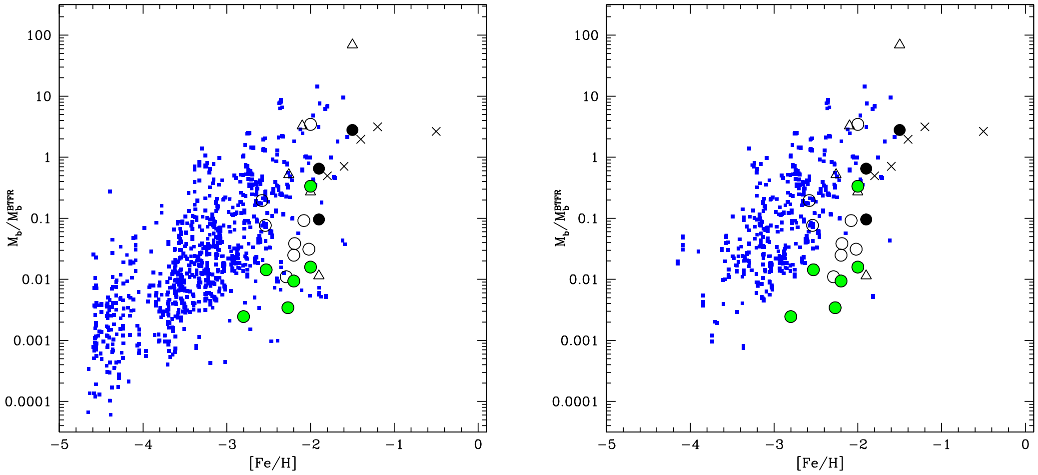

Figure 4.11: (*Left*) : The $[Fe/H]$ versus the residual of the BTF relation for the observed dwarfs (black symbols) and the simulated fossils (blue points). As in Figure 4.9, in this panel we show all of the simulated fossils. (*Right*) : Same as the left panel except with only fossils with $\Sigma > 10^{-1.4} L_{\odot}$ pc^{-2} (Koposov et al. 2008).

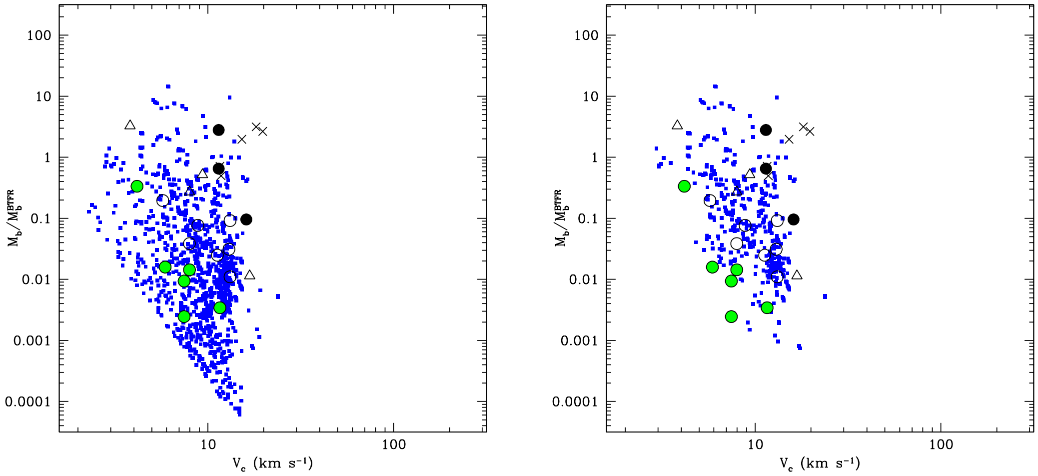

Figure 4.12: (*Left*) : The V_c versus the residual of the BTF relation for the observed dwarfs (black symbols) and the simulated fossils (blue points). As in Figure 4.9, in this panel we show all of the simulated fossils. (*Right*) : Same as the left panel except with only fossils with $\Sigma > 10^{-1.4} L_{\odot}$ pc^{-2} (Koposov et al. 2008).

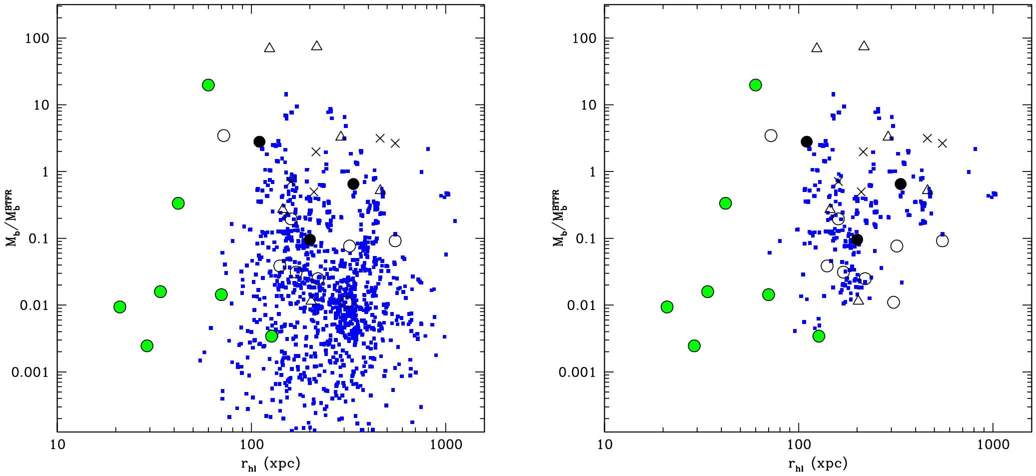

Figure 4.13: (*Left*) : The half-light radius, r_{hl}, versus the residual of the BTF relation for the observed dwarfs (black symbols) and the simulated fossils (blue points). As in Figure 4.9, in this panel we show all of the simulated fossils. (*Right*) : Same as the left panel except with only fossils with $\Sigma > 10^{-1.4} L_{\odot}$ pc^{-2} (Koposov et al. 2008).

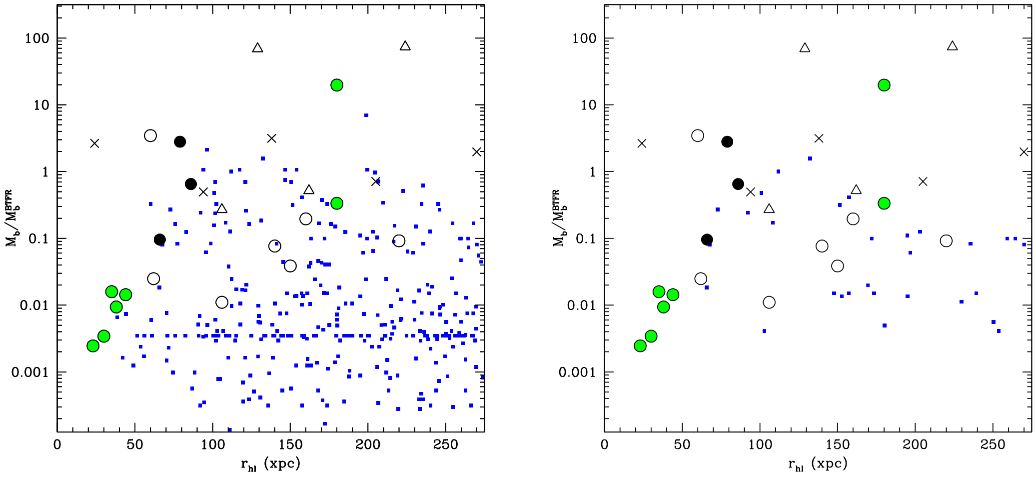

Figure 4.14: (*Left*) : The galactocentric versus the residual of the BTF relation for the observed dwarfs (black symbols) and the simulated fossils (blue points). In this panel we show all of the simulated fossils within 1 Mpc of MW.2 and MW.3. (*Right*) : Same as the left panel except with only fossils with $\Sigma > 10^{-1.4} L_{\odot}$ pc^{-2} (Koposov et al. 2008).

(Koposov et al. 2008; Walsh et al. 2009). For the classical dwarfs, we assume the entire sky has been covered and only apply sky coverage corrections to the ultra-faint population. To correct for the SDSS sky coverage, we assume that the satellite distribution around the Milky Way is isotropic, and multiply the number of ultra-faints by 3.54 to account for the nearly three-quarters of the sky not surveyed by SDSS, now past Data Release 7 (Abazajian et al. 2009).

Next, we apply a correction for the detection efficiency of the SDSS using the results from Walsh et al. (2009). If an ultra-faint is bright enough to be detected with 99% efficiency, we assume the sample is complete for that luminosity and distance. However, if the ultra-faint is too dim for 99% detection, but bright enough to be detected half the time, we assume that, statistically, there is another satellite with similar luminosity and distance missed by SDSS. This second correction produces only a minor increase in the number of satellites; approximately one additional satellite over a total of ~ 60 from sky coverage correction alone. We also use a correction factor of 2.0 to approximate a plane of satellites (Kroupa et al. 2005; Metz et al. 2007, 2009; Zentner et al. 2005) and explore the dependence of our conclusions on the assumption of an isotropic distribution of satellites.

As discussed in § 4.1.1, we also divide the ultra-faint dwarfs into two groups. The first is a group of seven, including CVnI and II, Coma Ber., Hercules, Leo IV, Leo T, and Ursa Major I and II, which have half light radii and surface brightnesses which are consistent with the stellar properties of fossils of the first galaxies. In contrast, the second group composed of five members, including Willman 1, Segue 1 and 2, Leo V, and Pisces II, have half light radii which are too small, and surface brightnesses which are too high, to be consistent with the simulated primordial population. Excepting Leo V and Pisces II, all the satellites in the later group are within 50 kpc of the Milky Way. We note that in addition to their larger distances, Leo V and Pisces II sit significantly closer to our predictions for primordial fossils than the Segues and Willman 1. We will refer to this second population collectively as the "inner ultra-faints," to emphasize their placement around our galaxy.

Though we are agnostic about its status, Segue 1 may be an exception. Recent work (Martinez et al. 2010; Simon et al. 2010) suggests that its stellar population has remained well within its tidal radius (thus tides are not important) and its stars are unaffected by interactions with the Milky Way. However, other work suggests that Segue 1 is a highly disrupted star cluster or dwarf (Niederste-Ostholt et al. 2009; Norris et al. 2010b). We note that, *if* Segue 1 is an undisrupted dwarf, the high concentration which has protected Segue 1's stars also identifies it as a rare object formed in a high sigma peak at high redshift. The 1 Mpc^3 volume of our pre-reionization simulations does not represent a large enough volume to contain a Segue 1. If Segue 1 is an undisrupted dwarf, than yes, if there are more than one or two additional Segue 1 like objects in the Milky Way halo it is a problem for our model that produces larger half-light radii than Segue 1's. However, if Segue 1 is disrupting then (i) we would not expect to see objects of that type beyond ~ 100 kpc from the Milky Way, and (ii) the presence of additional Segue 1 objects would not pose a problem.

The ultra-faint dwarfs in the first group, and the classical dSph mentioned in Ricotti and Gnedin (2005) are the best candidates for an observed population of primordial fossils, with stellar spheroids not significantly modified by tides. However, as noted in Chapter 3, classical dwarfs with $L_V > 10^6 L_\odot$ are too bright to be hosted in halos with $v_{max} < v_{filter}$ for $v_{filter} = 20$ km s^{-1} or 30 km s^{-1}. While they may have formed most of their stars before reionization, we exclude them from our comparison to be as conservative as possible.

Throughout this work, we compare the observed Milky Way satellites to our luminous $z = 0$ halos with $\Sigma_V > 10^{-1.4}$ L$_\odot$ pc^{-2}. We are also able to use our simulations to study the distribution of a hereto undetected population of ultra-faints with $\Sigma_V < 10^{-1.4}$ L$_\odot$ pc^{-2} and $L_V \lesssim 10^4$ L$_\odot$. The possible existence and undetectability of this population was first noticed in Chapter 2, from the analysis of RG05 simulations (see also Ricotti 2010 for a review). However, using independent arguments, Bullock et al. (2010) have also proposed the existence of this population they refer to as "stealth galaxies."

4.4 Fossil Distribution

In this section, we compare the distributions of non-fossils and true-fossils to the galactocentric radial distribution of the observed Milky Way satellites. We first compare the galactocentric radial distributions of our simulations to observations. We then make detailed comparisons between the observed cumulative luminosity function of the Milky Way satellites and the simulated cumulative luminosity functions of our non-fossil and true fossil populations. Note, that our simulated cumulative luminosity functions only include stellar populations formed before reionization. Therefore, we refer to our simulated cumulative luminosity functions as primordial cumulative luminosity functions. Any star formation that may take place in halos with $v_{max} > v_{filter}$ after reionization is not accounted for in our simulated luminosity functions. Thus, only the cumulative luminosity function of true fossils can be directly compared to observations, while the luminosities of the non-fossils are lower limits.

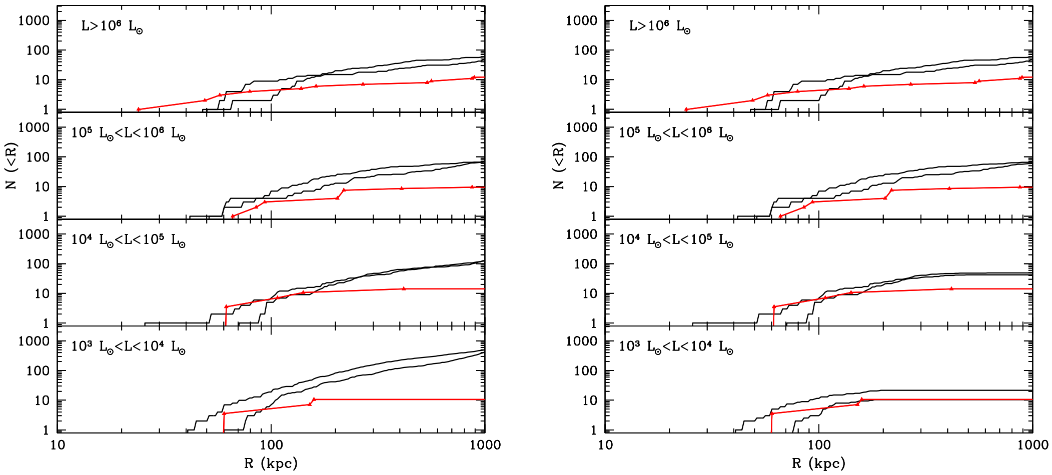

Figure 4.15: *Left* Galactocentric radial distribution of all simulated satellites for MW.2 and MW.3 from Run D (black curves) compared to the radial distribution of all observed Milky Way satellites (red triangles). We have included all simulated subhalos and known satellites regardless of their classification or whether they are detectable. *Right* Same as the left panel but we have convolved our populations with Walsh et al. (2009) detection limits and only included simulated subhalos which can be detected in the SDSS data.

4.4.1 Radial Distribution of Fossils Near Milky Ways

Figure 4.15 shows the galactocentric radial distribution of all the simulated and observed Milky Way satellites. In the left panel of Figure 4.15, we compare observations to simulations without correcting for the sensitivity limits of the SDSS (Koposov et al. 2008; Walsh et al. 2009) or whether a satellite is a fossil. In the right panel, we show all the satellites again, now applying the Walsh et al. (2009) limits to the simulated halos around MW.2 and MW.3. Figure 4.16 shows the galactocentric radial distribution for only the observed and simulated *fossils*. As in Figure 4.15, the right and left panels show the simulated true fossils with and without the Walsh et al. (2009) corrections. The observational and theoretical fossil definitions are discussed in § 3.2.4. Our simulations do not account for tidal stripping of stars, and do not reproduce the properties of the inner ultra-faint dwarfs, and we do not include them in Figure 4.16.

The left panels of Figures 4.15 and 4.16 show that at $L_V \sim 10^5 L_\odot$ the fossils become a significant fraction of the satellite population, with fossil dominance increasing as satellite luminosity decreases. This is further illustrated in Figure 4.18, which shows the fraction of subhalos which are fossils, N_{fos}/N_{all}, as a function of distance from the host for the same luminosity bins as Figure 4.16, excepting $L_V > 10^6 L_\odot$. We find that for $10^5 L_\odot < L_V < 10^6 L_\odot$ bin, the fraction of fossils is 0.05-0.1, with the fraction decreasing as host halo mass increases. For the lower luminosity bins, N_{fos}/N_{all} converges to $40-50\%$ and $70-80\%$ for $10^4-10^5 L_\odot$ and $10^3-10^4 L_\odot$ bins, respectively. If we include the inner ultra-faints in our galactocentric radial distributions, we find a significant overabundance of observed dwarfs within 50 kpc of the Milky Way. The stellar properties of the inner ultra-faint dwarfs do not agree with the simulated stellar properties of the fossils. As discussed in § 4.1.1, and § 4.3, we argue the majority of these objects may represent a population of tidally stripped remnants of once more luminous dwarfs. A possible exception, Segue 1, is discussed in § 4.3. Our simulations are also unable to reliably resolve $z = 0$ halos within 50 kpc of the Milky Way. We therefore have excluded anything with $R < 50$ kpc from our comparisons.

Without the ultra-faints with $R < 50$ kpc, the right panels of Figures 4.15 and 4.16 show good agreement between the simulated satellite distributions of the true fossils around MW.2 and MW.3 and the observed Milky Way galactocentric radial distribution. When we convolve our simulated satellite populations with the limits from Walsh et al. (2009), we find that the agreement between the distribution of dwarfs around MW.2 and MW.3 and that observed around the Milky Way agree at all radii and luminosity bins for $L_V < 10^6 L_\odot$ (see right panel of Figure 4.16). We thus argue that, in addition to matching the stellar properties of the ultra-faints,

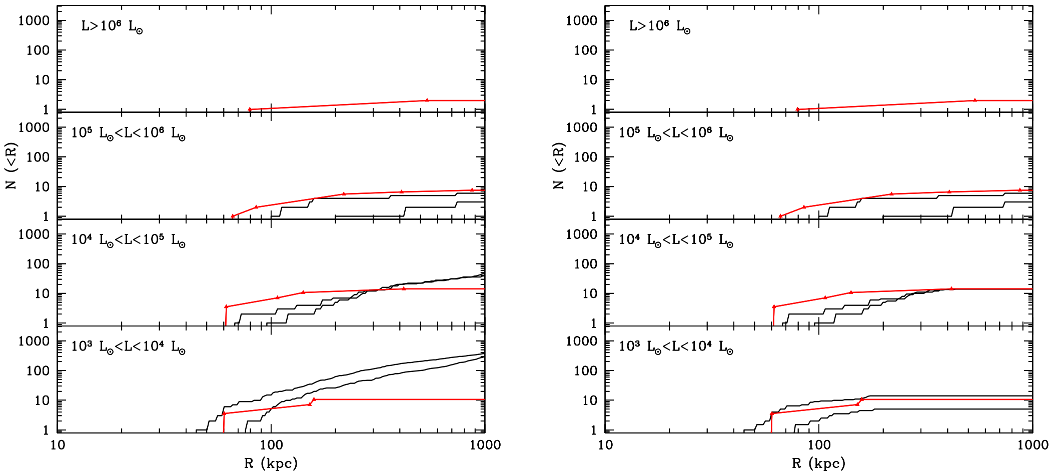

Figure 4.16: (*Left*) : Same as Fig. 4.15 but the observed satellite distributions only include bona fide fossils: the classical dSph which were designated fossils in Ricotti and Gnedin (2005) and the ultra-faints whose stellar properties match those of the simulated fossil population. Note that this excludes most of the ultra-faints within 50 kpc. In our simulated distributions we use $v_{filter} = 20$ km s^{-1} to define a fossil. We have included all simulated fossils, including those which would sit below the SDSS detection limits. (*Right*) : Same as the left panel but simulated radial distributions only include the true fossils which would fall within the Walsh et al. (2009) detection limits.

our simulated fossils also agree with their galactocentric radial distribution.

Figure 4.17 shows the galactocentric radial distribution of the *undetected* fossils in our simulations, after excluding detectable fossils according to the detection criterion from Walsh et al. (2009). We have not included the bins with $L_V > 10^5 L_\odot$ because there are no undetected fossils in this luminosity range within 1 Mpc of the Milky Way. In addition, all fossils with $L_V > 10^4 L_\odot$ are detected within 200 kpc. For the lowest luminosity fossils ($L_V < 10^4 L_\odot$) we find $\sim 400 - 500$ undetected dwarfs within 1 Mpc and 150 within 200 kpc. We have included a panel for the very low luminosity bin ($10^2 - 10^3 L_\odot$) to look at the distribution of the dimmest fossils which are invisible beyond a few tens of kpc. While the shape of the distribution in the lowest luminosity bins is similar, there are approximately two times fewer undetected fossils in the $10^2 - 10^3 L_\odot$ bin. Given that *fewer* of the fossils in this bin would be

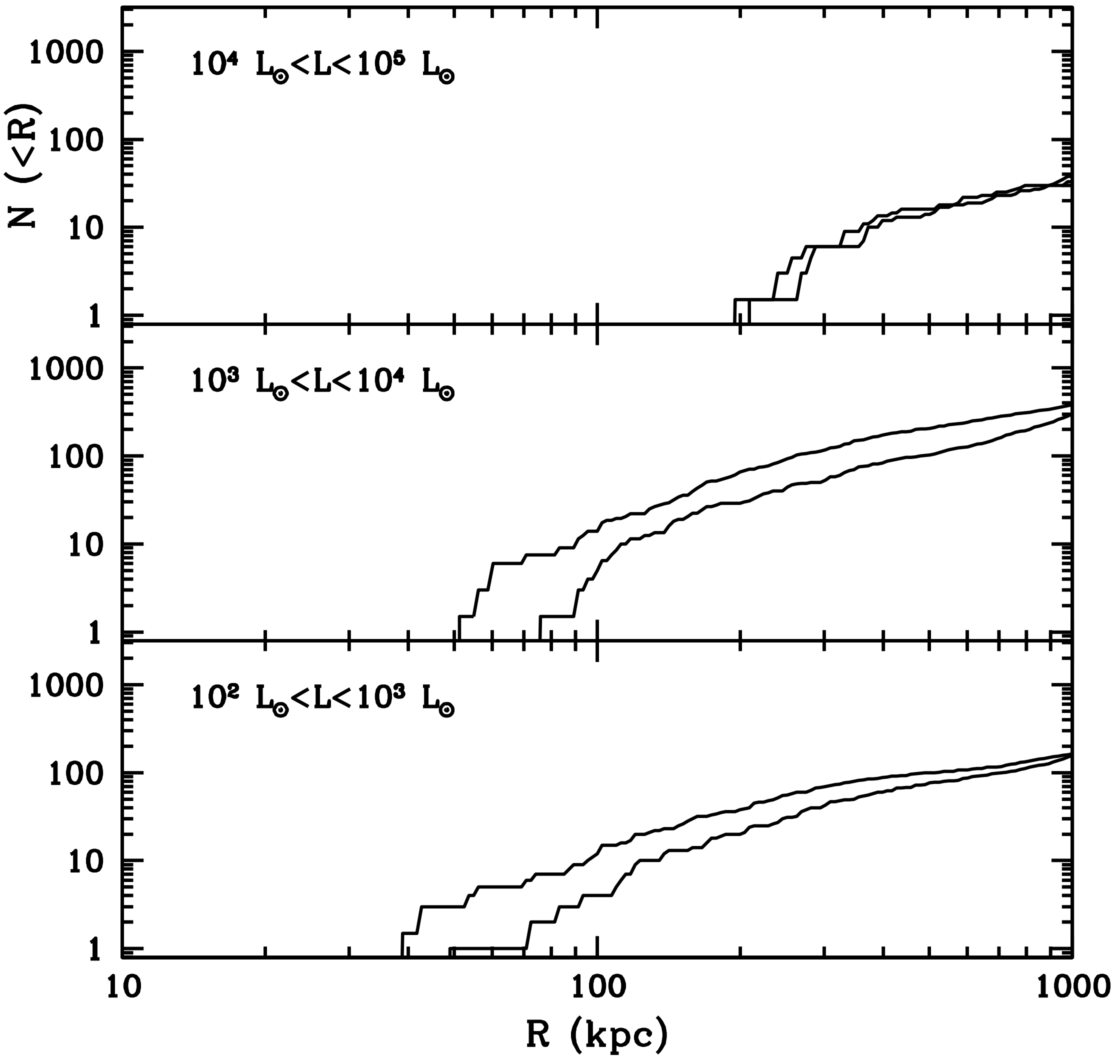

Figure 4.17: The galactocentric radial distribution of the fossils excluding the detectable dwarfs as determined by Walsh et al. (2009). Note that the bins have shifted down one order of magnitude in luminosity since there are no undetected fossils with $L_V > 10^5 L_\odot$ and we have included the distribution for the lowest luminosity fossils with $L_V < 10^3 L_\odot$.

detected compared to its higher luminosity counterpart, we are seeing the decline of star formation in the minihalos with the lowest mass. There are simply fewer $10^2 - 10^3 L_\odot$ pre-reionization fossils around the Milky Way than their $10^3 - 10^4 L_\odot$ counterparts.

On the other end of the luminosity function, the right panel of Figure 4.15 shows

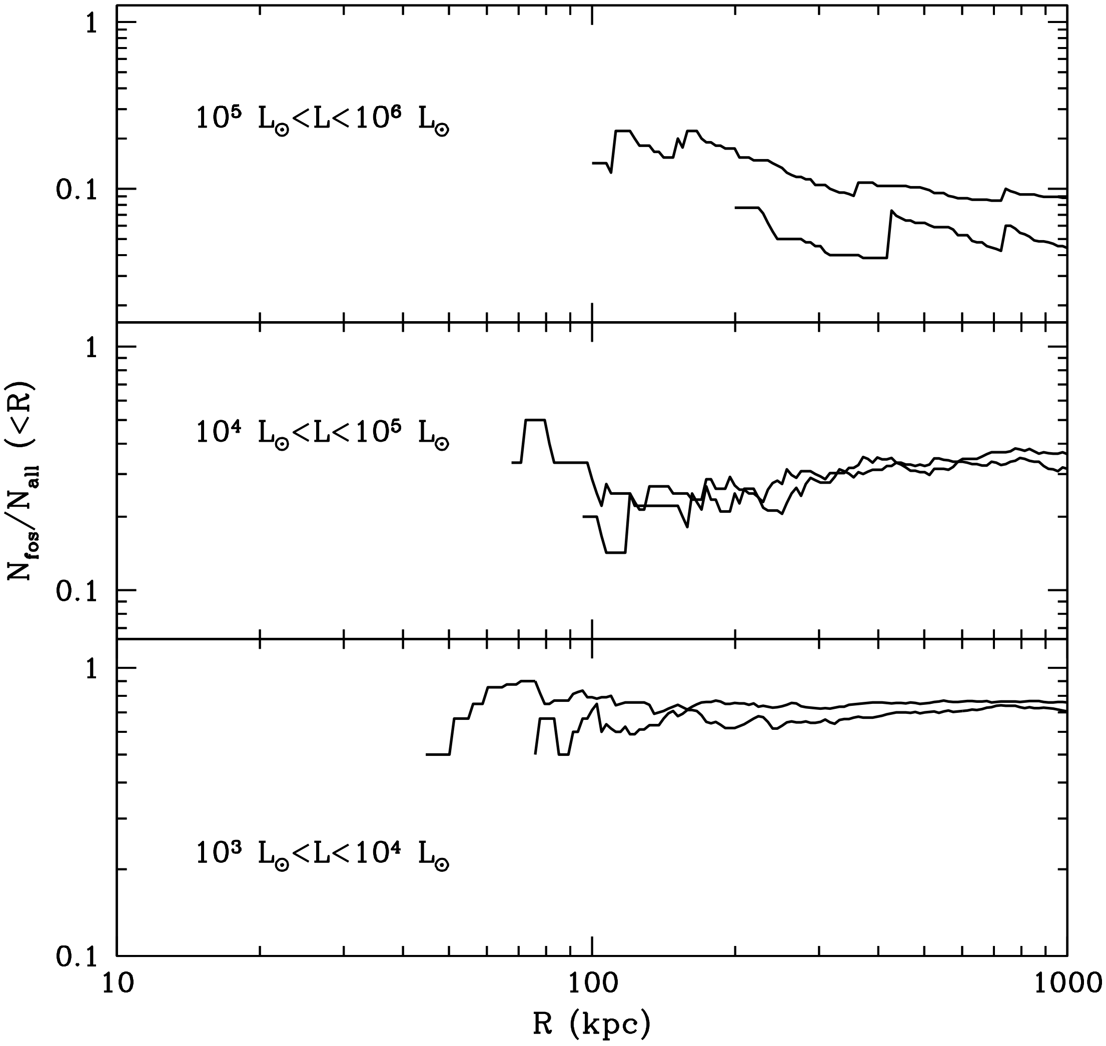

Figure 4.18: The galactocentric radial distribution of the fraction of luminous subhalos which are true fossils around MW.2 and MW.3 from Run D. They are divided in the luminosity bins from Figures 4.15 and 4.16 for which there is a fossil population ($L_V < 10^6 L_\odot$).

that while our simulated fossils are able to reproduce the ultra-faint distribution, we see too many bright ($L_V > 10^5 L_\odot$) satellites at $R > R_{vir}$, even after the Walsh et al. (2009) corrections are applied. This is the first evidence of an apparent discrepancy between simulations and observations we refer to as the "bright satellite problem." In the next sections, we will analyze this discrepancy, try to understand its origin, and whether it can be removed while maintaining the agreement of the simulations with observations at smaller radii and lower luminosities.

4.4.2 Primordial Cumulative Luminosity Functions

We next explore the fossil distribution and "bright satellite problem" from another angle via comparisons between simulated cumulative primordial luminosity functions and the observed cumulative luminosity function at different galactocentric distances from the Milky Way center. Results are equivalent for all three simulated Milky Ways and for both versions of our initial conditions. Therefore, for the remainder of this section and the next we will be discussing the results for MW.3 in Run D.

Each cumulative luminosity function in this paper is split into four radial bins to probe different regimes. We choose not to include the sample at $R < 50$ kpc, where the observational sample is the most complete, because tidal effects are prevalent and our simulations do not have sufficient resolution to determine whether or not pre-reionization halos stripped of their enveloping cloud of tracer particles have been tidally disrupted. The first bin we consider shows 50 kpc $< R <$ 100 kpc. The next bin out, the outer portion of the Milky Way halo from 100 kpc to 200 kpc, has observations which are fairly complete for $L_V > 10^4$ $L_\odot$, including the brightest ultra-faints. From 200 kpc to 500 kpc all but two of the ultra-faints (CVnI and Leo T) would be below the detection limits of the surveys and would not be visible. Roughly, this region corresponds to the virial radius ($R_{200} \sim 200$ kpc) to R_{50} for a Milky Way mass halo. Specific to our Local Group, this is the regime where M31 begins to play a significant role in the satellite counts, increasing the care required to separate the Milky Way and Local Group dwarfs from those bound to M31. The final radial bin, from 500 kpc to 1 Mpc, probes the transition region from the edge of the Milky Way halo to the surrounding filament and void. Subhalos at these radii

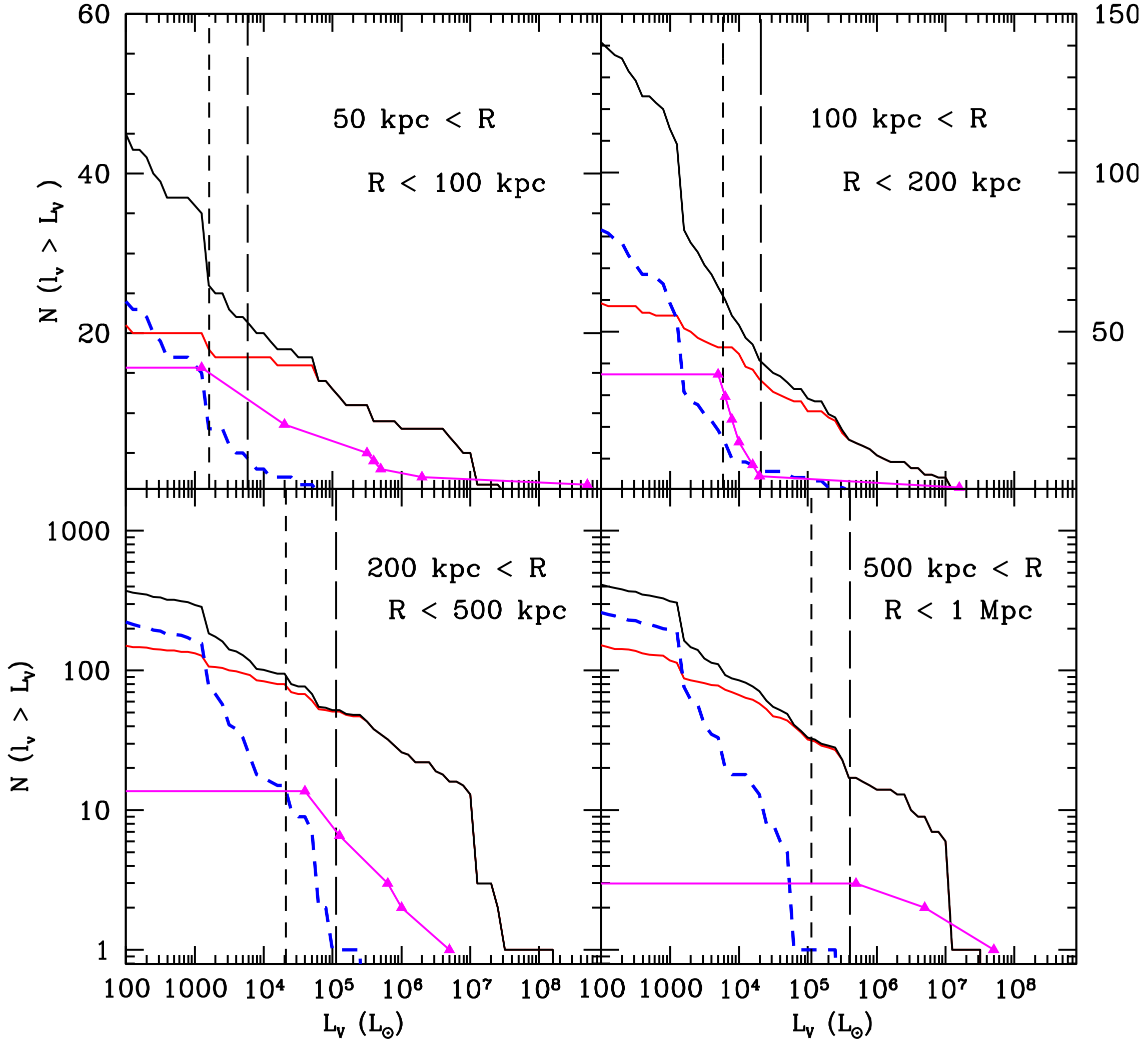

Figure 4.19: Cumulative primordial luminosity function of MW.3 from Run D with the observed luminosity function of Milky Way satellites. We have used a $v_{filter} = 20$ km s^{-1} to determine whether a simulated halo is a non-fossil or true fossil. We show the luminosity functions for four distance bins, 50 kpc$< R <$ 100 kpc (upper left), 100 kpc$< R <$ 200 kpc (upper right), 200 kpc$< R <$ 500 kpc (lower left), and 500 kpc$< R <$ 1 Mpc (lower right). In all distance bins the relevant populations are noted as follows. The solid black curves show the total cumulative luminosity function from our simulations, the red solid lines shows the same for only the star forming halos (non-fossils, including polluted fossils). We show the true fossil population with the blue dashed curve. The total observed population is shown as magenta triangles with the ultra-faint dwarf distribution corrected for sky coverage of the SDSS. The detection limits given in Walsh et al. (2009) are shown as vertical black, dashed lines. Long dashed for the luminosity limit for the outer radii and shorter dashes for the inner radii in a given bin.

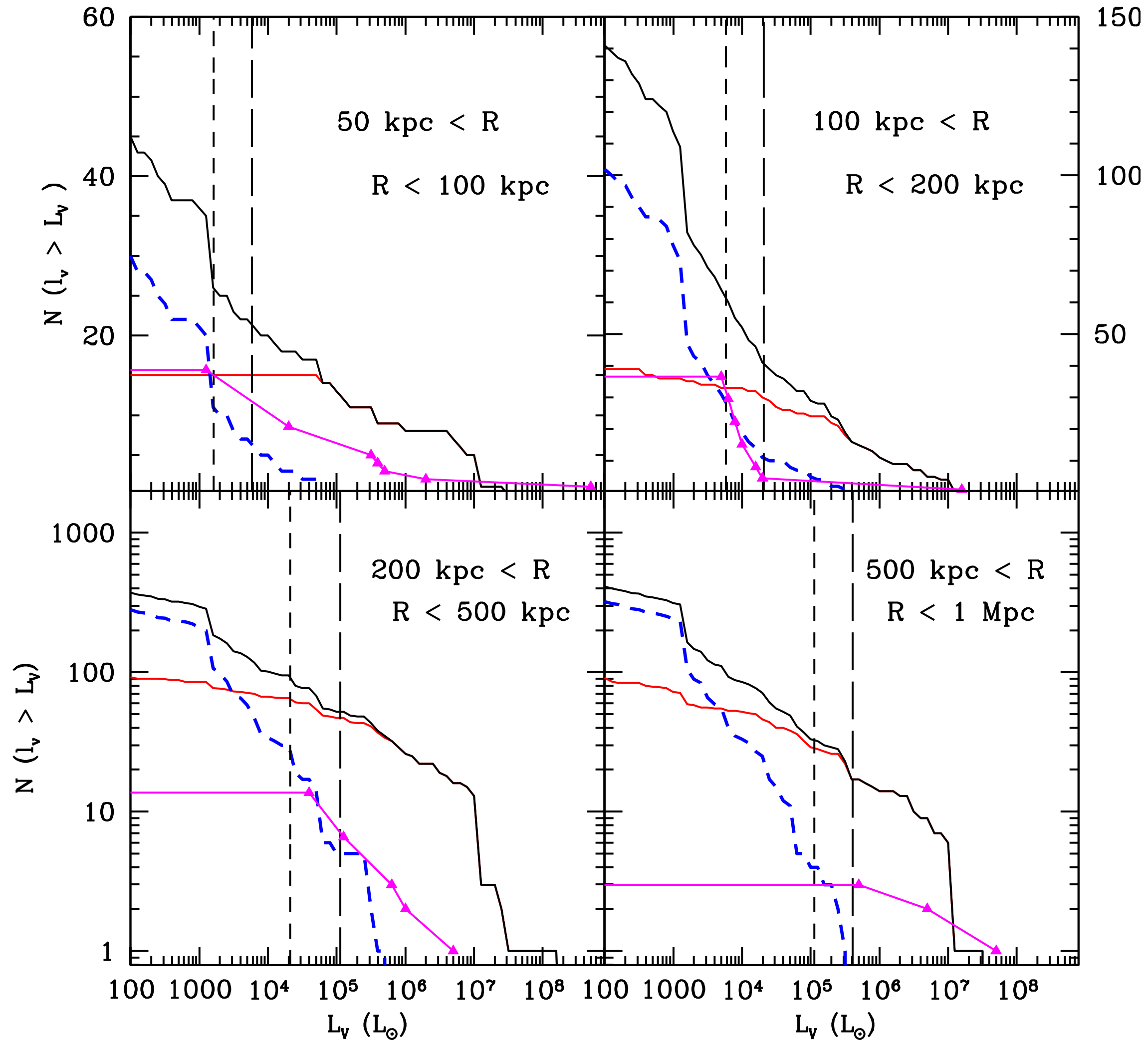

Figure 4.20: Cumulative primordial luminosity function of MW.3 from Run D and the observed luminosity function of the Milky Way satellites. The curves have the same meanings as Figure 4.19 but with a $v_{filter} = 30$ km s^{-1}.

are just beginning to fall into the host system, and all the ultra-faints are below detection limits.

We divide the simulated satellites into fossils and non-fossils: Figures 4.19 and 4.20 show the primordial cumulative luminosity functions in the four radial bins for fossil thresholds $v_{filter} = 20$ km/s and $v_{filter} = 30$ km/s, respectively. The observed cumulative luminosity function is shown as magenta lines and includes all the classical

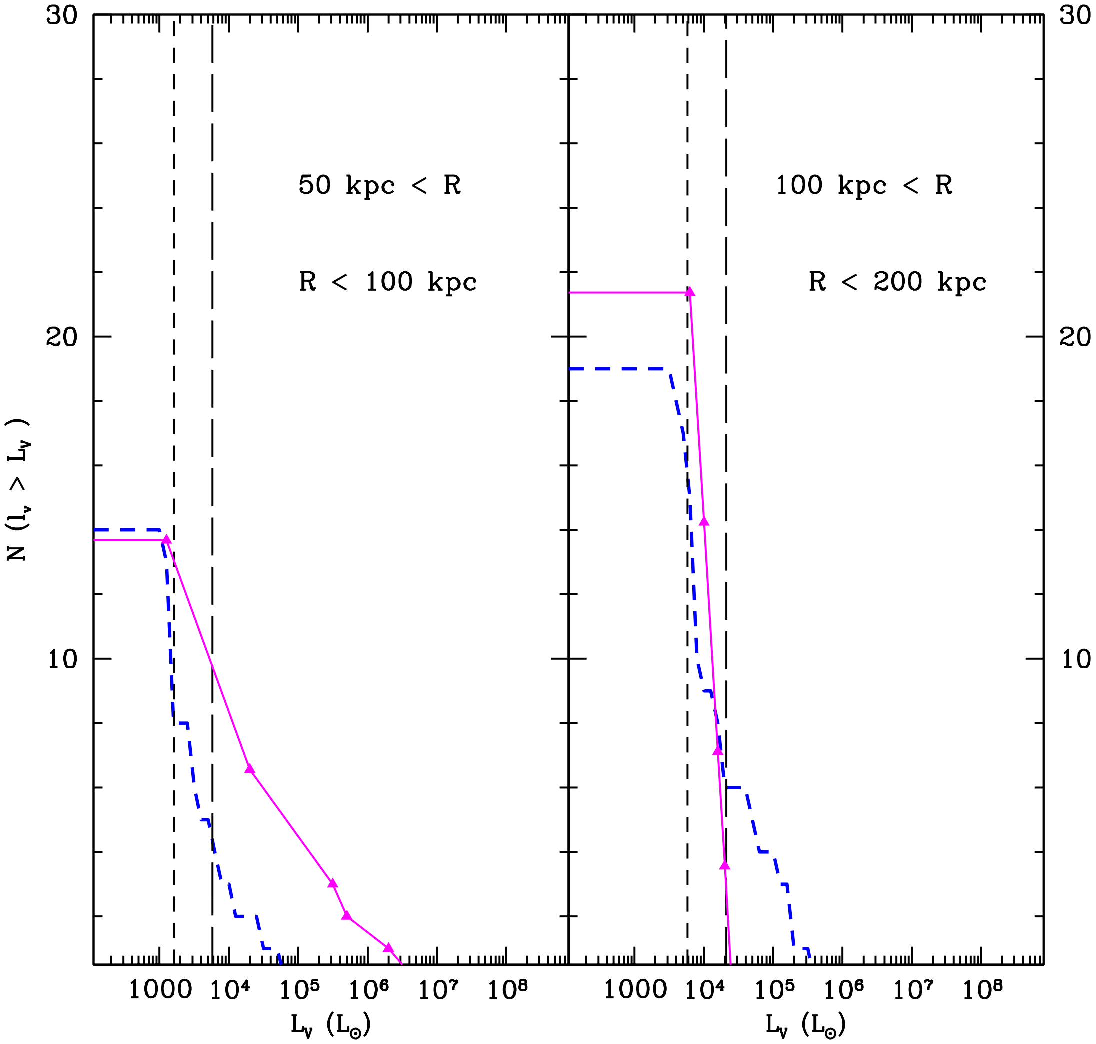

Figure 4.21: Cumulative primordial luminosity function for MW.3 in Run D and observations with only the fossils plotted. The simulated fossils are shown as the blue dashed line and the observed fossils as the magenta triangles. The fossil criteria for the observed satellites is the same as in Figure 4.16. We have only shown subhalos around MW.3 which would be detectable by SDSS.

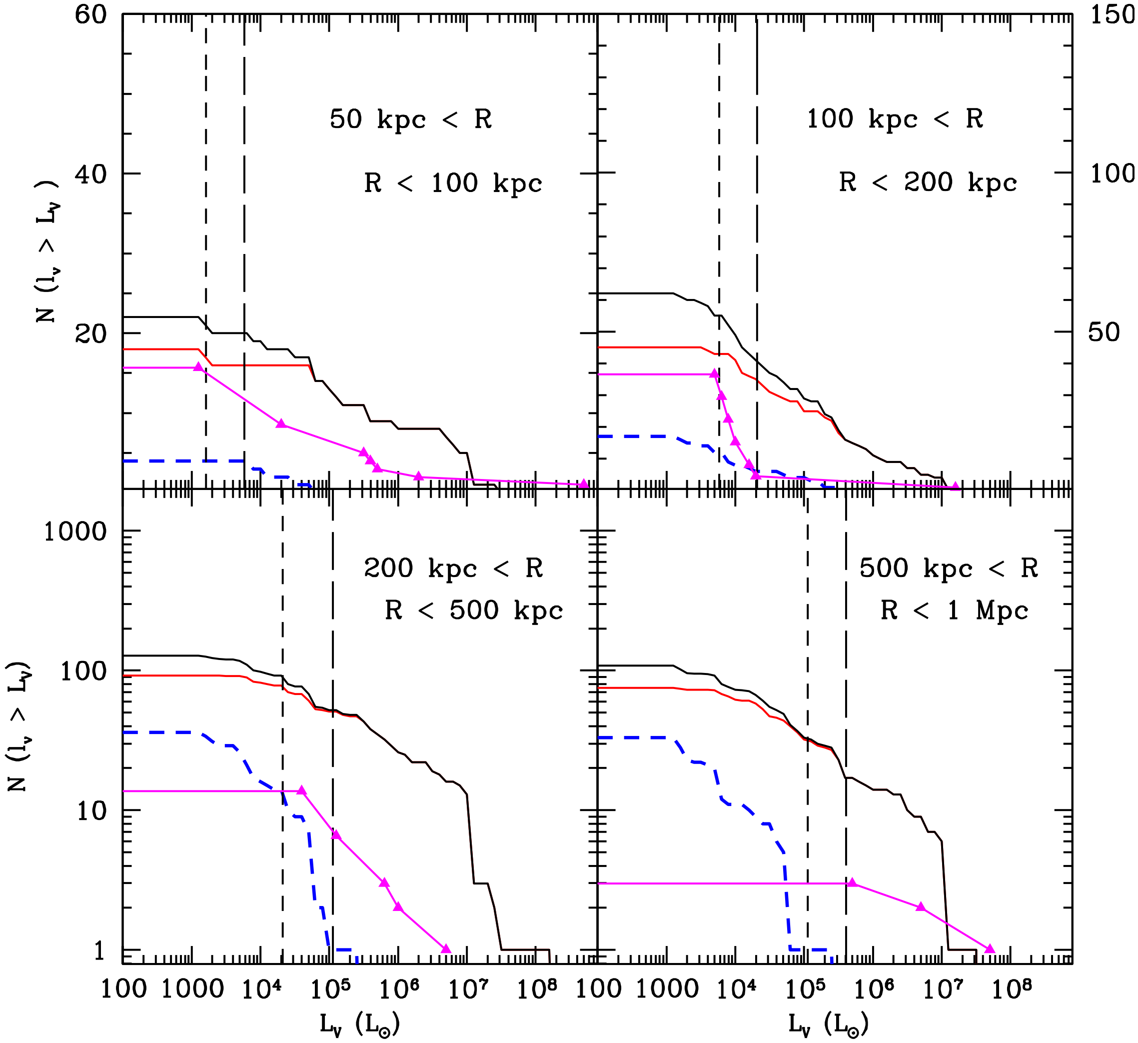

Figure 4.22: Cumulative primordial luminosity function for MW.3 in Run D and the total observed population. Only simulated dwarfs which have Σ_V above the Koposov et al. (2008) limit are shown.

dwarfs and the ultra-faints, excepting the population at $R < 50$ kpc. The simulated non-fossils are shown as the red solid curve, and for all bins they dominate for $L_V > 10^4 - 10^5$ L$_\odot$. These halos may have been able to accrete gas and form stars after reionization, and their primordial cumulative luminosities represent a lower limit for their present day luminosity. If we were to allow for additional star formation after reionization, the total number of luminous non-fossils would remain

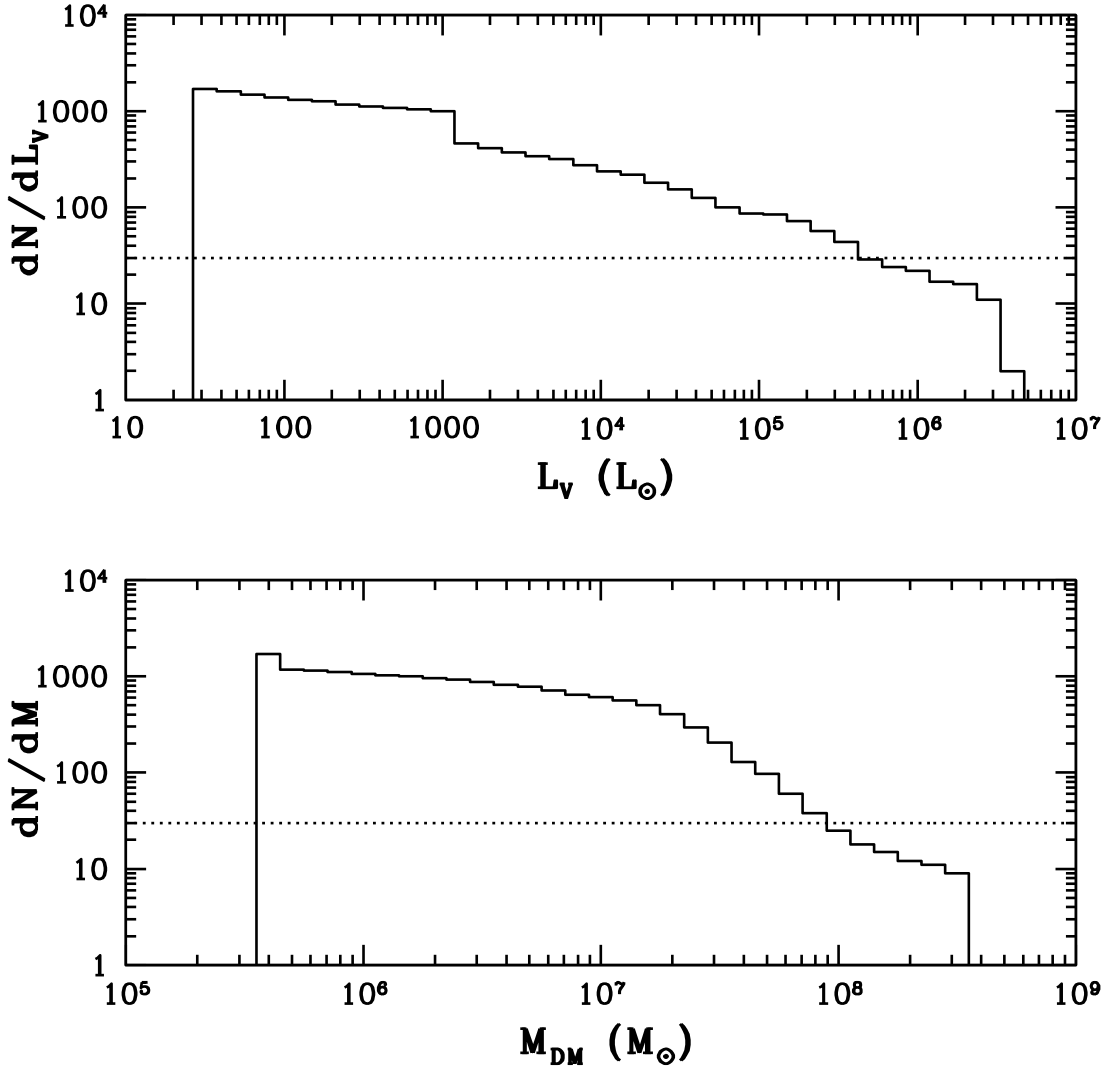

Figure 4.23: The luminosity (top) and mass (bottom) functions for pre-reionization halos within R_{vir} of MW.3 which are *not* part of a bound subhalo at $z = 0$. We only include those unbound luminous pre-reionization halos between 20 kpc and 50 kpc, where all but two of the known tidal ultra-faints are located. The horizontal dotted lines show the approximate number of stripped pre-reionization halos required to reproduce the inner ultra-faint dwarf population, ~ 30.

constant, but the curve would shift to higher luminosities (to the right). The primordial cumulative luminosity function of the true fossils (blue dashed curve) has no such caveat. Their luminosities are known since they have not undergone post-reionization baryonic evolution aside from the aging of their stellar populations. The primordial cumulative luminosity function of the entire simulated population is the solid black curve. Note, that for $L_V < 10^5 L_{\odot}$, the total primordial cumulative luminosity function is increasingly dominated by fossils.

Before looking at the primordial cumulative luminosity functions in detail, we insure we are comparing equivalent populations. By definition, all observed Milky Way satellites are above current detection limits, however, as seen in Figure 4.1, a subset of our simulated fossils have surface brightnesses below the detection limit of the SDSS. We use both the Walsh et al. (2009) and Koposov et al. (2008) limits to test the distribution of detectable true fossils against observations. Figure 4.21 shows the true fossil luminosity function convolved with the Walsh et al. (2009) limits (blue dashed line) and the observed fossil sample (magenta line) used in Figure 4.16. As in the galactocentric radial distributions, we find good agreement between the primordial luminosity function of the true fossils and the observed fossils for $50 - 100$ kpc and $100 - 200$ kpc. We do not make comparisons at $R > 200$ kpc because of the inability of current surveys to detect fossils at these larger distances. In Figure 4.22, we next use the surface brightness limits from Koposov et al. (2008) to remove any simulated fossil satellite not detectable by current surveys. Using the straight surface brightness cuts in Koposov et al we all but eliminates the fossil population for $v_{filter} = 20$ km s^{-1}. This is a much stronger effect on the detectability of our true fossils than that seen for the Walsh et al. luminosity and distance cuts.

In all distance bins, there is an overabundance of the bright satellites at luminosities typical of the classical dwarfs ($L_V > 10^5 L_{\odot}$). These should be easily detectable by the SDSS according to Walsh et al. (2009) (assuming the undetected dwarfs have the same distribution of half light radii as the ultra-faints). In Figure 4.19, the detectable dwarfs are to the right of the dashed line. During our discussion of the missing bright satellites, we use cumulative luminosity functions which have not been corrected for the SDSS limits. We now look at each distance bin individually.

Inner Ultra-Faint Dwarfs ($R < 50$ kpc)

In § 4.1, we argue that, while the inner ultra-faints have likely lost significant fractions of their stellar populations to tidal striping, they were not necessarily dIrr at the start of their encounters with the Milky Way. Instead, they may have been more massive primordial fossils. We base this conjecture on Figure 4.6 which shows that the inner ultra-faints have metallicities, [Fe/H], that are similar to fossils that are slightly more luminous. But are there enough massive fossils to account for the inner ultra-faints? Figure 4.23 shows the mass function (bottom) and luminosity function (top) of the pre-reionization halos which are not part of a bound halo at $z = 0$ and are between 20 kpc and 50 kpc from MW.3. The dotted horizontal lines show the approximate number of stripped fossils required to reproduce the inner ultra-faints. We see that to produce the ~ 30 inner ultra-faints around the Milky Way, we would only need to consider the largest primordial fossils with masses at reionization $M > 10^8$ M$_\odot$ and initial luminosities $L_V > 10^6$ L$_\odot$.

$50\ kpc < R < 100$ kpc

A strong piece of evidence for the primordial model would be the total number of observed satellites in one or more radial bins being greater than the number of non-fossils. When we look at $R < 100$ kpc without the $R < 50$ kpc cut, we see such an overabundance of observed dwarfs. However, when we do not include the dwarfs within 50 kpc of the galactic center the case is no longer clear cut. If the satellite count from $50 - 100$ kpc increases to greater than 25, there is a case for fossils even using the most conservative $v_{filter} = 20$ km s^{-1}. For $v_{filter} = 30$ km s^{-1} the number of non-fossils available from $50 - 100$ kpc drops to ~ 18.

For luminosities at which the observational sample is complete, to the right of the dashed lines, we see too many bright ($L_V > 10^4 L_\odot$) objects, even in this inner most radial bin. In addition, as our simulations do not account for post-reionization star formation, it is likely that the overabundance of bright objects is worse than shown in Figure 4.19. Unless all of the non-fossils have accreted no gas and formed no additional stars after reionization, the simulated curve must lie *below* the observations. This allows these star forming halos to increase in luminosity, shifting the luminosity function of the non-fossils to the right.

100 *kpc* $< R < 200$ **kpc**

In this bin, we probe the outer reaches of the Milky Way's virial halo and there are a few notable characteristics of the luminosity functions. First, with the addition of the observed dwarfs in this bin, the total number of known satellites around the Milky Way increases to ~ 65, ~ 45 not including the inner ultra-faint dwarfs. The sample at these larger radii is only complete for $L_V > 10^4$ L$_\odot$. For $100-200$ kpc, with a $v_{filter} = 20$ km s^{-1} and the less conservative $v_{filter} = 30$ km s^{-1} there are ~ 60 and ~ 40 simulated non-fossils, respectively. Second, the presence of undetected dwarfs is corroborated by the shape of the observed luminosity function around 10^4 L$_\odot$. Not only is it rising steeply to the detection limit at $R = 100$ kpc, but its shape is similar to the simulated primordial luminosity function for the true fossils.

In the outer virial halo, we once again overproduce the number of bright satellites. At these radii the discrepancy between theory and observation is more severe than for 50 kpc$< R < 100$ kpc since for these radii there is only one observed satellite with $L_V > 3 \times 10^4$ L$_\odot$.

$R > 200$ **kpc**

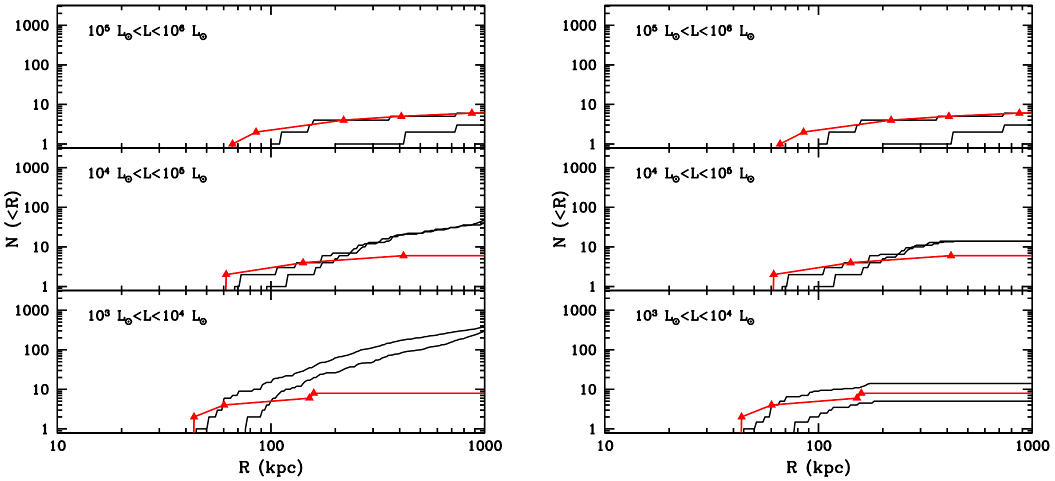

Figure 4.24: (*Left*) : Same as Fig. 4.15 but the observed satellite distributions only include bona fide fossils *and* assume the Milky Way satellites are distributed in a plane instead of isotropically. The fossils include classical dSph which were designated fossils in Ricotti and Gnedin (2005) and the ultra-faints whose stellar properties match those of the simulated fossil population. Note that this excludes most of the ultra-faints within 50 kpc. In our simulated distributions we use $v_{filter} = 20$ km s^{-1} to define a fossil. We have included all simulated fossils, including those which would sit below the SDSS detection limits. (*Right*) : Same as the left panel but simulated radial distributions only include the true fossils which would fall within the Walsh et al. (2009) detection limits.

For $R > 200$ kpc, we can only make observational comparisons for $L_V > 10^5$ L$_\odot$. Beyond the virial radius the discrepancy between the observed number of satellites and our simulations is up to $\sim$ 1.5 orders of magnitude, compared with factors of $\sim$ 2 and $\sim$ 10 for the 50 kpc $< R <$ 100 kpc and 100 kpc$< R <$ 200 kpc bins, respectively.

4.5 The Isotropy Assumption

In this section, we test our assumption of an isotropic distribution of subhalos and satellites. Rather than using an isotropic correction factor of 3.56 for the number of ultra-faint dwarfs, we use a correction factor of 2 to approximate a plane of satellites

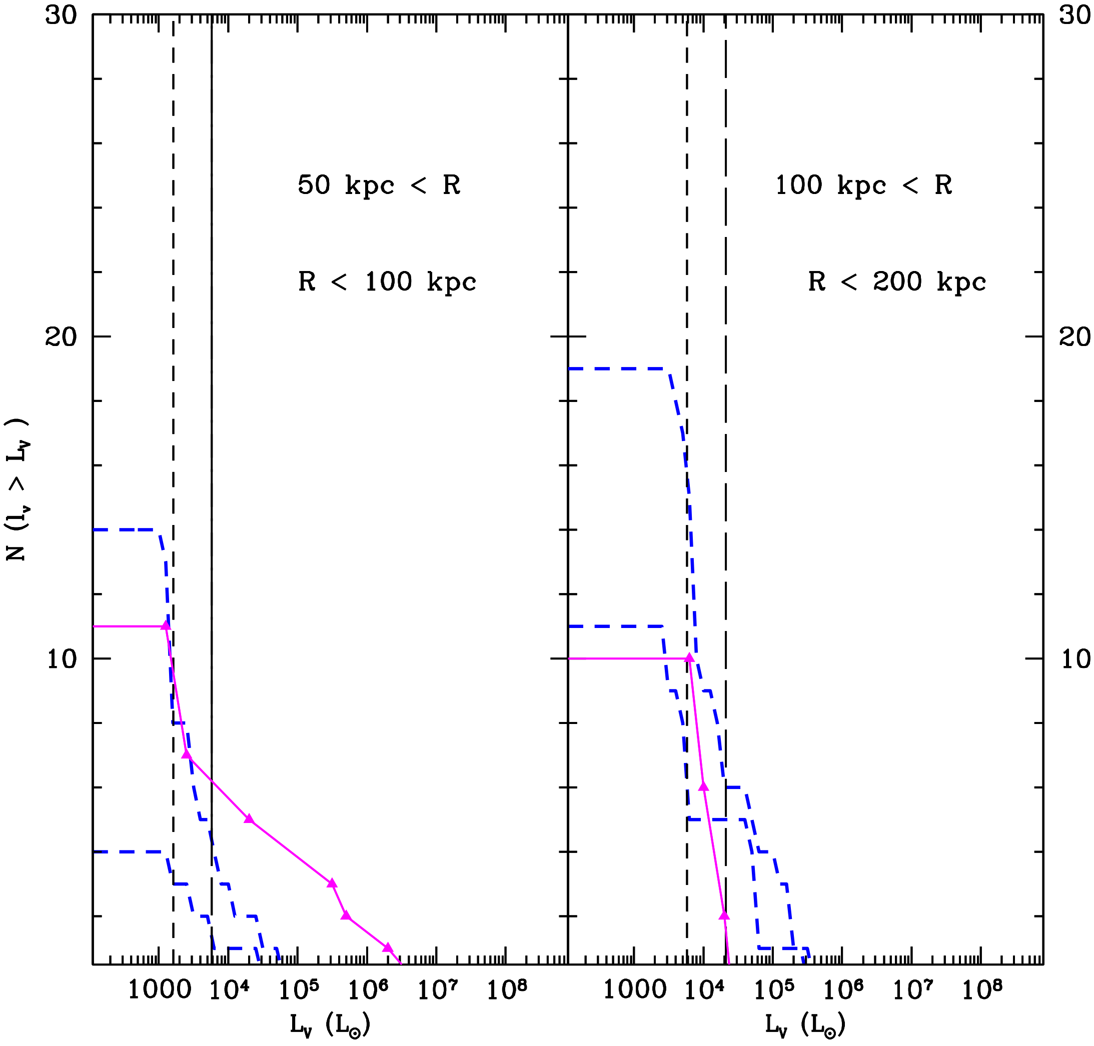

Figure 4.25: Cumulative primordial luminosity function for MW.3 in Run D and observations with only the fossils plotted and the distribution of fossils assumed to be in a plane perpendicular to the disk instead of isotropic. The simulated fossils are shown as the blue dashed line and the observed fossils as the magenta triangles. The fossil criteria for the observed satellites is the same as in Figure 4.16. We have only shown subhalos around MW.3 which would be detectable by SDSS.

roughly perpendicular to the disk. Figures 4.24 and 4.25 show the galactocentric radial distribution and cumulative primordial luminosity function for the fossils using the 2.0× planar correction factor. We find that the difference between isotropic and planar correction factors for the satellites does not affect our finding of a reasonably good match between the simulated and observed galactocentric radial distribution and cumulative luminosity function of the fossils.

4.6 Discussion

One of the key predictions of the primordial model is a total number of satellites for the Milky Way between $200-300$, only a maximum of 100 of which are non-fossils (here we assumed $v_{filter} = 20$ km s^{-1}). The number of Milky Way satellites which are not fossils provides an important test for star formation in minihalos at high redshift. If, after PanSTARRS and LSST are online, the number of ultra-faint Milky Way satellites remains < 100, we have a strong constraint on star formation in pre-reionization dwarfs. Either no pre-reionization fossils survived near the Milky Way, or almost none of the halos with masses at formation $M < 10^8 M_\odot$ formed stars. However, if the satellite count rises to > 100, some of the dimmest Milky Way dwarfs must be fossils of reionization. Using details of the stellar populations and their distributions, observations of these fossils can constrain models of star formation at high redshift.

A caveat to this picture is that the number of non-fossils is highly sensitive to the choice of the filtering velocity. When we raise the filtering velocity to 30 km s^{-1}, the number of non-fossils drops by a third to 60 ± 8 from the 90 ± 10 for $v_{filter} = 20$ km s^{-1}. The choice of 20 km s^{-1} assumes a constant IGM density with $T_{IGM} = 10^4$ K throughout a minihalo's evolution. In reality, the situation is not so simple.

The gas near 10^{12} $\mathrm{M}_\odot$ halos, and in the filaments between, may be heated to $\sim 10^5 - 10^6$ K by AGN feedback. The higher temperatures of this local intergalactic medium may correspond to $v_{filter} \gtrsim 40$ km s^{-1}. In addition to the higher filtering velocity, the higher density near a Milky Way mass halo reduces the effective potential depth of the subhalos, increasing the mass threshold for post-reionization gas accretion still further. Simulations to determine the temperature and density of the IGM near a Milky Way from reionization to the modern epoch are needed to determine the $v_{filter}(\mathbf{x}, z)$, and whether these factors can explain the existence of Milky Way and M31 dwarfs with the observed properties of fossils, but luminosities above the 10^6 $\mathrm{L}_\odot$ threshold.

The observed distributions, to which we compare our simulations, depend on how we correct for the incomplete sky coverage of the SDSS. In this work, we have assumed an isotropic satellite distribution at $R > 50$ kpc. Under this assumption, the SDSS completeness correction for the ultra-faints is 3.54. We briefly check if the agreement between the observed and simulated distributions is dependent on the isotropic assumption. Recent work (Bozek et al. 2011; Metz et al. 2007, 2009) has suggested that rather than being isotropic, the Milky Way satellites are oriented in a plane approximately perpendicular to the disk. We approximate this non-homogeneous satellite distribution by correcting for the SDSS sky coverage by a factor of 2.0 instead of 3.54. The number of classical fossils remains the same. The different correction does not change the consistency of our simulated galactocentric distribution with observations, though the lower correction factor suggests a higher Milky Way mass. It also does not change the bright satellite problem, in fact, the lower observational correction factor makes the overabundance of simulated $L_V > 10^4$ $\mathrm{L}_\odot$ dwarfs worse by about a factor of two.

Our simulated true fossils produce an excellent agreement in properties and distribution with the observed lowest luminosity Milky Way satellites. In § 4.1, we showed that a subset of the ultra-faints, all with $L_V < 10^5$ $L_\odot$, have half-light radii, surface brightnesses, mass-to-light ratios, velocity dispersions, metallicities and metallicity dispersions consistent with the expected stellar properties of the true fossils. We have now compared the galactocentric radial distributions and primordial cumulative luminosity functions of simulated fossils to observations of Milky Way satellites. When we compare the observed and simulated distributions, we find them to be in agreement with each other for $L_V < 10^5$ $L_\odot$. In addition, a large population of primordial fossils have surface brightness below the detection limits of current surveys (*e.g.*, SDSS). The following list summarizes the main results of this chapter.

- Overall $\sim 25\%$ (for $v_{filter} = 20$ km s^{-1}) to $\sim 30\%$ (for $v_{filter} = 30$ km s^{-1}) of the primordial fossils at the present day have undergone a merger with another luminous fossil. This fraction increases with the modern luminosity of the dwarf. Hence, the typical half light radii of this population can be larger than the original distribution at reionization. These fossils are even harder to detect due to their lower surface brightness. This effect also increases the spread of the relationship between half light radii vs. luminosity and surface brightness vs. luminosity of fossils at $z = 0$.

- Leo V, Pisces II. Segue 2 and Willman 1 have half-light radii which are too small, and metallicities too large, for their luminosities. Due to their proximity to the Milky Way, we speculate that their stars and dark halos have been affected by tides. Hence, these ultra-faints may represent a population of massive primordial dwarfs which have lost $\gtrsim 90\%$ of their stars via tidal interactions.

- We reiterate the existence of a yet undetected population of fossils with luminosities $L_V < 10^4$ L$_\odot$ and surface brightness $< 10^{-1.4} L_\odot$ /pc^2 . We present plots showing, in detail, the expected properties of this population. We also notice that some of the new ultra-faint satellites in Andromeda have half light radii in agreement with the properties of the undetected fossil population, but luminosities $\sim 10^5 L_\odot$.

- We are able to reproduce the distribution of the ultra-faints with our simulated primordial fossils. We find no missing satellites at the lower end of the mass and luminosity functions, but our model predicts ~ 150 additional Milky Way satellites that can be found in upcoming deeper surveys (PanSTARRS, LSST).

- At all radii, we see an overabundance of bright ($L_V > 10^4$ L$_\odot$) satellites which, even with only their primordial luminosities, would be easily detected by current surveys. Given the agreement between the stellar properties and distributions of the ultra-faints and those of our fossil dwarfs, we cannot account for the excess bright satellites by imposing a blanket suppression of star formation below a given mass.

Chapter 5

The “Missing” Bright Satellites

Our simulations of the fossils of the first galaxies are consistent with the observed Milky Way satellite galactocentric radial distributions (§ 4.4.1), primordial cumulative luminosity functions (Figure 4.21), and internal stellar properties (§ 4.1). More intriguing is, that at first glance, the model appears to fail in the outer parts of the Milky Way by over-producing the number of bright non-fossil satellites. In this chapter, we explore possible solutions to the bright satellite problem and whether the proposed solutions maintain the agreement between the observed ultra-faint dwarf population and our simulated true fossils. First, we will explore whether the pre-reionization simulations overestimate the star formation efficiency in pre-reionization dwarfs, and, then, whether we have too many luminous galaxies forming before reionization (§ 5.1.3). It would be of great interest if we could use current observations to constrain galaxy formation models before reionization. We conclude the analysis with a proposal in which the bright satellites do exist in the outer parts of the Milky Way halo but may still be elusive to detection due to their extremely low surface brightnesses (§ 5.1.4).

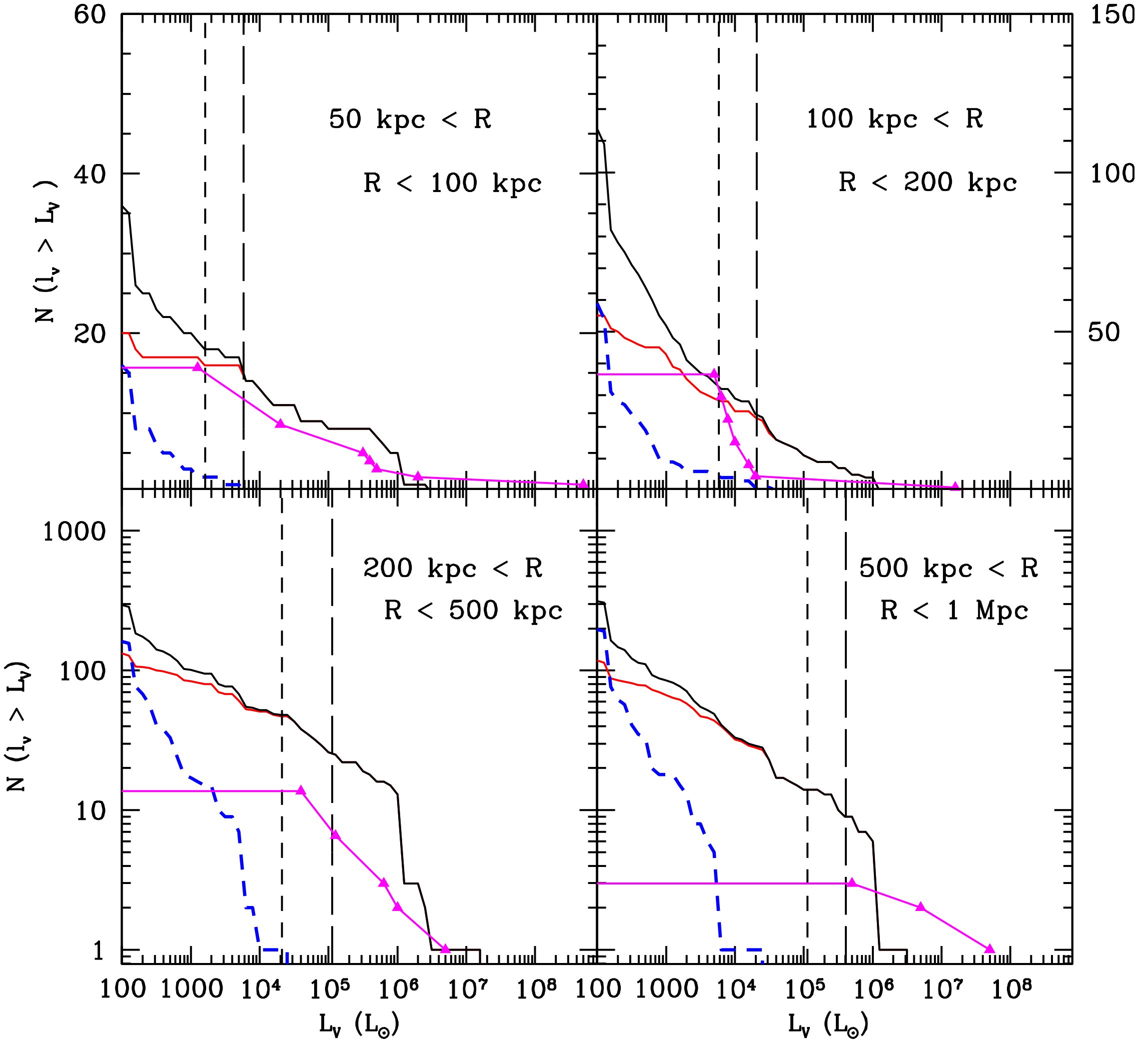

Figure 5.1: Cumulative luminosity functions of MW.3 from Run D (colored curves) with the total observed population (magenta triangles). All the symbols and lines mean the same as in Figure 4.19. Here we increase the stellar mass-to-light ratio by a factor of 10 to 50 $M_{\odot}/L_{\odot}$.

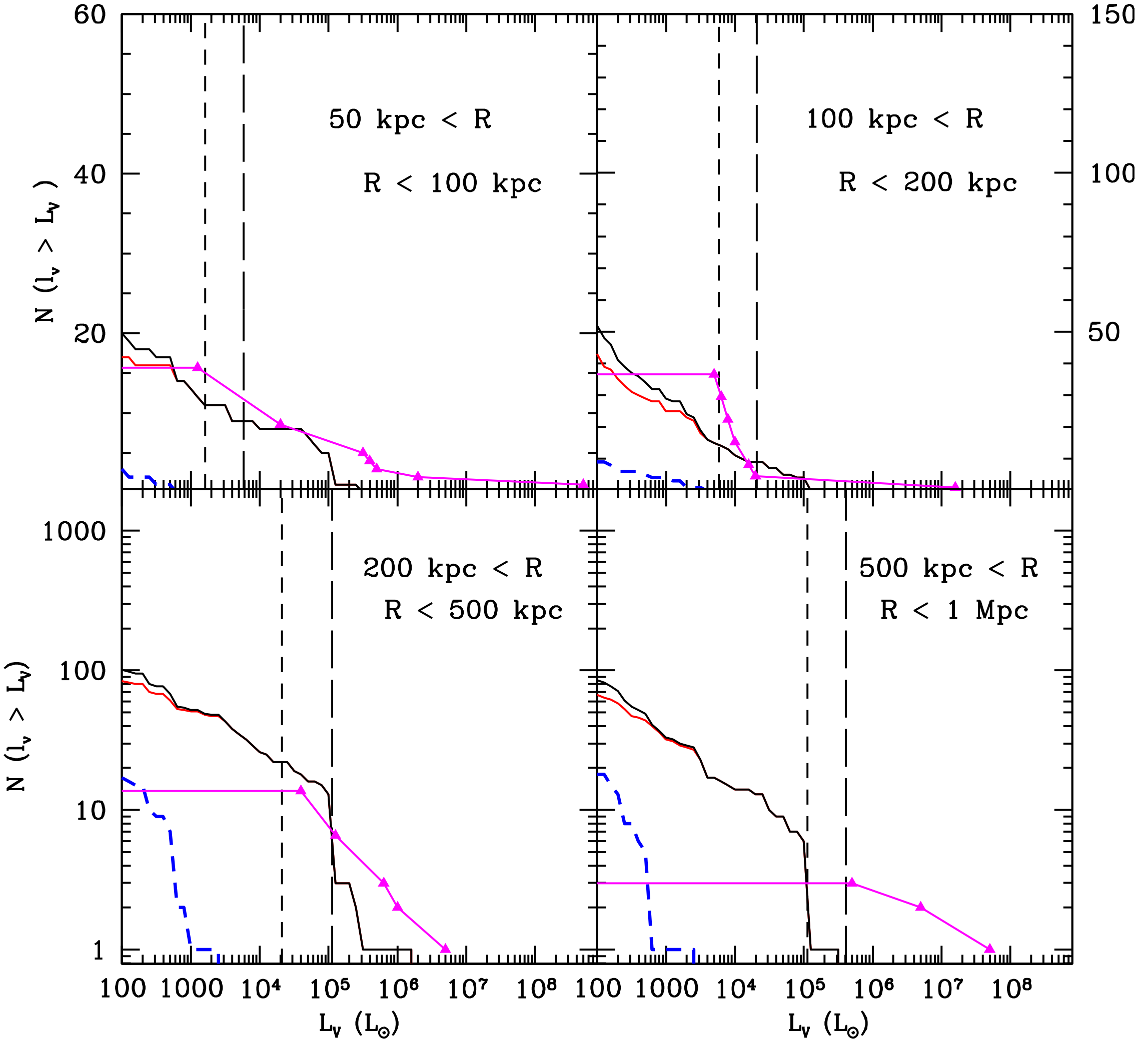

Figure 5.2: Cumulative luminosity functions of MW.3 from Run D (colored curves) with the total observed population (magenta triangles). All the symbols and lines mean the same as in Figure 4.19. Here we increase the stellar mass-to-light ratio by a factor of 100 to 500 $M_\odot/L_\odot$.

5.1 Removing the Bright Satellites

5.1.1 Increasing Mass to Light Ratios

First, we explore whether our pre-reionization simulations overestimate the luminosity of galaxies independent of dark matter halo masses. This could be due to using an incorrect IMF in the pre-reionization simulations. We use a mass-to-light ratio for the aged stellar population,

$$\frac{M_*^{rei}}{L} = \left(\frac{M_*^{today}}{L}\right)\left(\frac{M_*^{rei}}{M_*^{today}}\right) \tag{5.1}$$

where M_*^{rei} and is the mass of the stellar population at reionization, and M_*^{today} is the mass of the stellar population at $z = 0$. The ratio of M_*^{rei}/M_*^{today} depends on the primordial IMF. The ratio of M_*^{rei}/M_*^{today} depends on the primordial IMF, and $M_*^{today}/L \sim 1 - 2$ as for the oldest globular clusters in the Milky Way. A more top heavy IMF for the primordial stars will result in greater stellar mass loss after reionization and fewer low mass stars which can survive to the modern epoch. Conversely, the ratio drops as the primordial IMF produces fewer high mass stars.

To approximate this effect, in Figure 5.1 we plot the cumulative luminosity functions as in Figure 4.19, but increase the stellar mass to light ratio by a factor of 10 in our pre-reionization dwarfs to $50 M_\odot/L_\odot$. The figure shows that increasing the mass to light ratio to $50 M_\odot/L_\odot$ does not decrease the number of luminous satellites enough to match observations. In the 50 kpc $< R <$ 100 kpc bin, we can match observations. However, since the primordial luminosities of the non-fossils are only lower limits, the agreement disappears if the population formed *any* stars after reionization. If they did, we are still over-producing luminous satellites. We need to use a mass to light of $500 M_\odot/L_\odot$ to not over-produce the number of non-fossil satellites in any radial bin. However, this high mass to light ratio makes the fossils virtually dark, with $L_V < 10^2$ L$_\odot$.

A blanket suppression of star formation in all halos does not solve the bright satellite problem unless we suppress all star formation in most halos before reionizatioin. We next explore suppression mechanisms which are dependent on the environment or properties of the halos.

5.1.2 Suppression of Pre-Reionization Dwarf Formation in Voids

The formation of H_2 in the early universe is catalyzed by ionizing UV radiation emitted by nearby star forming regions (Ricotti et al. 2002b). In the voids, two factors work against H_2 formation. The delay of structure formation in the voids relative to higher density regions will prevent the minihalos from collapsing until lower redshifts when the H_2 dissociating background is stronger. In addition, the importance of positive feedback is reduced due to the larger mean distances between minihalos in the voids and sources of ionizing radiation (Ricotti et al. 2002a,b, 2008). The combination of these factors may result in a reduced abundance of H_2 relative to the regions around a Milky Way. This may produce a star formation efficiency before reionization that depends on the environment. We approximate the most extreme case of H_2 suppression in the voids by suppressing all star formation in halos in regions with $\delta \lesssim 0.4$. The extreme suppression of the star formation in the voids we use treats all halos but those in the overdense regions ($z_{eff} = 8.3$) as dark.

Since the bright satellite problem is most prominent in the outer regions of the Milky Way halo, the lack of star formation in low density regions may decrease the number of bright halos beyond the virial radius while leaving the satellite luminosity functions unchanged at smaller radii and lower luminosities. However, Figure 5.3 shows that, even in the most extreme case, suppressing H_2 formation in the voids

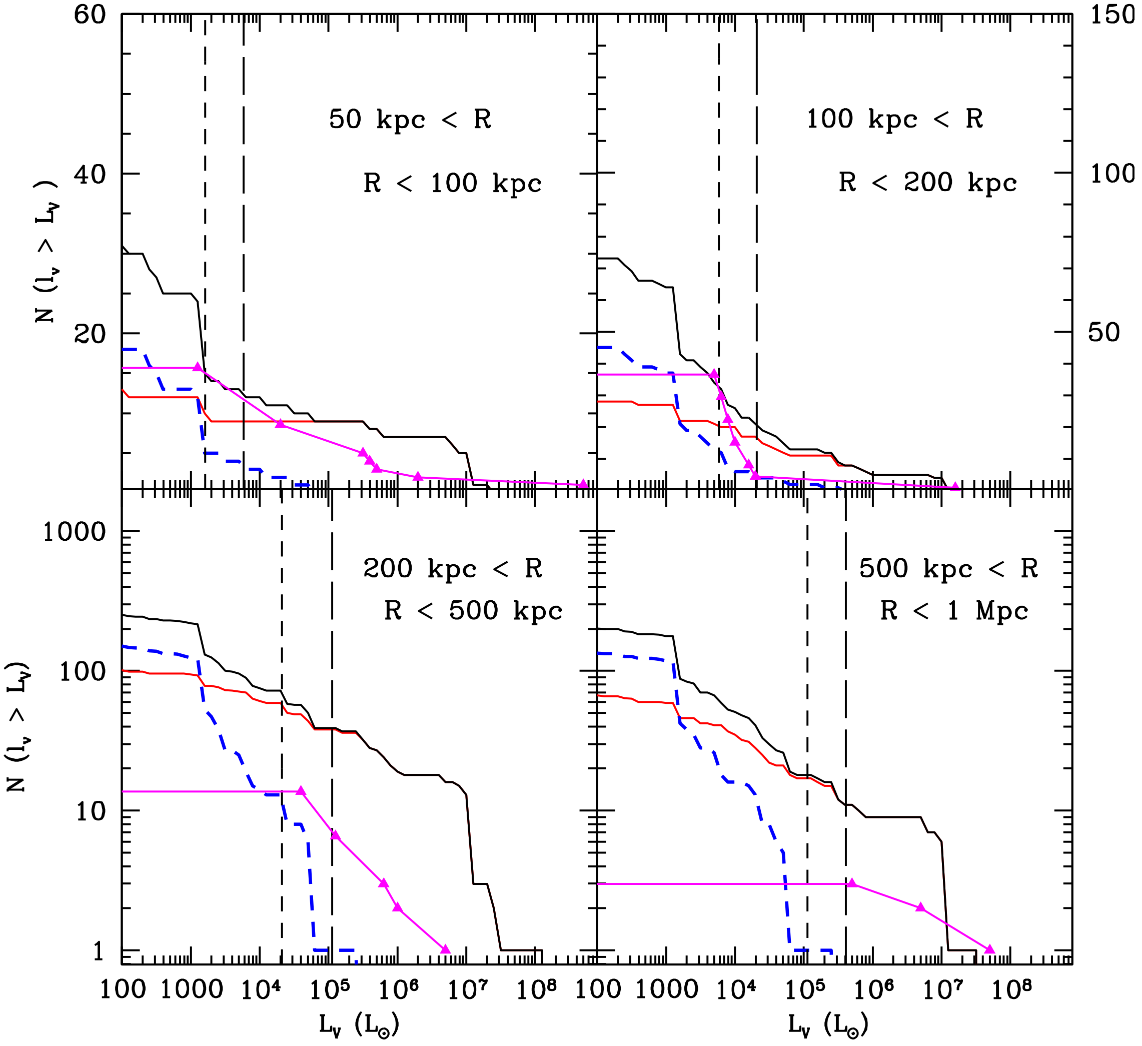

Figure 5.3: Cumulative luminosity functions of MW.3 from Run D (colored curves) with the total observed luminosity function (magenta triangles). All the symbols and lines mean the same as in Figure 4.19. Here we have completely suppressed star formation in any halo outside the highest density regions. This is the most extreme case of lower H_2 formation, and therefore lower star formation in the voids.

does not decrease the number of bright satellites enough in any radial bin to bring our simulations into agreement with observations. In this scenario, there is no appreciable reduction of the number of bright satellites for $R < 200$ kpc. There is a decrease in the luminosity function at larger radii, but it is neither strong nor focused enough on the high luminosity subhalos to solve the overabundance of bright satellites in the outer parts of the Milky Way. Enough of the region within 1 Mpc of our Milky Way is at the highest density in our simulation ($z_{eff} = 8.3$) that the complete suppression of star formation in even moderately less dense regions does not sufficiently change the luminosity functions or radial distributions.

With the inability of H_2 suppression in the voids and overall suppression of star formation to account for the missing bright satellites, we shift our focus to properties of the halos which vary with halo mass.

5.1.3 Lowering the Star Forming Efficiency

In the pre-reionization simulations, the sub-grid recipe for star formation depends on a free parameter, ϵ_*, controlling the efficiency of conversion of gas into stars per unit dynamical time. One of the main results of the pre-reionization simulations is that the global star formation rate and $f_*(M) = M_*/M_{bar}$ (the fraction of total mass converted into stars, where $M_{bar} = M_{dm}/7.5$) is nearly independent of ϵ_* in small mass dwarfs due to the self-regulation mechanisms of star formation. However, in halos with masses $M \gtrsim 5 - 10 \times 10^7$ M$_\odot$, $f_*(M)$ is typically proportional to ϵ_* since the higher mass minihalos are less sensitive to self-regulated feedback. We used $\epsilon_* = 5\%$ in our fiducial runs, but that may be too large (*e.g.*, Trenti et al. 2010). The pre-reionization simulations may have overestimated the luminosity of primordial dwarfs with $M \gtrsim 5 \times 10^7$ M$_\odot$, for which the f_* vs M relationship is tighter. We explore the effect of reducing ϵ_* by introducing a maximum stellar fraction, $f_{*,crit}$.

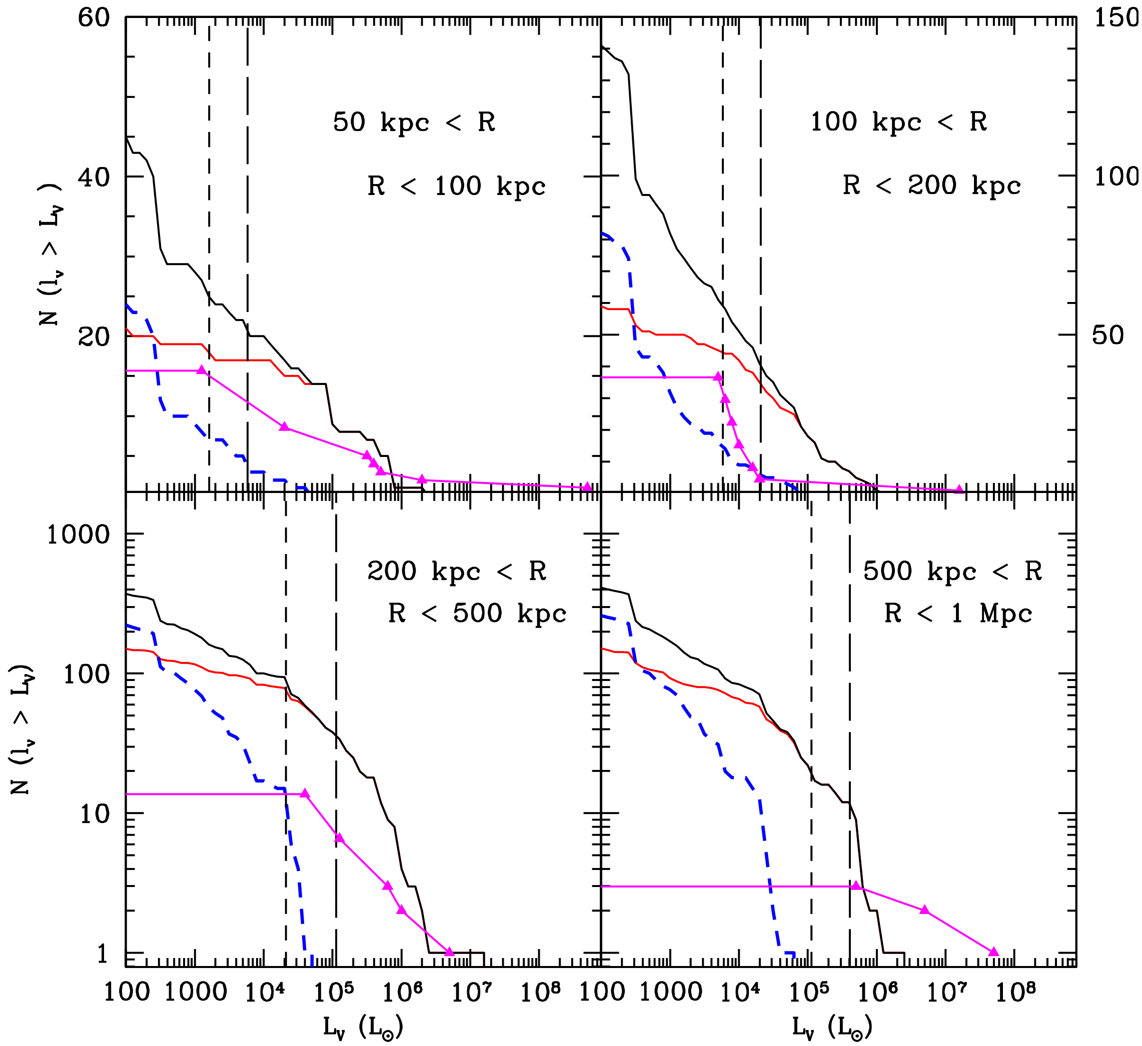

Figure 5.4: (*Left*). Cumulative luminosity function of MW.3 from Run D (colored curves) and the total observed population (magenta triangles). All symbols and lines mean the same as in Figure 4.19. We have applied an $f_{crit} = 1\%$.

Roughly, $f_{*,crit}$ corresponds to the mass threshold where feedback effects no longer dominate and where the value of ϵ_* becomes important. If we reduce $f_{*,crit}$, we will decrease the luminosities of our most luminous halos. Roughly, for halo masses $M \sim 3 \times 10^7$ M$_\odot$ (virial mass at formation) our simulations have $f_*(M) \sim 1\%$. This is in agreement with observed values for dwarfs with $v_c \sim 10$ km s^{-1} (McGaugh et al. 2010).

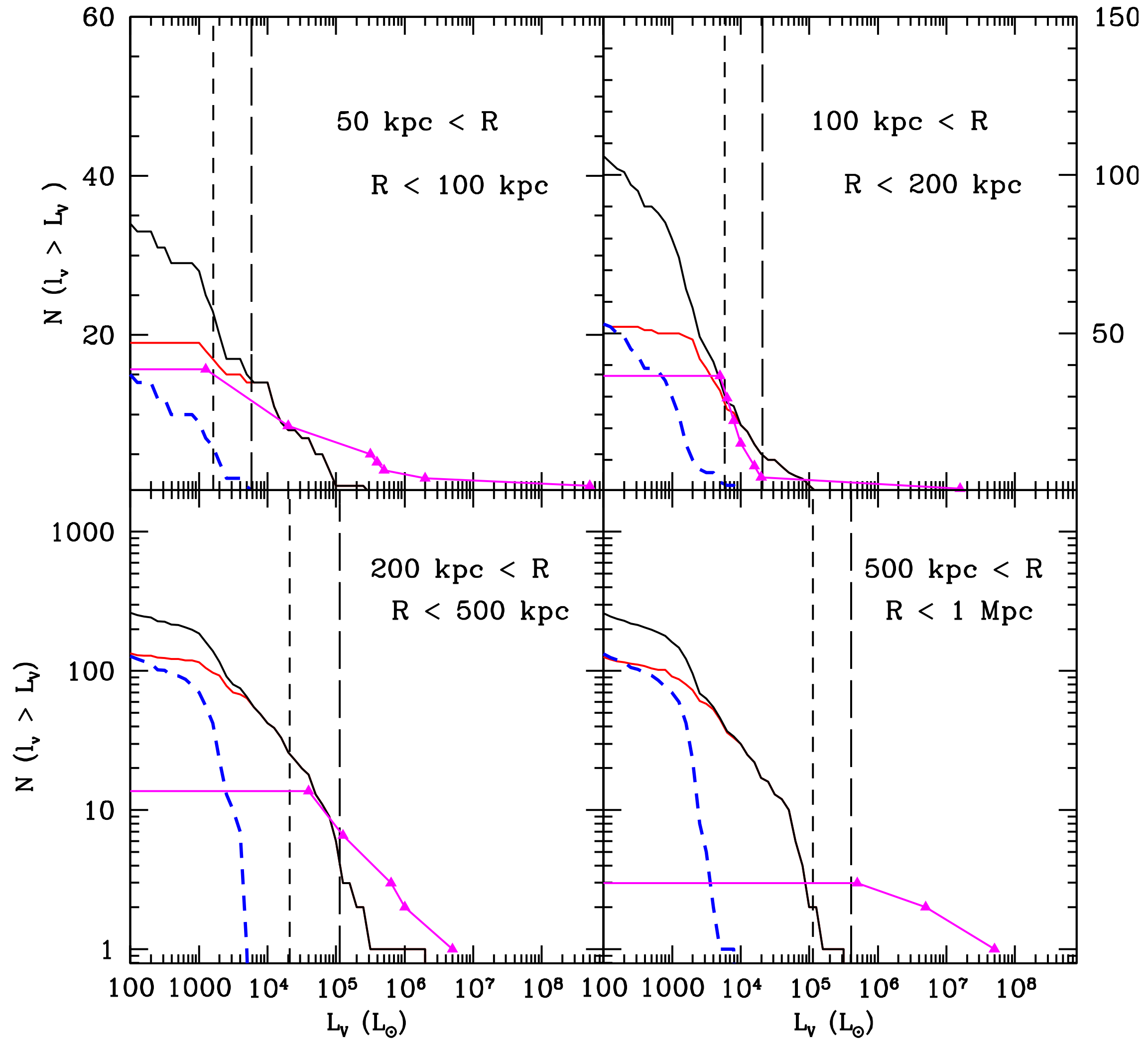

Figure 5.5: Same as Figure 5.4 but for $f_{crit} = 0.1\%$.

Figure 5.4 shows the luminosity functions of our simulations with all halos with $f_{*,crit} = 1\%$ and Figure 5.5 shows the same for $f_{*,crit} = 0.1\%$. The figures show that lowering the star formation efficiency preferentially for the higher mass halos is effective in decreasing the number of non-fossil subhalos with $L_V > 10^5$ L$_\odot$. Adopting $f_{*,crit} = 1\%$ decreases the number of luminous halos enough to bring the luminosity functions in agreement with observations, while preserving the agreement for the fossil population. However, in the radial bins 50 kpc $< R <$ 500 kpc, there

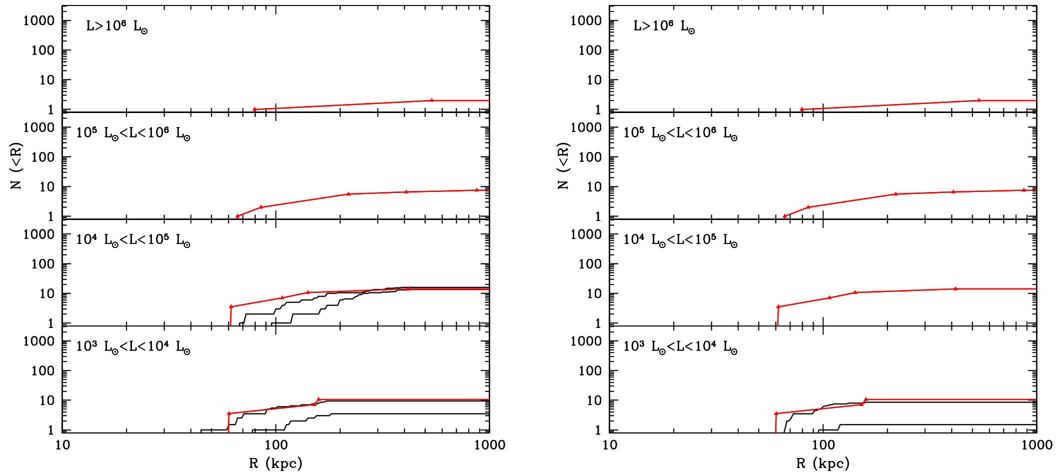

Figure 5.6: *Left* : Radial distribution for our simulated MW.2 and MW.3 with a $f_{crit} = 1\%$ (black solid curves) and for the fossil Milky Way satellites (red triangles). Note, that while we are still able to reproduce the radial distribution of the lowest luminosity bin, we are no longer able to match the fossil population for $L_V > 10^5$ L$_\odot$. *Right* : Radial distribution for $f_{crit} = 0.1\%$. Note that for the more extreme suppression, we have lost the fossils population with $L_V > 10^4$ L$_\odot$

still are too many subhalos with $L_V > 10^5$ L$_\odot$, though the discrepancy has dropped significantly. Coupling a lower ϵ_* with a higher mass to light ratio or H_2 suppression in the voids does not correct the remaining bright satellite overabundance. However, when we use an $f_{*,crit} = 0.1\%$, the cumulative primordial luminosity function of our simulated dwarfs becomes consistent with observations at all radii, but requires a deduction of f_* in halos with mass $M \sim 7 \times 10^6$ M$_\odot$ whose f_* is self-regulated and thus independent of ϵ_* (Ricotti et al. 2002b).

Any solution for the overabundance of bright satellites must preserve not only the existence of the true fossil population, but also its distribution and properties. We next look at the other dimensions of the agreement between the true fossil populations with an $f_{crit} = 1\%$ and 0.1% and the ultra-faints and classical dSph. Figure 5.6 shows the radial distribution of the true fossils around MW.2 and MW.3 from Run D, the observed Milky Way population for an $f_{crit} = 1\%$. While for

$10^3 L_\odot < L_V < 10^4$ $\mathrm{L}_\odot$ and $10^4 L_\odot < L_V < 10^5$ $\mathrm{L}_\odot$ the fossil population with $f_{crit} = 1\%$ reproduces the observed radial distribution; we no longer have any true fossils with $L_V > 10^5 L_\odot$. If the star formation efficiency of our pre-reionization halos is lowered enough to bring the number of luminous satellites in line with observations, the fossil luminosity threshold discussed in Chapter 3 is dropped to $L_V < 10^5 L_\odot$. For $f_{crit} = 0.1\%$ the threshold drops further to $10^4 L_\odot$.

The loss of the multi-dimensional agreement between our true fossils and the ultra-faints shows that lowering ϵ_* enough to account for the missing luminous satellites is not a viable solution for the bright satellite problem if the ultra-faint dwarfs are fossils of the first galaxies. In this interpretation, we need a different mechanism which will either preferentially suppress star formation in the most luminous pre-reionization halos to a greater degree, or cause their lower redshift counterparts to lose the majority of their primordial stellar population after reionization. We continue to seek a baryonic solution to the bright satellite problem before treating it as an issue for CDM cosmology.

5.1.4 The Ghost Halos

As discussed in Chapter 3, our N-body method does not allow us to determine the dynamics of the stars in halos that undergo mergers, or the degree to which those stars are tidally stripped. However, we have used analytic relationships to estimate the importance of dynamical heating of the stars when $z = 0$ fossils (about 20%) are produced by mergers of more than one pre-reionization dwarf (§ 4.1) We refer to such interactions as galaxy mergers. Here, we focus on those dynamical processes in non-fossils which result in the dispersion of the primordial stellar populations of the brightest satellites, the net effect of which is to either make the non-fossil populations invisible to current surveys by reducing their surface brightnesses below the SDSS

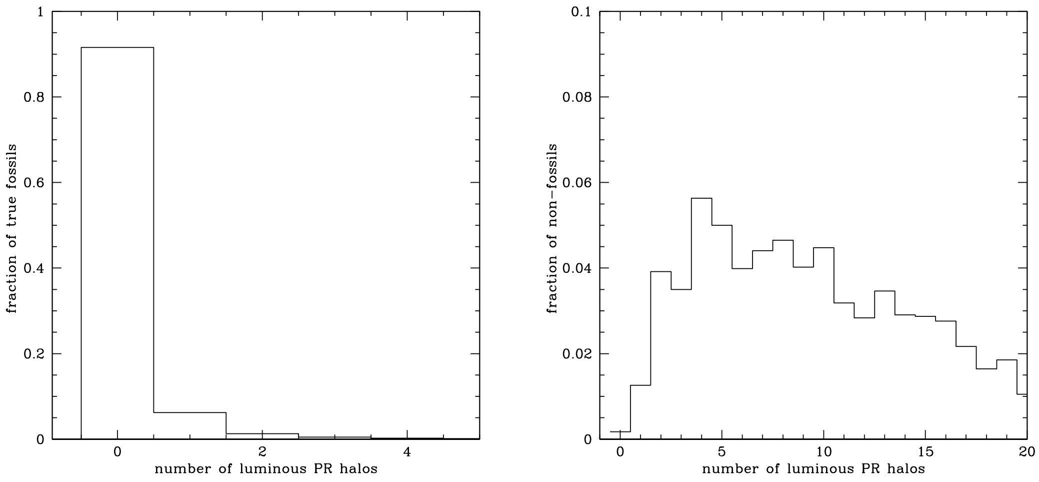

Figure 5.7: (*Left*). Histogram of the fraction of luminous true fossils with a given number of luminous pre-reionization halos, N_{lum}. N_{lum} is a proxy for the number of significant mergers the system has undergone. (*Right*). Histogram of the fraction of non-fossils with a given N_{lum}. Note, that unlike the N_{lum} histograms for the true fossils and polluted fossils the peak is not at $N_{lum} = 0$, but shifted to $N_{lum} \sim 5$. Note also, that the vertical scale is 0.1 instead of 1.0.

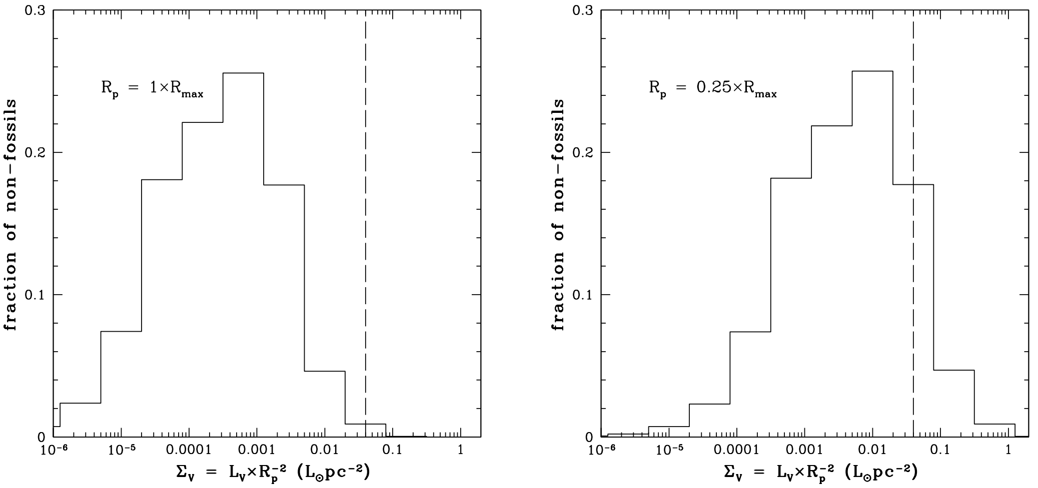

Figure 5.8: Histogram of the fraction of non-fossils with a given V-band surface brightness, Σ_V, for the primordial population. We assume that the primordial stars have been puffed up by interactions until they fill the full extent of the dark matter halo, giving us $\Sigma_V = L_V \times R_{max}^{-2}$, where R_{max} is the radius at which $v(r) = v_{max}$. The dashed vertical line is the surface brightness limit of the SDSS from Koposov et al. (2008). Only $\sim 1\%$ of the non-fossils are to the right of the dashed line, with expanded primordial populations detectable by the SDSS.

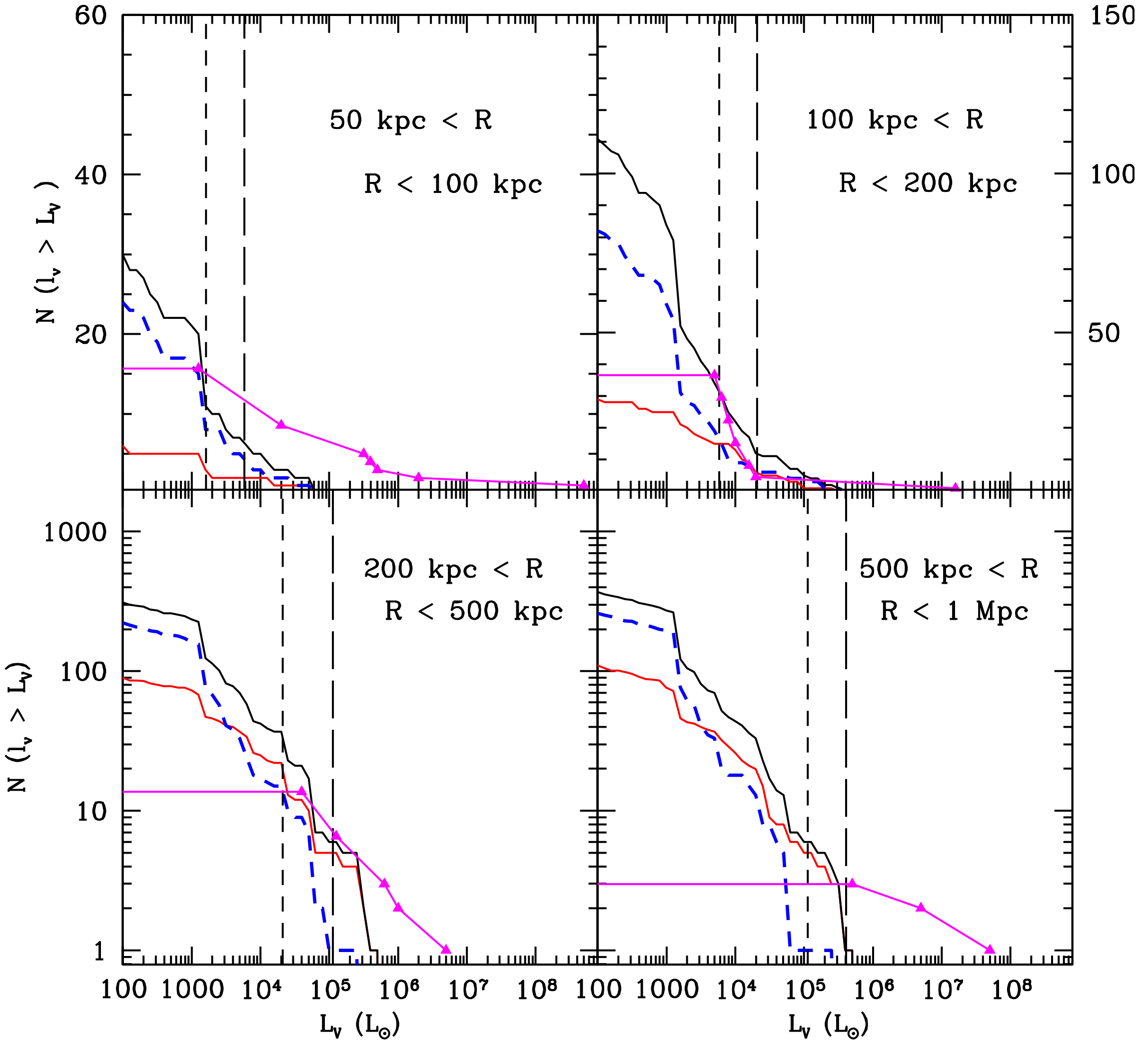

Figure 5.9: Cumulative luminosity functions of MW.3 from Run D (colored curves) with the total observed population (magenta triangles). All the symbols and lines mean the same as in Figure 4.19. In this figure we assume that all the non-fossils are below the detection limits or have lost their entire stellar populations due to a combination of heating due to major mergers and tidal interactions.

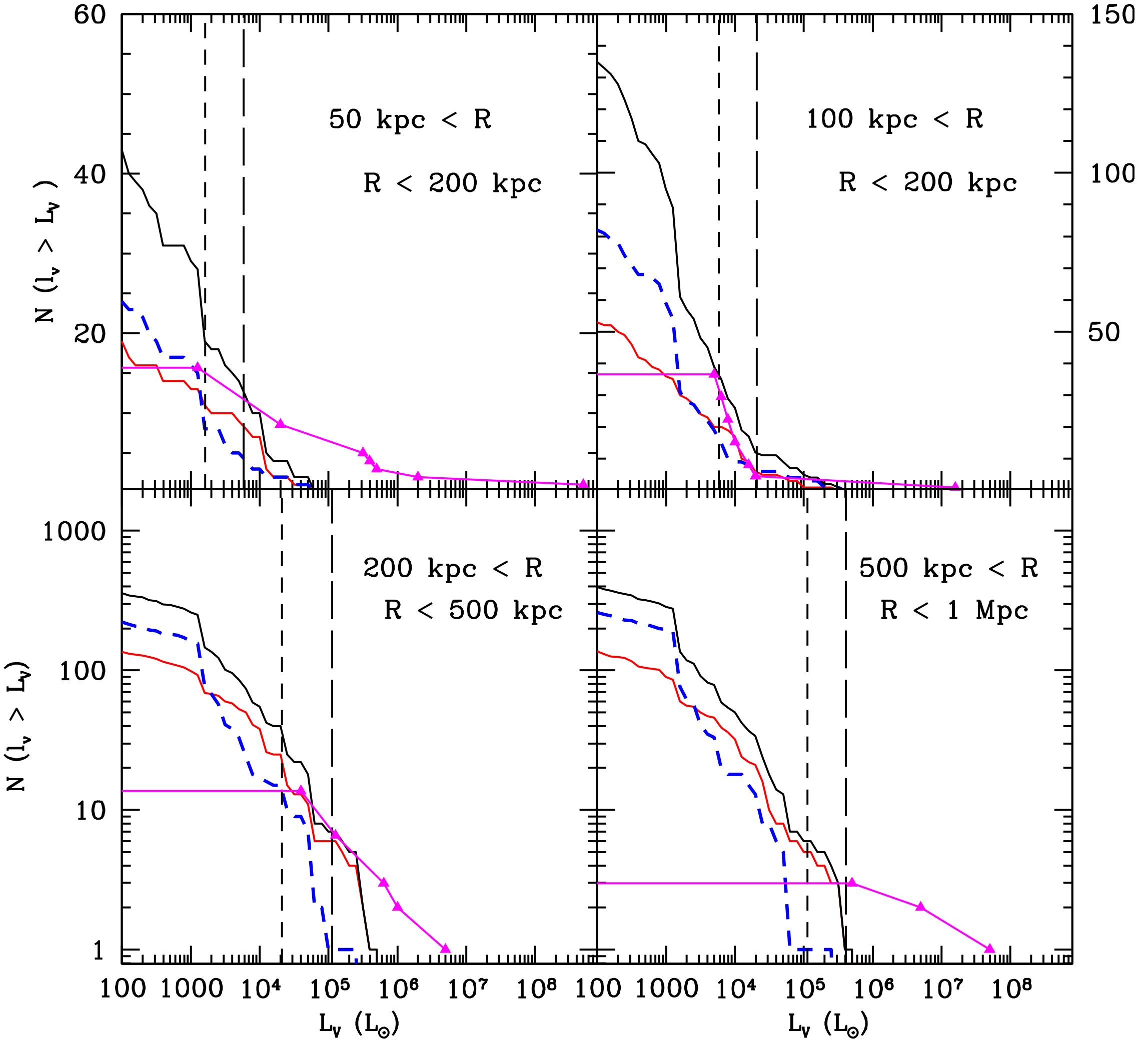

Figure 5.10: Cumulative luminosity functions of MW.3 from Run D (colored curves) with the total observed population (magenta triangles). All the symbols and lines mean the same as in Figure 4.19. Unlike Figure 5.9, here we allow the non-fossils to retain 0.1% of their stellar populations.

detection limits or preferentially strip them during interactions with more massive halos. The former mechanism would be relevant to non-fossils at $R \gtrsim 500$ kpc where tidal forces are negligible.

The number of pre-reionization halos in a $z = 0$ dwarf increases with mass. In this section, we explore the role of mergers to rend invisible, or strip, the primordial populations of stars in the the more massive dwarfs (non-fossils). Unlike in the previous sections, here we differentiate between the non-fossils and polluted fossils in our simulations. We remind the reader, that though both populations have v_{max} which were large enough for them to accrete gas from the IGM in the past, only the non-fossils are at or above that threshold at $z = 0$.

Throughout the next section we relax the assumption made in § 4.1 that kinetic energy is conserved during galaxy mergers and no energy is transferred from the movement of the component galaxies before merger to the stellar population of the daughter dwarf. When a system undergoes a galaxy merger, kinetic energy from the collision is imparted to the stars. Immediately after the collision, the new system will be in its most diffuse state. We define a galaxy merger as the interaction of two or more primordial galaxies. Although there is significant scatter in the luminosities of minihalos of the same mass, in general, those which host primordial galaxies are more massive than their dark counterparts. An interaction between two luminous minihalos is therefore more significant. We use N_{lum}, the number of primordial galaxies within at $z = 0$ halo, as a proxy for the number of galaxy mergers. If there are multiple galaxy mergers in a short amount of time, these stars will be susceptible to loss. In addition, recent work on increasing the extent of the stellar population in the bright ellipticals from $z = 2$ to $z = 0$ suggests that many minor interactions over several Gyrs can increase the size of the galaxy by a factor of 2-5 without significantly increasing mass (Naab et al. 2009). Roughly, the larger the number of significant interactions, the greater the spatial extent of the pre-reionization population and the more likely the halo will have lost a significant fraction of its primordial population to dynamical heating.

For isolated halos, with large N_{lum}, the radius of the primordial population increases, possibly until it fills the spatial extent of the dark matter halo. Such an extended system would have extremely low surface brightness and would be susceptible to tidal stripping. We next look at which of our three subhalo populations has a significant number of members with $N_{lum} > 3$. The fractions of the true fossil, and non-fossil populations with a given N_{lum} are shown in the left and right panels of Figure 5.7. Neither fossil population has a significant fraction of subhalos with $N_{lum} > 3$ with the fractions at $\sim 1\%$ and $\sim 10\%$ respectively. We therefore assume that, while a few of our true and polluted fossils may have had their primordial populations diffused by mergers, the vast majority remain dynamically cold.

The non-fossils show the opposite trend. The right panel of Figure 5.7 shows that $< 10\%$ of the non-fossils have $N_{lum} < 3$ and the distribution peaks at $N_{lum} \sim 5$. A population of non-fossils would be much more likely to have a primordial population dispersed by multiple major interactions than their fossil counterparts.

The non-fossil populations (see Figure 4.19) could have either lost their stellar populations, or had their primordial populations increase in size to the point where they are undetectable by the SDSS. Near the Milky Way, we assume they lost their entire primordial stellar population to tidal interactions. After falling into the Milky Way halo, the non-fossils were unable to form a significant younger stellar population.

At larger radii, the non-fossils are less likely to have their primordial populations stripped. However, as the stars expand to fill the spatial extent of the dark matter halo, the non-fossils end up with a primordial population with $\Sigma_V \sim L_V \times R_p^{-2}$, where L_V is the luminosity of the primordial population and R_p is the radius of the primordial population. Figure 5.8 shows the fraction of the non-fossils with a primordial population with surface brightness, Σ_V, for $R_p = R_{max}$ and $R_p = 0.25 \times R_{max}$, where R_{max} is the radius of the maximum circular velocity. We find that for $R_p = R_{max}$ about 1% of non-fossils would have an extended primordial halo above the SDSS detection limits (to the right of the dashed line), and, when R_p is decreased to $0.25 \times R_{max}$, the detectable fraction only rises to 20%. If these non-fossils formed few or no stars after reionization the majority would be undetectable by SDSS. The non-fossils which did form stars after reionization would be dIrr today or perhaps one of the few isolated dSphs or dSphs/Irrs: *e.g.*, Cetus, Tucana, Antlia. In our scenario, they would be surrounded by "ghost halos" of primordial stars $\sim$ 12 Gyr old with $[Fe/H] \lesssim -2$. But does this solve the "bright satellite problem"?

We quantitatively approximate this for our simulations by using a circular velocity cut. We look at the primordial luminosity functions as if all the ghost halos are either stripped or below SDSS detection limits. Practically, we set the luminosities to zero for all the non-fossils. We look to see if this cut solves the bright satellite problem while preserving the fossils better than lowering the star formation efficiency. We find it to be a good solution to the bright satellite problem.

Since setting the non-fossils luminosities to zero is able to decrease the number of luminous satellites, we look at the luminosity function it produces in more detail. All the curves in Figure 5.9 are the same as in Figure 4.19, excepting the red curve for the non-fossils that now represents only the polluted fossils.

We now look at each distance bin to see what turning off the non-fossil population has done to our various arguments. For 50 kpc $< R <$ 100 kpc, the necessity of a primordial dwarf population is even stronger when we only consider the fossil and polluted fossil populations. There are only ~ 7 polluted fossils within 100 kpc, less than one-fifth of what is required to account for the ~ 50 observed satellites. For $L_V > 10^4 L_\odot$, the luminosity function now sits below observations. This gives the remaining star forming halos room to form additional stars without overproducing subhalos with $L_V > 10^4 L_\odot$. The total number of subhalos within 100 kpc decreasing to 35 is consistent with observations. First, our MW.3 is on the low end of the mass range for the Milky Way for both observational estimates and simulations. Second, as seen in Figure 4.23, there are more than enough stripped down fossils which formed in halos with $M > 10^7 M_\odot$ and $L_V > 10^5 L_\odot$ to fill in the deficit. Since these objects would lack a cloud of tracer particles, they are marked as unbound by the halo finder AHF and included in the host halo and therefore not included in any of our dwarf luminosity functions.

The complete invisibility of the non-fossils is not quite as successful for 100 kpc$<$ $R <$ 200 kpc as we are still slightly overproducing the number of $L_V > 10^5$ $\mathrm{L}_\odot$ satellites compared to observations. However, we are better able to reproduce the sudden steepening in the observed luminosity function in Figure 5.9 than with any of our other suppression mechanisms (Figures 5.2, 5.3, and especially 5.4). This feature may be unique to the Milky Way so we are not unduly concerned with matching it. In addition, if the non-fossils are dark, our argument for the existence of primordial fossils becomes straightforward. There are only ~ 30 polluted fossils in this distance bin, only 75% of the ~ 40 observed galaxies, with any dwarf with $L_V < 10^4$ $\mathrm{L}_\odot$ difficult, if not impossible, to detect with current surveys.

Beyond the MW.3 virial radius ($R \sim 200$ kpc), turning the non-fossils dark easily places the primordial luminosity function into agreement with observations. This allows for the formation of post-reionization populations of stars in the polluted fossils and non-fossils. We remind the reader that the $z = 0$ halos at these radii would likely be on first approach to the Milky Way system and more likely to accrete and retain gas at later times. The diffuse primordial population in these distant non-fossils is an observational test of star formation in pre-reionization dwarfs and the existence of pre-reionization fossils.

5.2 Discussion

Through this work, we have used results of the simulations described in Chapter 3 to study the origin of the observed Milky Way and M31 satellites and understand whether they are compatible with models of star formation before reionization. In the primordial model, a subset of the Milky Way satellites formed with their current properties with minimal modifications by tidal stripping. However, the primordial model produces too many bright ($L_V > 10^5 L_\odot$) satellites at all distances from the Milky Way. Our attempts to reduce the bright satellite problem while preserving the fossils are summarized below.

- Lower H_2 formation rates and subsequent lower minihalo star formation rates in the voids are not able to bring the number of bright satellites into agreement with observations.
- Effectively lowering the star formation efficiency can fix the bright satellite problem if we assume only pre-reionization halos with $M < 7 \times 10^6$ $\mathrm{M}_\odot$ had SFR dominated by local, stochastic feedback. However, not only is this contrary to current understanding of star formation in minihalos, but the fossil population this "solution" produces cannot reproduce the distribution of the ultra-faint population.
- We bring the number of bright satellites into agreement with observations,

> while leaving the fossil population untouched, by assuming the primordial stellar populations of our non-fossils (with maximum circular velocities, $v_{max}(z = 0) > v_{filter}$) become extremely diffuse via kinetic energy from galaxy mergers. The existence of "ghost halos" of primordial stars is a new powerful observational prediction of our model that can be straight forwardly tested using HST observations of isolated dwarfs around the Local Group.

We have suggested two solutions which correct for the overabundance of bright satellites while preserving at least a fraction of the primordial fossil population. Each presents a different picture when we consider it in the context of the voids. The first, and less effective, solution calls for a low star formation efficiency. In this picture, the 10^{10} $M_\odot$ halos visible in current surveys will have their star formation dampened, however as we move to $\sim 10^7$ $M_\odot$ we enter the regime where stochastic feedback effects dominate over the choice of ϵ_*. Thus, the voids would appear relatively empty, but only because we cannot yet detect the less than 10^5 $L_\odot$ fossil populations which formed in the 10^7 $M_\odot$ halos before reionization.

The dispersal of the non-fossils' primordial populations into ghost halos is a more effective solution to the "bright satellite problem" within 1 Mpc of the Milky Way, but leaves a conundrum in the voids. Regardless of whether the primordial population would be detectable, how do we keep the post-reionization star formation in these non-fossils low enough to prevent this later star formation from producing more $M_V > -16$ galaxies than are currently observed?

Any post-reionization star formation in the non-fossils results in a young population which would be (i) brighter, (ii) more concentrated, since enriched gas will cool faster and sink deeper into the gravitational potential, and (iii) possibly accompanied by an H I reservoir. Any of these properties would make the post-reionization population easier to see, and the non-fossil harder to hide. To suppress the post-reionization baryonic evolution in the non-fossils, we examine our naive assumption that they all undergo significant baryonic evolution after reionization.

The easiest way to suppress star formation in the lower mass non-fossils is to raise the filtering velocity. As has already been discussed in Chapter 4, any non-fossil embedded in the WHIM ($T \sim 10^5$ K) would have a $v_{filter} \sim 40$ km s^{-1}. However, the WHIM is predicted to exist at $z < 1$ (Smith et al. 2010), leaving $\sim$ 6 Gyr after reionization when the non-fossils could have accreted gas and formed stars. A final possibility is that reionization was extremely efficient at quenching star formation in $20 - 40$ km s^{-1} halos and the non-fossils were never able to build up enough gas from the post-reionization IGM to form additional stars.

In summary, while the bright satellite problem can be "solved" for the primordial population alone, we still need to account for the post-reionization evolution of the non-fossils. In order to maintain the agreement with observations, only $\sim$ 10% of the non-fossils can form significant stellar populations after reionization. Determining how and if the other $\sim$ 90% can be suppressed will tell us how much of a problem the bright satellite problem is.

Chapter 6

Observational Tests for the Primordial Model

In this chapter, we present a set of observational tests which can provide support for a primordial formation scenario for the faintest Milky Way satellites and constrain models of high redshift star formation. We will begin with what the currently known ultra-faints can tells us, before presenting a set of predictions for the properties of the ~ 100 undetected fossils the primordial model predicts are orbiting the Milky Way. We then explain what the current number of known satellites and the number which will be detected, or not, by upcoming surveys can tell us about star formation in minihalos at high redshift. Finally, we discuss two predictions for more distant, isolated non-fossils and fossils; the ghost halos and late stage gas accretion.

6.1 The Ultra-Faint Dwarfs

6.1.1 Tidal Disruption

Better determination of whether the ultra-faints are being tidally disrupted can help determine whether a subset of the faintest Milky Way satellites are pristine fossils. The ultra-faint dwarfs whose r_{hl} do not match our simulated true fossils, shown as filled green circles in Figures 4.1 - 4.8, display the signs of being tidally disrupted by the Milky Way, including proximity to the Milky Way ($R < 50$ kpc). While Willman 1, Segue 1 & 2, Leo V, and Pisces II show signs of tidal disruption, this does not prove the primordial scenario. However, it would place their origin as disrupted objects in line with our proposal in § 4.1.1 and 4.2. If additional observations show these tidal ultra-faints are *not* tidally disrupted, then our primordial formation model can not explain their current properties. The exception to this picture is Segue 1. The tidal status of Segue 1 has been recently debated (Martinez et al. 2010; Niederste-Ostholt et al. 2009; Norris et al. 2010b; Simon et al. 2010) and it remains unclear whether it is a disrupting system or a highly concentrated halo which formed at high redshift in a rare, high σ peak.

6.1.2 The Undetected Dwarfs

We next outline the stellar properties we can expect of the undetected dwarfs around the Milky Way if they are part of a population of fossils of the first galaxies. The red contours of Figures 4.1 - 4.8 show the properties of the predicted population.

1. *Half-light radii*

   The undetected dwarfs should have the same distribution of half-light radii as the currently known, ultra-faint population, from ~ 100 pc to ~ 1000 pc.

2. *Mass to Light Ratio*

   The mass to light ratio of undetected dwarfs should generally be greater than $10^3 M_\odot/L_\odot$ and as high as approximately $10^5 M_\odot/L_\odot$ and follow a roughly linear relation for dwarfs with $L_V < 10^5 L_\odot$.

3. *Stellar velocity dispersion*

   There should be no decrease in the stellar velocity dispersion, σ_*, with V-band luminosity. This directly contradicts the decreasing σ_* with L_V seen for tidally stripped dwarfs in Figure 4 of Wadepuhl and Springel (2010).

4. *Metallicity*

   The undetected dwarfs should have typical $[Fe/H] < -2.5$, a significant number with $[Fe/H] < -3.0$. This would make these undetected dwarfs excellent candidates for the search for ultra-metal poor stars (Frebel and Bromm 2010; Frebel et al. 2010; Norris et al. 2010a,b,c).

6.1.3 Number of Satellites

The number of Milky Way satellites alone provides a test for star formation in minihalos. For a given filtering velocity, there is a number of satellites, N_{nf}, which have a v_{max}^{max} above the filtering velocity. Roughly, v_{max}^{max} occurs as the halo falls into the Milky Way, before its accumulated mass has enough time to be tidally stripped. For $v_{filter} = 20$ km s^{-1}, N_{nf} is 90 ± 10 and for $v_{filter} = 30$ km s^{-1}, N_{nf} is 60 ± 8, the latter is equivalent to the number of currently known Milky Way satellites after applying the sky coverage correction. If the number of satellites, N_{sat}, is greater than N_{nf}, some minihalos had to have formed stars before reionization. Conversely, if $N_{sat} < N_{nf}$, either no minihalos formed stars or none survived near the Milky Way.

6.2 Into the Voids

Although the existence of pre-reionization fossils seems likely, observations do not unequivocally demonstrate their existence due to the large uncertainties in estimating the number of yet undiscovered ultra-faint dwarfs (Tollerud et al. 2008). In this section, we summarize three observational tests for the existence of fossils of the first galaxies that we propose based on our results. The first test of our model is especially interesting as it can be performed using HST observations and does not require waiting for future all sky surveys deeper than SDSS, like PanSTARRS or LSST, to be online.

1. *"Ghost halos" around dwarfs on the outskirts of the Local Group*

   The primordial stellar populations in minihalos that formed before reionization should produce diffuse "ghost halos" of primordial stars around isolated dwarfs. We have shown that the total luminosity of the "ghost halos" is comparable to the one of classical dwarfs, but the surface brightness of the stars is well below the SDSS detection limits. Contrary to the difficulties of finding ultra-faints, we know where these diffuse stars are and we can plan deep observations to detect them. The diffuse primordial stellar populations around non-fossils should not be tidally stripped in dwarfs with galactocentric distance > 1 Mpc from the Milky Way. We do not know within which distance tidal stripping would become important, but due to their large half light radii, they certainly are the stellar population that would be stripped first. "Ghost halos" can be best detected by resolving their individual main sequence stars around isolated dIrrs or dSphs before using spectra to determine their metallicities and dynamics. Unlike younger stars dispersed from the central galaxy, the primordial ghost halo would have a $[Fe/H] < -2.5$, and we are currently running simulations to determine their dynamics.

Recent HST observations of M31 have resolved the main sequence using ACS (Brown et al. 2008, 2009, 2006). A low-luminosity dwarf at $\sim$ 800 kpc on the other side of the Milky Way from M31 would be an excellent candidate for the ghost halo search, and detection of its main-sequence primordial stars would be within the reach of HST. At 800 kpc, the field of view of WFC3 (162") is $\sim$ 630 pc, at 1 Mpc, $\sim$ 785 pc, and at 2 Mpc, $\sim$ 1.6 kpc. The ghost halos are > 1 kpc, often up to a few tens of kpc in radius therefore, WFC3 would not be able to image the entire dwarf with its ghost halo. However, aimed at the outskirts of a likely ghost halo host, it could look for signs of a primordial halo in the color magnitude diagram and radial surface brightness distribution. We would be able to resolve the individual stars in the ghost halos at $\sim$ 1 Mpc. The ghost halos have surface densities of stars of 0.001 and 1 star pc^{-2} depending on the extent of the ghost halos and the slope of the IMF at low masses. Assuming a stellar density of 1 star pc^{-2}, the angular distance between each star is $\sim 0.26''$, larger than the WFC3 resolution of $0.04''$ per pixel. Since the stellar population can be resolved, determining the details of a ghost halo population is a matter of taking deep enough exposure to detect the main sequence stars and differentiate those faint stars from the extremely distant, equally faint background galaxies. Red giant branch stars, while brighter and easier to detect, have a density three orders of magnitude lower than the main sequence.

Deep observations work well for detecting the ghost halos when we already know where they are. These primordial populations surround dwarf galaxies that have undergone significant star formation since reionization and may have detectable gas and active star formation today. However, as discussed in

§ 5.1.4, in order to reproduce the observed satellite distribution, only a fraction of the ghost halos can have formed a significant younger stellar population. We remind the reader that our definition of a fossil versus a non-fossil in the simulations assumes a constant $v_{filter} = 20$ km s^{-1}. Assuming a larger filtering velocity would produce a smaller number of non-fossils (see Table 2.7). Therefore, some of the halos we define as non-fossils, and containing ghost halos, may have been unable to accrete gas and form stars after reionization due to additional heating of the IGM. This population of "dead" ghost halos would have only an extremely diffuse, primordial population. Without H I or more concentrated, younger stars, the best chance for detecting these ghost halos would be large scale surveys. Figure 5.8 shows that the majority of the ghost halos are beyond the reach of the SDSS, but what about upcoming, deeper surveys such as PanSTARRS?

Diffuse stellar systems like the ultra-faint dwarfs and the ghost halos are found in surveys by looking for overdensities of stars relative to the background. In many cases, by detecting stars at the tip of the red giant branch (RGB). In low luminosity systems the detection of the RGB depends on two factors, the distance to the halo and the population of the RGB. Low luminosity systems, like the ultra-faint dwarfs, can have as few as a thousand stars, and therefore a sparsely populated, and difficult to detect, RGB. For example, with SDSS (magnitude limit r = 22.5) Hercules ($1.1 \times 10^4 L_\odot$) could only be detected to 300 kpc, while the more luminous CVn I ($2.3 \times 10^5 L_\odot$) would be seen at a Mpc from the Milky Way (Koposov et al. 2008). PanSTARRS (magnitude limit r=24) will reach 1.5 magnitudes deeper that SDSS, detecting the same RGB twice as far. However, the primordial populations in the ghost halos are *extremely* diffuse, and it is unclear that the overdensity of their RGB stars would be high enough to be detected against foreground M dwarfs and distant galaxies. In short, while PanSTARRS is expected to detect new ultra-faint dwarfs, it may not the best tool for finding ghost halos.

If some of the discovered ultra-faint dwarfs are fossils, then "ghost halos" should exist. Vice versa, the detection of "ghost halos," regardless of the method, can be used to constrain the star formation rates before reionization and would imply the existence of fossils, although these fossils may not have yet been discovered due to their low surface brightnesses.

2. *Dark and ultra-faint gas rich dwarfs in the voids*

   According to the model proposed in Ricotti (2009), a subset of minihalos in the voids may have been able to condense gas from the IGM after Helium II reionization (at $z \sim 3$). However, they would not form stars unless their gas reached a critical density that is dependent on the metallicity of the gas. These minihalos may or may not have formed stars before reionization, and any stellar populations they did have would be below the detection limits of both current and future surveys. The H I in these objects could be detected by blind 21 cm surveys. Recently, ALFALFA and GALFA surveys have reported the discovery of several small and compact clouds of neutral hydrogen, some of which may represent a population of pre-reionization minihalos. Some of these clouds could be "dark galaxies" and represent the smallest detectable halos around the Milky Way and others may be ultra-faint dwarfs in the voids. The location of unassociated H I detections could then guide optical surveys to these primordial fossils in a focused deep search for their ancient populations.

Chapter 7

Summary and Future Work

Below we summarize the results of this dissertation before briefly sketching out our future plans. The bullet points are compiled from the Discussion and Conclusions sections of Bovill and Ricotti (2009, 2010a,b).

Conclusions

- Voids contain many low luminosity fossil galaxies. However they have surface brightnesses and luminosities making them undetectable by SDSS. One possible way to detect these void dwarfs is if they experience a late phase of gas condensation from the IGM as proposed in (Ricotti 2009). Future and present 21cm surveys such as ALFALFA and GALFA may be used to find these objects (Begum et al. 2010; Giovanelli et al. 2005).

- We find a linear scaling relation between the number of luminous satellites and the mass of host halos. The scaling has scatter similar to the relationship between the total number of sub-halos with $M > 10^7$ M$_\odot$ ($v_{max} > 5$ km s^{-1}) and the host mass, although the normalization is $3 - 4$ times lower.

- Due to the dependence of the properties of primordial dwarfs on their formation environment (Ricotti et al. 2008), we find very few true fossils with $L_V > 10^6 L_\odot$, and none within 1 Mpc of our Milky Ways. This places the identification of some of the more luminous classical dSphs fossils in doubt.

- Overall $\sim 25\%$ (for $v_{filter} = 20$ km s^{-1}) to $\sim 30\%$ (for $v_{filter} = 30$ km s^{-1}) of the primordial fossils at the present day have undergone a merger with another luminous fossil. This fraction increases with the modern luminosity of the dwarf. Hence, the typical half light radii of this population can be larger than the original distribution at reionization. These fossils are even harder to detect due to their lower surface brightness. This effect also increases the spread of the relationship between half light radii vs. luminosity and surface brightness vs. luminosity of fossils at $z = 0$.

- Leo V, Coma Berenics, Segue 2 and Willman 1 have half light radii which are too small, and metallicities too large, for their luminosities. Due to their proximity to the Milky Way, we speculate that their stars and dark halos have been affected by tides. Hence, these ultra-faints may represent a population of massive primordial dwarfs which have lost $\gtrsim 90\%$ of their stars via tidal interactions.

- We reiterate the existence of a yet undetected population of fossils with luminosities $L_V < 10^4$ L$_\odot$ and surface brightness $< 10^{-1.4} L_\odot$ /pc^2 . We present plots showing, in detail, the expected properties of this population. We also notice that some of the new ultra-faint satellites in Andromeda have half light radii in agreement with the properties of the undetected fossil population, but luminosities $\sim 10^5 L_\odot$.

- We are able to reproduce the distribution of the ultra-faints with our simulated primordial fossils. We find no missing satellites at the lower end of the mass and luminosity functions, but our model predicts ~ 150 additional Milky Way satellites that can be found in upcoming deeper surveys (PanSTARRS, LSST).

- At all radii, we see an overabundance of bright ($L_V > 10^4$ $\mathrm{L}_\odot$) satellites which, even with only their primordial luminosities, would be easily detected by current surveys. Given the agreement between the stellar properties and distributions of the ultra-faints and those of our fossil dwarfs, we cannot account for the excess bright satellites by imposing a blanket suppression of star formation below a given mass.

- Lower H_2 formation rates and subsequent lower minihalo star formation rates in the voids are not able to bring the number of bright satellites into agreement with observations.

- Effectively lowering the star formation efficiency can fix the bright satellite problem if we assume only pre-reionization halos with $M < 7 \times 10^6$ $\mathrm{M}_\odot$ had SFR dominated by local, stochastic feedback. However, not only is this contrary to current understanding of star formation in minihalos, but the fossil population this "solution" produces cannot reproduce the distribution of the ultra-faint population.

- We bring the number of bright satellites into agreement with observations, while leaving the fossil population untouched, by assuming the primordial stellar populations of our non-fossils (with maximum circular velocities, $v_{max}(z = 0) > v_{filter}$) become extremely diffuse via kinetic energy from galaxy mergers. The existence of "ghost halos" of primordial stars is a new powerful observational prediction of our model that can be easily tested using HST observations of isolated dwarfs around the Local Group.

Simulating the Ghost Halos

We are currently running a set of higher resolution simulations to determine the radial distribution and dynamics of the primordial population in the ghost halos. To do this, we need to resolve the stellar populations during the galaxy mergers to determine how much the primordial stars have been puffed up by the galaxy and dark mergers. In addition, we want to derive an estimate of the primordial stellar mass lost during mergers to refine our calculations of the properties of fossils and non-fossils which have undergone galaxy mergers.

Generating the initial conditions for the new simulations uses the same method described in Chapter 3, with one significant difference. After we have identified an isolated $10^9 - 10^{10} M_\odot$ halo at $z = 0$, we build a high resolution region which contains the component pre-reionization halos of our $z = 0$ non-fossil. Unlike the simulations presented in this thesis, the high resolution region of the new simulations will trace the *stellar and dark matter particles* of the pre-reionization simulation instead of the halos. This will allow us to resolve the dynamical evolution of the chosen non-fossil from reionization to the present. We note that, once again, we are not including the post-reionization baryonic evolution of our halo and assuming that all star formation was quenched by reionization.

Our current initial conditions have a mass resolution of $m_{dm} = 4935.3\ M_\odot$ for the dark matter particles and $m_{st} \sim 10^2 - 10^4 M_\odot$ for the stellar particles in a $1 \times 1 \times 2$ Mpc^3 region embedded within our 50^3 Mpc^3 box. As this thesis is printed we are attempting to discern if and how we can increase the new simulation's speed so it will use a reasonable amount of computational resources.

Bibliography

Abazajian, K. N., Adelman-McCarthy, J. K., Agüeros, M. A., Allam, S. S., Allende Prieto, C., An, D., Anderson, K. S. J., Anderson, S. F., Annis, J., Bahcall, N. A., and et al. (2009). The Seventh Data Release of the Sloan Digital Sky Survey. *ApJS*, 182:543–558.

Adelman-McCarthy, J. K., Agüeros, M. A., Allam, S. S., Allende Prieto, C., Anderson, K. S. J., Anderson, S. F., Annis, J., Bahcall, N. A., Bailer-Jones, C. A. L., Baldry, I. K., Barentine, J. C., Bassett, B. A., Becker, A. C., Beers, T. C., Bell, E. F., Berlind, A. A., Bernardi, M., Blanton, M. R., Bochanski, J. J., Boroski, W. N., Brinchmann, J., Brinkmann, J., Brunner, R. J., Budavári, T., Carliles, S., Carr, M. A., Castander, F. J., Cinabro, D., Cool, R. J., Covey, K. R., Csabai, I., Cunha, C. E., Davenport, J. R. A., Dilday, B., Doi, M., Eisenstein, D. J., Evans, M. L., Fan, X., Finkbeiner, D. P., Friedman, S. D., Frieman, J. A., Fukugita, M., Gänsicke, B. T., Gates, E., Gillespie, B., Glazebrook, K., Gray, J., Grebel, E. K., Gunn, J. E., Gurbani, V. K., Hall, P. B., Harding, P., Harvanek, M., Hawley, S. L., Hayes, J., Heckman, T. M., Hendry, J. S., Hindsley, R. B., Hirata, C. M., Hogan, C. J., Hogg, D. W., Hyde, J. B., Ichikawa, S., Ivezić, Ž., Jester, S., Johnson, J. A., Jorgensen, A. M., Jurić, M., Kent, S. M., Kessler, R., Kleinman, S. J., Knapp, G. R., Kron, R. G., Krzesinski, J., Kuropatkin, N., Lamb, D. Q., Lampeitl, H., Lebedeva, S., Lee, Y. S., Leger, R. F., Lépine, S., Lima, M., Lin, H., Long, D. C., Loomis, C. P., Loveday, J., Lupton, R. H., Malanushenko, O., Malanushenko, V., Mandelbaum, R., Margon, B., Marriner, J. P., Martínez-Delgado, D., Matsubara, T., McGehee, P. M., McKay, T. A., Meiksin, A., Morrison, H. L., Munn, J. A., Nakajima, R., Neilsen, Jr., E. H., Newberg, H. J., Nichol, R. C., Nicinski, T., Nieto-Santisteban, M., Nitta, A., Okamura, S., Owen, R., Oyaizu, H., Padmanabhan, N., Pan, K., Park, C., Peoples, Jr., J., Pier, J. R., Pope, A. C., Purger, N., Raddick, M. J., Re Fiorentin, P., Richards, G. T., Richmond, M. W., Riess, A. G., Rix, H., Rockosi, C. M., Sako, M., Schlegel, D. J., Schneider, D. P., Schreiber, M. R., Schwope, A. D., Seljak, U., Sesar, B., Sheldon, E., Shimasaku, K., Sivarani, T., Smith, J. A., Snedden, S. A., Steinmetz, M., Strauss, M. A., SubbaRao, M., Suto, Y., Szalay, A. S., Szapudi, I., Szkody, P., Tegmark, M., Thakar, A. R., Tremonti, C. A., Tucker, D. L., Uomoto, A., Vanden Berk, D. E., Vandenberg, J., Vidrih, S., Vogeley, M. S., Voges, W., Vogt, N. P., Wadadekar, Y., Weinberg, D. H., West, A. A., White, S. D. M., Wilhite, B. C., Yanny, B., Yocum, D. R., York, D. G., Zehavi, I., and Zucker, D. B. (2008). The Sixth Data Release of the Sloan Digital Sky Survey. *ApJS*, 175:297–313.

Adelman-McCarthy, J. K., Agüeros, M. A., Allam, S. S., Anderson, K. S. J., Anderson, S. F., Annis, J., Bahcall, N. A., Bailer-Jones, C. A. L., Baldry, I. K., Barentine, J. C., Beers, T. C., Belokurov, V., Berlind, A., Bernardi, M., Blanton, M. R., Bochanski, J. J., Boroski, W. N., Bramich, D. M., Brewington, H. J., Brinchmann, J., Brinkmann, J., Brunner, R. J., Budavári, T., Carey, L. N., Carliles, S., Carr, M. A., Castander, F. J., Connolly, A. J., Cool, R. J., Cunha, C. E., Csabai, I., Dalcanton, J. J., Doi, M., Eisenstein, D. J., Evans, M. L., Evans, N. W., Fan, X., Finkbeiner, D. P., Friedman, S. D., Frieman, J. A., Fukugita, M., Gillespie, B., Gilmore, G., Glazebrook, K., Gray, J., Grebel, E. K., Gunn, J. E., de Haas, E., Hall, P. B., Harvanek, M., Hawley, S. L., Hayes, J., Heckman, T. M., Hendry, J. S., Hennessy, G. S., Hindsley, R. B., Hirata, C. M., Hogan, C. J., Hogg, D. W., Holtzman, J. A., Ichikawa, S.-i., Ichikawa, T., Ivezić, Ž., Jester, S., Johnston, D. E., Jorgensen, A. M., Jurić, M., Kauffmann, G., Kent, S. M., Kleinman, S. J., Knapp, G. R., Kniazev, A. Y., Kron, R. G., Krzesinski, J., Kuropatkin, N., Lamb, D. Q., Lampeitl, H., Lee, B. C., Leger, R. F., Lima, M., Lin, H., Long, D. C., Loveday, J., Lupton, R. H., Mandelbaum, R., Margon, B., Martínez-Delgado, D., Matsubara, T., McGehee, P. M., McKay, T. A., Meiksin, A., Munn, J. A., Nakajima, R., Nash, T., Neilsen, Jr., E. H., Newberg, H. J., Nichol, R. C., Nieto-Santisteban, M., Nitta, A., Oyaizu, H., Okamura, S., Ostriker, J. P., Padmanabhan, N., Park, C., Peoples, J. J., Pier, J. R., Pope, A. C., Pourbaix, D., Quinn, T. R., Raddick, M. J., Re Fiorentin, P., Richards, G. T., Richmond, M. W., Rix, H.-W., Rockosi, C. M., Schlegel, D. J., Schneider, D. P., Scranton, R., Seljak, U., Sheldon, E., Shimasaku, K., Silvestri, N. M., Smith, J. A., Smolčić, V., Snedden, S. A., Stebbins, A., Stoughton, C., Strauss, M. A., SubbaRao, M., Suto, Y., Szalay, A. S., Szapudi, I., Szkody, P., Tegmark, M., Thakar, A. R., Tremonti, C. A., Tucker, D. L., Uomoto, A., Vanden Berk, D. E., Vandenberg, J., Vidrih, S., Vogeley, M. S., Voges, W., Vogt, N. P., Weinberg, D. H., West, A. A., White, S. D. M., Wilhite, B., Yanny, B., Yocum, D. R., York, D. G., Zehavi, I., Zibetti, S., and Zucker, D. B. (2007). The Fifth Data Release of the Sloan Digital Sky Survey. *ApJS*, 172:634–644.

Adelman-McCarthy, J. K., Agüeros, M. A., Allam, S. S., Anderson, K. S. J., Anderson, S. F., Annis, J., Bahcall, N. A., Baldry, I. K., Barentine, J. C., Berlind, A., Bernardi, M., Blanton, M. R., Boroski, W. N., Brewington, H. J., Brinchmann, J., Brinkmann, J., Brunner, R. J., Budavári, T., Carey, L. N., Carr, M. A., Castander, F. J., Connolly, A. J., Csabai, I., Czarapata, P. C., Dalcanton, J. J., Doi, M., Dong, F., Eisenstein, D. J., Evans, M. L., Fan, X., Finkbeiner, D. P., Friedman, S. D., Frieman, J. A., Fukugita, M., Gillespie, B., Glazebrook, K., Gray, J., Grebel, E. K., Gunn, J. E., Gurbani, V. K., de Haas, E., Hall, P. B., Harris, F. H., Harvanek, M., Hawley, S. L., Hayes, J., Hendry, J. S., Hennessy, G. S., Hindsley, R. B., Hirata, C. M., Hogan, C. J., Hogg, D. W., Holmgren, D. J., Holtzman, J. A., Ichikawa, S.-i., Ivezić, Ž., Jester, S., Johnston, D. E., Jorgensen, A. M., Jurić, M., Kent, S. M., Kleinman, S. J., Knapp, G. R., Kniazev, A. Y., Kron, R. G., Krzesinski, J., Kuropatkin, N., Lamb, D. Q., Lampeitl, H., Lee, B. C., Leger, R. F., Lin, H., Long, D. C., Loveday, J., Lupton, R. H., Margon, B., Martínez-Delgado, D., Mandelbaum, R., Matsubara, T., McGehee, P. M., McKay, T. A., Meiksin, A., Munn, J. A., Nakajima, R., Nash, T., Neilsen, Jr., E. H., Newberg, H. J., Newman, P. R., Nichol, R. C., Nicinski, T., Nieto-Santisteban, M., Nitta, A., O'Mullane, W., Okamura, S., Owen, R., Padmanabhan, N., Pauls, G., Peoples, J. J., Pier, J. R., Pope, A. C., Pourbaix, D., Quinn, T. R., Richards, G. T., Richmond, M. W., Rockosi, C. M., Schlegel, D. J., Schneider, D. P., Schroeder, J., Scranton, R., Seljak, U., Sheldon, E., Shimasaku, K., Smith, J. A., Smolčić, V., Snedden, S. A., Stoughton, C., Strauss, M. A., SubbaRao, M., Szalay, A. S., Szapudi, I., Szkody, P., Tegmark, M., Thakar, A. R., Tucker, D. L., Uomoto, A., Vanden Berk, D. E., Vandenberg, J., Vogeley, M. S., Voges, W., Vogt, N. P., Walkowicz, L. M., Weinberg, D. H., West, A. A., White, S. D. M., Xu, Y., Yanny, B., Yocum, D. R., York, D. G., Zehavi, I., Zibetti, S., and Zucker, D. B. (2006). The Fourth Data Release of the Sloan Digital Sky Survey. *ApJS*, 162:38–48.

Ahn, K., Shapiro, P. R., Alvarez, M. A., Iliev, I. T., Martel, H., and Ryu, D. (2006). The 21 centimeter background from the cosmic dark ages: Minihalos and the intergalactic medium before reionization. *New Astronomy Review*, 50:179–183.

Babul, A. and Rees, M. J. (1992). On dwarf elliptical galaxies and the faint blue counts. *MNRAS*, 255:346–350.

Babusiaux, C., Gilmore, G., and Irwin, M. (2005). A near-infrared and optical photometric study of the Sculptor dwarf spheroidal galaxy: implications for the metallicity spread. *MNRAS*, 359:985–992.

Becker, R. H., Fan, X., White, R. L., Strauss, M. A., Narayanan, V. K., Lupton, R. H., Gunn, J. E., Annis, J., Bahcall, N. A., Brinkmann, J., Connolly, A. J., Csabai, I., Czarapata, P. C., Doi, M., Heckman, T. M., Hennessy, G. S., Ivezić, Ž., Knapp, G. R., Lamb, D. Q., McKay, T. A., Munn, J. A., Nash, T., Nichol, R., Pier, J. R., Richards, G. T., Schneider, D. P., Stoughton, C., Szalay, A. S., Thakar, A. R., and York, D. G. (2001). Evidence for Reionization at z˜6: Detection of a Gunn-Peterson Trough in a z=6.28 Quasar. *AJ*, 122:2850–2857.

Begum, A., Stanimirović, S., Peek, J. E., Ballering, N. P., Heiles, C., Douglas, K. A., Putman, M., Gibson, S. J., Grcevich, J., Korpela, E. J., Lee, M., Saul, D., and Gallagher, J. S. (2010). Compact H I Clouds from the GALFA-H I Survey. *ApJ*, 722:395–411.

Belokurov, V., Walker, M. G., Evans, N. W., Faria, D. C., Gilmore, G., Irwin, M. J., Koposov, S., Mateo, M., Olszewski, E., and Zucker, D. B. (2008). Leo V: A Companion of a Companion of the Milky Way Galaxy? *ApJ*, 686:L83–L86.

Belokurov, V., Walker, M. G., Evans, N. W., Gilmore, G., Irwin, M. J., Just, D., Koposov, S., Mateo, M., Olszewski, E., Watkins, L., and Wyrzykowski, L. (2010). Big Fish, Little Fish: Two New Ultra-faint Satellites of the Milky Way. *ApJ*, 712:L103–L106.

Belokurov, V., Walker, M. G., Evans, N. W., Gilmore, G., Irwin, M. J., Mateo, M., Mayer, L., Olszewski, E., Bechtold, J., and Pickering, T. (2009). The discovery of Segue 2: a prototype of the population of satellites of satellites. *MNRAS*, 397:1748–1755.

Belokurov, V., Zucker, D. B., Evans, N. W., Kleyna, J. T., Koposov, S., Hodgkin,

S. T., Irwin, M. J., Gilmore, G., Wilkinson, M. I., Fellhauer, M., Bramich, D. M., Hewett, P. C., Vidrih, S., De Jong, J. T. A., Smith, J. A., Rix, H.-W., Bell, E. F., Wyse, R. F. G., Newberg, H. J., Mayeur, P. A., Yanny, B., Rockosi, C. M., Gnedin, O. Y., Schneider, D. P., Beers, T. C., Barentine, J. C., Brewington, H., Brinkmann, J., Harvanek, M., Kleinman, S. J., Krzesinski, J., Long, D., Nitta, A., and Snedden, S. A. (2007). Cats and Dogs, Hair and a Hero: A Quintet of New Milky Way Companions. *ApJ*, 654:897–906.

Belokurov, V., Zucker, D. B., Evans, N. W., Wilkinson, M. I., Irwin, M. J., Hodgkin, S., Bramich, D. M., Irwin, J. M., Gilmore, G., Willman, B., Vidrih, S., Newberg, H. J., Wyse, R. F. G., Fellhauer, M., Hewett, P. C., Cole, N., Bell, E. F., Beers, T. C., Rockosi, C. M., Yanny, B., Grebel, E. K., Schneider, D. P., Lupton, R., Barentine, J. C., Brewington, H., Brinkmann, J., Harvanek, M., Kleinman, S. J., Krzesinski, J., Long, D., Nitta, A., Smith, J. A., and Snedden, S. A. (2006). A Faint New Milky Way Satellite in Bootes. *ApJ*, 647:L111–L114.

Benson, A. J., Sugiyama, N., Nusser, A., and Lacey, C. G. (2006). The epoch of reionization. *MNRAS*, 369:1055–1080.

Bovill, M. S. and Ricotti, M. (2009). Pre-Reionization Fossils, Ultra-Faint Dwarfs, and the Missing Galactic Satellite Problem. *ApJ*, 693:1859–1870.

Bovill, M. S. and Ricotti, M. (2010a). Where are the Fossils of the First Galaxies? I. Local Volume Maps and Properties of the Undetected Dwarfs. *ArXiv e-prints*.

Bovill, M. S. and Ricotti, M. (2010b). Where are the Fossils of the First Galaxies? II. True Fossils, Ghost Halos, and the Missing Bright Satellites. *ArXiv e-prints*.

Bozek, B., Wyse, R. F. G., and Gilmore, G. F. (2011). Clustering of Milky Way Dwarf Galaxies. In *American Astronomical Society Meeting Abstracts #217*, volume 43 of *Bulletin of the American Astronomical Society*, page 147.06.

Brasseur, C. M. (2011). personal communication.

Brown, T. M., Beaton, R., Chiba, M., Ferguson, H. C., Gilbert, K. M., Guhathakurta, P., Iye, M., Kalirai, J. S., Koch, A., Komiyama, Y., Majewski, S. R., Reitzel, D. B., Renzini, A., Rich, R. M., Smith, E., Sweigart, A. V., and Tanaka, M. (2008). The Extended Star Formation History of the Andromeda Spheroid at 35 kpc on the Minor Axis. *ApJ*, 685:L121–L124.

Brown, T. M., Smith, E., Ferguson, H. C., Guhathakurta, P., Kalirai, J. S., Kimble, R. A., Renzini, A., Rich, R. M., Sweigart, A. V., and Vanden Berg, D. A. (2009). Deep Optical Photometry of Six Fields in the Andromeda Galaxy. *ApJS*, 184:152–157.

Brown, T. M., Smith, E., Ferguson, H. C., Rich, R. M., Guhathakurta, P., Renzini, A., Sweigart, A. V., and Kimble, R. A. (2006). The Detailed Star Formation History in the Spheroid, Outer Disk, and Tidal Stream of the Andromeda Galaxy. *ApJ*, 652:323–353.

Bullock, J. S., Stewart, K. R., Kaplinghat, M., Tollerud, E. J., and Wolf, J. (2010). Stealth Galaxies in the Halo of the Milky Way. *ApJ*, 717:1043–1053.

Chapman, S. C., Peñarrubia, J., Ibata, R., McConnachie, A., Martin, N., Irwin, M., Blain, A., Lewis, G. F., Letarte, B., Lo, K., Ludlow, A., and O'neil, K. (2007). Strangers in the Night: Discovery of a Dwarf Spheroidal Galaxy on Its First Local Group Infall. *ApJ*, 662:L79–L82.

Choi, J., Weinberg, M. D., and Katz, N. (2009). The dynamics of satellite disruption in cold dark matter haloes. *MNRAS*, 400:1247–1263.

Cioni, M.-R. L. and Habing, H. J. (2005). The Draco dwarf galaxy in the near-infrared. *A&A*, 442:165–176.

Cole, S. (1997). Adding Long-Wavelength Power to N-body simulations. *MNRAS*, 286:38–47.

Collins, M. L. M., Chapman, S. C., Irwin, M. J., Martin, N. F., Ibata, R. A., Zucker,

D. B., Blain, A., Ferguson, A. M. N., Lewis, G. F., McConnachie, A. W., and Peñarrubia, J. (2010). A Keck/DEIMOS spectroscopic survey of the faint M31 satellites AndIX, AndXI, AndXII and AndXIII†. *MNRAS*, 407:2411–2433.

Collins, M. L. M., Chapman, S. C., Rich, R. M., Ibata, R. A., Irwin, M. J., Peñarrubia, J., Arimoto, N., Brooks, A. M., Lewis, G. F., McConnachie, A. W., and Venn, K. (2011). The scatter about the "Universal" dwarf spheroidal mass profile: A kinematic study of the M31 satellites, And V and And VI. *ArXiv e-prints*.

Crain, R. A., Theuns, T., Dalla Vecchia, C., Eke, V. R., Frenk, C. S., Jenkins, A., Kay, S. T., Peacock, J. A., Pearce, F. R., Schaye, J., Springel, V., Thomas, P. A., White, S. D. M., and Wiersma, R. P. C. (2009). Galaxies-intergalactic medium interaction calculation - I. Galaxy formation as a function of large-scale environment. *MNRAS*, 399:1773–1794.

Dall'Ora, M., Clementini, G., Kinemuchi, K., Ripepi, V., Marconi, M., Di Fabrizio, L., Greco, C., Rodgers, C. T., Kuehn, C., and Smith, H. A. (2006). Variable Stars in the Newly Discovered Milky Way Satellite in Bootes. *ApJ*, 653:L109–L112.

Davis, M., Efstathiou, G., Frenk, C. S., and White, S. D. M. (1985). The evolution of large-scale structure in a universe dominated by cold dark matter. *ApJ*, 292:371–394.

de Jong, J. T. A., Harris, J., Coleman, M. G., Martin, N. F., Bell, E. F., Rix, H.-W., Hill, J. M., Skillman, E. D., Sand, D. J., Olszewski, E. W., Zaritsky, D., Thompson, D., Giallongo, E., Ragazzoni, R., DiPaola, A., Farinato, J., Testa, V., and Bechtold, J. (2008). The Structural Properties and Star Formation History of Leo T from Deep LBT Photometry. *ApJ*, 680:1112–1119.

Diemand, J., Kuhlen, M., and Madau, P. (2007). Dark Matter Substructure and Gamma-Ray Annihilation in the Milky Way Halo. *ApJ*, 657:262–270.

Diemand, J., Kuhlen, M., Madau, P., Zemp, M., Moore, B., Potter, D., and Stadel, J. (2008). Clumps and streams in the local dark matter distribution. *Nature*, 454:735–738.

Efstathiou, G. (1992). Suppressing the formation of dwarf galaxies via photoionization. *MNRAS*, 256:43P–47P.

Eisenstein, D. J. and Hut, P. (1998). HOP: A New Group-Finding Algorithm for N-Body Simulations. *ApJ*, 498:137–+.

Fan, X., Narayanan, V. K., Strauss, M. A., White, R. L., Becker, R. H., Pentericci, L., and Rix, H.-W. (2002). Evolution of the Ionizing Background and the Epoch of Reionization from the Spectra of z˜6 Quasars. *AJ*, 123:1247–1257.

Fan, X., Strauss, M. A., Becker, R. H., White, R. L., Gunn, J. E., Knapp, G. R., Richards, G. T., Schneider, D. P., Brinkmann, J., and Fukugita, M. (2006). Constraining the Evolution of the Ionizing Background and the Epoch of Reionization with z˜6 Quasars. II. A Sample of 19 Quasars. *AJ*, 132:117–136.

Frebel, A. and Bromm, V. (2010). Dwarf archaeology: Probing the first enrichment events with low-luminosity galaxies. *ArXiv e-prints*.

Frebel, A., Simon, J. D., Geha, M., and Willman, B. (2010). High-Resolution Spectroscopy of Extremely Metal-Poor Stars in the Least Evolved Galaxies: Ursa Major II and Coma Berenices. *ApJ*, 708:560–583.

Geha, M., Willman, B., Simon, J. D., Strigari, L. E., Kirby, E. N., Law, D. R., and Strader, J. (2009). The Least-Luminous Galaxy: Spectroscopy of the Milky Way Satellite Segue 1. *ApJ*, 692:1464–1475.

Giovanelli, R., Haynes, M. P., Kent, B. R., Perillat, P., Saintonge, A., Brosch, N., Catinella, B., Hoffman, G. L., Stierwalt, S., Spekkens, K., Lerner, M. S., Masters, K. L., Momjian, E., Rosenberg, J. L., Springob, C. M., Boselli, A., Charmandaris, V., Darling, J. K., Davies, J., Garcia Lambas, D., Gavazzi, G., Giovanardi, C., Hardy, E., Hunt, L. K., Iovino, A., Karachentsev, I. D., Karachentseva, V. E., Koopmann, R. A., Marinoni, C., Minchin, R., Muller, E., Putman, M., Pantoja, C., Salzer, J. J., Scodeggio, M., Skillman, E., Solanes, J. M., Valotto, C., van Driel, W., and van Zee, L. (2005). The Arecibo Legacy Fast ALFA Survey. I. Science Goals, Survey Design, and Strategy. *AJ*, 130:2598–2612.

Gnedin, N. Y. (2000). Local Group Dwarf Galaxies and the Star Formation Law at High Redshift. *ApJ*, 535:L75–L78.

Gnedin, N. Y. and Kravtsov, A. V. (2006). Fossils of Reionization in the Local Group. *ApJ*, 645:1054–1061.

Haiman, Z., Rees, M. J., and Loeb, A. (1996). H 2 Cooling of Primordial Gas Triggered by UV Irradiation. *ApJ*, 467:522–+.

Harbeck, D., Gallagher, J. S., Grebel, E. K., Koch, A., and Zucker, D. B. (2005). Andromeda IX: Properties of the Faintest M31 Dwarf Satellite Galaxy. *ApJ*, 623:159–163.

Hoeft, M., Yepes, G., Gottlöber, S., and Springel, V. (2006). Dwarf galaxies in voids: suppressing star formation with photoheating. *MNRAS*, 371:401–414.

Ibata, R., Martin, N. F., Irwin, M., Chapman, S., Ferguson, A. M. N., Lewis, G. F., and McConnachie, A. W. (2007). The Haunted Halos of Andromeda and Triangulum: A Panorama of Galaxy Formation in Action. *ApJ*, 671:1591–1623.

Illingworth, G. (1976). The masses of globular clusters. II - Velocity dispersions and mass-to-light ratios. *ApJ*, 204:73–93.

Irwin, M. J., Belokurov, V., Evans, N. W., Ryan-Weber, E. V., de Jong, J. T. A., Koposov, S., Zucker, D. B., Hodgkin, S. T., Gilmore, G., Prema, P., Hebb, L., Begum, A., Fellhauer, M., Hewett, P. C., Kennicutt, Jr., R. C., Wilkinson, M. I., Bramich, D. M., Vidrih, S., Rix, H.-W., Beers, T. C., Barentine, J. C., Brewington, H., Harvanek, M., Krzesinski, J., Long, D., Nitta, A., and Snedden, S. A.

(2007). Discovery of an Unusual Dwarf Galaxy in the Outskirts of the Milky Way. *ApJ*, 656:L13–L16.

Irwin, M. J., Ferguson, A. M. N., Huxor, A. P., Tanvir, N. R., Ibata, R. A., and Lewis, G. F. (2008). Andromeda XVII: A New Low-Luminosity Satellite of M31. *ApJ*, 676:L17–L20.

Jacobs, B. A., Tully, R. B., Rizzi, L., Karachentsev, I. D., Chiboucas, K., and Held, E. V. (2011). The Star Formation History of Isolated Dwarf UGC 4879. *AJ*, 141:106–+.

Johnson, J. L., Greif, T. H., Bromm, V., Klessen, R. S., and Ippolito, J. (2009). The first galaxies: signatures of the initial starburst. *MNRAS*, 399:37–47.

Kalirai, J. S., Beaton, R. L., Geha, M. C., Gilbert, K. M., Guhathakurta, P., Kirby, E. N., Majewski, S. R., Ostheimer, J. C., Patterson, R. J., and Wolf, J. (2010). The SPLASH Survey: Internal Kinematics, Chemical Abundances, and Masses of the Andromeda I, II, III, VII, X, and XIV Dwarf Spheroidal Galaxies. *ApJ*, 711:671–692.

Kallivayalil, N., Besla, G., Sanderson, R., and Alcock, C. (2009). Revisiting the Role of M31 in the Dynamical History of the Magellanic Clouds. *ApJ*, 700:924–930.

Karachentsev, I. D. (2005). The Local Group and Other Neighboring Galaxy Groups. *AJ*, 129:178–188.

Karachentsev, I. D., Dolphin, A., Tully, R. B., Sharina, M., Makarova, L., Makarov, D., Karachentseva, V., Sakai, S., and Shaya, E. J. (2006). Advanced Camera for Surveys Imaging of 25 Galaxies in Nearby Groups and in the Field. *AJ*, 131:1361–1376.

Karachentsev, I. D., Karachentseva, V. E., Huchtmeier, W. K., and Makarov, D. I. (2004). A Catalog of Neighboring Galaxies. *AJ*, 127:2031–2068.

Karachentsev, I. D., Makarov, D. I., Sharina, M. E., Dolphin, A. E., Grebel, E. K., Geisler, D., Guhathakurta, P., Hodge, P. W., Karachentseva, V. E., Sarajedini, A., and Seitzer, P. (2003). Local galaxy flows within 5 Mpc. *A&A*, 398:479–491.

Kirby, E. N., Cohen, J. G., Smith, G. H., Majewski, S. R., Sohn, S. T., and Guhathakurta, P. (2011a). Multi-element Abundance Measurements from Medium-resolution Spectra. IV. Alpha Element Distributions in Milky Way Satellite Galaxies. *ApJ*, 727:79–+.

Kirby, E. N., Lanfranchi, G. A., Simon, J. D., Cohen, J. G., and Guhathakurta, P. (2011b). Multi-element Abundance Measurements from Medium-resolution Spectra. III. Metallicity Distributions of Milky Way Dwarf Satellite Galaxies. *ApJ*, 727:78–+.

Kirby, E. N., Simon, J. D., Geha, M., Guhathakurta, P., and Frebel, A. (2008). Uncovering Extremely Metal-Poor Stars in the Milky Way's Ultrafaint Dwarf Spheroidal Satellite Galaxies. *ApJ*, 685:L43–L46.

Klypin, A., Kravtsov, A. V., Valenzuela, O., and Prada, F. (1999). Where Are the Missing Galactic Satellites? *ApJ*, 522:82–92.

Klypin, A., Zhao, H., and Somerville, R. S. (2002). ΛCDM-based Models for the Milky Way and M31. I. Dynamical Models. *ApJ*, 573:597–613.

Knollmann, S. R. and Knebe, A. (2009). AHF: Amiga's Halo Finder. *ApJS*, 182:608–624.

Koch, A., Wilkinson, M. I., Kleyna, J. T., Irwin, M., Zucker, D. B., Belokurov, V., Gilmore, G. F., Fellhauer, M., and Evans, N. W. (2009). A Spectroscopic Confirmation of the Bootes II Dwarf Spheroidal. *ApJ*, 690:453–462.

Komatsu, E., Smith, K. M., Dunkley, J., Bennett, C. L., Gold, B., Hinshaw, G., Jarosik, N., Larson, D., Nolta, M. R., Page, L., Spergel, D. N., Halpern, M., Hill, R. S., Kogut, A., Limon, M., Meyer, S. S., Odegard, N., Tucker, G. S., Weiland, J. L., Wollack, E., and Wright, E. L. (2011). Seven-year Wilkinson Microwave

Anisotropy Probe (WMAP) Observations: Cosmological Interpretation. *ApJS*, 192:18–+.

Koposov, S., Belokurov, V., Evans, N. W., Hewett, P. C., Irwin, M. J., Gilmore, G., Zucker, D. B., Rix, H.-W., Fellhauer, M., Bell, E. F., and Glushkova, E. V. (2008). The Luminosity Function of the Milky Way Satellites. *ApJ*, 686:279–291.

Kormendy, J. and Freeman, K. C. (2004). Scaling Laws for Dark Matter Halos in Late-Type and Dwarf Spheroidal Galaxies. In *IAU Symposium*, pages 377–+.

Kravtsov, A. V., Gnedin, O. Y., and Klypin, A. A. (2004). The Tumultuous Lives of Galactic Dwarfs and the Missing Satellites Problem. *ApJ*, 609:482–497.

Kroupa, P., Theis, C., and Boily, C. M. (2005). The great disk of Milky-Way satellites and cosmological sub-structures. *A&A*, 431:517–521.

Leitherer, C., Schaerer, D., Goldader, J. D., Delgado, R. M. G., Robert, C., Kune, D. F., de Mello, D. F., Devost, D., and Heckman, T. M. (1999). Starburst99: Synthesis Models for Galaxies with Active Star Formation. *ApJS*, 123:3–40.

Letarte, B., Chapman, S. C., Collins, M., Ibata, R. A., Irwin, M. J., Ferguson, A. M. N., Lewis, G. F., Martin, N., McConnachie, A., and Tanvir, N. (2009). A Keck/DEIMOS spectroscopic survey of the faint M31 satellites AndXV and AndXVI. *MNRAS*, 400:1472–1478.

Li, Y. and White, S. D. M. (2008). Masses for the Local Group and the Milky Way. *MNRAS*, 384:1459–1468.

Madau, P., Diemand, J., and Kuhlen, M. (2008). Dark Matter Subhalos and the Dwarf Satellites of the Milky Way. *ApJ*, 679:1260–1271.

Majewski, S. R., Beaton, R. L., Patterson, R. J., Kalirai, J. S., Geha, M. C., Muñoz, R. R., Seigar, M. S., Guhathakurta, P., Gilbert, K. M., Rich, R. M., Bullock, J. S., and Reitzel, D. B. (2007). Discovery of Andromeda XIV: A Dwarf Spheroidal Dynamical Rogue in the Local Group? *ApJ*, 670:L9–L12.

Makino, N., Sasaki, S., and Suto, Y. (1998). X-Ray Gas Density Profile of Clusters of Galaxies from the Universal Dark Matter Halo. *ApJ*, 497:555–+.

Martin, N. F., de Jong, J. T. A., and Rix, H.-W. (2008). A Comprehensive Maximum Likelihood Analysis of the Structural Properties of Faint Milky Way Satellites. *ApJ*, 684:1075–1092.

Martin, N. F., Ibata, R. A., Chapman, S. C., Irwin, M., and Lewis, G. F. (2007). A Keck/DEIMOS spectroscopic survey of faint Galactic satellites: searching for the least massive dwarf galaxies. *MNRAS*, 380:281–300.

Martin, N. F., Ibata, R. A., Irwin, M. J., Chapman, S., Lewis, G. F., Ferguson, A. M. N., Tanvir, N., and McConnachie, A. W. (2006). Discovery and analysis of three faint dwarf galaxies and a globular cluster in the outer halo of the Andromeda galaxy. *MNRAS*, 371:1983–1991.

Martin, N. F., McConnachie, A. W., Irwin, M., Widrow, L. M., Ferguson, A. M. N., Ibata, R. A., Dubinski, J., Babul, A., Chapman, S., Fardal, M., Lewis, G. F., Navarro, J., and Rich, R. M. (2009). PAndAS' CUBS: Discovery of Two New Dwarf Galaxies in the Surroundings of the Andromeda and Triangulum Galaxies. *ApJ*, 705:758–765.

Martinez, G. D., Minor, Q. E., Bullock, J., Kaplinghat, M., Simon, J. D., and Geha, M. (2010). A Complete Spectroscopic Survey of the Milky Way satellite Segue 1: Dark matter content, stellar membership and binary properties from a Bayesian analysis. *ArXiv e-prints*.

Mateo, M. L. (1998). Dwarf Galaxies of the Local Group. *ARA&A*, 36:435–506.

Mayer, L., Kazantzidis, S., Mastropietro, C., and Wadsley, J. (2007). Early gas stripping as the origin of the darkest galaxies in the Universe. *Nature*, 445:738–740.

Mayer, L., Mastropietro, C., Wadsley, J., Stadel, J., and Moore, B. (2006). Simultaneous ram pressure and tidal stripping; how dwarf spheroidals lost their gas. *MNRAS*, 369:1021–1038.

McConnachie, A. W., Huxor, A., Martin, N. F., Irwin, M. J., Chapman, S. C., Fahlman, G., Ferguson, A. M. N., Ibata, R. A., Lewis, G. F., Richer, H., and Tanvir, N. R. (2008). A Trio of New Local Group Galaxies with Extreme Properties. *ApJ*, 688:1009–1020.

McConnachie, A. W., Irwin, M. J., Ibata, R. A., Dubinski, J., Widrow, L. M., Martin, N. F., Côté, P., Dotter, A. L., Navarro, J. F., Ferguson, A. M. N., Puzia, T. H., Lewis, G. F., Babul, A., Barmby, P., Bienaymé, O., Chapman, S. C., Cockcroft, R., Collins, M. L. M., Fardal, M. A., Harris, W. E., Huxor, A., Mackey, A. D., Peñarrubia, J., Rich, R. M., Richer, H. B., Siebert, A., Tanvir, N., Valls-Gabaud, D., and Venn, K. A. (2009). The remnants of galaxy formation from a panoramic survey of the region around M31. *Nature*, 461:66–69.

McGaugh, S. S., Schombert, J. M., Bothun, G. D., and de Blok, W. J. G. (2000). The Baryonic Tully-Fisher Relation. *ApJ*, 533:L99–L102.

McGaugh, S. S., Schombert, J. M., de Blok, W. J. G., and Zagursky, M. J. (2010). The Baryon Content of Cosmic Structures. *ApJ*, 708:L14–L17.

McGaugh, S. S. and Wolf, J. (2010). Local Group Dwarf Spheroidals: Correlated Deviations from the Baryonic Tully-Fisher Relation. *ArXiv e-prints*.

Metz, M., Kroupa, P., and Jerjen, H. (2007). The spatial distribution of the Milky Way and Andromeda satellite galaxies. *MNRAS*, 374:1125–1145.

Metz, M., Kroupa, P., and Jerjen, H. (2009). Discs of satellites: the new dwarf spheroidals. *MNRAS*, 394:2223–2228.

Mirabel, I. F., Dijkstra, M., Laurent, P., Loeb, A., and Pritchard, J. R. (2011). Stellar black holes at the dawn of the universe. *A&A*, 528:A149+.

Moore, B., Ghigna, S., Governato, F., Lake, G., Quinn, T., Stadel, J., and Tozzi, P.

(1999). Dark Matter Substructure within Galactic Halos. *ApJ*, 524:L19–L22.

Naab, T., Johansson, P. H., and Ostriker, J. P. (2009). Minor Mergers and the Size Evolution of Elliptical Galaxies. *ApJ*, 699:L178–L182.

Navarro, J. F., Frenk, C. S., and White, S. D. M. (1996). The Structure of Cold Dark Matter Halos. *ApJ*, 462:563–+.

Navarro, J. F. and Steinmetz, M. (1997). The Effects of a Photoionizing Ultraviolet Background on the Formation of Disk Galaxies. *ApJ*, 478:13–+.

Niederste-Ostholt, M., Belokurov, V., Evans, N. W., Gilmore, G., Wyse, R. F. G., and Norris, J. E. (2009). The origin of Segue 1. *MNRAS*, 398:1771–1781.

Norris, J. E., Gilmore, G., Wyse, R. F. G., Yong, D., and Frebel, A. (2010a). An Extremely Carbon-rich, Extremely Metal-poor Star in the Segue 1 System. *ApJ*, 722:L104–L109.

Norris, J. E., Wyse, R. F. G., Gilmore, G., Yong, D., Frebel, A., Wilkinson, M. I., Belokurov, V., and Zucker, D. B. (2010b). Chemical Enrichment in the Faintest Galaxies: the Carbon and Iron Abundance Spreads in the Bo\"otes I Dwarf Spheroidal Galaxy and the Segue 1 System. *ArXiv e-prints*.

Norris, J. E., Yong, D., Gilmore, G., and Wyse, R. F. G. (2010c). Boo-1137: an Extremely Metal-Poor Star in the Ultra-Faint Dwarf Spheroidal Galaxy Boötes I. *ApJ*, 711:350–360.

Okamoto, T., Gao, L., and Theuns, T. (2008). Mass loss of galaxies due to an ultraviolet background. *MNRAS*, 390:920–928.

Peñarrubia, J., McConnachie, A. W., and Navarro, J. F. (2008a). The Cold Dark Matter Halos of Local Group Dwarf Spheroidals. *ApJ*, 672:904–913.

Peñarrubia, J., Navarro, J. F., and McConnachie, A. W. (2008b). The Tidal Evolution of Local Group Dwarf Spheroidals. *ApJ*, 673:226–240.

Peebles, P. J. E. (2001). The Void Phenomenon. *ApJ*, 557:495–504.

Polisensky, E. and Ricotti, M. (2010). Constraints on the Dark Matter Particle Mass from the Number of Milky Way Satellites. *ArXiv e-prints*.

Press, W. H. and Schechter, P. (1974). Formation of Galaxies and Clusters of Galaxies by Self-Similar Gravitational Condensation. *ApJ*, 187:425–438.

Quinn, T., Katz, N., and Efstathiou, G. (1996). Photoionization and the formation of dwarf galaxies. *MNRAS*, 278:L49–L54.

Reed, D. S., Bower, R., Frenk, C. S., Jenkins, A., and Theuns, T. (2007). The halo mass function from the dark ages through the present day. *MNRAS*, 374:2–15.

Richardson, J. C., Irwin, M., McConnachie, A. W., Martin, N. F., Dotter, A., Ferguson, A. M. N., Ibata, R. A., Chapman, S., Lewis, G. F., Tanvir, N. R., and Rich, R. M. (2011). PAndAS' progeny: extending the M31 dwarf galaxy cabal. *ArXiv e-prints*.

Ricotti, M. (2003). Dependence of the inner dark matter profile on the halo mass. *MNRAS*, 344:1237–1249.

Ricotti, M. (2009). Late gas accretion on to primordial minihaloes: a model for Leo T, dark galaxies and extragalactic high-velocity clouds. *MNRAS*, 392:L45–L49.

Ricotti, M. and Gnedin, N. Y. (2005). Formation Histories of Dwarf Galaxies in the Local Group. *ApJ*, 629:259–267.

Ricotti, M., Gnedin, N. Y., and Shull, J. M. (2001). Feedback from Galaxy Formation: Production and Photodissociation of Primordial H_2. *ApJ*, 560:580–591.

Ricotti, M., Gnedin, N. Y., and Shull, J. M. (2002a). The Fate of the First Galaxies. I. Self-consistent Cosmological Simulations with Radiative Transfer. *ApJ*, 575:33–48.

Ricotti, M., Gnedin, N. Y., and Shull, J. M. (2002b). The Fate of the First Galaxies. II. Effects of Radiative Feedback. *ApJ*, 575:49–67.

Ricotti, M., Gnedin, N. Y., and Shull, J. M. (2008). The Fate of the First Galaxies.

III. Properties of Primordial Dwarf Galaxies and Their Impact on the Intergalactic Medium. *ApJ*, 685:21–39.

Ricotti, M. and Ostriker, J. P. (2004). X-ray pre-ionization powered by accretion on the first black holes - I. A model for the WMAP polarization measurement. *MNRAS*, 352:547–562.

Ricotti, M., Ostriker, J. P., and Gnedin, N. Y. (2005). X-ray pre-ionization powered by accretion on the first black holes - II. Cosmological simulations and observational signatures. *MNRAS*, 357:207–219.

Ripamonti, E., Mapelli, M., and Zaroubi, S. (2008). Radiation from early black holes - I. Effects on the neutral intergalactic medium. *MNRAS*, 387:158–172.

Saigo, K., Matsumoto, T., and Umemura, M. (2004). The Formation of Population III Binaries. *ApJ*, 615:L65–L68.

Salvadori, S. and Ferrara, A. (2009). Ultra faint dwarfs: probing early cosmic star formation. *MNRAS*, 395:L6–L10.

Shapiro, P. R., Giroux, M. L., and Babul, A. (1994). Reionization in a cold dark matter universe: The feedback of galaxy formation on the intergalactic medium. *ApJ*, 427:25–50.

Shapiro, P. R., Iliev, I. T., and Raga, A. C. (2004). Photoevaporation of cosmological minihaloes during reionization. *MNRAS*, 348:753–782.

Sheth, K. (2011). personal communication.

Shetrone, M., Venn, K. A., Tolstoy, E., Primas, F., Hill, V., and Kaufer, A. (2003). VLT/UVES Abundances in Four Nearby Dwarf Spheroidal Galaxies. I. Nucleosynthesis and Abundance Ratios. *AJ*, 125:684–706.

Shull, J. M. and Venkatesan, A. (2008). Constraints on First-Light Ionizing Sources from Optical Depth of the Cosmic Microwave Background. *ApJ*, 685:1–7.

Siegel, M. H., Shetrone, M. D., and Irwin, M. (2008). Trimming Down the Willman

1 dSph. *AJ*, 135:2084–2094.

Simon, J. D. and Geha, M. (2007). The Kinematics of the Ultra-faint Milky Way Satellites: Solving the Missing Satellite Problem. *ApJ*, 670:313–331.

Simon, J. D., Geha, M., Minor, Q. E., Martinez, G. D., Kirby, E. N., Bullock, J. S., Kaplinghat, M., Strigari, L. E., Willman, B., Choi, P. I., Tollerud, E. J., and Wolf, J. (2010). A Complete Spectroscopic Survey of the Milky Way Satellite Segue 1: The Darkest Galaxy. *ArXiv e-prints*.

Smith, B. D., Hallman, E. J., Shull, J. M., and O'Shea, B. W. (2010). The Nature of the Warm/Hot Intergalactic Medium I. Numerical Methods, Convergence, and OVI Absorption. *ArXiv e-prints*.

Sokasian, A., Yoshida, N., Abel, T., Hernquist, L., and Springel, V. (2004). Cosmic reionization by stellar sources: population III stars. *MNRAS*, 350:47–65.

Springel, V. (2005). The cosmological simulation code GADGET-2. *MNRAS*, 364:1105–1134.

Springel, V., Wang, J., Vogelsberger, M., Ludlow, A., Jenkins, A., Helmi, A., Navarro, J. F., Frenk, C. S., and White, S. D. M. (2008). The Aquarius Project: the subhaloes of galactic haloes. *MNRAS*, 391:1685–1711.

Stark, D. V., McGaugh, S. S., and Swaters, R. A. (2009). A First Attempt to Calibrate the Baryonic Tully-Fisher Relation with Gas-Dominated Galaxies. *AJ*, 138:392–401.

Stinson, G. S., Dalcanton, J. J., Quinn, T., Kaufmann, T., and Wadsley, J. (2007). Breathing in Low-Mass Galaxies: A Study of Episodic Star Formation. *ApJ*, 667:170–175.

Strigari, L. E., Bullock, J. S., Kaplinghat, M., Simon, J. D., Geha, M., Willman, B., and Walker, M. G. (2008). A common mass scale for satellite galaxies of the Milky Way. *Nature*, 454:1096–1097.

Susa, H. and Umemura, M. (2004). Formation of Dwarf Galaxies during the Cosmic Reionization. *ApJ*, 600:1–16.

Tassis, K., Kravtsov, A. V., and Gnedin, N. Y. (2008). Scaling Relations of Dwarf Galaxies without Supernova-driven Winds. *ApJ*, 672:888–903.

Thoul, A. A. and Weinberg, D. H. (1996). Hydrodynamic Simulations of Galaxy Formation. II. Photoionization and the Formation of Low-Mass Galaxies. *ApJ*, 465:608–+.

Tikhonov, A. V. and Klypin, A. (2009). The emptiness of voids: yet another overabundance problem for the Λ cold dark matter model. *MNRAS*, 395:1915–1924.

Tinker, J. L. and Conroy, C. (2009). The Void Phenomenon Explained. *ApJ*, 691:633–639.

Tollerud, E. J., Bullock, J. S., Strigari, L. E., and Willman, B. (2008). Hundreds of Milky Way Satellites? Luminosity Bias in the Satellite Luminosity Function. *ApJ*, 688:277–289.

Tolstoy, E., Venn, K. A., Shetrone, M., Primas, F., Hill, V., Kaufer, A., and Szeifert, T. (2003). VLT/UVES Abundances in Four Nearby Dwarf Spheroidal Galaxies. II. Implications for Understanding Galaxy Evolution. *AJ*, 125:707–726.

Tormen, G. and Bertschinger, E. (1996). Adding Long-Wavelength Modes to an N-Body Simulation. *ApJ*, 472:14–+.

Trachternach, C., de Blok, W. J. G., McGaugh, S. S., van der Hulst, J. M., and Dettmar, R. (2009). The baryonic Tully-Fisher relation and its implication for dark matter halos. *A&A*, 505:577–587.

Trenti, M., Stiavelli, M., Bouwens, R. J., Oesch, P., Shull, J. M., Illingworth, G. D., Bradley, L. D., and Carollo, C. M. (2010). The Galaxy Luminosity Function During the Reionization Epoch. *ApJ*, 714:L202–L207.

Tully, R., Rizzi, L., Dolphin, A., Karachentsev, I., Karachentseva, V., Makarov, D., Makarova, L., Sakai, S., and Shaya, E. (2006). Associations of Dwarf Galaxies. *ArXiv Astrophysics e-prints*.

van der Marel, R. P. and Guhathakurta, P. (2008). M31 Transverse Velocity and Local Group Mass from Satellite Kinematics. *ApJ*, 678:187–199.

Venkatesan, A., Giroux, M. L., and Shull, J. M. (2001). Heating and Ionization of the Intergalactic Medium by an Early X-Ray Background. *ApJ*, 563:1–8.

Verheijen, M. A. W. (2001). The Ursa Major Cluster of Galaxies. V. H I Rotation Curve Shapes and the Tully-Fisher Relations. *ApJ*, 563:694–715.

Wadepuhl, M. and Springel, V. (2010). Satellite galaxies in hydrodynamical simulations of Milky Way sized galaxies. *ArXiv e-prints*.

Walker, M. G., Belokurov, V., Evans, N. W., Irwin, M. J., Mateo, M., Olszewski, E. W., and Gilmore, G. (2009). Leo V: Spectroscopy of a Distant and Disturbed Satellite. *ApJ*, 694:L144–L147.

Walker, M. G., McGaugh, S. S., Mateo, M., Olszewski, E. W., and Kuzio de Naray, R. (2010). Comparing the Dark Matter Halos of Spiral, Low Surface Brightness, and Dwarf Spheroidal Galaxies. *ApJ*, 717:L87–L91.

Walsh, S. M., Jerjen, H., and Willman, B. (2007). A Pair of Boötes: A New Milky Way Satellite. *ApJ*, 662:L83–L86.

Walsh, S. M., Willman, B., and Jerjen, H. (2009). The Invisibles: A Detection Algorithm to Trace the Faintest Milky Way Satellites. *AJ*, 137:450–469.

Walsh, S. M., Willman, B., Sand, D., Harris, J., Seth, A., Zaritsky, D., and Jerjen, H. (2008). Boötes II ReBoöted: An MMT/MegaCam Study of an Ultrafaint Milky Way Satellite. *ApJ*, 688:245–253.

Watkins, L. L., Evans, N. W., and An, J. H. (2010). The masses of the Milky Way and Andromeda galaxies. *MNRAS*, 406:264–278.

Whalen, D., O'Shea, B. W., Smidt, J., and Norman, M. L. (2008). How the First

Stars Regulated Local Star Formation. I. Radiative Feedback. *ApJ*, 679:925–941.

Willman, B., Blanton, M. R., West, A. A., Dalcanton, J. J., Hogg, D. W., Schneider, D. P., Wherry, N., Yanny, B., and Brinkmann, J. (2005a). A New Milky Way Companion: Unusual Globular Cluster or Extreme Dwarf Satellite? *AJ*, 129:2692–2700.

Willman, B., Dalcanton, J. J., Martinez-Delgado, D., West, A. A., Blanton, M. R., Hogg, D. W., Barentine, J. C., Brewington, H. J., Harvanek, M., Kleinman, S. J., Krzesinski, J., Long, D., Neilsen, Jr., E. H., Nitta, A., and Snedden, S. A. (2005b). A New Milky Way Dwarf Galaxy in Ursa Major. *ApJ*, 626:L85–L88.

Wise, J. H. and Cen, R. (2009). Ionizing Photon Escape Fractions From High-Redshift Dwarf Galaxies. *ApJ*, 693:984–999.

Wolf, J., Martinez, G. D., Bullock, J. S., Kaplinghat, M., Geha, M., Muñoz, R. R., Simon, J. D., and Avedo, F. F. (2010). Accurate masses for dispersion-supported galaxies. *MNRAS*, pages 778–+.

Yanny, B., Rockosi, C., Newberg, H. J., Knapp, G. R., Adelman-McCarthy, J. K., Alcorn, B., Allam, S., Allende Prieto, C., An, D., Anderson, K. S. J., Anderson, S., Bailer-Jones, C. A. L., Bastian, S., Beers, T. C., Bell, E., Belokurov, V., Bizyaev, D., Blythe, N., Bochanski, J. J., Boroski, W. N., Brinchmann, J., Brinkmann, J., Brewington, H., Carey, L., Cudworth, K. M., Evans, M., Evans, N. W., Gates, E., Gänsicke, B. T., Gillespie, B., Gilmore, G., Gomez-Moran, A. N., Grebel, E. K., Greenwell, J., Gunn, J. E., Jordan, C., Jordan, W., Harding, P., Harris, H., Hendry, J. S., Holder, D., Ivans, I. I., Ivezič, Ž., Jester, S., Johnson, J. A., Kent, S. M., Kleinman, S., Kniazev, A., Krzesinski, J., Kron, R., Kuropatkin, N., Lebedeva, S., Lee, Y. S., Leger, R. F., Lépine, S., Levine, S., Lin, H., Long, D. C., Loomis, C., Lupton, R., Malanushenko, O., Malanushenko, V., Margon, B., Martinez-Delgado, D., McGehee, P., Monet, D., Morrison, H. L., Munn, J. A., Neilsen, E. H., Nitta, A., Norris, J. E., Oravetz, D., Owen, R., Padmanabhan, N., Pan, K., Peterson, R. S., Pier, J. R., Platson, J., Fiorentin, P. R., Richards, G. T., Rix, H., Schlegel, D. J., Schneider, D. P., Schreiber, M. R., Schwope, A., Sibley, V., Simmons, A., Snedden, S. A., Smith, J. A., Stark, L., Stauffer, F., Steinmetz, M., Stoughton, C., Subba Rao, M., Szalay, A., Szkody, P., Thakar, A. R., Thirupathi, S., Tucker, D., Uomoto, A., Vanden Berk, D., Vidrih, S., Wadadekar, Y., Watters, S., Wilhelm, R., Wyse, R. F. G., Yarger, J., and Zucker, D. (2009). SEGUE: A Spectroscopic Survey of 240,000 Stars with g = 14-20. *AJ*, 137:4377–4399.

Zaritsky, D., Olszewski, E. W., Schommer, R. A., Peterson, R. C., and Aaronson, M. (1989). Velocities of stars in remote Galactic satellites and the mass of the Galaxy. *ApJ*, 345:759–769.

Zentner, A. R. and Bullock, J. S. (2003). Halo Substructure and the Power Spectrum. *ApJ*, 598:49–72.

Zentner, A. R., Kravtsov, A. V., Gnedin, O. Y., and Klypin, A. A. (2005). The Anisotropic Distribution of Galactic Satellites. *ApJ*, 629:219–232.

Zucker, D. B., Belokurov, V., Evans, N. W., Kleyna, J. T., Irwin, M. J., Wilkinson, M. I., Fellhauer, M., Bramich, D. M., Gilmore, G., Newberg, H. J., Yanny, B., Smith, J. A., Hewett, P. C., Bell, E. F., Rix, H.-W., Gnedin, O. Y., Vidrih, S., Wyse, R. F. G., Willman, B., Grebel, E. K., Schneider, D. P., Beers, T. C., Kniazev, A. Y., Barentine, J. C., Brewington, H., Brinkmann, J., Harvanek, M., Kleinman, S. J., Krzesinski, J., Long, D., Nitta, A., and Snedden, S. A. (2006a). A Curious Milky Way Satellite in Ursa Major. *ApJ*, 650:L41–L44.

Zucker, D. B., Belokurov, V., Evans, N. W., Wilkinson, M. I., Irwin, M. J., Sivarani, T., Hodgkin, S., Bramich, D. M., Irwin, J. M., Gilmore, G., Willman, B., Vidrih, S., Fellhauer, M., Hewett, P. C., Beers, T. C., Bell, E. F., Grebel, E. K., Schneider,

D. P., Newberg, H. J., Wyse, R. F. G., Rockosi, C. M., Yanny, B., Lupton, R., Smith, J. A., Barentine, J. C., Brewington, H., Brinkmann, J., Harvanek, M., Kleinman, S. J., Krzesinski, J., Long, D., Nitta, A., and Snedden, S. A. (2006b). A New Milky Way Dwarf Satellite in Canes Venatici. *ApJ*, 643:L103–L106.

Zucker, D. B., Kniazev, A. Y., Bell, E. F., Martínez-Delgado, D., Grebel, E. K., Rix, H.-W., Rockosi, C. M., Holtzman, J. A., Walterbos, R. A. M., Annis, J., York, D. G., Ivezić, Ž., Brinkmann, J., Brewington, H., Harvanek, M., Hennessy, G., Kleinman, S. J., Krzesinski, J., Long, D., Newman, P. R., Nitta, A., and Snedden, S. A. (2004). Andromeda IX: A New Dwarf Spheroidal Satellite of M31. *ApJ*, 612:L121–L124.

Zucker, D. B., Kniazev, A. Y., Martínez-Delgado, D., Bell, E. F., Rix, H.-W., Grebel, E. K., Holtzman, J. A., Walterbos, R. A. M., Rockosi, C. M., York, D. G., Barentine, J. C., Brewington, H., Brinkmann, J., Harvanek, M., Kleinman, S. J., Krzesinski, J., Long, D., Neilsen, Jr., E. H., Nitta, A., and Snedden, S. A. (2007). Andromeda X, a New Dwarf Spheroidal Satellite of M31: Photometry. *ApJ*, 659:L21–L24.